Universidad de Alcalá

Campus Universitario
Dpto. de Teoría de la Señal y Comunicaciones
Ctra. Madrid-Barcelona, Km. 36.6
28805 Alcalá de Henares (Madrid)
Telf: +34 91 885 66 90
Fax: +34 91 885 66 99

D. ROBERTO GÓMEZ GARCÍA, Profesor Titular de Universidad del Área de Conocimiento de Teoría de la Señal y Comunicaciones de la Universidad de Alcalá, y Dª. DIMITRA PSYCHOGIOU, Investigador Científico Senior de Universidad del Área de Conocimento de Ingeniería Eléctrica e Informática de la Universidad de Purdue,

CERTIFICAN

Que la tesis **"Advanced Microwave Filtering Devices Based on Signal-Interference Techniques"**, presentada por D. Raúl Loeches Sánchez, realizada en el Departamento de Teoría de la Señal y Comunicaciones bajo nuestra dirección, reúne méritos suficientes para optar al grado de Doctor, por lo que puede procederse a su depósito y defensa.

Alcalá de Henares, de de 2016.

Fdo. Dr. D. Roberto Gómez García Fdo. Dr. Dª. Dimitra Psychogiou

Universidad de Alcalá

Campus Universitario
Dpto. de Teoría de la Señal y Comunicaciones
Ctra. Madrid-Barcelona, Km. 36.6
28805 Alcalá de Henares (Madrid)
Telf: +34 91 885 66 90
Fax: +34 91 885 66 99

D. Raúl Loeches Sánchez ha realizado en el Departamento de Teoría de la Señal y Comunicaciones y bajo la dirección del Dr. D. Roberto Gómez García y del Dr. D^{a}. Dimitra Psychogiou, la tesis doctoral titulada **"Advanced Microwave Filtering Devices Based on Signal-Interference Techniques"**, cumpliéndose todos los requisitos para la tramitación que conduce a su posterior lectura.

Alcalá de Henares, de de 2016.

EL COORDINADOR DEL PROGRAMA DE DOCTORADO

Fdo. Dr. D. Sancho Salcedo Sanz

UNIVERSIDAD DE ALCALÁ

ADVANCED MICROWAVE FILTERING DEVICES BASED ON SIGNAL-INTERFERENCE TECHNIQUES

PHD THESIS

Raúl Loeches Sánchez
PhD Candidate

2016

DEPARTAMENTO DE TEORÍA DE LA SEÑAL Y COMUNICACIONES

Universidad de Alcalá

ADVANCED MICROWAVE FILTERING DEVICES BASED ON SIGNAL-INTERFERENCE TECHNIQUES

PHD THESIS

Author:

Raúl Loeches Sánchez

PhD Candidate

Advisors:

Roberto Gómez García

Associate Professor with the Department of Signal Theory and Communications
University of Alcalá

Dimitra Psychogiou

Senior Research Scientist with the Department of Electrical and Computer Engineering
Purdue University

2016

Tesis Doctoral

ADVANCED MICROWAVE FILTERING DEVICES BASED ON SIGNAL-INTERFERENCE TECHNIQUES

AUTOR: Raúl Loeches Sánchez
DIRECTORES: Roberto Gómez García
Dimitra Psychogiou

El tribunal nombrado por el Mgfco. y Excmo. Sr. Rector de la Universidad de Alcalá, el día __ de _____ de 2016.

PRESIDENTE:

VOCALES:

SECRETARIO:

Realizado el acto de defensa y lectura de la Tesis el día __ de _____ de 2016, en Alcalá de Henares.

Calificación:

EL PRESIDENTE LOS VOCALES

EL VOCAL SECRETARIO

Dedicado a los que me acompañan en la aventura de la vida

«Sé breve en tus razonamientos,
que ninguno hay gustoso si es largo.»

Miguel de Cervantes.

Institutional Acknowledgements

Among the projects and fellowships with different institutions that have given support to the developed research activities, it must be highlighted that:

- The research of this Ph.D. Thesis has been supported in part by the Community of Madrid and the University of Alcalá, under the regional project "Arquitecturas Multi-Frecuencia de Banda Ultra-Ancha para Radares Coherentes de Alta Resolución (AMBUARAD)", reference CCG10-UAH/TIC-5983.

- The research of this Ph.D. Thesis has been supported in part by the University of Alcalá, under the fellowship program "Ayudas de Iniciación en la Actividad Investigadora".

- The research of this Ph.D. Thesis has been supported in part by the Spanish Ministry of Education, Culture and Sports, under the fellowship program "Formación del Profesorado Universitario", reference FPU13/01291.

- The research of this Ph.D. Thesis has been supported in part by the IEEE Microwave Theory and Techniques Society, under the fellowship program "MTT-S Graduate Microwave Engineering Fellowship".

- The author of this Ph.D. Thesis wishes to acknowledge the Adaptive Radio Electronics and Sensors (ARES) Group from the Department of Electrical and Computer Engineering of Purdue University for its support during a doctoral stay for the development of part of this work.

Acknowledgements

I would like to express my sincere gratitude to my advisors Prof. Roberto Gómez García and Ph.D. Dimitra Psychogiou for their endless and invaluable guidance, patience and support during the realization of this Doctoral Thesis.

I would also like to thank Prof. Dimitrios Peroulis for hosting me in his research group at Purdue University.

I want to express special gratitude to my colleagues from the Signal Theory and Communications department, specially those from the 'S22' office.

Finally, I would like to thank my parents, brother, family and friends for their encouragement and support.

Abstract

Radiofrequency-(RF)/microwave analog filters are essential components of telecommunication and radar systems. Their basic function is to allow the transmission of some frequency components within a certain spectral range and inhibit, as much as possible, the other components that are out of this frequency interval. Required features for these devices are high selectivity, low in-band power insertion loss, low manufacturing cost, and small physical size. In compliance with these requirements, transversal signal-interference filters, mostly fabricated in planar technologies, have become an attractive alternative for moderate-to-ultra-wideband-(UWB) applications. The term *"signal interference"* refers here to the philosophy adopted by these filter architectures in which the input signal is divided into multiple components that after passing through different electrical paths interfere at the output node. Thus, constructive signal-energy interactions in the passbands and destructive ones in the stopbands are produced for the shaping of the desired transfer function.

However, emerging applications, such as software-defined radio (SDR), continue to challenge the field of RF/microwave filters with even more stringent requirements to be met. New generations of wireless communication systems also demand high-frequency transceivers with multi-band and reconfigurable capabilities and, hence, need for flexible pre-selection filter solutions able to find a reasonable compromise among all their operational figures of merit.

The purpose of the present Ph.D. Dissertation is the analysis, design, construction, and characterization of novel filtering topologies based on signal-interference principles that feature enhanced electrical performance, reduced occupied area, narrow-to-wideband operation, and multi-function capability.

This Ph.D. Thesis can be divided into four different parts:

- In the first part, classic filtering techniques are combined with signal-interference principles to design novel filter architectures with advanced features in two senses: the attainment of low-order in-band group-delay profile for high-selectivity requirements through a new concept of "signal-interference source/load coupling", and the achievement of strongly-asymmetric transfer functions by means of stub-loading techniques.

- The second part addresses the size reduction of classic signal-interference filters exploiting three different philosophies: the use of lumped-element transversal networks, the employment of capacitive-loading miniaturization techniques, and the proposal of discrete-element quadrature-coupler-based transversal fil-

tering sections (TFSs).

- The third part concentrates on extending the applicability of signal-interference filters to narrow-band designs. This is done through mixed-technology surface-acoustic-wave (SAW)/microstrip implementations.

- In the fourth part, multi-function microwave devices are developed under the signal-interference formalism. In particular, Wilkinson-type power dividers, impedance transformers, and balanced frequency-selective devices with single/multi-band filtering capabilities are attained by embedding signal-interference TFSs into them.

Note that the synthesis methodologies and circuit schemes associated to the microwave filters proposed in this Ph.D. Thesis will be carefully examined and verified through the manufacturing and testing of a rich variety of physical prototypes.

Resumen

Los filtros analógicos de radiofrecuencia (RF) y microondas son componentes esenciales de los sistemas de telecomunicación y radar. Su principal función es permitir la transmisión de las componentes de frecuencia de un determinado rango espectral e inhibir, tanto como sea posible, aquellas componentes que se encuentran fuera de este intervalo de frecuencias. Dentro de las características requeridas para este tipo de dispositivos se encuentran: alta selectividad, bajas pérdidas de inserción en la banda de paso, bajos costes de fabricación y pequeño tamaño físico. En conformidad con estos requesitos, los filtros basados en técnicas de interferencia transversal de señales, principalmente fabricados en tecnologías planares, se han convertido en una alternativa atractiva para aplicaciones de banda moderada a ultra ancha. El término *"interferencia transversal de señales"* se refiere a la filosofía adoptada por este tipo de estructuras filtrantes, en las cuales la señal de entrada se divide en múltiples componentes que después de propagarse por distintos caminos eléctricos interfieren en el puerto de salida.

Sin embargo, aplicaciones emergentes en el ámbito de las telecomunicaciones tales como la radio definida por software (SDR), continuan desafiando el área de los filtros de RF y microondas con prestaciones cada vez más exigentes de satisfacer. Las nuevas generaciones de sistemas de comunicación inalámbrica también exigen un funcionamiento de tipo multi-banda y reconfigurable y, por lo tanto, necesitan de soluciones de filtrado flexibles capaces de encontrar un compromiso razonable entre todos sus parámetros operacionales.

El propósito fundamental de la presente Tesis Doctoral es el análisis, diseño, construcción y caracterización de topologías filtrantes innovadoras basadas en principios de interferencia transversal de señales de altas prestaciones con tamaño reducido, funcionamiento de banda estrecha a moderada/ancha y capacidad multi-funcional.

Esta Tesis Doctoral se puede dividir en cuatro partes diferenciadas:

- En la primera parte, se combinan técnicas de filtrado clásicas con principios de interferencia transversal de señales para diseñar arquitecturas filtrantes innovadoras que exhiben características avanzadas en dos sentidos: la consecución de una respuesta de alta selectividad filtrante y perfil de retardo de grupo de bajo orden mediante un nuevo concepto de "acoplamiento fuente/carga basado en principios de interferencia transversal de señales" y la obtención de funciones de transferencia de gran asimetría espectral mediante la carga de stubs.

- La segunda parte propone la reducción del tamaño de filtros basados en interferencia transversal de señales mediante tres filosofías diferentes: el uso de redes transversales de elementos concentrados, el empleo de técnicas de miniaturización mediante procedimientos de carga capacitiva y la propuesta de secciones filtrantes transversales de elementos concentrados basadas en el acoplador direccional de potencia en cuadratura.

- La tercera parte se centra en extender la aplicabilidad de los filtros basados en interferencia transversal de señales a diseños de banda estrecha. Esto se consigue a través de realizaciones en tecnología mixta de onda acústica superficial y microstrip.

- En la cuarta parte, se desarrollan dispositivos de microondas multi-funcionales basados en principios de interferencia transversal de señales. En particular, se lleva a cabo el diseño de divisores de potencia Wilkinson, transformadores de impedancia y filtros balanceados con capacidad de filtrado de una o múltiples bandas de paso mediante la incorporación de secciones de interferencia transversal.

Las metodologías de síntesis y los esquemas de circuitos asociados a los filtros de microondas propuestos en esta Tesis Doctoral serán cuidadosamente examinados y verificados por medio de la fabricación y medida de diversos prototipos experimentales.

List of Acronyms

3-D	Three-Dimensional
3G	3rd Generation of mobile telecommunications
4G	4th Generation of mobile telecommunications
5G	5th Generation of mobile telecommunications
ACPS	Asymmetric Coplanar Stripline
AW	Acoustic Wave
BAW	Bulk Acoustic Wave
BPF	Bandpass Filter
BSF	Bandstop Filter
BVD	Butterworth-Van Dyke
CAD	Computer-Aided Design
CRLH	Composite Right/Left-Handed
dB	Decibel
DC	Direct Current
DGS	Defected Ground Structure
DSPSL	Double-Sided Parallel-StripLine
EM	ElectroMagnetic
EMI	ElectroMagnetic Interference
FEM	Finite Element Method
FBW	Fractional Bandwidth
GPS	Global Positioning System
GSM	Global System for Mobile communications

HPF	Highpass Filter
HTS	High-Temperature Super-conductor
ICT	Information and Communication Technologies
IEEE	Institute of Electrical and Electronics Engineers
IL	Insertion Loss
ITU	International Communication Union
LPF	Lowpass Filter
LTE	Long Term Evolution
LTTC	Low-Temperature Cofired Ceramic
MEMS	MicroElectroMechanical Systems
MMIC	Monolithic Microwave Integrated Circuit
MoM	Method of Moments
NRN	Non-Resonating Node
PCB	Printed Circuit Board
PNA	Power Network Analyzer
Q	Quality factor
RF	RadioFrequency
SAW	Surface Acoustic Wave
SIR	Stepped Impedance Resonator
SIW	Substrate Integrated Waveguide
SDR	Software-Defined Radio
SMA	SubMiniature version A
SMD	Surface Mount Device
SMT	Surface-Mount Technology
SRF	Self-Resonant Frequency
TFS	Transversal Filtering Section
TRL	Through-Reflect-Line
TZ	Transmission Zero
UHF	Ultra High Frequency

UWB Ultra-WideBand

WiMAX Worldwide Interoperability for Microwave Access

Contents

List of Figures

List of Tables

Chapter 1

Introduction

1.1 Overview and motivation

Since the advent of information and communication technologies (ICT), the society has witnessed a technological race where ever more sophisticated services are offered to the end user. Clear evidence of this technological evolution is the current and the upcoming generation of mobile telecommunications—4^{th} generation of mobile telecommunications (4G) and 5^{th} generation of mobile telecommunications (5G), respectively—capable of providing with voice telephony, video calls, mobile web access, high-definition mobile TV, video on demand, and cloud computing among other services, all of them demanding a large amount of bandwidth [1]–[3]. If, in addition to the cellular communication network, other signals from services such as TV and radio broadcasting, global positioning system (GPS), and remote sensing and radar for both civilian and defense applications are radiated to the free space, the final result is the current saturation of the RF spectrum. For the coexistence of the aforementioned services, a more efficient use of the electromagnetic (EM) spectrum is therefore required. This is reflected in the evolution of RF/microwave architectures and the high-frequency devices integrating them, in which enhanced electrical performance, flexibility, and size compactness are basic requested features.

Among these components, high-frequency analog filters are essential RF devices to discriminate between the desired and the unwanted signals. In other words, they allow the frequency range of interest to be transmitted while rejecting the unwanted out-of-band spectral components [4], [5]. In general, microwave filters should have high selectivity with close-to-passband transmission zeros (TZs), low in-band insertion loss, high power rejection levels in the stopbands, and low in-band group-delay variation in terms of electrical performance. Compact physical dimensions and low production cost are also demanded in a plurality of RF front-end architectures. Besides, in order to support numerous standards in the same systems, RF transceivers should feature wide-band and/or multi-band operation, in addition to tunable capabilities. This is, for example, the case for cell phones equipped with Global System for Mobile communications (GSM) technology operating at 900/1800 MHz, 3^{rd} Generation of mobile telecommunications (3G) technology at 900/2100 MHz, 4G/Long-Term-Evolution-(LTE) technology at 800/1800/2600 MHz, and IEEE 802.16 wire-

less technology—also known as Worldwide Interoperability for Microwave Access (WiMAX)—at 3500 MHz (all these frequencies according to Spanish legislation [6]).

It is in this context that significant effort has been made to meet these stringent specifications for RF/microwave filters, following two main trends: the invention of new materials and fabrication processes and the development of innovative and more efficient filtering topologies. However, despite the enormous amount of research effort in this area, there are still design limitations for these devices to be overcome.

1.1.1 Brief description of the state-of-the-art

Well-known RF/microwave filter design procedures start with the synthesis of a lumped-element equivalent low-pass prototype, following a Butterworth or Chebyshev approach, which is subsequently transformed into the required high-frequency filter. This ideal lumped-element circuit is then turned into a physically implementable structure that often consists of electromagnetically-coupled resonators [7]. This procedure has been widely extended in RF/microwave filter design due in large part to its systematic methodology. However, the selectivity in this type of filters for basic responses is rather limited and, consequently, cross-coupling between non-adjacent resonators is needed in case of high-selectivity requirements. These new couplings generate TZs at both sides of the passband range at the expense of increased design complexity and higher in-band group-delay variation when the TZs are placed close to the passband [8]. Other shortcomings of basic coupled-resonator-based approaches to be remarked are their difficulty to feature wideband filtering actions, due to physical constraints imposed by the minimum separation between coupled lines feasible in the fabrication process, and the limitation of the maximum number of experimentally-proven passbands in multi-band designs to date.

In carrying out the implementation of coupled-resonator-based filters, planar technologies, such as microstrip or stripline, are conventionally chosen as a low-cost and compact solution when power-handling capability is not a requisite. Nevertheless, this kind of planar resonators have relatively low unloaded quality factor (Q_u) resulting in the degradation of the overall filtering response in case of multiple-resonator arrangements at high frequencies. Other classic technologies, such as those based on waveguide and dielectric resonators, present higher Q_u and, subsequently, are more suitable to realize highly-selective filtering actions. However, the big size of the resulting filters can be a limiting factor for their inclusion in certain RF systems. On the basis of the above, novel proposals on materials and fabrication processes have been devised in recent years in order to keep circuits compact and improve their electrical performance. Although it is beyond the scope of this Doctoral Thesis, Monolithic Microwave Integrated Circuits (MMICs), MicroElectroMechanical Systems (MEMSs), High-Temperature Superconductors (HTSs), and Low-Temperature Cofired Ceramics (LTCCs) are among the main technological advances that have stimulated the field of filter design for different applications [8]. Despite the remarkable electrical performance of all the latter regarding different figures of merit, it is worth noting that these designs rely heavily on three-dimensional (3-D) modeling and EM simulation, instead of circuit simulation. Thus, high computational computer-aided-design (CAD) cost and complex manufacturing processes

are needed for their development.

The other alternative for the realization of advanced microwave filters is the proposal of novel circuit topologies. To this end, a variety of untypical configurations have been recently reported, among which signal-interference filters are a good exponent. Inspired by classic digital filter design techniques, their operating principle is to split the signal to be processed into several weaker components which, after traveling by different electrical paths, interfere at the output port. For illustration purposes, Figure 1.1 depicts the flow diagram of an N-channel feed-forward structure in which most of transversal signal-interference filters are based on. Note that this transversal-like approach permits each signal component to be individually processed by the correspondent branch. Subsequently, a large variety of filtering responses can be synthesized by properly combining those particular channel actions at the overall output node [9].

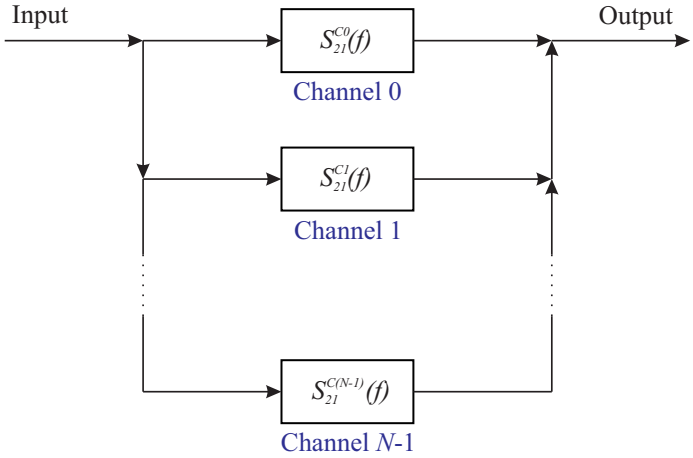

Figure 1.1: Flow diagram of an N-channel feed-forward signal-interference microwave filter.

As an example of this filtering philosophy, the most basic signal-interference TFS is introduced here. As can be seen in Figure 1.2, it consists of two different transmission-line segments connected in parallel. This configuration was first introduced in 2005 for the design of high-selectivity wideband bandpass filters (BPFs) with high power rejection levels in the stopbands [10]. The design parameters are then determined by enforcing the power transmission maximum condition at the center frequency, f_0. By properly adjusting the electrical lengths and the characteristic impedances of both transmission-line segments according to the design equations and guidelines provided in [10], the locations of the TZs closest to the passband and the 3-dB relative bandwidth can be controlled. This is illustrated in Figure 1.3 in which, for a given pair of line impedances Z_1 and Z_2 and an index m, different values of the index n vary the passband-width. Moreover, it is worth mentioning that higher-order filters can be attained when multiple TFSs are cascaded in series. This leads to a subsequent increase in the attenuation levels in the stopbands and the sharpness of the cut-off slopes.

The applicability of this filtering configuration was later demonstrated in the design of dual-band BPFs [11] and its extension to more-than-two-band BPFs [12]. The approach of [12], that reported the physical realization of a six-band planar

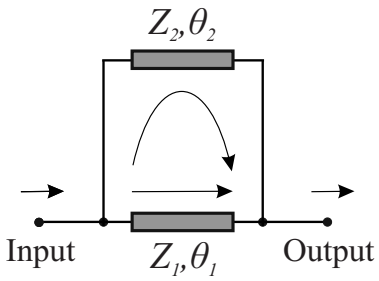

Figure 1.2: Signal-interference TFS based on two in-parallel transmission-line segments.

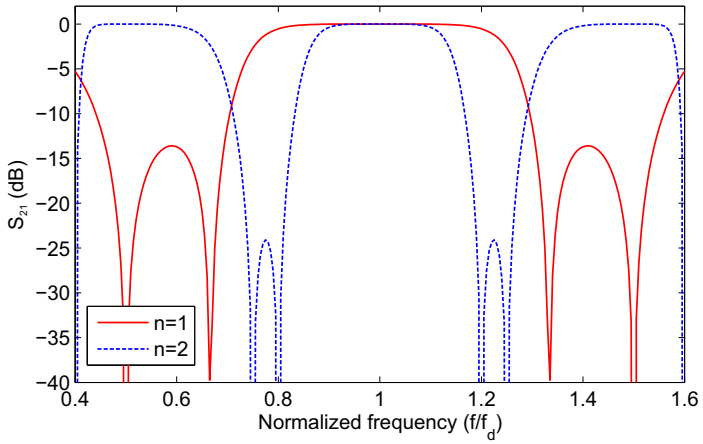

Figure 1.3: Power transmission response of an ideal synthesized TFS based on two transmission-line segments connected in parallel for $Z_1 = Z_2 = 2Z_0$ and $m = 1$. ($n = 1$: $\theta_1(f_d) = 90°$ and $\theta_2(f_d) = 450°$; $n = 2$: $\theta_1(f_d) = 90°$ and $\theta_2(f_d) = 810°$ [10]).

BPF, presented a remarkable contribution to the field of multi-band BPFs since only quad-band filtering responses had been achieved to that moment. Furthermore, this circuit topology was generalized for any arbitrary number of passbands unlike prior-art quad-band BPF alternatives based on complex multi-layer and defected-ground structures (DGSs) [13], [14]. Thus, by means of such a simple circuit network, several of the general requirements in microwave filters were accomplished: high selectivity for moderate-to-wideband passbands, stopbands with high power rejection levels, low in-band power insertion loss due to the avoidance of EM couplings, and multi-band operation with inter-band transmission nulls.

In addition to this contribution, numerous topologies based on these signal-interference principles have been proposed over the last decade. The most noticeable ones, along with their advantages, will be reviewed in Section 1.1.2.

1.1.2 Literature review on signal-interference filters

The framework of this Ph.D. Dissertation is defined within the field of microwave signal-interference filter design. Thus, this sub-section is intended to provide a short report of main works published to date concerning this RF filtering philosophy. Notwithstanding, a thorough review of the available literature is included in every chapter of this Thesis regarding the subject of interest.

Signal-interference techniques were soon extended from the initial solution of Figure 1.2 to other configurations with the aim of providing moderate-to-UWB filtering capabilities, which was one of the bottlenecks in most of basic coupled-line-based filter schemes. To this aim, this principle was applied to power directional couplers. Thus, a branch-line directional coupler whose direct and coupled ports are loaded with stubs was used to synthesize a BPF in [15]. In that work, the cascade of three TFSs led to a moderate 3-dB relative bandwidth of 10% at 5 GHz despite it is also suitable for broader bandwidths. Similarly, a stub-loaded rat-race coupler whose isolated port is taken as the TFS output node was reported in [16]. Note that in the whole filtering structure of [16] based on three cascaded TFSs of this version, the adjacent stopbands referred to 60-dB power rejection level have the same absolute bandwidth (1.3 GHz) as the 1-dB passband centered at $f_0 = 6.5$ GHz. This makes this prototype useful in full-duplex/multi-band communications. Moreover, this topology was expanded to UWB filtering in [17], where a BPF with a 3-dB relative bandwidth of 40% at 5 GHz with only two cascaded TFSs was presented. In line with this work, [18] described a filtering structure shaped by a short-ended coupled-line coupler connected in parallel to a transmission line, showing a 3-dB relative bandwidth higher than 100% at 7 GHz and remarkable in-band group-delay flatness. Also, a novel filtering scheme featuring a 110-% 3-dB relative bandwidth centered at 6.9 GHz was proposed in [19]. It consists of two planar Marchand baluns connected through their output ports in a symmetrical arrangement. As a practical drawback of it, since a high line impedance ratio is required in the coupled-line couplers forming both baluns, a patterned ground-plane technique was needed. As a final remarkable example, stub-loaded Bagley-polygon-type four-port power dividers were utilized as TFSs in [20]. Specifically, an UWB two-stage BPF with a 3-dB relative bandwidth of 70% centered at 4 GHz is implemented and tested as a

practical demonstrator.

The realizations reported in the preceding paragraph concentrate on the synthesis of single-band BPFs. However, signal-interference principles have been also applied to the synthesis of other classes of transfer functions. Thus, the work presented in [21] was aimed at the design of a sharp-rejection lowpass filter (LPF) with ultra-large stopband. Its principle consists of cascading several dissimilar TFSs with adjacent stopbands so as to broaden the overall attenuated band. Its main advantage when compared to other LPF solutions available in the open literature is the avoidance of coupled-line stages and patterned ground-planes. It simplifies the circuit simulation and manufacturing processes. For illustrative purposes, three LPF prototypes with 1-GHz cut-off frequency were built in [21]. The first one, in which the TFSs are based on uniform-based hybrid rings, exhibits a minimum stopband power rejection level of 20 dB over a frequency range of 4.6 GHz. In the second approach, the minimum out-of-band attenuation level is increased up to 40 dB over a frequency range of 4.2 GHz by allowing heterogeneous line-impedance segments in the TFSs. Finally, the third approach replaces the hybrid ring configuration forming the TFSs with branch-line hybrids. It shows a minimum attenuation level in the stopband of 30 dB over 3.3 GHz. In addition, a modified version of the latter was utilized to realize a BPF prototype exhibiting a 3-dB relative bandwidth of 110% around 640 MHz while keeping the same broad upper attenuated band.

From the point of view of bandstop-type implementations, there have been many recent contributions as well. By simply modifying the electrical lengths and line impedances of the well-known bi-path signal-interference TFS of Figure 1.2, sharp-rejection wideband bandstop filters (BSFs) can be designed, as in [22]. Particularly, two one-stage BSF prototypes were implemented in [22] showing a relative bandwidth of 30% around 1 GHz for minimum 20-dB and 30-dB stopband attenuation levels, respectively. For the same purpose, a structure based on an open-ended coupled-line coupler in parallel with a transmission-line segment was used in the design of a BSF with a minimum 20-dB rejection bandwidth of 100% centered at 2 GHz in [23]. Following this trend, a novel circuit topology which includes open-loop resonators in the signal-propagation path with larger electrical length of the bi-path TFS was devised in [24]. It allows to add two additional TZs with respect to its two in-parallel-transmission-line-type counterpart. This BSF topology was experimentally proven by an implemented prototype with a 20-dB-referred rejection relative bandwidth of 41% around 2 GHz. The last example of signal-interference BSF described in [25] consists of a single TFS in which a U-shaped short-circuited stepped-impedance resonator (SIR) structure is embedded again in the electrically-longer path of the conventional approach. By doing so, an attenuation band with four transmission nulls and sharp cut-off slopes was achieved. Its implemented prototype showed a minimum 20-dB rejection bandwidth of 50% centered at 2.4 GHz.

As previously stated, signal-interference techniques are also suitable for the development of multi-band BPFs [11], [12]. In this field, a large variety of dual- and multi-band configurations have been explored over the last few years. With the purpose of broadening the passband-width of conventional dual-band signal-interference BPFs, as the ones in [11], stub-loading techniques were adopted in [26]—note that higher-order transfer functions are achieved through its incorporation—. Its prin-

ciple is to add open-circuited stubs at the input and output terminals of the entire structure. As practical example, a two-stage 1.5/2.5 GHz fourth-order dual-band BPF prototype with 3-dB absolute bandwidth of 690 MHz in both passbands was built and tested. Another contribution is found in [27], where the generalized branch-line hybrid is used to perform a 2.1/3.9 dual-band wideband filtering with an absolute bandwidth of 450 MHz for both transmission bands by cascading in series two TFSs. In [28], the adopted strategy focused on the employment of a stub-loaded Bagley-polygon four-port power divider as a TFS. In this manner, two passbands fairly close to each other at 2.75 and 3.25 GHz—3-dB absolute bandwidth of 125 MHz for both—were obtained in a two-stage realization. Moreover, Bagley-polygon-type-based structures were utilized to develop quad-band bandpass and dual-band bandstop transfer functions by properly modifying the length of the stubs according to the design equations in [20]. Lastly, other innovative approaches are the ones reported in [29], where hybrid couplers arranged in reflection mode are loaded by double stubs in the input and isolated ports. The short-ended loading stubs transform the inherent bandstop response of the TFSs into two-pole dual-band wideband bandpass transfer functions, while the open-ended stubs increase the power rejection levels in the attenuated band between both passbands. The first reported prototype with the passbands centered at 0.63 and 2.37 GHz and absolute bandwidth of 435 MHz is based on the hybrid-ring-based TFS. The second circuit with the passbands around 0.68 and 2.32 GHz and 3-dB absolute bandwidth of 675 MHz exploits the branch-line-hybrid-based TFS. Both prototypes consist of the series-cascade connection of two TFSs.

The topologies reviewed at this point demonstrate the capability of signal-interference principles to synthesize a large variety of filtering transfer functions, going from bandpass to bandstop ones and from single- to multi-band ones. However, they all exhibit frequency-symmetrical responses with regard to the design frequency f_d. Note that spectral asymmetry can be particularly interesting in multi-channel/multi-mode communication systems asssociated to different services. For instance, in duplexing devices, the inter-channel power-rejection levels inherent to each channel filter can be increased at one stopband side by means of asymmetrical patterns in the frequency response. Other scenario is in multi-standard systems where these passbands might need of distinct absolute bandwidth. This has been partially addressed so far in signal-interference approaches by replacing the uniform-impedance lines that shape these TFSs with stepped-impedance lines. Following the theoretical foundations in [30], a duplexer with the lower and upper channels centered at 1.7 and 2.25 GHz and of absolute bandwidths of 395 and 265 MHz, respectively, were built. Specifically, an inter-channel rejection level higher than 40 dB is attained at both output terminals. In the same work, a two-stage 1.3/2.5 GHz dual-band BPF with 3-dB absolute bandwidths of 400 and 100 MHz, respectively, was also reported.

In addition to passive filtering structures, signal-interference techniques have also proven their potential in active filtering, widely understood as the presence of active components in the electrical branches of the circuit to compensate for the effects of the lossy passive elements in terms of passband insertion loss and frequency selectivity. The theoretical foundations of the active-filter approaches examined here exploit transversal, recursive, and channelized principles, whose operative differences

are expounded hereafter. In transversal approaches, the sub-components of the signal, after being divided at the input node, are individually amplitude-weighted and time-delayed before they are combined at the output node. Recursive approaches include feedback loops from the output to the input terminal. This allows to reduce the number of weighting elements needed for a given degree of filtering selectivity but compromises circuit stability [31]. Channelized filters, as in [9], [32], and [33], can be viewed as generalized transversal filters based on frequency-selective amplitude weighting. This results in a reduction in the number of feedforward branches. As an extension of these works, recursive active filtering structures can be modified to feature dual-band operation, as demonstrated in [34]. To this aim, the conventional transmission line section in the feedback branch is replaced with a composite right/left-handed (CRLH) transmission-line segment, that meets the phase condition needed for the recursive-filter operation in two arbitrary frequencies—788 and 1700 MHz in the built prototype—. As a last example of signal-interference-based active filters, [35] introduced a novel two-stage recursive BPF in silicon technology, in which center frequency—around 2 GHz in this case—, bandwidth, and power transmission gain can be independently tuned. This work also presented a MMIC reconfigurable three-branch channelized BPF based on a new divider arrangement.

Lastly, due to the latest trends towards the development of highly-flexible RF transceivers, electronic reconfiguration is highly demanded for microwave filters. Regarding spectrally-controllable signal-interference filters, in addition to the tunable active filter already presented in [35], another contribution based on active recursive principles exhibiting frequency agility was reported in [36]. In this case, two feedback branches are employed to separately control the center frequency of the passbands of a dual-band BPF in the frequency range of 698-831 MHz for the lower passband and 1630-1730 MHz for the upper transmission band. In accordance with these advances, an innovative method to suppress the spurious responses and extend the passband-width of BSFs was presented in [37]. It is sought to generate constructive interferences at the spurious frequencies and a destructive one at the fundamental bandstop frequency. As proof-of-concept, a fixed-varactor pure-distributed-element BSF at 951 MHz where the second and the third spurious were cancelled was proposed. Specifically, it shows a passband-width extended to more than nine times the fundamental response. In the same work, a varactor-tuned BSF with suppressed second spurious was developed as a second approach. Its center frequency tunes from 838.3 MHz to 1308.6 MHz—56% in relative terms—and its passband-width is broadened 8.9 times the fundamental frequency. Finally, within the field of reconfigurable signal-interference filters, it should be highlighted another completely different methodology involving the use of p-i-n diodes. Following this technique, the implementation of a three-state reconfigurable LPF prototype is reported in [38]. This is a two-stage filter whose filtering block is formed by three transmission lines connected in parallel. Each state—with cut-off frequencies at 2, 3, and 4 GHz—is obtained by properly switching on/off the constituent transmission lines through the p-i-n diodes. Similarly, a filtering device based on two cascaded stub-loaded branch-line-coupler-based TFSs was described in [39]. It exhibits four 3-dB bandwidth states of 10%, 11%, 19% and 52% respectively, by properly connecting and disconnecting those loading stubs. [39] also presented another reconfigurable-bandwidth

BPF based on two cascaded TFSs formed by the generalized Bagley-polygon-type four-port power divider. It results in four states with 3-dB relative bandwidth of 16%, 29%, 34% and 48%—these two prototypes are synthesized at f_d=2 GHz—.

Despite the large variety of signal-interference filters developed up to now, as evidenced by the previous review, there are still some shortcomings to overcome. To sum up, some of the main remaining limitations for this class of filtering configurations are as follows:

- The combination of classic filtering techniques with signal-interference ones can be even further exploited in order to carry out more efficient filtering actions. Among the unsolved problems on signal-interference filters with sharp-rejection capabilities, a common lack is the noticeable in-band group-delay variation. This means that the more selective the filter is, then the larger the in-band group-delay variation is. This factor is particularly important on digital communications, sometimes causing an undesired effect known as inter-symbol interference (ISI) [40]. Concerning multi-band communication systems, another design aspect to be addressed is the incorporation of spectral asymmetry in their transfer functions. This is difficult to achieve due to the fact that the lengths of transmission-line segments forming signal-interference filters are conventionally set as integer multiples of 90 degrees, leading to spectral symmetry and periodic frequency responses with regard to the design frequency, f_d, in the interval $[0, 2f_d]$.

- Most of the experimentally-proven signal-interference filters have been developed in fully-planar technologies. This gives rise to large physical circuit size, especially for designs aimed at the lower part of the RF spectrum, where a hybrid or pure-lumped-element implementation would be more appropriate.

- The practical suitability of signal-interference techniques to design very-narrow-band BPFs remains still unexplored. In such case, the conventional topologies proposed so far would need excessive lengths for the transmission-line paths of their TFSs, resulting in an unviable implementation owing to the consequent huge circuit size and the insertion-loss limitations caused by the planar substrate.

- The design of multi-function microwave devices is a current hot topic that needs to be explored under the signal-interference formalism. This means the combination of multiple RF processing functions, such as filtering, power splitting, power combination, impedance transformation or amplifying, among others, in the same electrical network. These multi-function components have benefits in terms of size and optimized electrical performance.

All the aforementioned drawbacks are the motivation of this doctoral research and will inspire the microwave circuits reported in this Ph.D. Thesis, according to the objectives established in Section 1.2.

1.2 Objective

Once the motivation and the state-of-the-art related to the topic of microwave signal-interference filters have been summed up, the aim of the current Ph.D. Thesis can be established. This is as follows:

"Analysis, design, construction and characterization of novel advanced microwave filtering devices based on transversal signal-interference techniques"

This general purpose has been divided into four main sub-objectives, as indicated below:

1. **Proposal of novel microwave filtering circuits exploiting the combination of classic filtering techniques and signal-interference principles;** specifically, the improvement of the filtering selectivity without sacrificing the in-band group-delay response and the achievement of asymmetric frequency responses on signal-interference filters for different kinds of filtering functions, ranging from low-pass to multi-band type, will be approached.

2. **Invention of hybrid- and lumped-element-based feedforward signal-interference filtering networks;** here, especial emphasis will be made on the proposal of size-reduced circuit models suitable to be implemented in the lower part of the microwave band.

3. **Development of very-narrow-band transversal signal-interference filtering sections;** in particular, the implementation of signal-interference BPFs in hybrid transmission-line/SAW-resonator technology will be contemplated.

4. **Design of multi-function microwave circuits inspired on transversal signal-interference techniques;** this research task will mainly focus on dual-function passive components with single/multi-band operation and their application to more-complex high-frequency components.

Throughout the chapters of this Ph.D. Thesis, a considerable effort will be made in obtaining theoretical design methodologies for the suggested signal-interference microwave circuits. In addition, several proof-of-concept prototypes will be implemented to experimentally validate the described topologies.

1.3 Thesis outline

In this section, the detailed thesis plan is expounded. The structure is divided into five more chapters, apart from this introductory one, according to the research tasks previously described.

In **Chapter 2**, the achievement of high-performance features in microwave filters is addressed through the mixed use of classic filtering and signal-interference principles. On the one hand, a new method to produce out-of-band TZs and consequently increase the filter selectivity but without deteriorating the in-band group-delay variation is introduced. It consists of adding an external signal-interference coupling

between the input and the output nodes of the original basic filter to create two signal-propagation paths. This technique is verified by means of the physical realization of low-pass, high-pass, and single/multi-band bandpass filtering circuits. On the other hand, a principle based on the inclusion of loading stubs in specific locations of conventional signal-interference TFSs is devised with the aim of obtaining frequency-asymmetrical filtering responses. A dual-band BPF prototype is built and measured to corroborate its practical usefulness.

In **Chapter 3**, three different topologies for the design of compact lumped-element and hybrid distributed/lumped-element circuits are presented, in order to reduce the circuit size of signal-interference filters in the lower part of the RF spectrum. The idea behind the first approach is to replace short-length transmission-line segments with LC T-type transversal circuit networks. As a proof of concept, a LPF and a BPF are designed at the layout level. In the second methodology, the miniaturization of signal-interference filters is faced up by means of capacitive-loading and line-meandering techniques. For the verification of the proposed approach, single- and multi-band BPF prototypes are implemented. In both previous synthesis techniques, the trade-off between frequency-response convergence and level of size reduction with regard to the conventional counterpart is carefully examined. Finally, in the third approach, the TFS based on the distributed-element quadrature coupler arranged in reflection mode is substituted by a pure-lumped-element counterpart. Its suitability is demonstrated through lumped- and mixed distributed/lumped-element realizations at the simulation level. The insertion loss and the suppression of spurious bands in the lumped-element implementation are also shown.

In **Chapter 4**, the applicability of signal-interference BPFs is extended to narrow-band specifications. To this aim, on-chip SAW resonators and SAW filters are embedded into the branches of the classic signal-interference TFS composed by two transmission lines connected in parallel. The inclusion of these SAW devices allows to notably shorten the transmission-line segments of the building block with its subsequent size reduction and lower in-band power insertion loss when compared to its fully-planar counterpart. Following these premises, three different approaches are presented. The first one includes a one-port or a two-port SAW resonator in the TFS, acting as an in-band resonant node, so that the high-Q properties of the SAW device are substantially transferred to the overall transfer function. The second one takes advantage of the abrupt slope existing between the resonance and the anti-resonance of the one-port SAW resonator itself to conform one of the pass-band edges. And finally, in the third approach, the inherent bandwidth of the SAW BPF is broadened by means of constructive signal-energy interactions taking place within the signal-interference structure. In all three design techniques, the impact of the spurious modes from the SAW devices in the overall BPF response is carefully examined with four built prototypes.

In **Chapter 5**, multi-function signal-interference microwave devices are engineered. Particularly, the incorporation of single- and multi-band filtering actions through embedded signal-interference TFSs into microwave devices designed to perform another type of RF processing function is addressed. Firstly, single/multi-band filtering operation is added to a planar Wilkinson-type power divider. This is demonstrated with the implementation of a triple- and quad-band BPF pro-

totypes in microstrip technology. Moreover, a dual-band Wilkinson-type filtering power divider is implemented in lumped-element technology, being more convenient at low microwave frequencies. As an extension to more sophisticated devices, a two-branch channelized active BPF using this type of dual-function device for its signal-division/combination blocks is also built and characterized. As second family of dual-function microwave devices, impedance transformers exhibiting filtering capability are also reported. They are corroborated through the development and testing of single- and dual-band prototypes. Finally, balanced BPFs are addressed by the incorporation of signal-interference TFSs into the two identical halves of their symmetrical structure. For illustrative purposes, single- and dual-band examples are synthesized. As a proof-of-concept, a single-band prototype is fully built and characterized.

Finally, in **Chapter 6** a summary of the results extracted from this Ph.D. Dissertation along with the conclusion is provided. In addition, further research work is discussed and a list with the international journal and conference papers derived from this study is attached.

Chapter 2

Design of mixed classic/signal-interference microwave filters

There are several important performance parameters involved in RF/microwave filter design. In most cases, these parameters are very often interlinked in such a way that the improvement of one of them implies deteriorating the others. Thus, the achievement of a particular set of filtering specifications can be hindered by the existing trade-off among the different electrical characteristics of the filter. Besides, some of these features are sometimes difficult to attain in certain types of filter configurations. For example, in relation with signal-interference filters, the simultaneous attainment of low in-band group-delay variation and high selectivity or the achievement of frequency-asymmetrical transfer functions remain almost unexplored.

As already outlined in Chapter 1, one of the most relevant characteristics of signal-interference BPFs is their high selectivity. As in the vast majority of microwave filter topologies, this is obtained at the expense of increasing the in-band group-delay variation especially at the filter flanks. Nevertheless, this performance parameter is essential in digital communication systems. When a finite-bandwidth signal consisting of multiple frequency components passes through a RF/microwave device, all these components are delayed. If the delay is different for each signal spectral component, phase distortion is produced which may give rise to intersymbol interference (ISI) in the demodulation of the digital information [40]. In other words, one symbol interferes with the subsequent symbol, making the communication less reliable. To date, this effect has been mostly counteracted through external group-delay equalizers or self-equalizing structures, as subsequently outlined in Section 2.1, leading to increased circuit complexity.

The other aspect that can act as a limiting factor for the exploitation of signal-interference filters in modern multi-mode high-frequency systems is their low suitability to synthesize of spectrally-asymmetrical transfer functions especially for multi-band devices. Due to the fact that most of conventional signal-interference TFSs are composed by transmission-line segments whose electrical lengths are integer multiples of 90° at the design frequency f_d, the resulting frequency responses are spectrally

symmetrical with regard to f_d in the interval $[0, 2f_d]$ and follow a periodic pattern. Note that the spectral symmetry along with the periodicity of the frequency response can be detrimental to comply, for instance, with the frequency specification mask for channels of multi-standard communication systems. The design of spectrally-asymmetric filters has been partially addressed in signal-interference approaches by means of stepped-impedance TFSs so far, as introduced in [30]. However, these solutions exhibit increased design complexity and reduced power rejection levels in the attenuated bands when compared to their basic counterparts.

This chapter is therefore intended to overcome the aforementioned limitations through the combination of classic filtering and signal-interference structures. First, a method to produce out-of-band transmission nulls and, hence, increase the filtering selectivity without deteriorating the in-band group-delay variation is presented. It is based on coupling the input/output nodes of a basic low-order filter, resulting in a mixed classic/signal-interference filter configuration with two propagation paths. Secondly, the spectral-asymmetry limitation is approached through the application of stub-loading techniques over conventional signal-interference bi-path TFSs.

The organization of this chapter is as follows. Firstly, the selectivity-improvement technique based on the concept of "signal-interference source-load coupling" is introduced in Section 2.1. After describing its theoretical foundations, five different prototypes are presented showing additional TZs within the rejection bands of their transfer function. Secondly, the principle to obtain strongly-asymmetrical frequency responses based on the incorporation of short-circuited stubs in a signal-interference TFS is expounded in Section 2.2. To validate this technique, an experimental dual-band BPF circuit is built and tested. Finally, the main conclusions of this chapter are presented in Section 2.3.

2.1 Filters with selectivity-enhancement based on signal-interference source-load coupling

As it has been pointed out above, high power rejection levels in the stopbands and flat in-band group-delay profile in the passband are simultaneously demanded in microwave filters aimed at digital communication systems for two main reasons: to efficiently reject the out-of-band interfering and jamming signals and to assure low phase-distortion levels for in-band processed signals, respectively. In order to fulfill both requirements, two traditional approaches have been mainly used in the past. The first one focuses on the design of a filter that only takes into account the amplitude specifications to be later cascaded with an external equalizer for group-delay flattering purposes, as expounded in [41]. The second approach (self-equalized or phase-linear filter) consists of designing the filter with an imposed linear phase requirement in addition to the amplitude one, as in [42]. However, both approaches lead to higher complexity in terms of hardware and theoretical synthesis methodology.

An alternative solution to this problem is based on the technique reported in [43] and [44] in which new TZs are added to a pre-designed single-band filter. Its principle is to couple the input/output terminals of a low-order classic filter to

introduce additional TZs and improve filtering selectivity while preserving the in-band features. In this section, an advanced version of this method is presented in order to increase the number of feasible TZs while keeping in-band group-delay performance. It is firstly applied to low-order filters with narrow-band stopbands and secondly extended to more challenging filter designs, such as highpass filters (HPFs) and dual-band BPFs.

2.1.1 Theoretical foundations

The proposed idea to enhance selectivity in a basic filter without altering its in-band characteristics is to connect an external multi-TZ-generation transversal cell to its input/output ports as illustrated in Figure 2.1. This multi-TZ-creation transversal cell is ideally shaped by a coupled-line section that introduces a weak signal interaction between the input/output accesses of the entire circuit, and two transmission lines inserted between the coupled-line stage and the input/output terminals of the basic filter. Thus, two signal-propagation paths are generated in the overall filter, as follows:

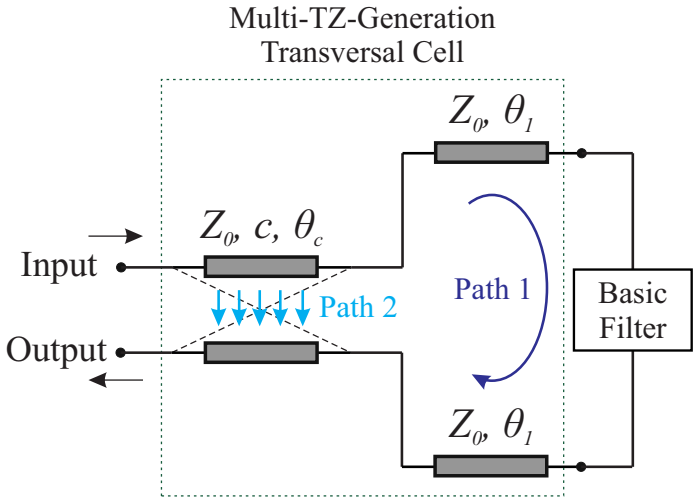

Figure 2.1: Proposed filter concept (Z_0 is the reference impedance, c is the coupling factor, and θ_c and θ_1 are the electrical lengths).

- Path 1: direct (strong) path associated with the basic filter and the additional transmission-line segments of the transversal cell at its input/output terminals.
- Path 2: indirect (weak) path generated by the coupled-line stage.

The overall filtering response is then obtained from the feed-forward signal-interference action at the output node of these two electrical paths, once the signal components have travelled by them. With regard to the latter aspect, the following points must be remarked:

- The in-band characteristics of the basic filter in terms of amplitude and group-delay response are directly transferred to the whole transfer function. Inside

the passband, the magnitude of the path-1 signal component is much higher than that of the path-2 one, so that the interference effect becomes negligible. Thus, only a frequency-constant shifting in the group-delay response, some minor amplitude ripple, and a small increase in the passband insertion loss due to the new transmission lines of the transversal cell are expected.

- For the attenuated bands, the magnitude of the two signal components become comparable. Thus, out-of-band TZs are produced from the signal-energy cancelations taking place between the two electrical paths. Note that the higher the values for the θ_c and –especially– θ_1 parameters are, then the greater the number of TZs that can be set. This is due to a faster frequency-variation velocity in the phase difference produced between the two signal components that are interfered. In such a case, more signal-energy suppressions occur in a narrower frequency span. This adds more degrees of freedom in the amount of created TZs and their spectral locations when compared to [43] and [44].

Since the overall filter is a symmetrical network—i.e., its physical structure can be divided into two identical halves with regard to its input/output ports—, even- and odd-mode analysis can be applied in order to deduce its S-parameters [8]. Note that this is only possible if the geometry of the low-order filter of the direct path is also symmetrical. Thus, the overall S-parameters can be derived as follows:

$$S_{11} = \frac{1}{2}(\Gamma_{in}^{e} + \Gamma_{in}^{o}) \tag{2.1}$$

$$S_{21} = \frac{1}{2}(\Gamma_{in}^{e} - \Gamma_{in}^{o}) \tag{2.2}$$

with

$$\Gamma_{in}^{e} = \frac{Z_{in}^{e} - Z_0}{Z_{in}^{e} + Z_0} \tag{2.3}$$

$$\Gamma_{in}^{o} = \frac{Z_{in}^{o} - Z_0}{Z_{in}^{o} + Z_0} \tag{2.4}$$

where Z_{in}^{e} and Z_{in}^{o} correspond to the even- and odd-mode input impedances of the overall filter after adding the multi-TZ-generation transversal cell and Z_0 denotes the reference impedance. These input impedances can be calculated as a function of Z_{basic}^{e} and Z_{basic}^{o}, which refer to the even- and odd-mode impedances at the terminals of the basic filter:

$$Z_{in}^{e} = \frac{Z_0 \cos\theta_c \left[Z_{basic}^{e} + jZ_0 \tan\theta_1\right] + jZ_0 Z_0^{e} \sin\theta_c - Z_0^{e} Z_{basic}^{e} \sin\theta_c \tan\theta_1}{j\frac{Z_0}{Z_0^{e}} \sin\theta_c \left[Z_{basic}^{e} + jZ_0 \tan\theta_1\right] + Z_0 \cos\theta_c + jZ_{basic}^{e} \cos\theta_c \tan\theta_1} \tag{2.5}$$

$$Z_{in}^{o} = \frac{Z_0 \cos\theta_c \left[Z_{basic}^{o} + jZ_0 \tan\theta_1\right] + jZ_0 Z_0^{o} \sin\theta_c - Z_0^{o} Z_{basic}^{o} \sin\theta_c \tan\theta_1}{j\frac{Z_0}{Z_0^{o}} \sin\theta_c \left[Z_{basic}^{o} + jZ_0 \tan\theta_1\right] + Z_0 \cos\theta_c + jZ_{basic}^{o} \cos\theta_c \tan\theta_1} \tag{2.6}$$

where θ_c and θ_1 denote the electrical lengths of the coupled-line stage and the two additional transmission lines incorporated between them and the terminals of the basic filter, as illustrated in Figure 2.1. Note that Z_0^e and Z_0^o are the even- and odd-mode characteristic impedances of the coupled-line stage, so that the following two equations must be satisfied:

$$Z_0 = \sqrt{Z_0^e Z_0^o} \tag{2.7}$$

$$c(dB) = -20\log\left(\frac{Z_0^e - Z_0^o}{Z_0^e + Z_0^o}\right) \tag{2.8}$$

To validate the theoretical analysis previously described, a single signal-interference TFS shaped by two transmission lines connected in parallel is adopted as the basic filter. In particular, its design parameters are chosen according to equations (1)-(3) in [11] with the purpose of providing a dual-band behavior. These parameter values for the basic TFS are $Z_{1,basic} = Z_0/2$, $Z_{2,basic} = Z_0$, $\theta_{1,basic} = 180°$, and $\theta_{2,basic} = 360°$ at f_d. The design values for the multi-TZ-generation transversal cell are set as $Z_0^e = 6/5Z_0$, $Z_0^o = 5/6Z_0$, $\theta_c = 90°$, and $\theta_1 = 270°$ at f_d. As can be seen in Figure 2.2, two additional inter-band TZs are generated through the use of the external transversal cell, therefore enhancing the overall filter selectivity while nearly preserving the in-band characteristics of the original filter in its dual passbands. As it will be shown in the next section, this phenomenon is even more noticeable when the basic filter is a multi-stage arrangement.

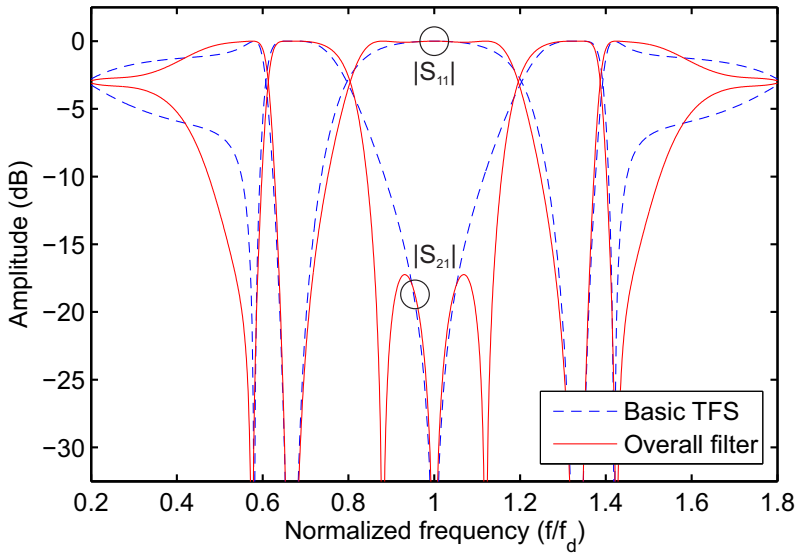

Figure 2.2: Ideal power transmission ($|S_{21}|$) and reflection ($|S_{11}|$) responses of a synthesized enhanced-selectivity dual-band BPF and its basic dual-band TFS.

2.1.2 Experimental results

With the aim of experimentally validating the previously-expounded technique, five different prototypes are designed here in planar technology. For their implemen-

tation, two different microstrip substrates have been employed. In particular:

- The substrate CER-10 of *Taconic*^{TM} with the following parameters was used for the manufacturing of prototypes 1, 2, and 3, and the EM simulation of prototype 5: relative dielectric permittivity $\varepsilon_r = 9.8$, dielectric thickness $h = 1.19$ mm, dielectric loss tangent $\tan\delta_D = 0.003$, and metal thickness $t = 35$ μm [45].
- The substrate RO4003C of *Rogers*^{TM} was employed in the fabrication of prototype 4. Its parameters are as follows: relative dielectric permittivity $\varepsilon_r = 3.55$, dielectric thickness $h = 1.52$ mm, dielectric loss tangent $\tan\delta_D = 0.0027$, and metal thickness $t = 35$ μm [46].

For the design, simulation, and measurement of the prototypes, the logistic media listed below were used:

- Commercial software package *AWR Microwave Office*^{TM} of *AWR Corporation*: circuit simulation of all prototypes [47].
- Commercial software package *High Frequency Structure Simulator v10.0 (HFSS)* of *Ansoft*^{TM}: 3-D full-wave EM simulation by the Finite Element Method (FEM) of prototype 3 [48].
- Commercial software package *Sonnet*^{TM} of *Sonnet Software, Inc.*: 3-D planar EM simulation by the Shielded-Domain Method of Moments (MoM) of prototypes 4 and 5 [49].
- HP-8720C network analyzer of *Agilent*^{TM}: measurements [50].

Prototype 1: Hairpin-type bandpass filter I

As a first practical example, the engineered approach has been applied to a 2.2-GHz third-order hairpin-type BPF exhibiting a moderate bandwidth [51]. Figure 2.3 shows the layout and a photograph of the resulting microstrip implementation referred to a 50-Ω impedance. As can be seen, the proposed topology has been slightly modified regarding the scheme of Figure 2.1 so that the weak-coupling signal path incorporates a detuned coupled line between the input and output nodes acting as a non-resonating node (NRN). It allows a more-flexible control of the TZs generated in the bandstop range [52].

The simulated and measured power transmission, reflection, and group-delay responses of this filter prototype are depicted in Figure 2.4. Note that two set of measurements are given regarding the whole BPF prototype: one belonging to a first iteration of the circuit and another in which the prototype has been tuned by properly adjusting the length of the NRN. As Figure 2.5 illustrates, this length is essential for the proper generation of the new TZs. As can be seen, the selectivity in the upper attenuated band is notably enhanced—with two additional TZs—while the in-band group-delay variation is nearly similar to that of the low-order BPF. The previously-referred frequency-constant shifting in the overall group-delay profile due to the additional transmission lines is also observed.

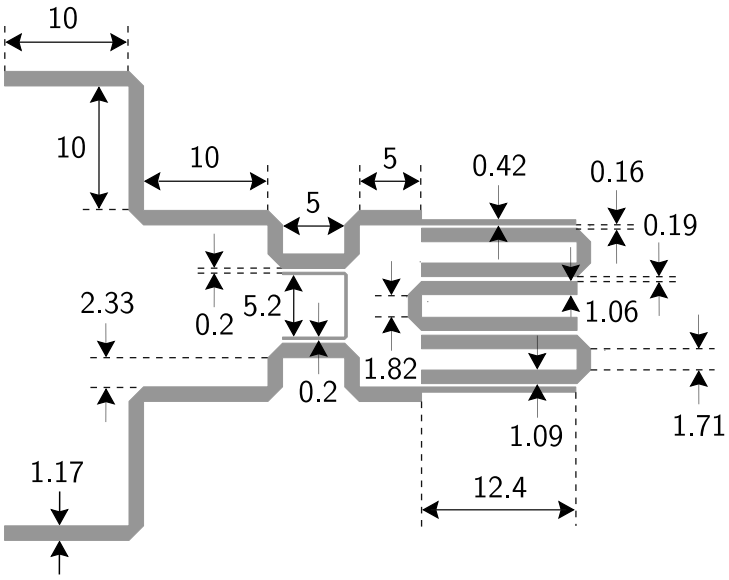

(a) Layout (non-redundant dimensions, in mm, are indicated).

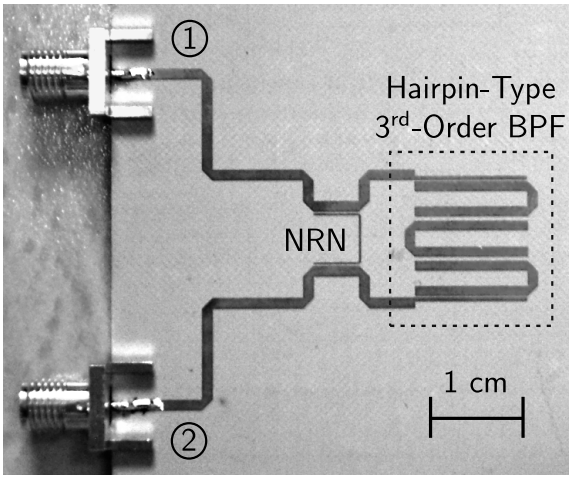

(b) Photograph (microstrip substrate: CER-10 of *Taconic*).

Figure 2.3: Layout and photograph of the manufactured microstrip BPF (prototype 1) [51].

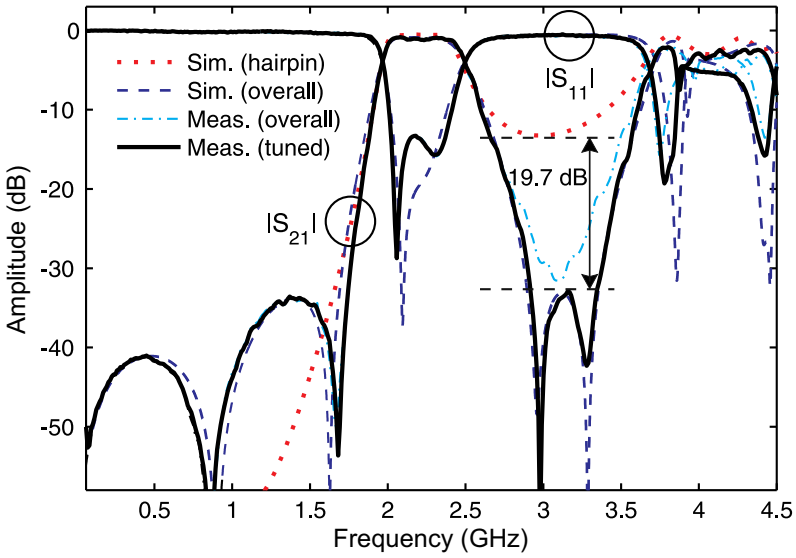

(a) $|S_{21}|$ and $|S_{11}|$.

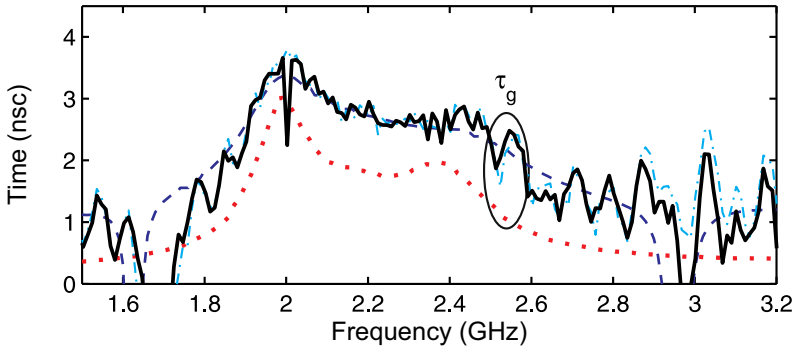

(b) τ_g.

Figure 2.4: Simulated and measured power transmission ($|S_{21}|$), reflection ($|S_{11}|$), and group delay (τ_g) curves of the manufactured prototype 1, along with the simulated $|S_{21}|$ and τ_g curves of its basic low-order—third-order hairpin-type—filter prototype [51].

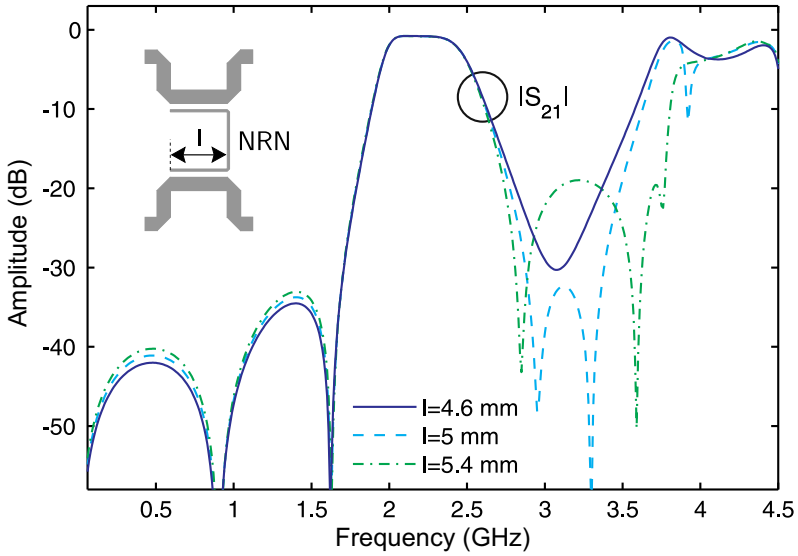

Figure 2.5: Influence of the NRN coupled-side length on the simulated power transmission response of the built prototype 1.

Prototype 2: Hairpin-type bandpass filter II

Prototype 2 is an advanced version of the previous circuit. It incorporates an additional coupling stage with a different NRN. This second stage allows increasing the number of TZs in the stopband. Note that the impedance of the transmission-line segments connecting both coupling stages differs from the 50-Ω reference impedance to make feasible the attainment of adequate in-band power matching levels. The layout and a photograph of this microstrip BPF prototype are shown in Figure 2.6.

The simulated and measured results—power transmission, reflection, and group-delay responses—of prototype 2 are depicted in Figure 2.7. When compared to prototype 1, the upper stopband shows a new TZ which broadens its bandwidth. Besides, the maximum in-band group-delay variation remains almost unaltered.

Prototype 3: Stepped-impedance lowpass filter

In order to verify the suitability of this selectivity-improvement technique in other type of filtering transfer functions, prototype 3 shows its application to a LPF without TZs. For this circuit, a 3-dB cut-off frequency of 2 GHz has been chosen and four out-of-band TZs have been generated. The layout and a photograph of the built microstrip high-selectivity LPF prototype are provided in Figure 2.8. The transmission lines between the low-order LPF and the coupled-line stage play here an important role to compensate some spurious effects not contemplated by the circuit simulator, such as the EM coupling appearing between the line bends. Note that the characteristic impedances of these lines are different from the 50-Ω reference impedance for in-band power matching purposes.

Once again, the measured power transmission, reflection, and in-band group-delay curves represented in Figure 2.9 show a fairly-close agreement with the pre-

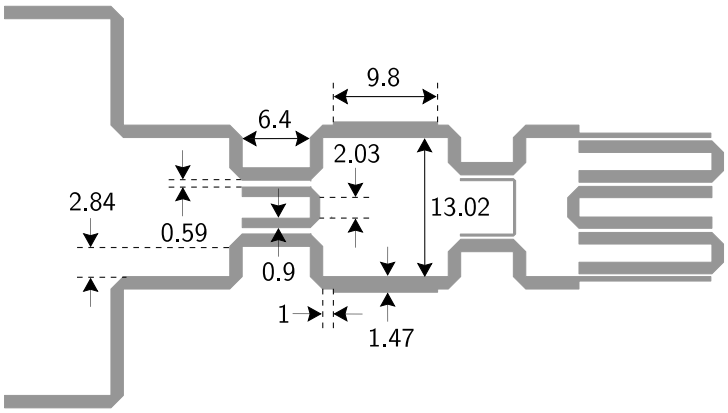

(a) Layout (non-redundant dimensions, in mm, are indicated).

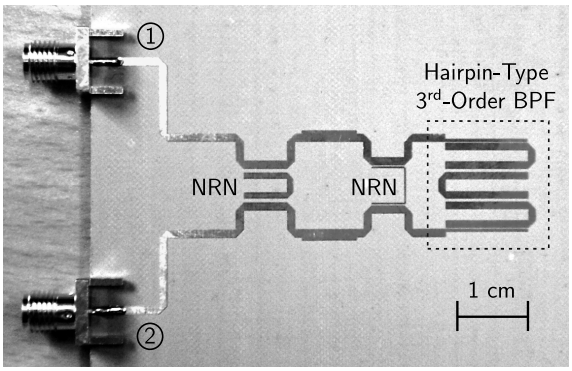

(b) Photograph (microstrip substrate: CER-10 of *Taconic*).

Figure 2.6: Layout and photograph of the manufactured microstrip BPF (prototype 2) [51].

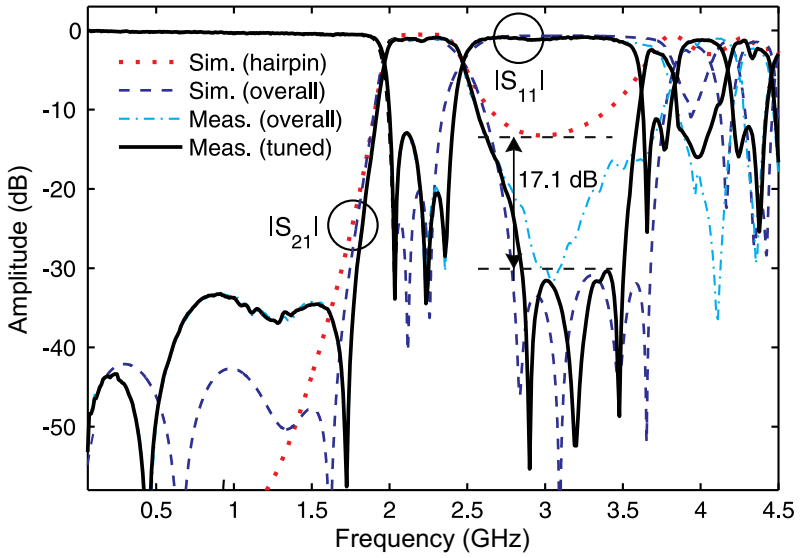

(a) $|S_{21}|$ and $|S_{11}|$.

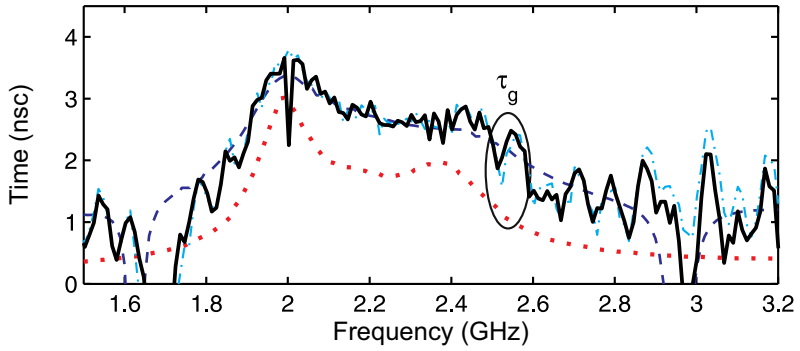

(b) τ_g.

Figure 2.7: Simulated and measured power transmission ($|S_{21}|$), reflection ($|S_{11}|$), and group delay (τ_g) curves of the manufactured prototype 2, along with the simulated $|S_{21}|$ and τ_g curves of its basic low-order—third-order hairpin-type—filter prototype [51].

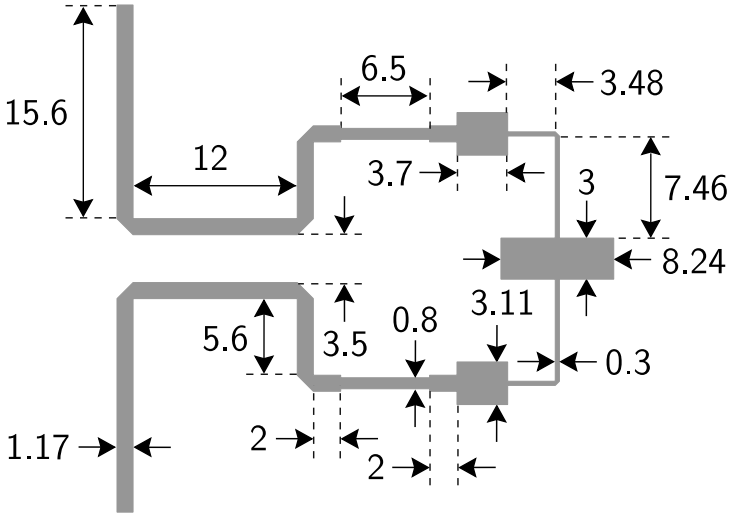

(a) Layout (non-redundant dimensions, in mm, are indicated).

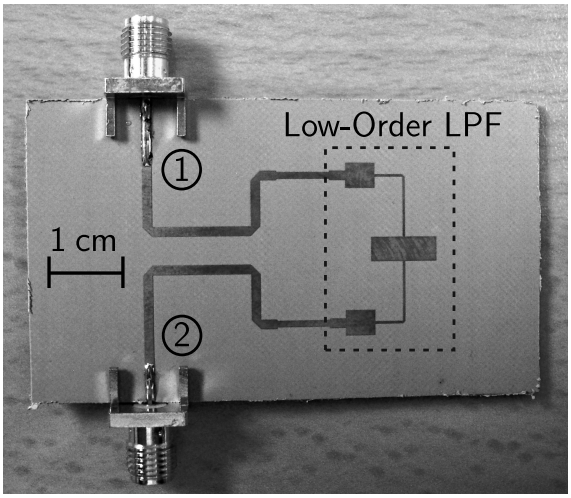

(b) Photograph (microstrip substrate: CER-10 of *Taconic*).

Figure 2.8: Layout and photograph of the manufactured microstrip LPF (pototype 3) [51].

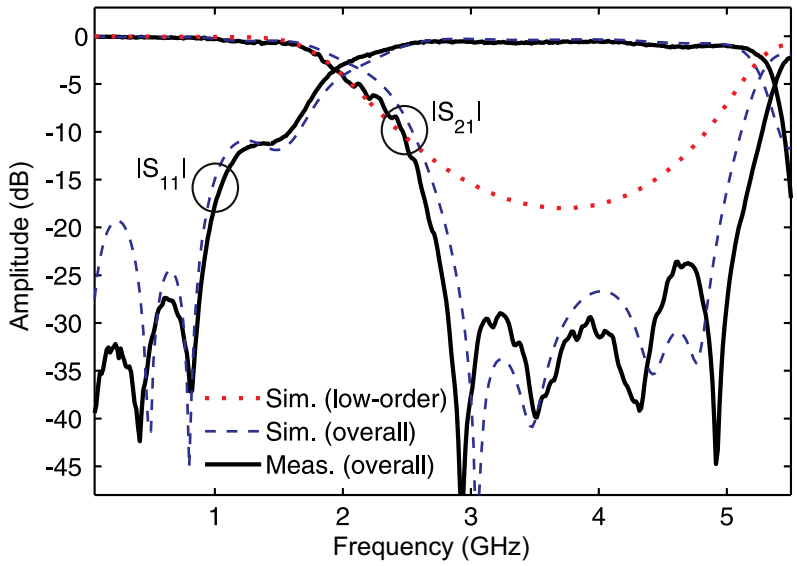

(a) $|S_{21}|$ and $|S_{11}|$

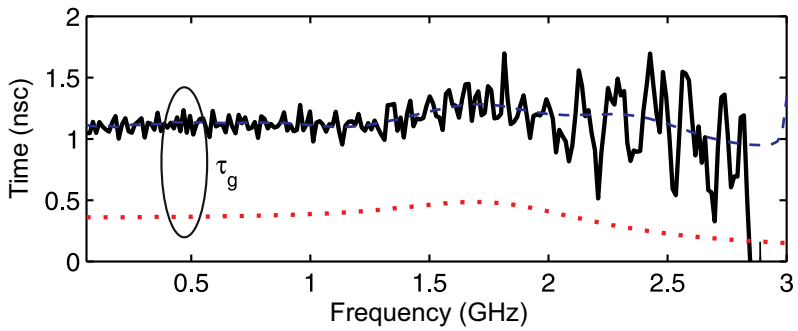

(b) τ_g

Figure 2.9: Simulated and measured power transmission ($|S_{21}|$), reflection ($|S_{11}|$), and group delay (τ_g) curves of the manufactured prototype 3, along with the simulated $|S_{21}|$ and τ_g curves of its basic low-order—stepped-impedance type—filter prototype [51].

dicted results, hence validating the devised concept.

Prototype 4: Hybrid Π-type highpass filter

Prototype 4 also contributes to the extension of the devised technique to other transfer functions different from the bandpass type by addressing a HPF design [124]. In this case, the basic filter consists of two short-circuited transmission-line stubs connected with a lumped capacitor—2.9 pF as capacitance value—. This initial filter exhibits a 3-dB cut-off frequency of 860 MHz and has no TZs in the stopband apart from the one located at direct current (DC). The layout and a photograph of the manufactured prototype after adding the multi-TZ-creation transversal cell are

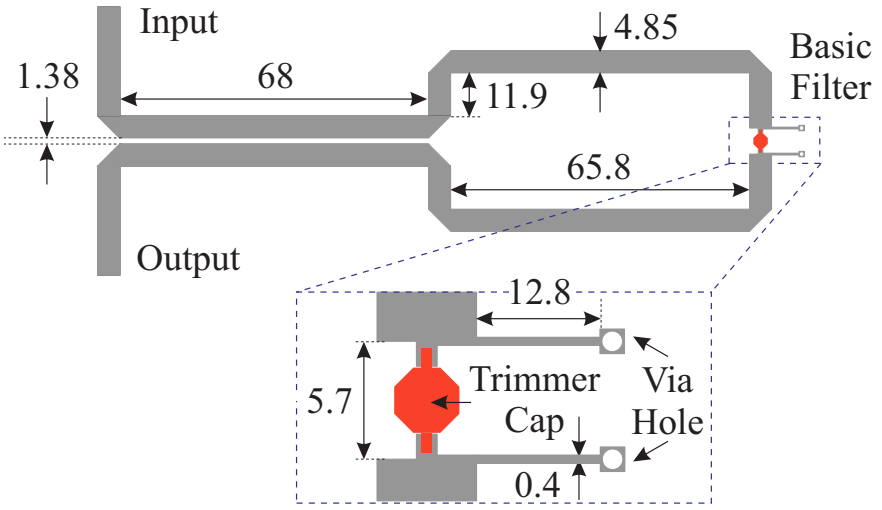

(a) Layout (non-redundant dimensions, in mm, are indicated).

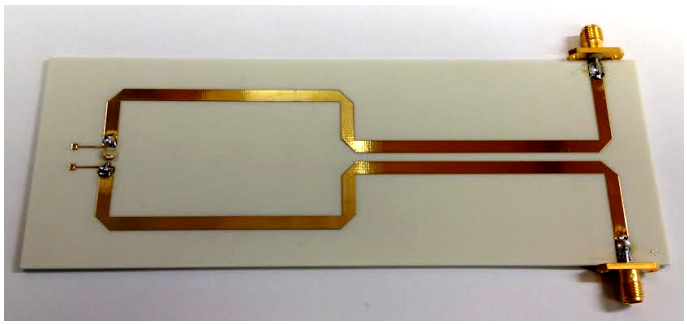

(b) Photograph (microstrip substrate: RO4003 of *Rogers*).

Figure 2.10: Layout and photograph of the manufactured microstrip HPF (prototype 4) [124].

depicted in Figure 2.10.

The simulated and measured S-parameters—$|S_{11}|$ and $|S_{21}|$—of the overall HPF circuit, altogether with the simulated results for its basic counterpart, are drawn in Figure 2.11. As can be seen, the sharpness of the cut-off slope is significantly increased owing to the three additional TZs. As in the preceding prototypes, the in-band performance of the basic HPF is preserved—including the maximum variation of the in-band group delay—. However, some deterioration of the input power matching and a minor in-band amplitude ripple is observed. They are attributed to imperfections in the basic HPF design due to the combination of distributed and lumped components, which make it more sensitive.

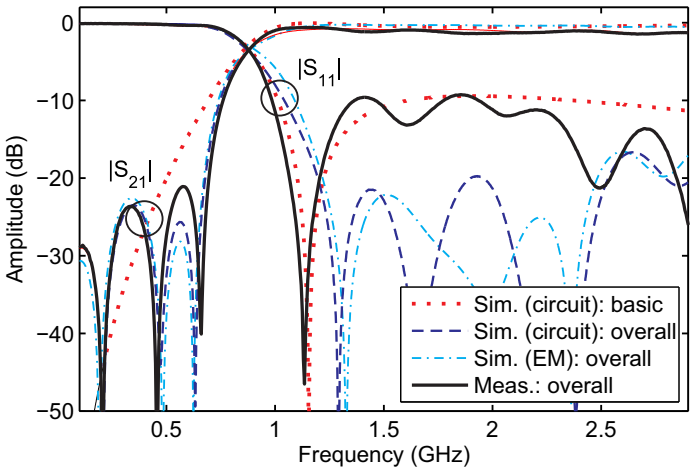

Figure 2.11: Simulated and measured power transmission ($|S_{21}|$) and reflection ($|S_{11}|$) parameters of the manufactured prototype 4, along with the simulated $|S_{21}|$ and $|S_{11}|$ curves of its building basic—hybrid lumped/distributed-element—filter prototype [124].

Prototype 5: Three-stage bi-path-TFS-based signal-interference dual-band bandpass filter

Finally, prototype 5 addresses the design of an enhanced-selectivity dual-band BPF prototype [124]. The creation of extra TZs in this transfer function is quite demanding because they must be generated in a much broader and non-continuous part of the spectrum—i.e., the attenuated bands at both sides of the dual passbands—.

In this case, the circuit chosen as the basic filter of the entire structure is the one reported in [11]. It consists of three series-cascaded signal-interference TFSs shaped by two transmission-line segments connected in parallel. Its ideal synthesized design parameters are detailed in the caption of Figure 2.12 in [11], where those of the proposed signal-interference coupling cell are as follows: $Z_0 = 50\ \Omega$, $c = 21.94$ dB, $\theta_c(f_d) = 360^{\text{o}}$, $\theta_1(f_d) = 180^{\text{o}}$, and $f_d = 2$ GHz. The comparison between the ideal power transmission and reflection curves of the basic and the overall circuit is shown in Figure 2.12. As can be seen, ten additional TZs are produced in the whole attenuated frequency range of the overall circuit.

It should be mentioned that the creation of the TZs is highly sensitive to the homogeneity of the transmission medium in this particular design. Since the even- and odd-mode propagation constants in stripline coupled lines are equal, this technology would be more suitable for this circuit than microstrip one.

The layout of the dual-band BPF is shown in 2.13. Note that, for such a stripline implementation, the substrate RO4003C has been employed with the spacing between ground planes being $h = 2.38$ mm. This is equivalent to bond two microstrip laminates. Its simulated power transmission and reflection responses are drawn in Figure 2.14. It also shows the equivalent curves using microstrip lines to emphasize the aforementioned dependency of the filter behavior to the homogeneity of the transmission medium. Once again, it is demonstrated that the influence of the

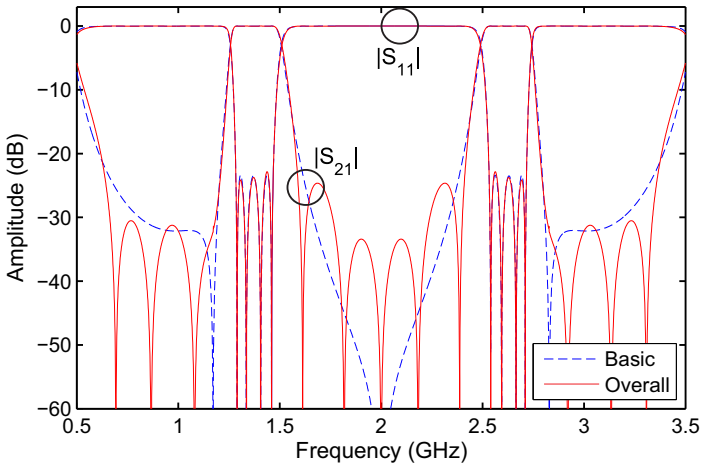

Figure 2.12: Ideal power transmission ($|S_{21}|$) and reflection ($|S_{11}|$) responses of the synthesized overall dual-band BPF and its building basic dual-band BPF [124].

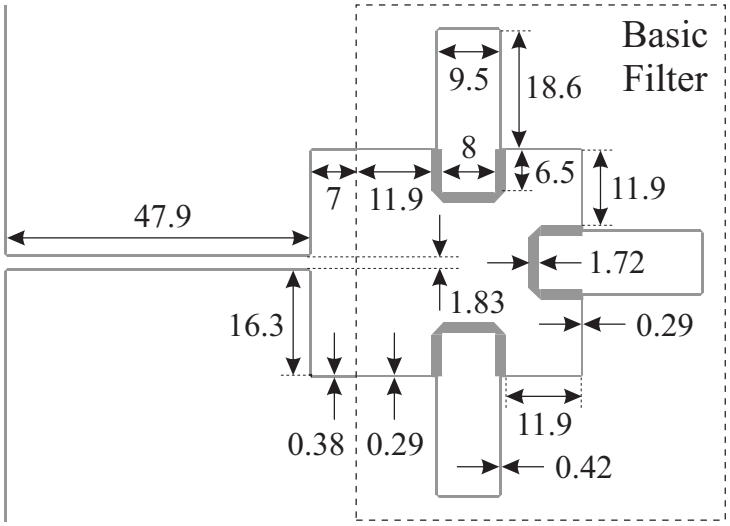

Figure 2.13: Layout of the devised stripline dual-band BPF (prototype 5) [124]. Non-redundant dimensions, in mm, are indicated.

signal-interference coupling cell in the in-band frequency response is negligible.

2.2 Filters with frequency-asymmetrical response based on the stub-loading technique

Since most of the structures based on signal-interference principles are shaped by transmission-line segments whose electrical lengths are integer multiples of a quarter wavelength at f_d, they exhibit frequency-symmetrical responses. This could be a shortcoming in multi-standard receivers with multi-band requirements because different absolute bandwidths are usually needed for their operative bands.

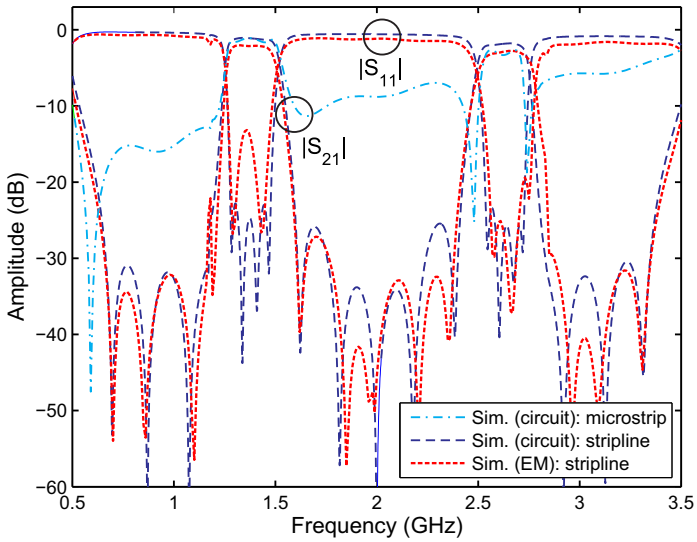

Figure 2.14: Simulated (circuit and EM simulator) power transmission ($|S_{21}|$) and reflection ($|S_{11}|$) responses of the synthesized stripline dual-band BPF and power transmission response of its microstrip counterpart [124].

As already stated, the only contribution to date with the aim of obtaining spectrally-asymmetrical transfer functions under signal-interference principles was reported in [30]. Its strategy is to introduce stepped-impedance lines into the branches of the TFS formed by two transmission lines connected in parallel. However, such procedure increases the design complexity and normally leads to lower power rejection levels in the attenuated bands when compared to their homogeneous-line-impedance counterparts.

For the above reason, a new approach of signal-interference filters exhibiting strong spectral asymmetry is introduced here. Its principle consists of inserting short-circuited stubs at strategic points of the electrical paths forming conventional signal-interference TFSs. Moreover, through the proper design of these stubs, filtering selectivity as well as power rejection levels and bandwidths of the attenuated bands can be increased.

2.2.1 Theoretical foundations

The engineered method to obtain spectral asymmetry is here applied to the aforementioned in-parallel-two-transmission-line-based TFS with single- and dual-band behavior [10], [11]. Nevertheless, it can be extended to other class of TFSs, such as those based on baluns or directional couplers in reflection mode [19], [27]. Its concept is illustrated in Figure 2.15, where the electrical paths of the TFS are loaded with a plurality of short-ended stubs. These stubs have three different objectives. Firstly, they allow to modify the TFS transfer function to incorporate spectral asymmetry into it; secondly, they permit to create additional TZs; and thirdly, some of these TZs help to attain sharp-rejection capabilities when located close to the passband

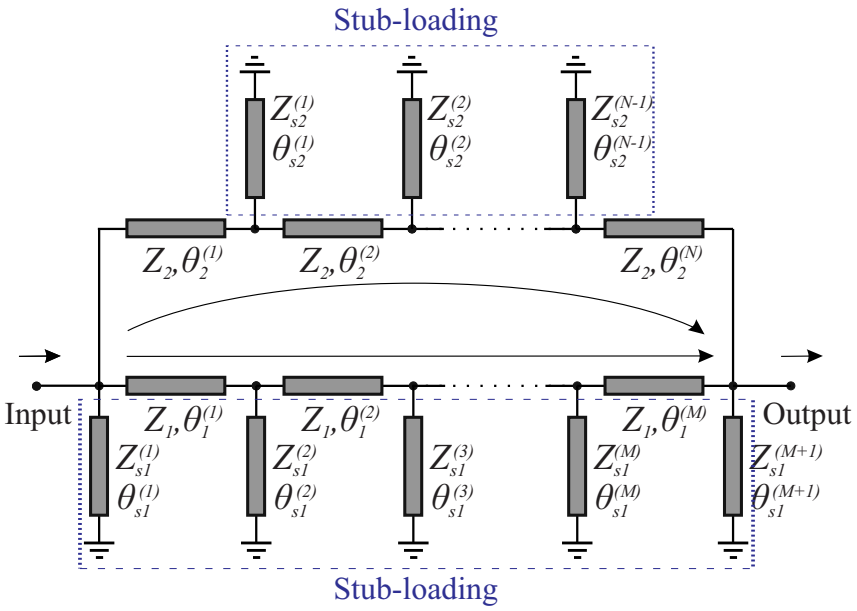

Figure 2.15: Schematic of the proposed stub-loaded bi-path TFS.

range.

To carry out the design of the stub-loaded TFS, the guidelines below must be followed:

- As initial step, the design parameters—line impedances and electrical lengths—of the transmission-line segments that make up the TFS before its stub loading must meet the theoretical foundations of the conventional approach. This means that their values are chosen according to the equations provided in [10] and [11] for single- and dual-band TFSs, respectively.
- The electrical lengths of the loading stubs must be equal to an odd-integer multiple of $\pi/2$ at the design frequency f_d except those connected in the TFS input/output terminals. This is done to preserve at this frequency the maximum power transmission condition in the case of the single-band BPF [10] and the null power transmission condition in the case of the dual-band BPF [11], respectively.
- The remaining design parameters must be optimized to fulfill the prefixed selectivity requirements imposed by the specified filtering mask.

For the purpose of verifying the devised approach, a single- and a dual-band prototype have been synthesized. Figure 2.16 represents the ideal power transmission responses for a stub-loaded single-band TFS and its conventional counterpart described in [10]. Similarly, Figure 2.17 depicts the ideal power transmission curves for a stub-loaded dual-band TFS and its basic counterpart presented in [11]. Note that in both cases the design parameters are included in the caption of Figures 2.16 and 2.17, respectively. As can be observed, spectrally-asymmetrical transfer functions are obtained. In addition, a remarkable improvement of the close-to-passband

selectivity is attained along with increased power rejection levels and bandwidths for the attenuated bands.

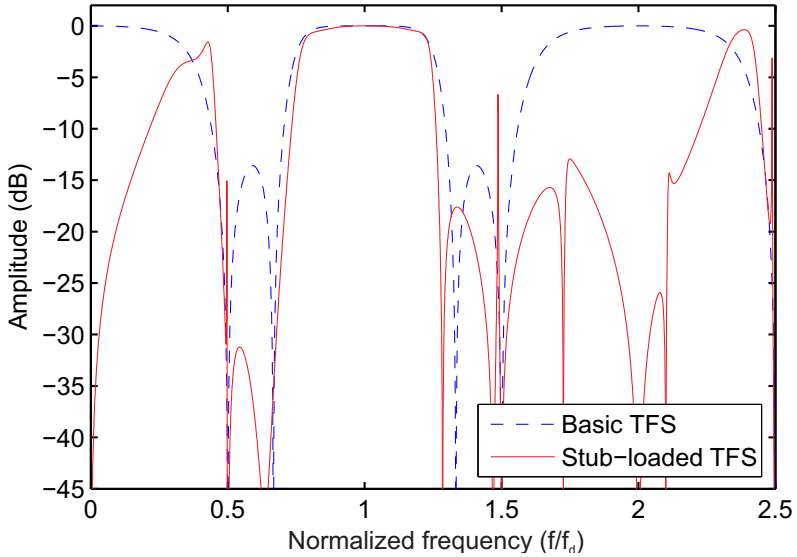

Figure 2.16: Ideal theoretical power transmission ($|S_{21}|$) response of the synthesized stub-loaded single-band bandpass TFS and its basic counterpart [10]. Design parameters ($M = 2$, $N = 3$, $Z_0 = 50\ \Omega$): $Z_1 = Z_2 = Z_{s1}^{(1)} = Z_{s1}^{(3)} = Z_{s2}^{(1)} = Z_{s2}^{(2)} = 100\ \Omega$, $Z_{s1}^{(2)} = 30\ \Omega$, $\theta_1^{(1)}(f_d) = 0.447\pi$, $\theta_1^{(2)}(f_d) = 0.053\pi$, $\theta_2^{(1)}(f_d) = 0.947\pi$, $\theta_2^{(2)}(f_d) = 3\pi/2$, $\theta_2^{(3)}(f_d)$=0.053π, $\theta_{s1}^{(1)}(f_d)$=$\theta_{s1}^{(3)}(f_d)$=π, $\theta_{s1}^{(2)}(f_d) = \theta_{s2}^{(1)}(f_d) = \theta_{s2}^{(2)}(f_d) = \pi/2$.

2.2.2 Experimental results

As experimental example, a 50-Ω-referred signal-interference dual-band BPF prototype showing spectral asymmetry is developed in microstrip technology. In relation with the design, fabrication, and testing processes of this circuit, the following points must be highlighted:

- The microstrip substrate CER-10 of *Taconic*^{TM} is used in the manufacturing process whose parameters are: relative dielectric permittivity $\varepsilon_r = 10$, dielectric thickness $h = 1.19$ mm, dielectric loss tangent $\tan\delta_D = 0.0025$, and metal thickness $t = 35\ \mu$m [45]. The ground connections were implemented by means of 1-mm-diameter metallic via holes.
- The commercial software package *AWR Microwave Office*^{TM} of *AWR Corporation* is employed for the ideal circuit simulation of the prototype [47].
- The commercial software package *Sonnet*^{TM} of *Sonnet Software, Inc.* is used for 3-D planar EM simulation of the prototype by the Shielded-Domain MoM [49].
- An 8713B network analyzer of *Agilent*^{TM} is utilized to carry out the measurements [50].

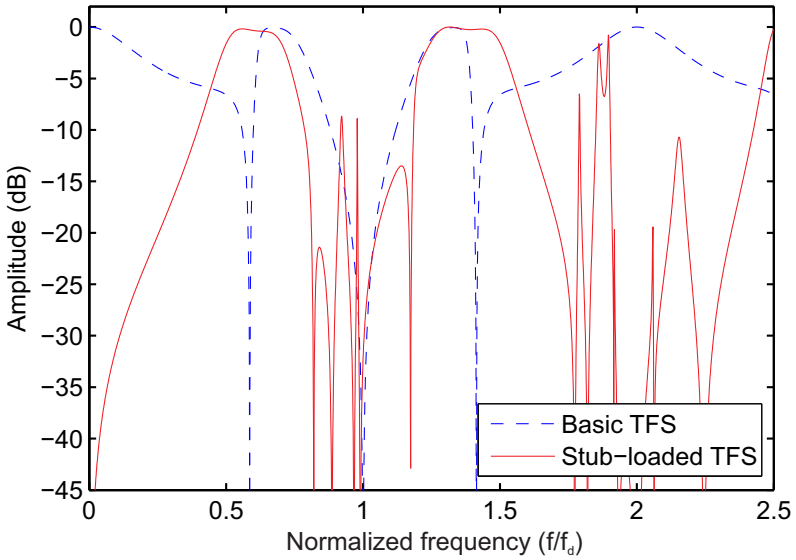

Figure 2.17: Ideal theoretical power transmission ($|S_{21}|$) response of the synthesized stub-loaded dual-band bandpass TFS and its basic counterpart [10]. Design parameters ($M = 3$, $N = 4$, $Z_0 = 50\ \Omega$): $Z_1 = 26.5\ \Omega$, $Z_2 = 49.6\ \Omega$, $Z_{s1}^{(1)} = 97.6\ \Omega$, $Z_{s1}^{(3)} = Z_{s2}^{(2)} = Z_{s2}^{(3)} = 20\ \Omega$, $Z_{s1}^{(4)} = 100\ \Omega$, $Z_{s2}^{(1)} = 57.6\ \Omega$, $\theta_1^{(1)}(f_d) = 0.541\pi$, $\theta_1^{(2)}(f_d) = 0.053\pi$, $\theta_1^{(3)}(f_d) = 0.418\pi$, $\theta_2^{(1)}(f_d) = 0.429\pi$, $\theta_2^{(2)}(f_d) = 0.452\pi$, $\theta_2^{(3)}(f_d) = 0.019\pi$, $\theta_2^{(4)}(f_d) = 1.1\pi$, $\theta_{s1}^{(1)}(f_d) = 1.128\pi$, $\theta_{s1}^{(2)}(f_d) = \theta_{s1}^{(3)}(f_d) = \theta_{s2}^{(1)}(f_d) = \theta_{s2}^{(2)}(f_d) = \theta_{s2}^{(3)}(f_d) = \pi/2$, $\theta_{s1}^{(4)}(f_d) = 1.034\pi$.

Prototype: Dual-band bandpass filter

The built and tested microstrip prototype is a dual-band BPF referred to a 50-Ω reference impedance whose lower and upper passbands exhibit center frequencies at 0.56 GHz and 1.28 GHz and a 3-dB absolute bandwidths of 185 and 310 MHz, respectively [54]. The overall filter consists of a mirrored cascade of two replicas of the dual-band TFS of Figure 2.17. To connect both TFSs, a transmission line with a characteristic impedance of 60 Ω and $\lambda/4$-length at $f_d = 0.95$ GHz is employed. As already known in signal-interference circuits, the cascade of two TFSs significantly increases the filtering selectivity and the power rejection levels in the attenuated bands when compared to a single TFS. Besides, two input/output lines with characteristic impedance of 37.5 Ω and electrical length of $\lambda/4$ at f_d are inserted into the overall prototype to maximize the in-band power matching levels. The layout and a photograph of the developed circuit are shown in Figure 2.18.

The ideal-circuit, EM-simulated, and measured power transmission and reflection curves of the prototype are depicted in Figure 2.19. As can be seen, there is a reasonable agreement between the simulated and the experimental results, especially in the lower frequency band with regard to f_d. Indeed, a sharp-rejection dual-band bandpass filtering response showing spectral asymmetry along with multiple inter-band TZs is attained. However, there are some discrepancies concerning the appearance of some inter-band transmission peaks and some degradation of the upper-passband power matching. This is attributed to several effects, such as manufacturing tolerances, unexpected coupling or radiation, etc.

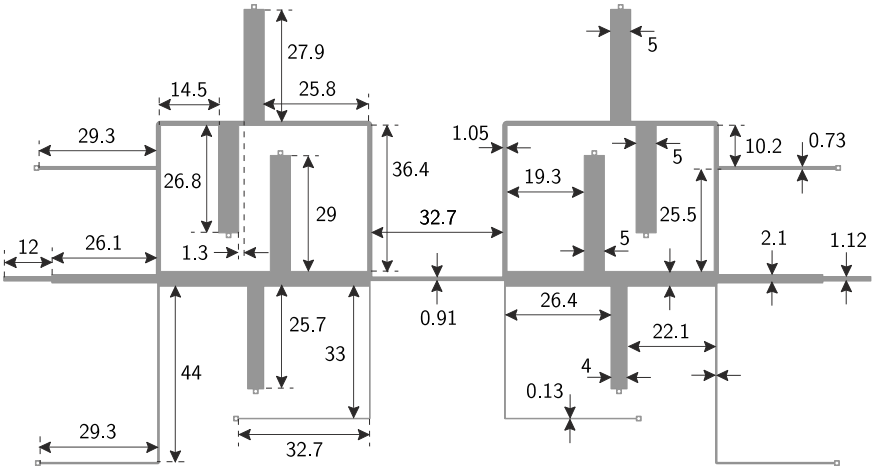

(a) Layout (non-redundant dimensions, in mm, are indicated).

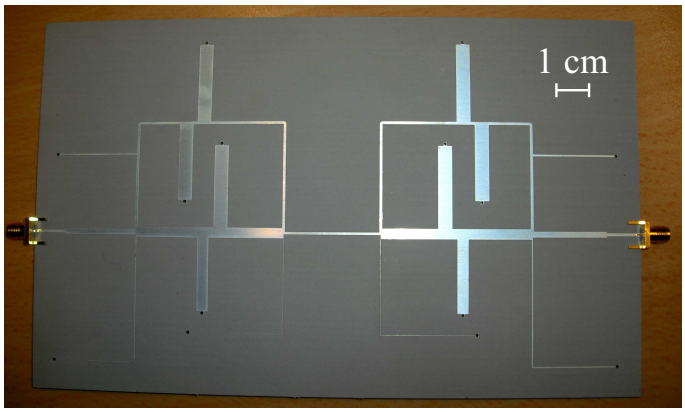

(b) Photograph (microstrip substrate: CER-10 of *Taconic*).

Figure 2.18: Layout and photograph of the manufactured stub-loaded microstrip dual-band BPF [54].

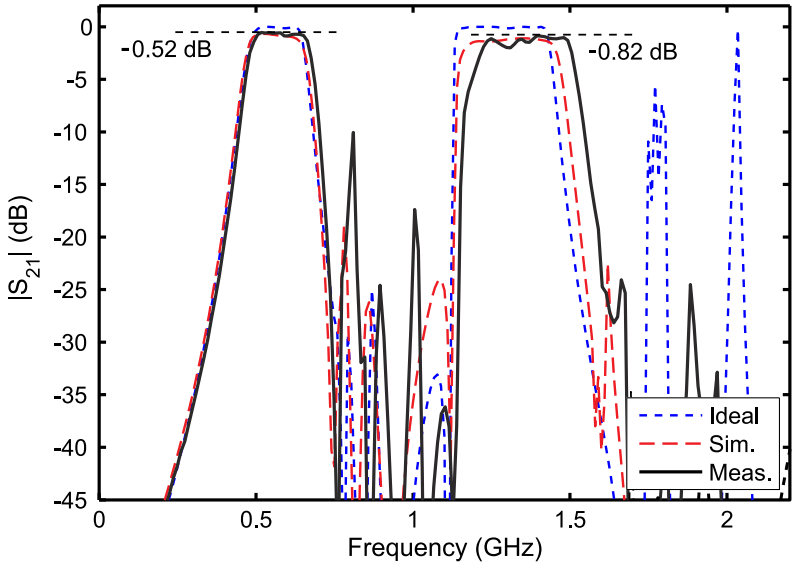

(a) $|S_{21}|$.

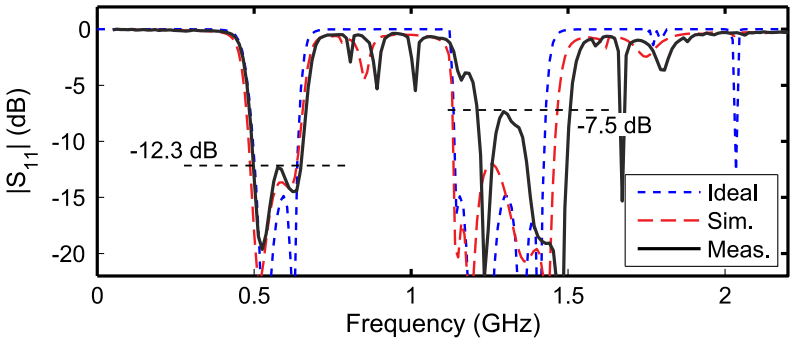

(b) $|S_{21}|$.

Figure 2.19: Ideal theoretical, simulated, and measured power transmission ($|S_{21}|$) and reflection ($|S_{11}|$) curves of the manufactured microstrip dual-band BPF prototype [54].

2.3 Conclusion

This chapter has addressed the design of novel signal-interference filters simultaneously exhibiting high selectivity and low in-band group-delay variation as well as frequency-asymmetrical transfer functions.

First, a novel technique to implement high-selectivity planar filters has been described. Given a basic low-order filter whose in-band group-delay profile fulfills the requirements imposed by a certain phase-distortion specification, its selectivity can be improved by adding a multi-TZ-generation transversal cell to its input/output terminals. This is done without nearly affecting the in-band amplitude and group-delay flatness characteristics imposed by the basic filter. Besides, it should be remarked upon the simplicity of this external transversal cell, which is generally composed of a coupled-line stage and two additional transmission-line segments between the basic filter and the coupled-line structure. For practical verification, several single-band prototypes have been built and tested in microstrip technology, such as two BPFs, a LPF, and a HPF. Furthermore, its applicability to dual-band filtering responses has also been corroborated with a stripline prototype simulated at the layout level.

Regarding the attainment of spectrally-asymmetrical transfer functions in signal-interference filters, this chapter has demonstrated the suitability of the stub-loading technique for it. Through the incorporation of short-ended stubs in strategic points of conventional single- and multi-band signal-interference TFSs, higher-selectivity filtering actions can be synthesized. In addition to spectral asymmetry, both broader bandwidths and higher power rejection levels in the attenuated bands can be achieved. This technique has been verified through an implemented dual-band BPF microstrip prototype with sharp-rejection characteristics that exhibits an upper passband whose bandwidth is nearly twice that of the lower passband.

Chapter 3

Design of lumped-element-based signal-interference microwave filters

Since the first appearance of signal-interference filters in 2005 [10], they have been mostly fabricated in planar technologies, such as microstrip and stripline. This is due to a large extent to compactness and low-insertion-loss advantages in the resulting circuits, in addition to low production costs associated with the materials and the manufacturing processes of printed circuit boards (PCBs) [8]. However, the occupied area by these distributed-element circuits can be excessive in the lower frequency part of the RF/microwave band. In such spectral region, pure-lumped- and hybrid lumped/distributed-element realizations would be more appropriate in terms of size.

On the basis of the above, lumped elements—inductors and capacitors—with easy integration on PCBs are required [55]. Surface mount devices (SMDs) respond to this need and are therefore used in the physical circuit realizations developed in this chapter. Nevertheless, its applicability to RF/microwave filter design is limited to the end of the ultra high frequency (UHF) band [56]—which covers the radio spectrum from 0.3 to 3.0 GHz according to International Communication Union (ITU) nomenclature—.

In addition to the aforementioned size-reduction benefit of the overall filter, the use of commercially available SMDs is a low-cost solution owing to the high-volume production by the manufacturers. Besides, lumped-element filters do not present multiple replicas of the operative bands unlike their distributed-element counterparts due in part to the frequency-periodic behavior of their building transmission-line elements. Note that these spurious frequencies are usually undesired. Nonetheless, they present some limitations as well. The electrical behavior of lumped elements is deteriorated as the frequency increases, owing to the appearance of parasitic effects that turn these components into RLC networks. These real lumped elements present relatively low Q, so that they can hardly be employed to realize narrow-band BPFs above 3 GHz. Moreover, the value of the inductors must be very often controlled to avoid exceeding their self-resonant frequencies (SRFs). And last but not least,

these circuits that are ideally synthesized as pure lumped-element realizations actually require short sections of microstrip lines to interconnect them. The microstrip discontinuities and footprints associated to them must be taken into account in the optimization process. This is necessary to predict possible effects on the overall filtering response.

The purpose of this chapter is the proposal of alternative realizations of signal-interference structures more suitable for the low part of the EM spectrum. Fully-lumped-element implementations and the hybrid combination of lumped and distributed elements in the design of signal-interference circuits is addressed with its subsequent size reduction regarding their classic counterparts. In particular, three alternatives for the implementation of signal-interference filters with discrete elements are presented here. The first methodology replaces the electrically-short transmission-line segments that shape a signal-interference TFS with pure LC components. Similarly, the second approach has the purpose of miniaturizing the 90°-at-f_d transmission-line segments making up signal-interference structures through capacitive-loading techniques, giving rise to hybrid realizations. These two approaches are suitable for any class of transfer function to be synthesized. Finally, a lumped-element realization of the TFS based on a power quadrature coupler operating in reflection mode is presented.

The organization of this chapter is as follows. Firstly, the method to convert planar signal-interference filters into lumped-element circuits by means of symmetric LC T-type equivalent networks is described in Section 3.1. The design formulas for the single-band bandpass TFS based on two in-parallel transmission-line segments are derived along with the convergence analysis with its distributed-element counterpart. For practical verification, a LPF and a BPF prototype are designed at layout level. Secondly, the capacitive-loading technique for miniaturization purposes is applied to signal-interference filters in Section 3.2. Then, the design equations for the single- and the multi-cell approach are provided and its electrical convergence is studied. This technique is additionally combined with line-meandering miniaturization procedures for further size reduction. Its experimental usefulness is demonstrated through single- and dual-band physical realizations. Moreover, a reduced-size reconfigurable-bandwidth filter using this technique is also shown. Finally, the synthesis of single- and dual-band BPFs based on lumped-element power quadrature couplers—branch-line type—operating in reflection mode is presented in Section 3.3. The lumped- and mixed lumped/distributed-element versions of an UWB single-band BPF prototype designed at the layout level are presented as a proof of concept. The main conclusions of this work are summarized in Section 3.4.

3.1 Filters based on LC T-type transversal circuit networks

It is well known that the traditional synthesis of analog filters begins with lumped-element ladder structures, according to Butterworth or Chebyshev transfer function profiles, that are eventually transformed into distributed-element networks [7]. On the contrary, the design of signal-interference filters does not require a

preliminar lumped-element equivalent as an initial step, since the final distributed-element circuit is directly synthesized. Thus, the aim of this sub-section is to present a methodology for the synthesis of lumped-element analog filters exploiting signal-interference principles regardless of the class of filtering profile to be attained. Note that lumped elements have already been successfully used in other types of low- and intermediate-frequency RF filters. For example, in [57] where lumped-element reflectionless filters exhibiting lowpass, highpass, bandpass, and stopband behavior are reported or in [58] where they are incorporated in GaAs MMIC active BPFs.

3.1.1 Theoretical foundations

In the proposed approach, short transmission-line segments are replaced with symmetrical LC T-type sections, as illustrated in Figure 3.1. This basic LC network is inspired by the equivalent discrete-element model of a lossless differential-length transmission line and constitutes an artificial transmission-line segment. Note that such equivalence is perfect at the design frequency $f_c = f_d$, so that its behavior differs from the original transmission line as the spectral distance from f_d increases. Therefore, the electrically-shorter the transmission line is, then the more accurate the equivalent model is in a given frequency interval around f_d. The design values of L and C for a given transmission-line segment of characteristic impedance Z and electrical length θ can be determined as follows:

$$L = \frac{Z(1-\cos(\theta(f_d)))}{2\pi f_d \sin(\theta(f_d))} \qquad C = \frac{\sin(\theta(f_d))}{2\pi f_d Z} \tag{3.1}$$

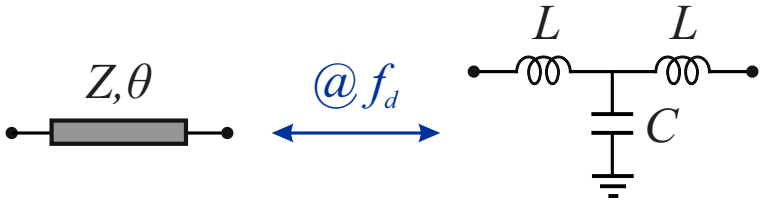

Figure 3.1: LC T-type equivalent model of a transmission-line segment.

Then, this LC T-type equivalent network is applied to a signal-interference TFS consisting of two transmission lines connected in parallel. Figure 3.2 depicts the scheme of the devised lumped-element realization. As can be seen, the original transmission-line segments are divided into M and N transmission-line sub-segments, respectively, each of them being replaced with a LC T-type section ($M, N \in \mathbb{R}$). The design equations for the synthesis of the engineered lumped-element signal-interference TFS along with a convergence analysis between the distributed- and the lumped-element approaches (depending on the number of LC cells) will be shown in this section.

Design equations

As stated before, the perfect equivalence between the basic LC cell and its associated transmission-line sub-segment is established at a certain design frequency f_d.

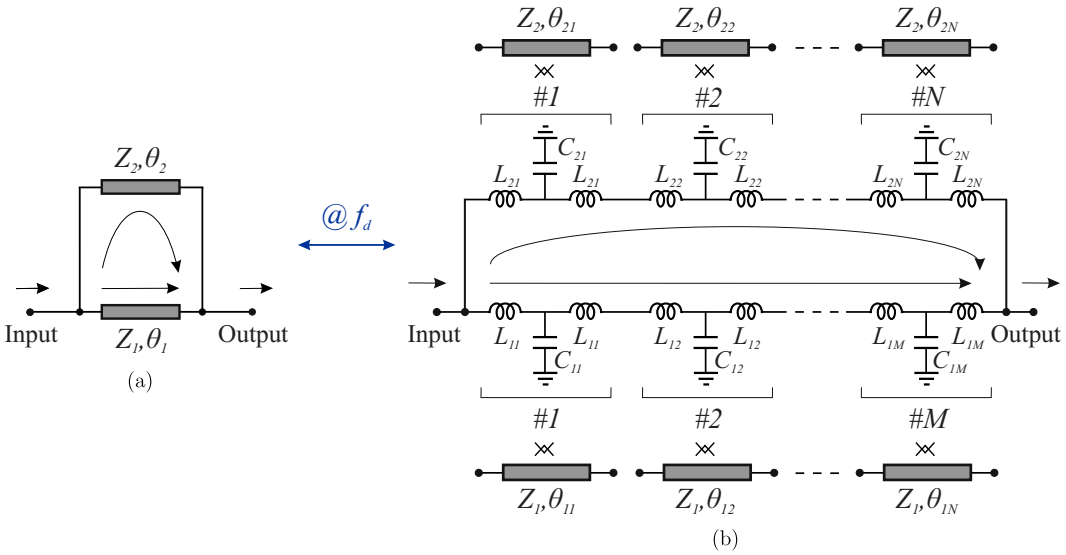

Figure 3.2: Signal-interference TFS based on two in-parallel transmission-line segments. (a) Basic approach. (b) Lumped-element model.

The L and C values can thus be derived by making equal the impedance parameters $\{Z_{kl}\}_{k,l=1,2} \in \mathbb{C}$ of the LC cell and the transmission-line sub-segment at f_d because they are both symmetrical two-port networks. For the overall TFS, the following design equations are obtained:

$$L_{1k} = \frac{Z_1(1-\cos(\theta_{1k}(f_d)))}{2\pi f_d \sin(\theta_{1k}(f_d))} \qquad C_{1k} = \frac{\sin(\theta_{1k}(f_d))}{2\pi f_d Z_1} \tag{3.2}$$

$$L_{2l} = \frac{Z_2(1-\cos(\theta_{2l}(f_d)))}{2\pi f_d \sin(\theta_{2l}(f_d))} \qquad C_{2l} = \frac{\sin(\theta_{2l}(f_d))}{2\pi f_d Z_2} \tag{3.3}$$

$$\forall k \in \{1,2,...,M\} \qquad \forall l \in \{1,2,...,N\} \tag{3.4}$$

where it is satisfied that:

$$\sum_{k=1}^{M} \theta_{1k}(f_d) = \theta_1(f_d) \qquad \sum_{l=1}^{N} \theta_{2l}(f_d) = \theta_2(f_d) \tag{3.5}$$

In the previous expressions, $Z_1, Z_2 \in \mathbb{R}^+$ and $\theta_1, \theta_2 \in \mathbb{R}^+$ ($\theta_2 > \theta_1$ is assumed without loss of generality) are the characteristic impedances and electrical lengths of the circuit lines of Figure 3.2(a); $L_{11}, L_{12}...L_{1M}, L_{21}, L_{22}...L_{2N} \in \mathbb{R}^+$ and $C_{11}, C_{12}...C_{1M}, C_{21}, C_{22}...C_{2N} \in \mathbb{R}^+$ are the inductances and capacitances of the LC cells of Figure 3.2(b), whereas $\theta_{11}, \theta_{12}...\theta_{1M}, \theta_{21}, \theta_{22}...\theta_{2N} \in \mathbb{R}^+$ refer to the electrical lengths of their equivalent transmission-line subsegments; $f \in \mathbb{R}^+$ denotes the real frequency variable.

Through the design formulas provided in (3.2)–(3.5) the values for the lumped-element components shaping the signal-interference TFS based on two in-parallel

transmission lines can be derived. Note that such design formulas are applicable to any class of transfer function synthesized by this particular bi-path TFS, covering single-band BPFs [10], dual-band BPFs [11], multi-band BPFs [12], and single-band BSFs [22]. This requires obtaining the values Z_1, Z_2, θ_1, and θ_2 according to the synthesis formulas provided in these works. For example, in the case of single-band signal-interference BPFs, the following equations from [10] must be taken into account:

$$\frac{1}{Z_1} + \frac{1}{Z_2} = \frac{1}{Z_0} \tag{3.6}$$

$$\theta_1\left(f_d\right) = \frac{m\pi}{2} \qquad \theta_2\left(f_d\right) = \frac{(m+2n)\pi}{2} \tag{3.7}$$

where Z_0 is the reference impedance and $m, n \in \mathbb{N}$. These equations, as well as those of other works, allow some degrees of freedom in the final realization by means of lumped elements. They can be used to adjust the 3-dB relative bandwidth and the location of the TZs of the resulting bandpass filtering response.

Convergence analysis

Once the equivalence between the distributed- and the lumped-element TFSs is established, it is worth analyzing the convergence between their frequency responses. Figure 3.3 represents the power transmission and reflection curves of a synthesized distributed-element TFS and two solutions for its lumped-element approximation [59]. The three examples have as values for the design parameters $Z_0 = 50\ \Omega$ and $f_d = 1$ GHz. They are as follows:

- Response 1: distributed-element TFS with $Z_1 = Z_2 = 2Z_0 = 100\ \Omega$, $m = 1$, and $n = 1$.
- Response 2: lumped-element TFS made up of an LC cell with $L = 6.59$ nH and $C = 1.12$ pF for all the equivalent $\lambda_d/8$-length line segments of its two signal paths (i.e., $M = 2$ and $N = 10$).
- Response 3: lumped-element TFS made up of an LC cell with $L = 3.17$ nH and $C = 0.61$ pF for all the equivalent $\lambda_d/16$-length line segments of its two signal paths (i.e., $M = 4$ and $N = 20$).

As observed, there is fair agreement between the S-parameters of the lumped-element TFS and those of its distributed-element equivalents within a wide frequency range around the design frequency f_d. As expected, the accuracy of this model is higher as more LC networks are employed.

3.1.2 Simulation results

For practical validation, two examples have been designed at the layout level. The first prototype is a single-stage LPF and the second one is a three-stage BPF.

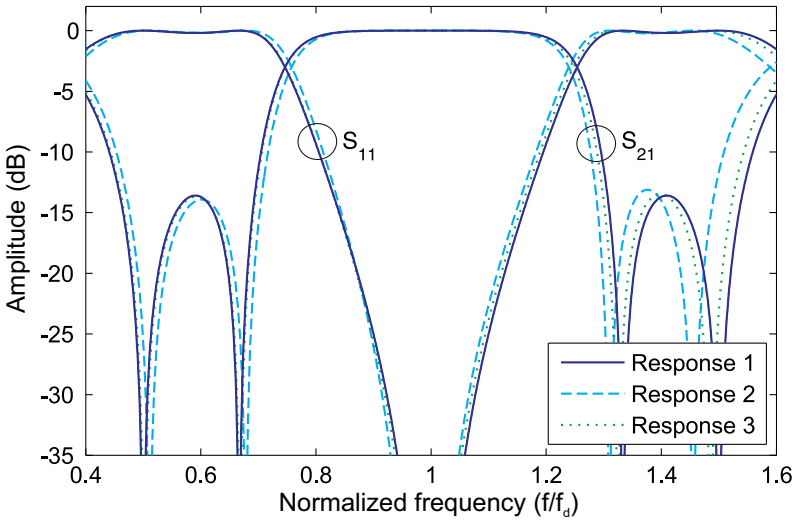

Figure 3.3: Ideal power transmission ($|S_{21}|$) and reflection ($|S_{11}|$) responses of a synthesized example of a distributed-element TFS and two equivalent lumped-element realizations: convergence analysis [59].

Starting with the synthesis of an approximate ideal design, both prototypes are optimized in order to fulfill the imposed requirements. It should be remarked upon that the practical suitability of this technique is also demonstrated in Chapter 5 in which a lumped-element Wilkinson-type power divider exhibiting dual-band filtering behavior is built and tested according to the design equations (3.2)–(3.5).

A microstrip substrate type TLC-30 from *Taconic*^{TM} was selected to interconnect the lumped elements in both circuits here presented, whose parameters are: relative dielectric permittivity $\varepsilon_r = 3$, dielectric thickness $h = 1.52$ mm, dielectric loss tangent $\tan\delta_D = 0.003$, and metal thickness $t = 35$ μm [60]. The ground connections were implemented by means of 1-mm-diameter metallic via holes.

Concerning the simulation and optimization processes of these filters, the commercial software package *AWR Microwave Office*^{TM} of *AWR Corporation* was employed [47].

Prototype 1: Quasi-elliptical-type lowpass filter

The first example is a single-TFS quasi-elliptical-type LPF prototype [59]. Its cut-off frequency is 300 MHz and a minimum in-band power matching level of 20 dB was imposed. Also, a 20-dB power rejection level for stopband frequencies above 350 MHz was enforced.

The layout of the designed filter is drawn in Figure 3.4. As can be seen, $M = 1$ and $N = 4$ are chosen as design parameters. Before finding the values of the inductances and capacitances of the LC T-type networks, the values of Z_1, Z_2, θ_1, and θ_2 were obtained according to the synthesis formulas provided in [22]. An optimization process is then carried out for the purpose of fulfilling the prefixed specifications. This optimization process is repeated once the commercial values of the available

lumped inductors and capacitors together with the microstrip transmission-line segments and discontinuities, such as tees and bends, are taken into account. The commercially available lumped components chosen for this prototype are listed in Table 3.1.

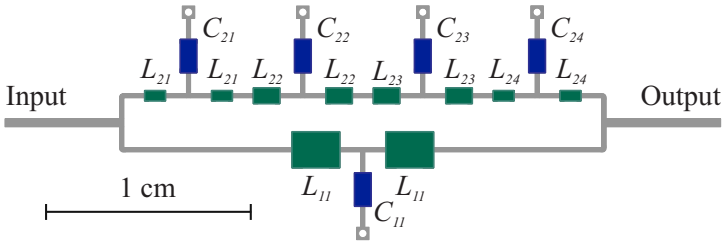

Figure 3.4: Layout of the final design of the lumped-element single-TFS LPF [59].

Table 3.1: Lumped-element components of the single-TFS LPF in Figure 3.4 based on LC T-type networks.

Lumped-element components for Prototype 1				
Component	Ideal value	Real value	Product Code	RS Code*
L_{11}	93.4 nH	91 nH	36502A91NJTDG	532-3392
C_{11}	4.2 pF	3.9 pF	GRM1885C1H3R9BZ01D	723-5884
L_{21}	0.24 nH	0.2 nH	36401E0N2ATDF	701-6771
C_{21}	4.1 pF	5.6 pF	GRM1885C1H5R6BZ01D	723-5938
L_{22}	35.9 nH	33 nH	36501E33NJTDG	532-2513
C_{22}	10.5 pF	10 nH	GRM1885C1H100FA01D	723-5770
L_{23}	35.9 nH	33 nH	36501E33NJTDG	532-2513
C_{23}	10.5 pF	10 pF	GRM1885C1H100FA01D	723-5770
L_{24}	0.24 nH	0.2 nH	36401E0N2ATDF	701-6771
C_{24}	4.1 pF	5.6 pF	GRM1885C1H5R6BZ01D	723-5938

*`http://es.rs-online.com/web/`

Figure 3.5 represents the power transmission and reflection frequency responses for the real simulated realization—i.e., considering commercial lumped elements—and its ideal pure-lumped-element counterpart. As can be seen, the specifications of the attenuation mask are perfectly met for both designs. Two TZs are generated close to the passband owing to perfect destructive signal-energy cancelations taking place at these frequencies between the TFS electrical paths.

Prototype 2: Quasi-elliptical-type bandpass filter

The second practical example is a multi-stage quasi-elliptical-type BPF prototype [59] whose center frequency and 3-dB absolute bandwidth are set as 250 MHz and 135 MHz, respectively—resulting in a 3-dB relative bandwidth of 55%—. In this case, a minimum in-band power matching level of 20 dB is enforced. In addition, power rejection levels higher than 25 dB for those frequencies above 350 MHz are

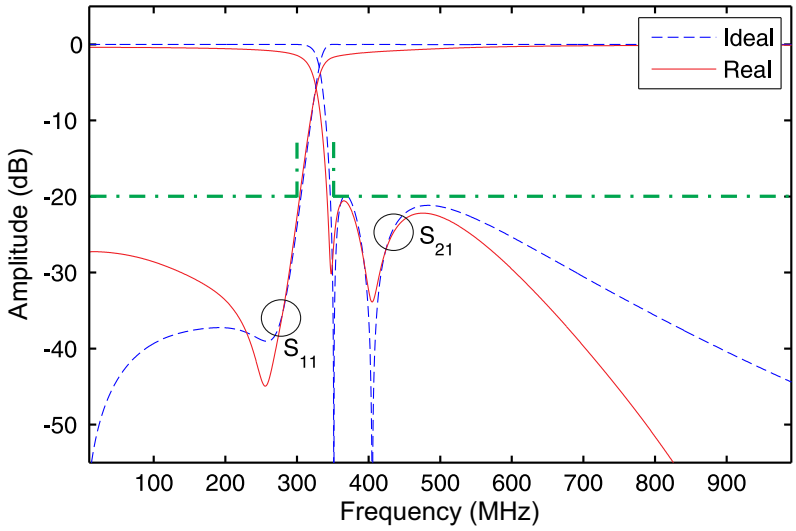

Figure 3.5: Power transmission ($|S_{21}|$) and reflection ($|S_{11}|$) responses with the attenuation mask of the designed LPF: ideal and real models [59].

imposed.

The three TFSs forming the overall filter have $M = 1$ and $N = 1$ as design parameters according to the lumped-element model of Figure 3.2. These TFSs are cascaded in series by transmission-line segments which have also been replaced by a LC T-type networks, where L_c and C_c denote its inductive and capacitive parameters, respectively. Note that the first and the third TFSs are identical—and different from the second one—leading to a network with physical symmetry. Similar to prototype 1, a final optimization process to satisfy the specifications of the attenuation mask is required in both ideal and real designs.

The layout of the real design of the BPF is illustrated in Figure 3.6. The ideal and commercial values of the inductors and capacitors forming this design are included in Table 3.2. Its power transmission and reflection curves are depicted in Figure 3.7. As expected, higher in-band insertion-loss levels when compared to prototype 1 are obtained due to the larger number of employed lumped elements—15 components in prototype 1 and 24 components in prototype 2—. However, the specifications are fulfilled for both the ideal and real cases. Moreover, two out-of-band transmission nulls are generated in the lower stopband.

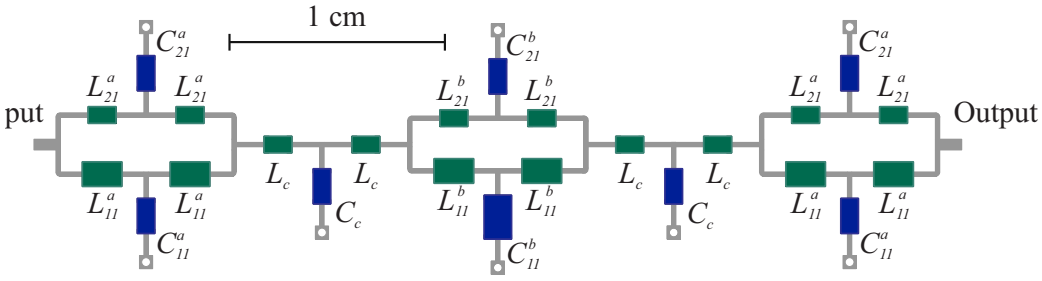

Figure 3.6: Layout of the real design of the lumped-element three-TFS BPF [59].

Table 3.2: Lumped-element components of the BPF in Figure 3.6 based on LC T-type networks.

Lumped-element components for Prototype 2				
Component	Ideal value	Real value	Product Code	RS Code*
L_{11}^a	30.9 nH	24 nH	36501E24NJTDG	532-2478
C_{11}^a	11.5 pF	12 pF	GRM1885C1H120FA01D	723-5799
L_{21}^a	167.8 nH	180 nH	36501JR18JTDG	532-3061
C_{21}^a	40.6 pF	27 pF	GRM1885C1H270FA01D	723-5862
L_{11}^b	38.2 nH	43 nH	36501E43NJTDG	532-2563
C_{11}^b	11.4 pF	10 pF	GRM1885C1H100FA01D	723-5770
L_{21}^b	92.7 nH	120 nH	36501JR12JTDG	532-3033
C_{21}^b	40 pF	24 pF	GRM2165C1H240JZ01D	723-6259
L_c	58.9 nH	56 nH	36501E56NJTDG	532-2591
C_c	9.2 pF	9.1 pF	GQM1885C1H9R1CB01D	647-7412

*`http://es.rs-online.com/web/`

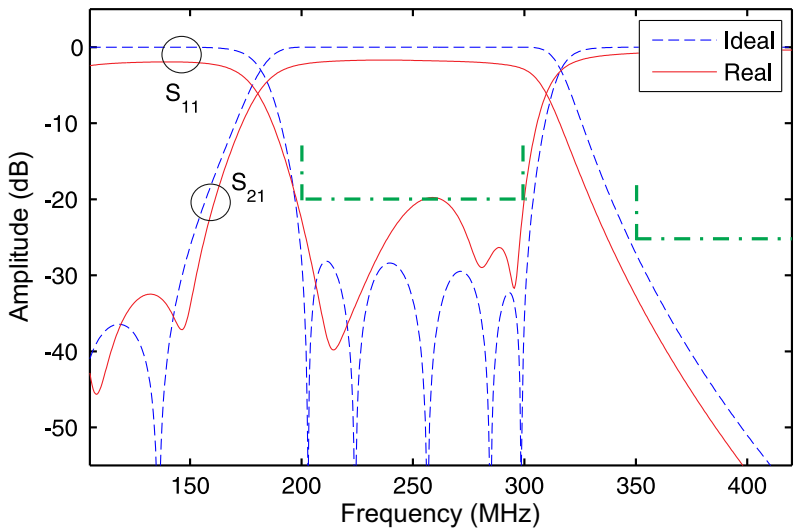

Figure 3.7: Power transmission ($|S_{21}|$) and reflection ($|S_{11}|$) responses with the attenuation mask of the designed BPF: ideal and real models [59].

3.2 Filters based on capacitive-loading and line-meandering techniques

Signal-interference filters present a design simplicity—building blocks made up of simple transmission-line segments directly interconnected and without EM couplings in most cases—that makes them perfect candidates for being miniaturized through traditional techniques employed in RF/microwave planar devices. Notable among these methodologies are the capacitive-loading and line-meandering techniques.

Since the proposal of capacitive-loading techniques in [61] with the objective of miniaturizing branch-line and rat-race hybrid couplers—with a resulting 80% size reduction in the reported prototypes—, its use has been extended to a plurality of planar microwave components. In line with this approach, some of the most significant exponents available in the technical literature are presented below. To begin with, [62] proposed the design of capacitively-loaded Wilkinson-type power dividers in asymmetric coplanar stripline (ACPS) technology and [63] addressed miniaturized branch-line hybrids with suppression of spurious frequencies. In both cases, the lumped loading capacitors are substituted by low-impedance short microstrip lines. Despite the remarkable performance of both approaches, it must be noted that they are less demanding structures than signal-interference filters in terms of frequency bandwidth to be covered. On the other hand, capacitive-loading techniques have already been demonstrated in RF filter design. In particular, a new method to downsize coupled-resonator filters exhibiting moderate bandwidth was presented in [64]. For such a case, both reactive loading—by lumped or distributed elements—and capacitive loading—by distributed elements—techniques were utilized. The suggested circuit in [65] is capable of featuring tunable bandpass filtering actions using varactors—instead of fixed capacitors—to load and couple the building slow-wave transmission lines. Following this trend, in [66], a capacitor connected in series between the feeding lines and the stubs of a dual-behavior resonator (DBR) allows to reduce the physical size in 70% when compared to its fully-distributed-element counterpart. Another example of such miniaturization technique, applied to filtering structures, can be found in [67] where a single-pole single-throw (SPST) switchable BPF was developed in MMIC technology. In the filter design process, capacitively-loaded short-ended hairpin resonators are utilized so as to be realized in a chip size and then make it suitable for most multi-band multi-mode mobile applications. And finally, as a more complex example, the 3-D miniaturized helical filter reported in [68] must be highlighted. The physical size of the helical resonator in the building block is reduced by capacitive loading as well. This is done by creating a gap between the helical conductor and the cavity upper wall. This capacitive gap can be controlled by a piezoelectric actuator so that the resulting frequency response can be tuned. With regard to line-meandering techniques, they have also become popular in recent years. As an example, by replacing straight transmission lines by meandered ones, rat-race and branch-line couplers exhibiting size-reduction factors of 87.4% and 75.4%, respectively, were reported in [69]. In this context, a must-read comparative study of the different miniaturization techniques applied to a microstrip 180° hybrid ring junction can be found in [70].

The current study is therefore intended to complement all previous works with

the application of these size-reduction techniques to signal-interference circuits. Such miniaturization is done through capacitively-loaded realizations as primary methodology. Line-meandering techniques are subsequently applied for further circuit-area saving as long as the physical lengths of the resulting microstrip lines are large enough to avoid potential couplings between them after applying the capacitive-loading procedure.

3.2.1 Theoretical foundations

According to [61], a transmission-line segment whose electrical length is 90° at the design frequency f_d can be converted into a shorter transmission line with higher characteristic impedance loaded by two shunt lumped capacitors as depicted in Figure 3.8. The accuracy of this hybrid cell is however limited as θ_c is reduced ($\theta_c < 90°$), showing a spectral-narrowing effect of its transfer function that is especially remarkable above f_d. Note also that the smallest-size equivalent approach is constrained by the maximum realizable line impedance by the manufacturing process—approximately 120 Ω in microstrip technology [71]—. The values of Z_c and C can be derived as follows:

$$Z_c = \frac{Z}{\sin\theta_c} \qquad C = \frac{\cos\theta_c}{2\pi f_d Z} \tag{3.8}$$

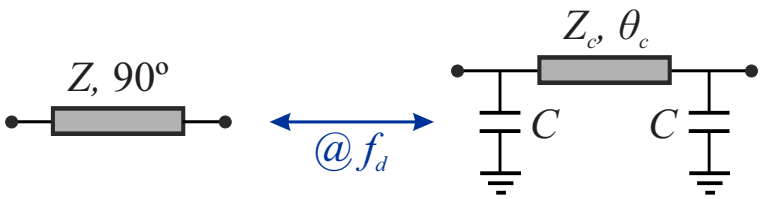

Figure 3.8: Capacitive-loaded equivalent model of a quarter-wavelength transmission-line segment.

Given the fact that signal-interference filters are mostly shaped by directly-connected transmission-line segments whose electrical lengths are 90°-multiples at f_d, the method described here focuses on splitting them into quarter-wavelength line sub-segments for subsequent miniaturization purposes. Besides, in order to improve the accuracy of such a model, each 90° transmission-line sub-segment can be approached by N capacitively-loaded cells. The design formulas for the multi-cell approximation and a convergence study between the single/multi-cell approach and the conventional one are provided below.

Design equations

Figure 3.9 depicts the generalized capacitively-loaded multi-cell approximation of a 90°-electrically-long transmission-line segment. The Z_c and C values can be obtained by making equal the admittance parameters of the capacitively-loaded cell and its transmission-line sub-segment counterpart at the design frequency f_d,

since they are both symmetrical two-port networks. For the whole transmission-line segment, the following design equations are derived:

$$Z_c = \frac{Z \sin(90°/N)}{\sin(\theta_c/N)} \qquad C = \frac{1}{2\pi f_d}\left(\frac{\cos(\theta_c/N)}{Z_c \sin(\theta_c/N)} - \frac{\cos(90°/N)}{Z \sin(90°/N)}\right) \tag{3.9}$$

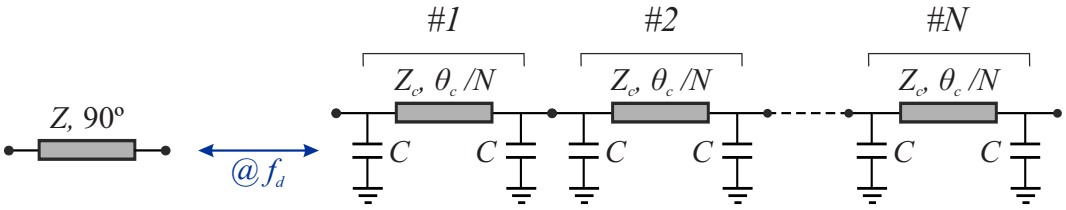

Figure 3.9: Generalization of the equivalent model of Figure 3.8 to N capacitively-loaded transmission-line cells.

The capacitively-loaded multi-cell approximation can be applied to any 90°-electrically-long transmission-line segment forming a signal-interference filter regardless of its topology—TFSs based on two transmission lines connected in parallel, hybrid couplers operating in reflection mode, etc—and its type of transfer function—bandpass, bandstop, etc—.

Convergence analysis

For theoretical verification, a convergence analysis of the single- and the multi-cell miniaturized approach is presented here [72]. Starting with the single-cell approximation $N = 1$, Figure 3.10 shows the power transmission and reflection curves of two examples of lossless signal-interference filters for their classic—i.e., fully-distributed-element design or $\theta_c = 90°$—and capacitively-loaded miniaturized designs ($\theta_c = 75°$, 60°, and 45°). These synthesized examples are as follows:

- Figure 3.10(a): single-band BPF shaped by the hybrid-ring-based TFS of Figure 3.11 [16].
- Figure 3.10(b): dual-band BPF formed by the generalized branch-line-coupler-based TFS of Figure 3.12 [27].

As illustrated in Figure 3.10, the miniaturized versions exhibit spectrally-narrower responses when compared to those of the original designs. As expected, higher levels of miniaturization—smaller values of θ_c—amplify this undesired effect. Therefore, there is usually a trade-off between miniaturization level and frequency accuracy of the capacitively-loading-based transformation.

The latter can be overcome by adopting the capacitively-loaded multi-cell equivalent model at f_d. Thus, Figure 3.13 shows the power transmission and reflection responses of the classic dual-band BPF example shown in Figure 3.10(b) and the generalized capacitively-loaded counterparts for $N = 1$ and 2 ($\theta_c = 45°$). As predicted, the multi-cell approach substantially improves the spectral convergence, but

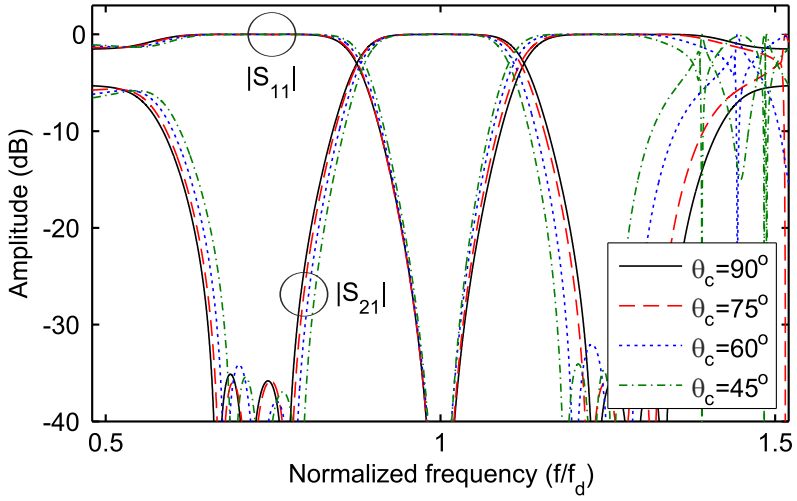

(a) Single-band BPF example.

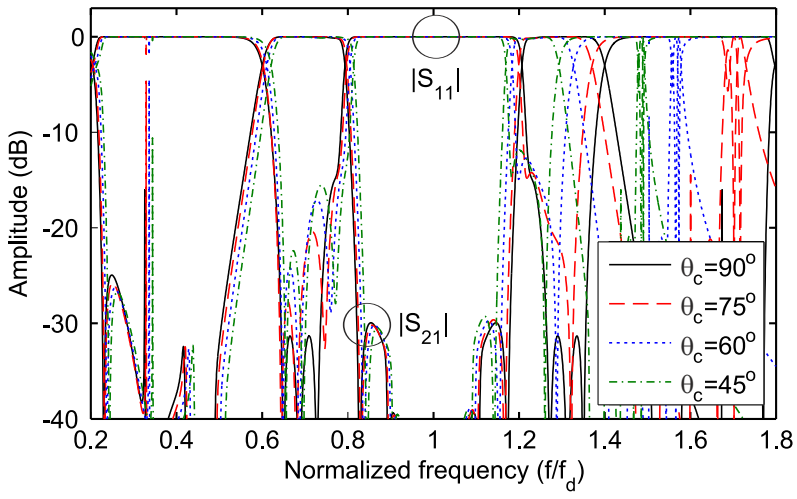

(b) Dualband BPF example.

Figure 3.10: Classic signal-interference filter designs ($\theta_c = 90^o$) and their capacitively-loaded miniaturized equivalents with the approach of Figure 3.8 (cases $\theta_c = 75^o$, 60^o, and 45^o).

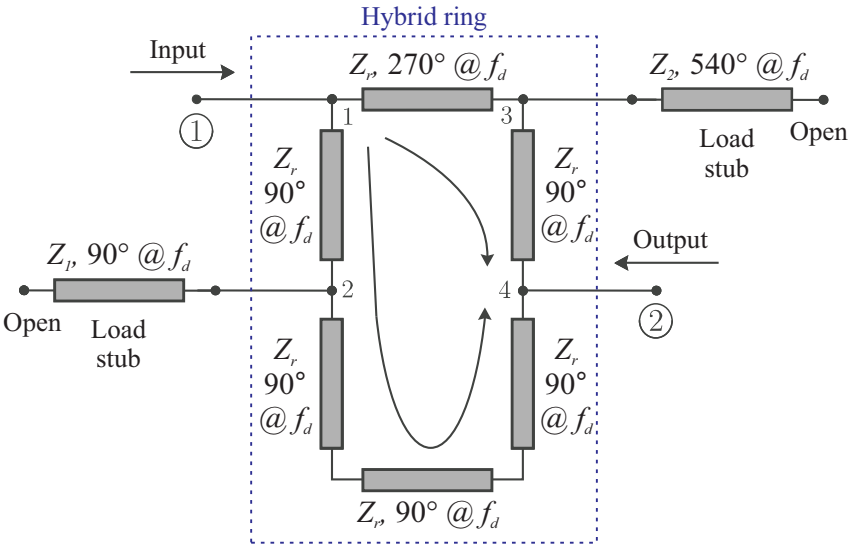

Figure 3.11: Schematic of the hybrid-ring-based TFS (Z_r = 50 Ω, Z_1 = 33.5 Ω, and Z_2 = 45 Ω) [16].

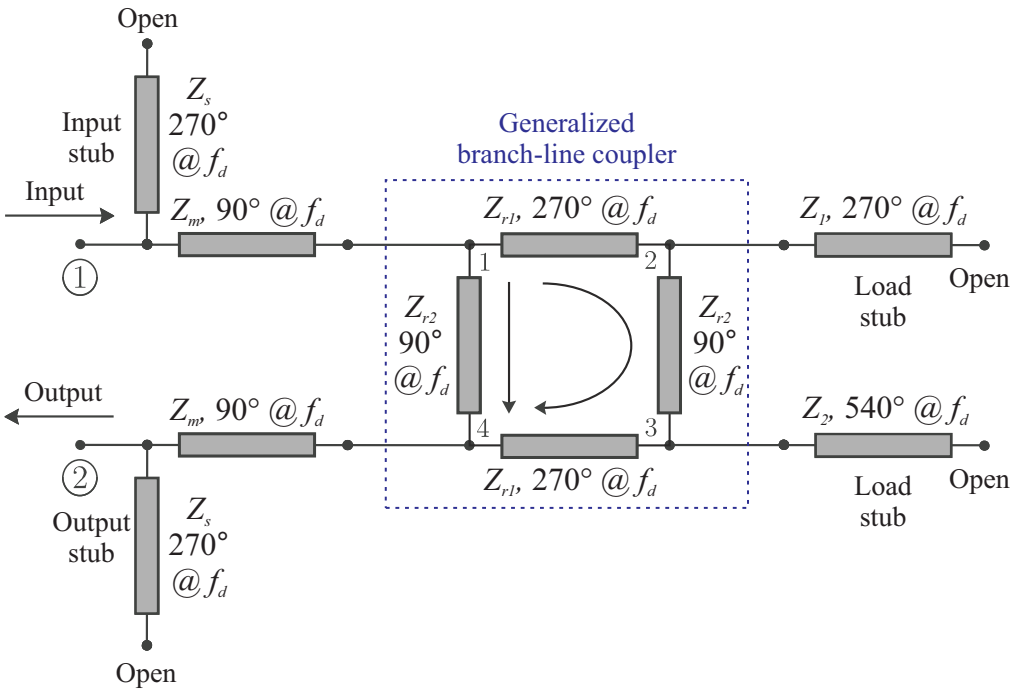

Figure 3.12: Schematic of the generalized-branch-line-coupler-based TFS (Z_{r1} = 30 Ω, Z_{r2} = 95 Ω, Z_1 = 35 Ω, Z_2 = 75 Ω, Z_m = 49 Ω, and Z_s = 35.7 Ω [27].

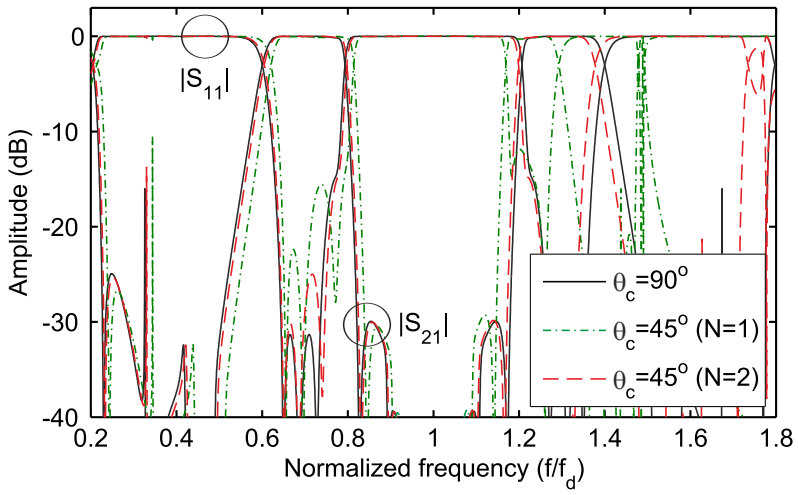

Figure 3.13: Classic signal-interference dual-band BPF filter design ($\theta_c = 90^o$) of Figure 3.12 and their capacitively-loaded miniaturized equivalents with $N = 1$ (approach of Figure 3.8) and $N = 2$ (generalized approach of Figure 3.9).

at the expense of adding more lumped capacitors. Note that this could lead to increased insertion loss in a fabricated prototype.

3.2.2 Experimental results

To experimentally validate the capacitive-loading miniaturization technique, three prototypes are presented here. They are the two previous synthesized examples in addition to a reconfigurable-bandwidth BPF based on Bagley-polygon-type four-port power-divider TFSs. With regard to the design, simulation, manufacturing, and testing processes of these circuits, the following points must be remarked:

- The microstrip substrate RO4003C of *Rogers*^{TM} is used in the manufacturing process whose parameters are: relative dielectric permittivity $\varepsilon_r = 3.55$, dielectric thickness $h = 1.52$ mm, dielectric loss tangent $\tan\delta_D = 0.0027$, and metal thickness $t = 35$ μm [46]. The ground connections were implemented by means of 0.8-mm-diameter metallic via holes.

- Surface-mounted ceramic capacitors with 0805 package size from *Johanson Tech.* Part. R15S are employed [73].

- The commercial software package *Advanced Design Systems*^{TM} of *Keysight Technologies* is used for the circuit simulation and 2.5-D EM simulation by the Frequency-Domain MoM of all prototypes [74].

- E8361A network analyzer of *Agilent*^{TM} is employed to take the measurements [75].

Prototype 1: Single-band bandpass filter

The first practical example is a 50-Ω-referred single-band signal-interference BPF prototype at $f_d = 1$ GHz consisting of two identical copies of the TFS drawn in Figure 3.11 after applying the single-cell miniaturization technique—$\theta_c = 45°$ is chosen for this case—and meandering the resulting distributed-element lines [72]. The capacitive-loading and line-meandering techniques are also applied to the inter-TFS cascading and the input-matching lines, both of them having a characteristic impedance of 32.5 Ω and electrical length of 90° at f_d for the original version. The resulting miniaturized filter occupies a 4× smaller physical area than its classic counterpart and shows an insertion loss increase of only 0.2 dB—if a finite Q of 350 is assumed for all capacitors in the simulations.

A photograph of the fabricated filter prototype and the size comparison between the miniaturized and the fully-distributed-element layouts are shown in Figure 3.14. The approximate 75% size reduction can be noticed from it.

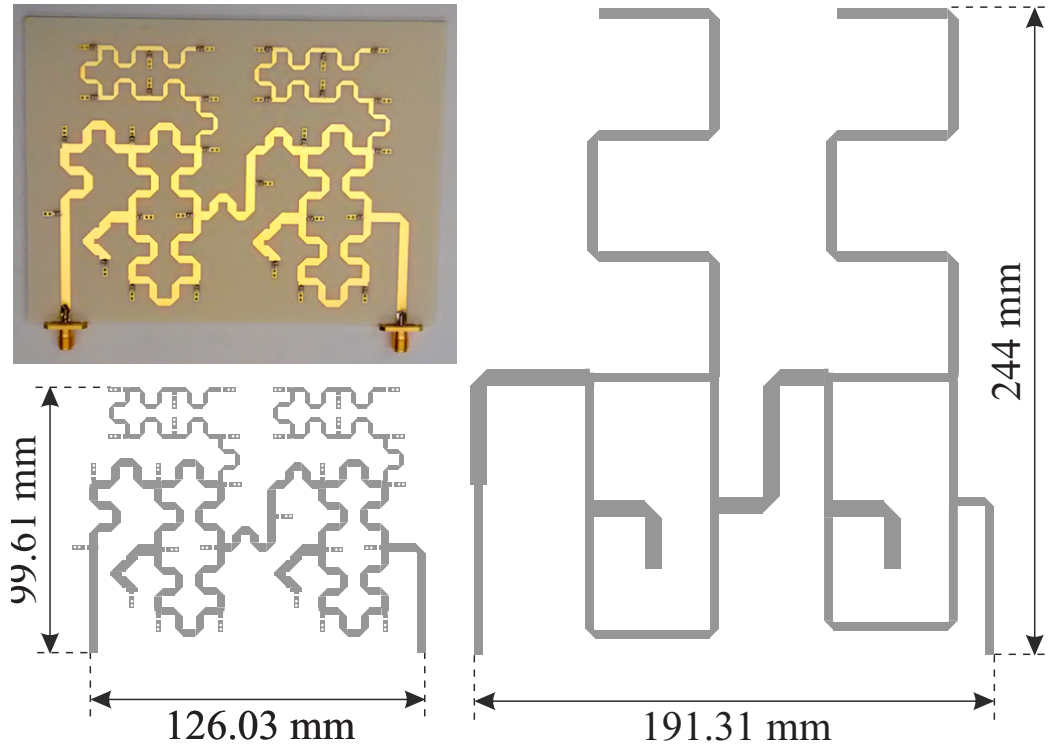

Figure 3.14: Photograph of the built miniaturized single-band BPF prototype and its layout size comparison with its classic counterpart [72].

The ideal theoretical, simulated, and measured power transmission, reflection, and in-band group-delay curves of the miniaturized prototype are compared to those of its classic counterpart in Figures 3.15 and 3.16, respectively. Note that the spectral-narrowing phenomenon in the measured results of the miniaturized approach is more critical than in the theoretical and the simulated ones due to the tolerances of the capacitors (±0.1 and ±0.25 pF depending on the capacitor value).

Besides, higher passband insertion loss is measured. This is attributed to the real Q of the lumped capacitors, being lower than the one estimated for the simulation process, and to radiation effects not taken into account by the circuit simulator. In addition, some narrow-band transmission peaks appear in the attenuated band. This is a common phenomenon in signal-interference planar filters that stems from non-perfect zero-pole cancelations [76]. Nevertheless, the agreement obtained between predicted and experimental results is close enough to validate this miniaturization technique.

Prototype 2: Dual-band bandpass filter

The second prototype is a 50-Ω-referred signal-interference dual-band BPF made up of a single TFS as the one in Figure 3.12. As a fair compromise between miniaturization level and frequency-response convergence, the multi-cell case is chosen with $\theta_c = 45°$ and $N = 2$ as design parameters at $f_d = 1.4$ GHz [77]. Note that the size-reduction technique has been applied to all transmission-line segments forming this prototype. A size reduction of 55.4% is achieved in this physical realization with respect to its fully-distributed-element counterpart and increased insertion loss of 0.7 and 1 dB is obtained for the lower and upper passband, respectively. This in-band insertion-loss levels are higher than in prototype 1 due to the larger number of lumped capacitors employed in this circuit (50 capacitors versus 29 capacitors).

A photograph of the manufactured filter prototype and the size comparison between the miniaturized and the fully-distributed-element layout are shown in Figure 3.17. Note that, unlike prototype 1, line-meandering techniques are not applied to this circuit (to avoid potential couplings) because the physical lengths of the transmission-line segments are too short.

Figure 3.18 shows the theoretical, simulated, and measured power transmission and reflection responses for this prototype. As observed, the agreement attained between simulated and measured results is close enough to validate this miniaturization technique for dual-band transfer functions. The frequency-narrowing effect is more noticeable in the measurements due to the tolerances of the capacitors. Higher in-band insertion-loss levels are appreciated specially in the upper band as a consequence of a potential underestimation of the Q of the capacitors and to higher-than-predicted radiation-loss effects.

Prototype 3: Reconfigurable-bandwidth single-band bandpass filter

As the third example, the miniaturization of a reconfigurable-bandwidth BPF is addressed. It is formed by two inter-cascaded TFSs that are based on the Bagley-polygon four-port power divider arranged in reflection mode, as reported in [78]. Its classic schematic is shown in Figure 3.19. Up to three different bandwidth states are attained through its switchable stubs. In this circuit, the miniaturization design parameters are $\theta_c = 45°$ at $f_d = 2$ GHz and $N = 1$. However, such a miniaturization technique is not applied to the first 90°-length-at-f_d transmission-line segment of these four stubs. This was done to avoid adding extra value to the capacitor in the confluent microstrip cross when the stubs are disconnected.

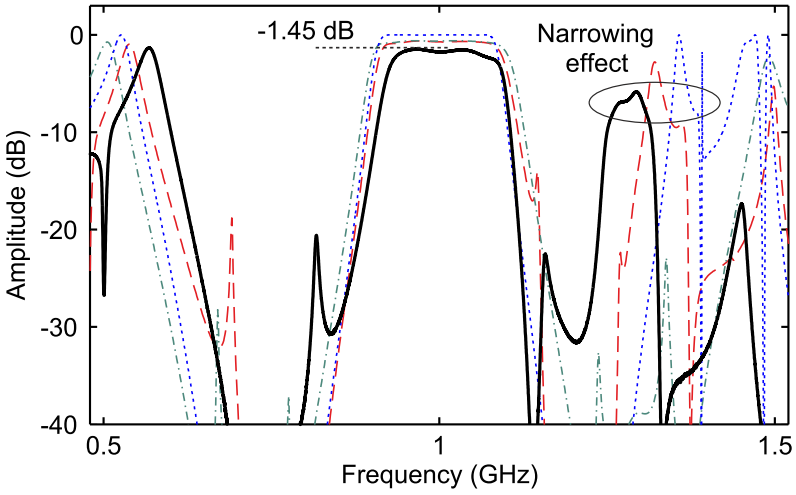

(a) $|S_{21}|$.

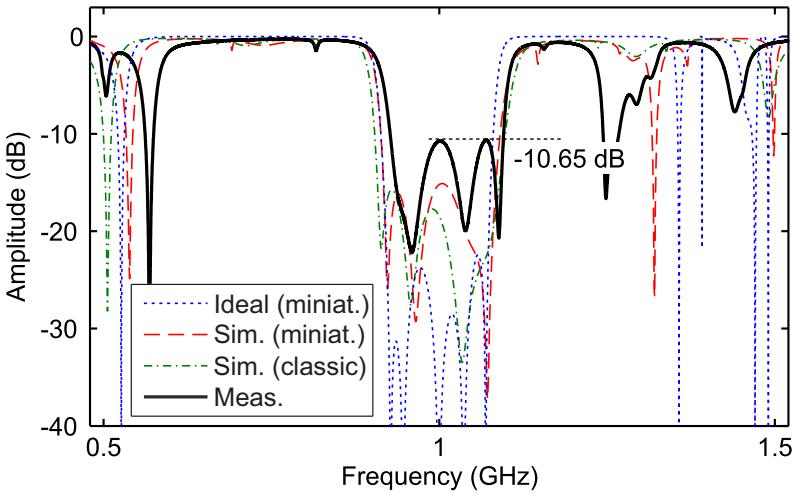

(b) $|S_{11}|$.

Figure 3.15: Ideal, circuit-simulated, and measured power transmission ($|S_{21}|$) and reflection ($|S_{11}|$) curves of the devised miniaturized single-band BPF prototype compared with those simulated for the classic design [72].

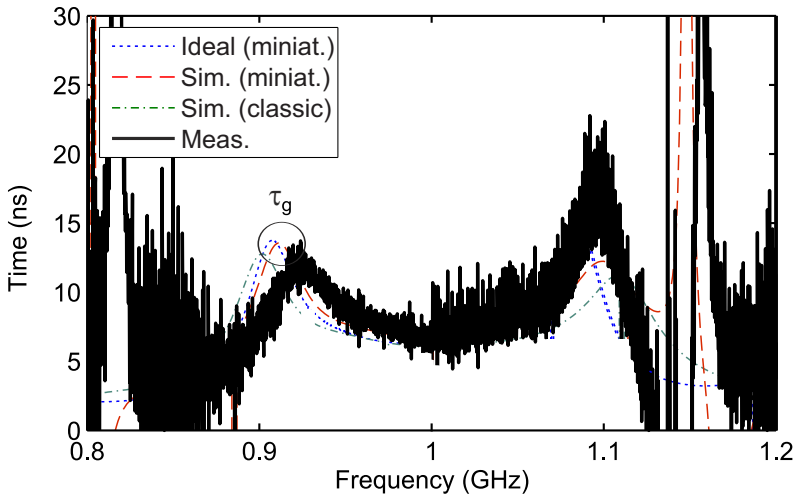

Figure 3.16: In-band group-delay (τ_g) curves of the devised miniaturized single-band BPF prototype compared with that simulated for the classic design [72].

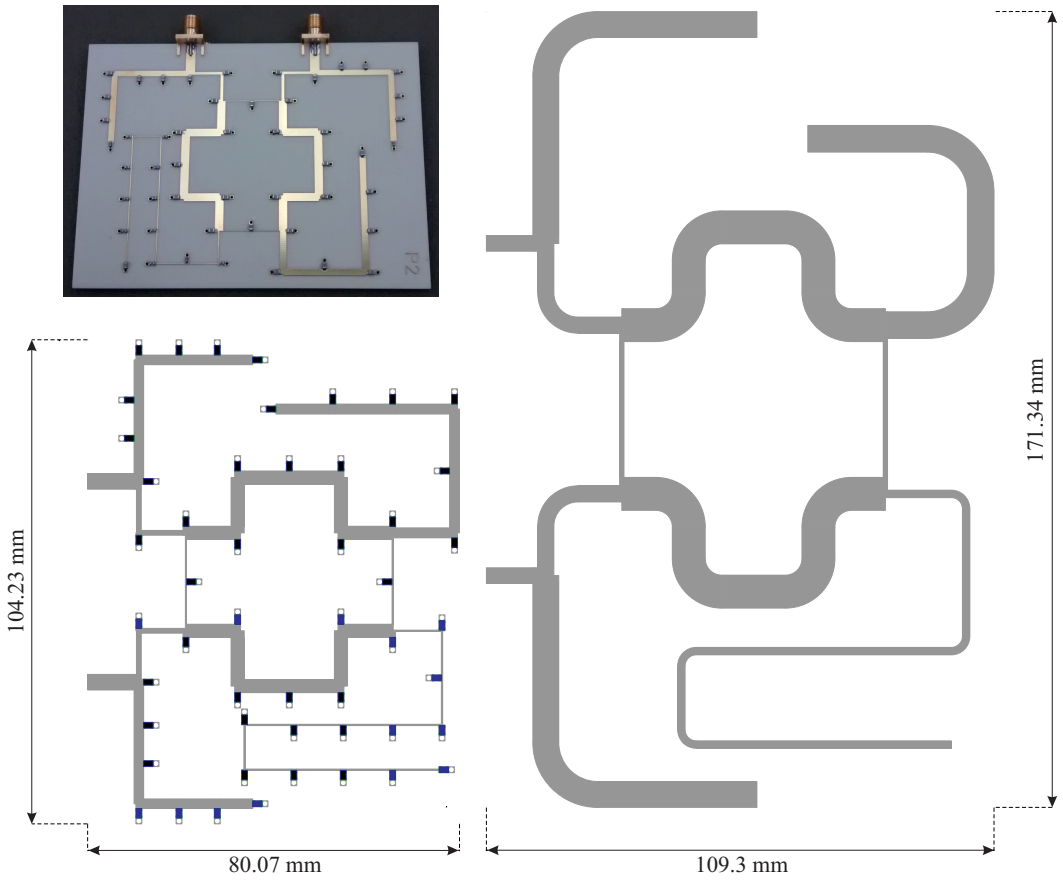

Figure 3.17: Photograph of the built miniaturized dual-band BPF prototype and its layout size comparison with its classic counterpart [77].

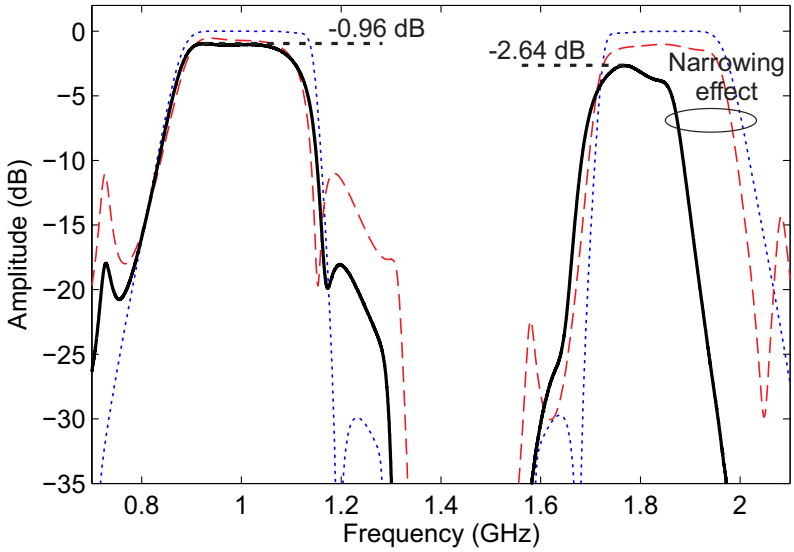

(a) $|S_{21}|$.

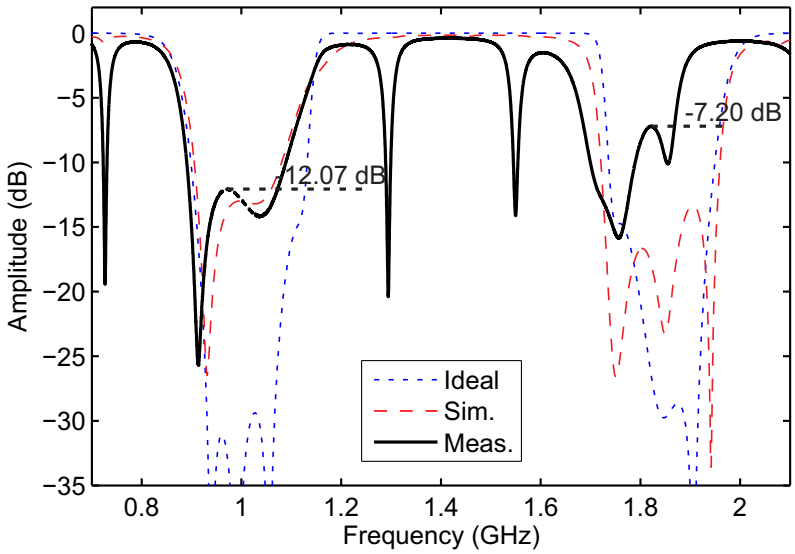

(b) $|S_{11}|$.

Figure 3.18: Ideal, circuit-simulated, and measured power transmission ($|S_{21}|$) and reflection ($|S_{11}|$) curves of the devised miniaturized dual-band BPF prototype [77].

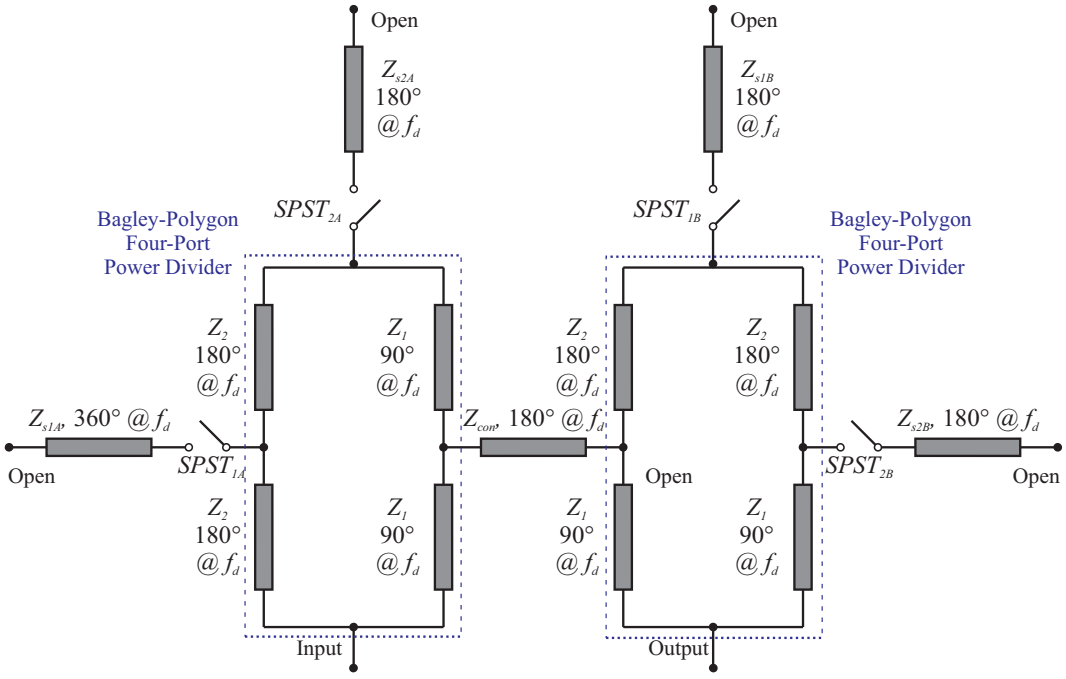

Figure 3.19: Schematic of the switchable-bandwidth BPF composed by two inter-cascaded Bagley-polygon-four-port-power-divider-based TFSs ($Z_1 = 100\ \Omega$, $Z_2 = 100\ \Omega$, $Z_{s1A} = 40\ \Omega$, $Z_{s2A} = 60\ \Omega$, $Z_{s1B} = 50\ \Omega$, $Z_{s2B} = 100\ \Omega$, and $Z_{con} = 20\ \Omega$) [77].

The layout of this switchable BPF prototype is depicted in Figure 3.20. Note that apart from 23 lumped capacitors, associated to the miniaturized implementation, four RF reflective Single-Pole Single-Throw (SPST) switches were utilized to switch on/off the four stubs. Particularly, the model *AMT2551011* from *AMTL* was selected, which offers a maximum insertion loss of 1 dB and a minimum isolation of 40 dB over the DC–20-GHz frequency range. The *S*-parameters provided by the manufacturer were used in the EM simulation.

Figure 3.21 represents the power transmission and reflection curves for the ideal and the EM-simulated designs for three different bandwidth states of prototype 3. Once again, the passband-widths for these three states are narrowed in the miniaturized circuit. Note also that, as a benefit, the undesired out-of-band narrow-band transmission peaks are suppressed in the EM simulation since finite-Q components are considered. The 3-dB relative bandwidths for states 1, 2, and 3 in the miniaturized design are 51.4%, 30.8%, and 19.2%, respectively.

3.3 Filters based on lumped-element quadrature-power-coupler-type TFSs

As already known, lumped-element and mixed distributed/lumped-element realizations are more appropriate for the lower part of the microwave spectrum and for some relevant technologies such as MMICs, where transmission lines become bulky and difficult to integrate. Under these premises, the approaches presented in

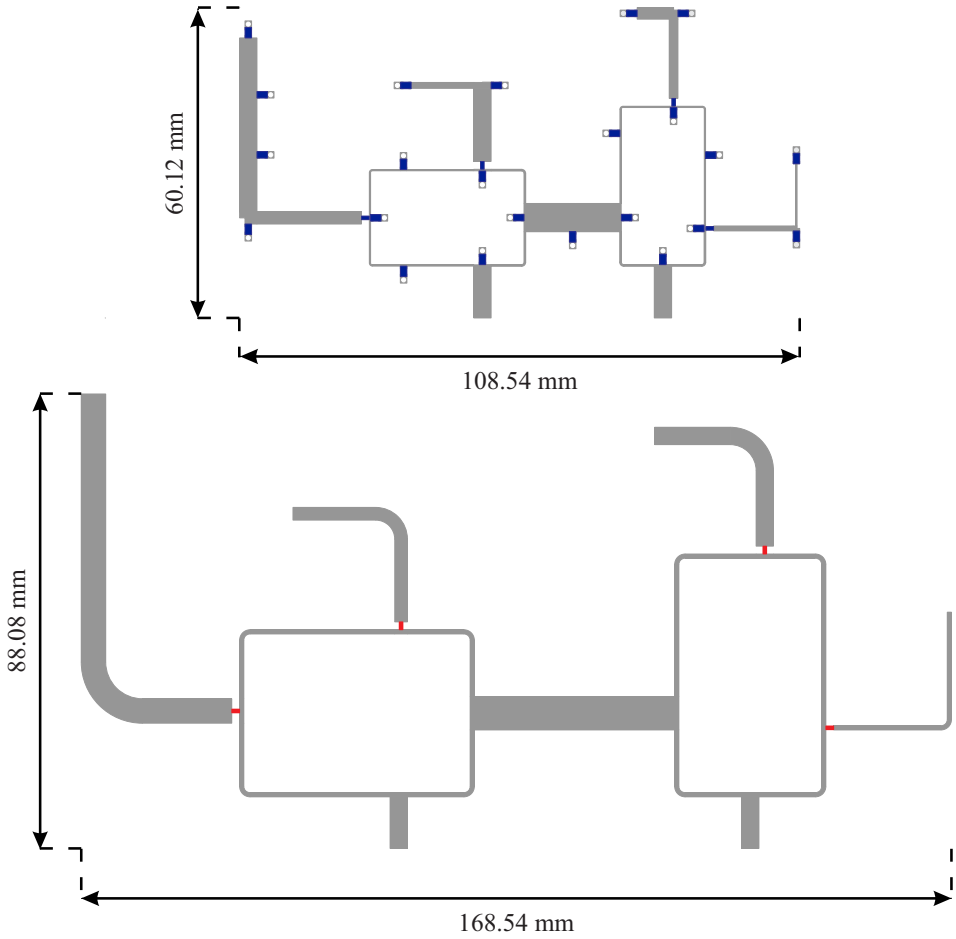

Figure 3.20: Layout size comparison of the miniaturized reconfigurable-bandwidth BPF prototype with its classic counterpart [77].

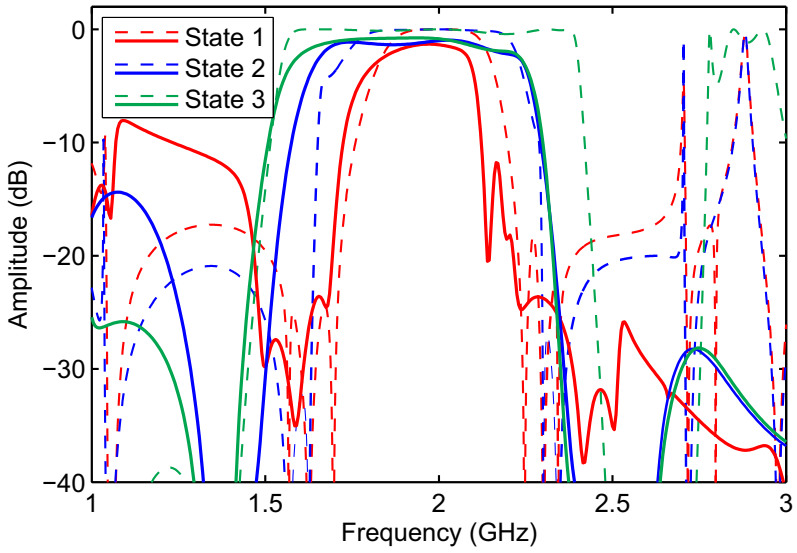

(a) $|S_{21}|$.

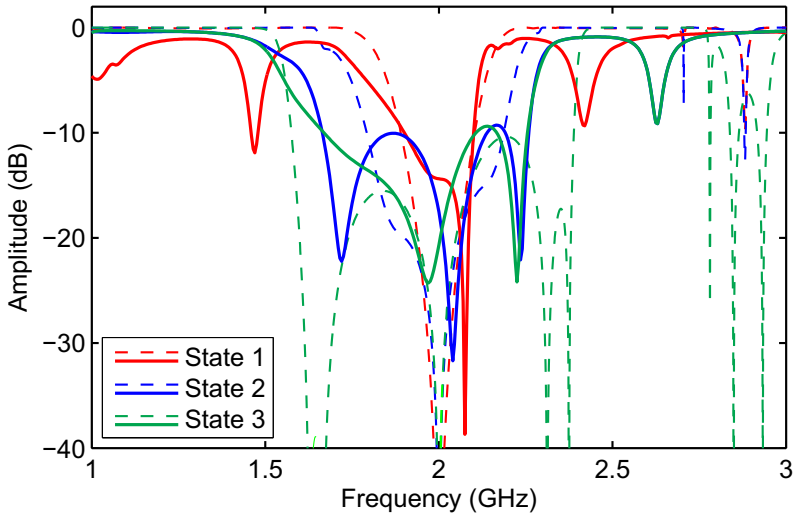

(b) $|S_{11}|$.

Figure 3.21: Ideal (dashed line) and EM-simulated (solid line) power transmission ($|S_{21}|$) and reflection ($|S_{11}|$) curves of the devised miniaturized prototype 3 compared with those simulated for the classic design. State 1: stubs 1A, 2A, and 2B are ON, stub 1B is OFF. State 2: stub 1B is ON, stubs 1A, 2A, and 2B are OFF. State 3: all stubs are OFF. [77].

Sections 3.1 and 3.2 are intended to replace the transmission-line segments forming signal-interference TFSs with their equivalent lumped-element circuit at f_d and then verify their impact on the overall frequency response. The aim of this section is to present a novel lumped-element realization for the TFS constituted by a quadrature power coupler operating in reflection mode. Unlike the approaches in previous sections, the discrete-element version does not substitute transmission-line segments but replaces the TFS as a whole.

3.3.1 Concept

Over the last few years, the use of conventional distributed-element quadrature power couplers in reflection mode—e.g. branch-line type as illustrated in Figure 3.22(a)—to carry out filtering actions under signal-interference principles has been widely extended. For example, in [15] for the design of BPF prototypes, in [79] with BPF circuits in the W-band—the frequency range between 75 and 110 GHz according to the radar-frequency letter band nomenclature [56]—, and in [27] to perform dual-band bandpass filtering actions. These designs take the isolated port as the output node of the TFS whereas the direct and the coupled ports are loaded with stubs. Thus, two signal-propagation paths are created and constructive and destructive interferences can be generated between them depending on the desired filtering profile. In this sub-section, a lumped-element version of this filter concept is reported. With this aim, the distributed-element branch-line power coupler has been replaced with one of the lumped-element realizations provided in [80]. This is illustrated in Figure 3.22(b). Note that the open-circuited transmission-line stubs loading the direct and the coupled ports are substituted by the ground-ended series connection of an inductor and a capacitor.

To verify the suitability of this approach, two synthesis examples using the engineered lumped-element TFS structure are presented hereafter.

Synthesis example I: Ultra-wideband bandpass filter

The first synthesis example is an UWB single-band BPF prototype [81]. Its center frequency and 3-dB absolute bandwidth are about 200 and 250 MHz, respectively, giving rise to a 3-dB relative bandwidth of 125%. Moreover, an input/output power matching level of 10 dB is set. The overall filter consists of four identical TFSs, as the one of Figure 3.22(b), that have been cascaded in series by means of *LC* Π-type networks. As well known, the cascade of several signal-interference TFSs increases notably the out-of-band power attenuation levels in the overall filtering response. Besides, a capacitive Π-type network is added to the input and output nodes of the whole circuit in order to comply with the specified in-band power matching levels. The topologies of the matching and cascading Π-type networks are detailed in Figure 3.23.

The values of the discrete components for this ideal synthesized UWB BPF example are listed in Table 3.3. The power transmission and reflection curves of the whole filter, along with those of its single building TFS, are depicted in Figure 3.24. As observed, a quasi-equirriple-passband transfer function is attained exhibit-

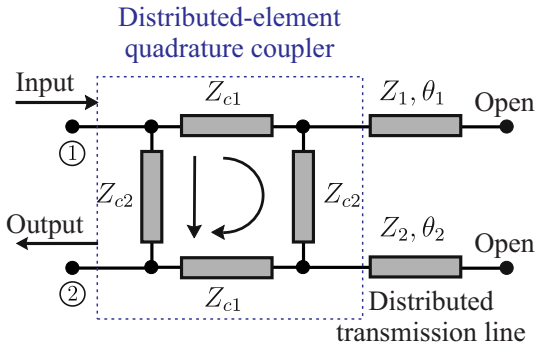

(a) Transmission-line version.

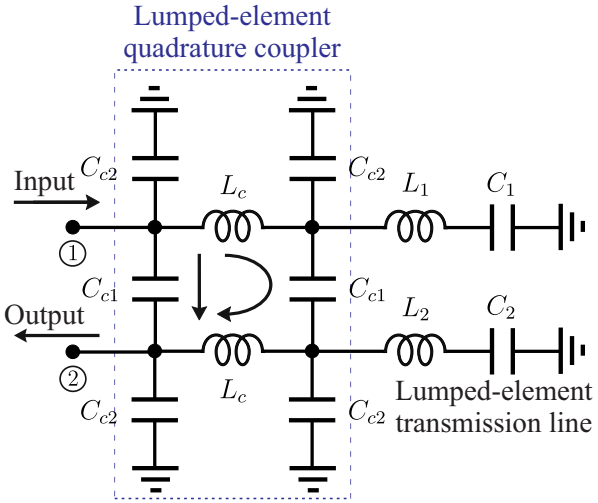

(b) Lumped-element version.

Figure 3.22: TFSs based on quadrature power couplers.

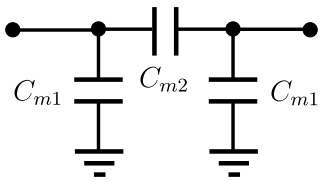

(a) Input/output matching section.

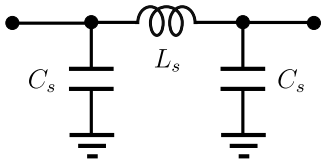

(b) Inter-stage cascading section.

Figure 3.23: Input/output matching and inter-stage cascading sections of the ideal synthesized UWB BPF example [81].

ing eight poles and some TZs at both sides of the band of interest. Note that such selectivity performance with high levels of out-of-band power rejection levels is difficult to achieve in conventional lumped-element filter realizations, such as ladder networks [7].

Table 3.3: Lumped-element components of the ideal synthesized UWB BPF example.

Lumped-element components for Synthesis example I	
Component	Value
L_c	11.1 nH
C_{c1}	18.6 pF
C_{c2}	0.1 pF
L_1	70.9 nH
C_1	180 pF
L_2	70.9 nH
C_2	180 pF
C_{m1}	180 pF
C_{m2}	2.3 pF
L_s	31 nH
C_s	15.5 pF

Synthesis example II: Dual-band bandpass filter

As a second example, a dual-band BPF with strong spectral asymmetry between passbands is synthesized [81]. In this case, the center frequencies are 135 and 345

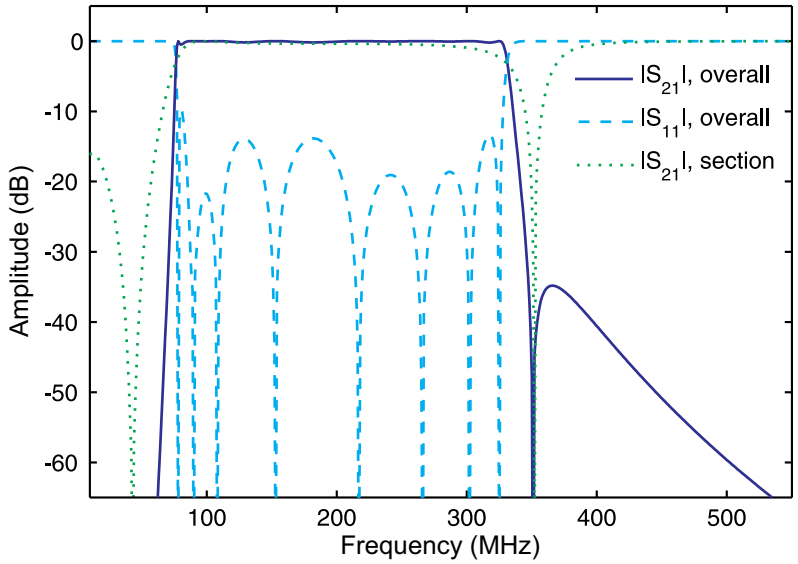

Figure 3.24: Power transmission ($|S_{21}|$) and reflection ($|S_{11}|$) responses of the ideal synthesized UWB BPF example and $|S_{21}|$ response of its building TFS [81].

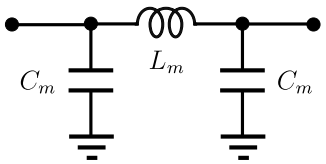

(a) Input/output matching section.

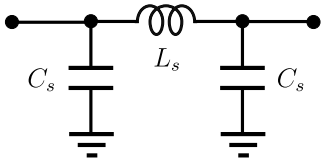

(b) Inter-stage cascading section.

Figure 3.25: Input/output matching and inter-stage cascading sections of the ideal synthesized dual-band BPF example [81].

MHz and the 3-dB absolute bandwidths of 130 and 200 MHz for the lower and the upper passband, respectively. This results in 3-dB relative bandwidths of 96% and 58%. Moreover, the in-band power matching level of the lower passband is enforced to be greater than 14 dB. Regarding the structure of the overall filter, it is shaped by two equal TFSs. For the same reason as in the previous synthesis example—in-band power matching and out-of-band attenuation improvement—, a LC Π-type network as cascading stage and two LC Π-type networks at the input/output accesses of the overall filter are employed. Their topologies are drawn in Figure 3.25.

The values of the lumped-element components for this ideal synthesized dual-band BPF example are listed in Table 3.4. In a comparative way, Figure 3.26 plots the power transmission and reflection responses of the two-stage filter and its single TFS. Once again, through the cascade, the low-order dual-band profile is converted into an improved-selectivity total transfer function exhibiting equirriple—lower band—and maximally-flat—upper band—fourth-order dual passbands and a sharp-rejection inter-band stopband. This advantage makes a real difference when compared to dual-band BPFs based on frequency transformations, in which the type of transfer function of both passbands is usually imposed to be the same from the synthesized equivalent normalized mono-band filtering profile, as described in [82].

Table 3.4: Lumped-element components of the ideal synthesized dual-band BPF example.

Lumped-element components for Synthesis example II	
Component	Value
L_c	32.7 nH
C_{c1}	23.6 pF
C_{c2}	0.5 pF
L_1	88.9 nH
C_1	100 pF
L_2	88.9 nH
C_2	100 pF
L_m	18.3 nH
C_m	3.5 pF
L_s	37 nH
C_s	11.5 pF

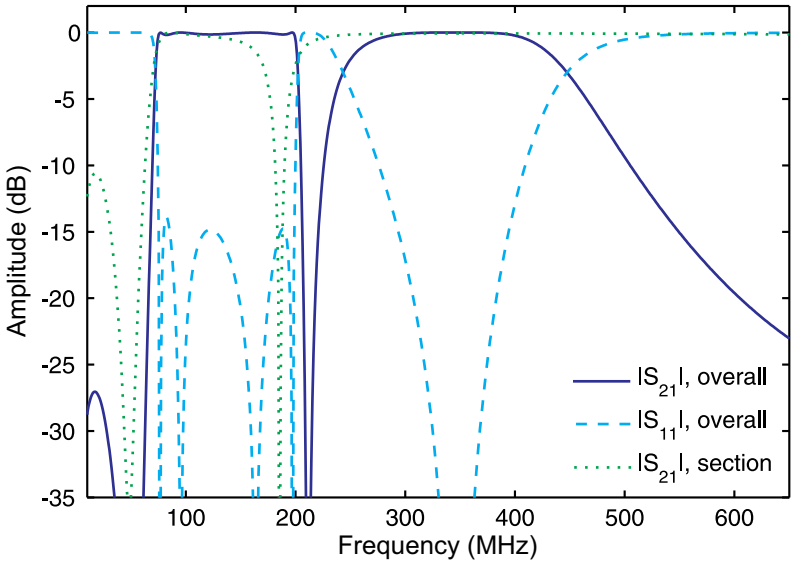

Figure 3.26: Power transmission ($|S_{21}|$) and reflection ($|S_{11}|$) responses of the ideal synthesized dual-band BPF example and $|S_{21}|$ response of its building TFS [81].

3.3.2 Simulation results

For practical validation, two prototypes have been designed at the layout level. They correspond to different implementations of the previously-synthesized UWB BPF. While the prototype 1 employs lumped capacitors and inductors, in prototype 2 high-impedance transmission-line segments substitute the lumped inductors. Note that this hybrid realization is more suitable for higher frequencies since the operative frequency range is not limited by the SRFs of on-chip inductors.

To interconnect the discrete components, the organic-ceramic microstrip substrate type TLC-30 from *Taconic*^{TM} was selected, whose parameters are: relative dielectric permittivity $\varepsilon_r = 3$, dielectric thickness $h = 1.52$ mm, dielectric loss tangent $\tan\delta_D = 0.003$, and metal thickness $t = 35$ μm [60]. The ground connections were implemented by means of 1-mm-diameter metallic via holes.

Concerning the design and simulation processes of these circuits, the commercial software package *AWR Microwave Office*^{TM} of *AWR Corporation* has been utilized [47].

Prototype 1: Lumped-element ultra-wideband bandpass filter

The first prototype is the fully-lumped-element implementation of the UWB BPF composed of four equal TFSs that are shaped by the power quadrature coupler in reflection mode [81]. Once the non-ideal effects of the commercial components, such as dissipative loss, microstrip substrate, and lumped-element auto-resonances are taken into account, the component values in Table 3.3 must be optimized in order to fulfill the desired specifications. The commercial components selected for this design are listed in Table 3.5. Its layout is depicted in Figure 3.27(a).

Table 3.5: Lumped-element components of the designed UWB BPF.

Lumped-element components for Prototype 1			
Component	Value	Product Code	RS Code*
L_c	19.5 nH	36501J9N5JTDG	532-2771
C_{c1}	20 pF	GRM2165C1H200JZ01D	723-6231
C_{c2}	0.1 pF	04023J0R1ABSTR	698-2706
L_1	72 nH	744761772A	737-3434
C_1	180 pF	GRM2165C1H188JA01D	723-6221
L_2	72 nH	744761772A	737-3434
C_2	180 pF	GRM2165C1H188JA01D	723-6221
C_{m1}	180 pF	GRM2165C1H188JA01D	723-6221
C_{m2}	2.2 pF	GRM2165C1H2R2CD01D	723-6234
L_s	30 nH	LQW15AN30NG00D	107-514
C_s	16 pF	GRM1885C1H160JA01D	723-5818

*`http://es.rs-online.com/web/`

Prototype 2: Hybrid ultra-wideband bandpass filter

As already mentioned, prototype 2 consists in a hybrid version of the UWB BPF where high-impedance transmission-line segments are used instead of lumped inductors [81]. Note that the capacitive values in this design remain the ones indicated in Table 3.5. Figure 3.27(b) shows its layout. As can be seen, line-meandering techniques have been applied to the high-impedance transmission lines to reduce the total area of the circuit [69].

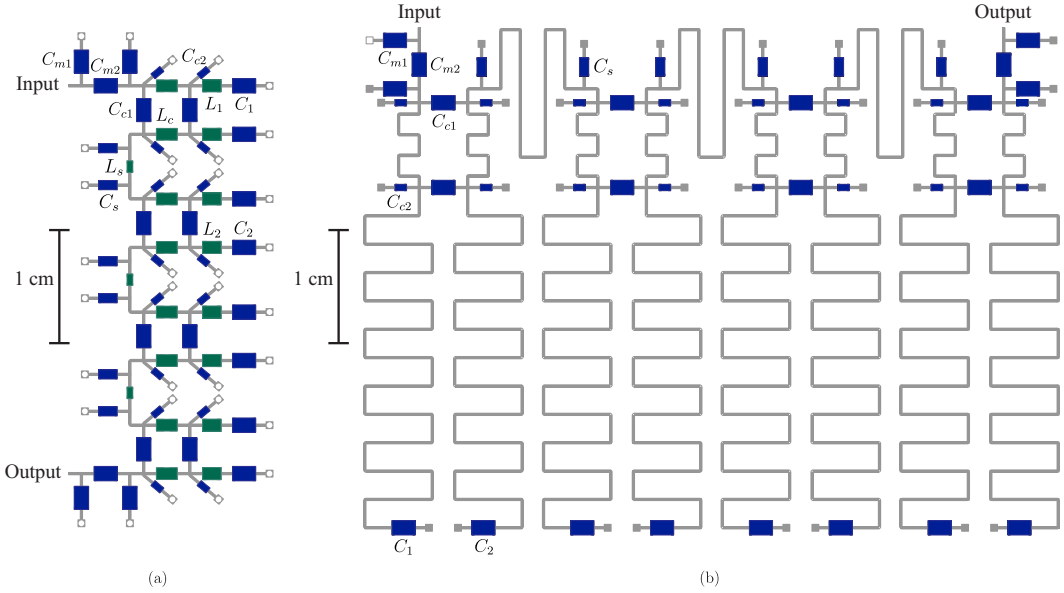

Figure 3.27: Layouts of the designed UWB BPFs. (a) Prototype 1: lumped-element realization. (b) Prototype 2: mixed distributed/lumped-element realization [81].

The power transmission and reflection curves of both prototypes (1 and 2) are depicted in Figure 3.28(a). Both designs nearly fulfill the pre-fixed specifications. Nevertheless, it is worth noting the better performance of the mixed lumped/distributed-element prototype in terms of in-band power insertion loss and close-to-passband selectivity because of the use of distributed-element-based inductors. This is achived at the expense of increased occupied area. In contrast, as can be seen in Figure 3.28(b) which covers a broader spectral range, the latter presents an spurious band around 2.4 GHz, whose attenuation level reaches up to 20 dB. This is caused by the frequency periodicity intrinsic to the behavior of the transmission lines. This comparison reveals a trade-off between pure lumped-element and mixed distributed/lumped-element realizations to be considered.

3.4 Conclusion

This chapter has proposed three new classes of lumped-element-based signal-interference filters. Note that the use of lumped elements extends the applicability of signal-interference structures to the low and intermediate microwave frequency ranges in which the area occupied by their pure distributed-element counterparts

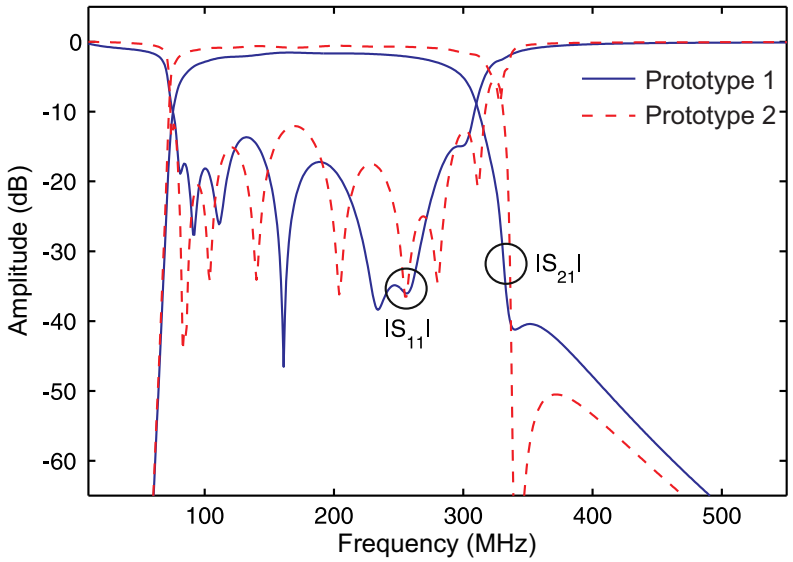

(a) Passband detail.

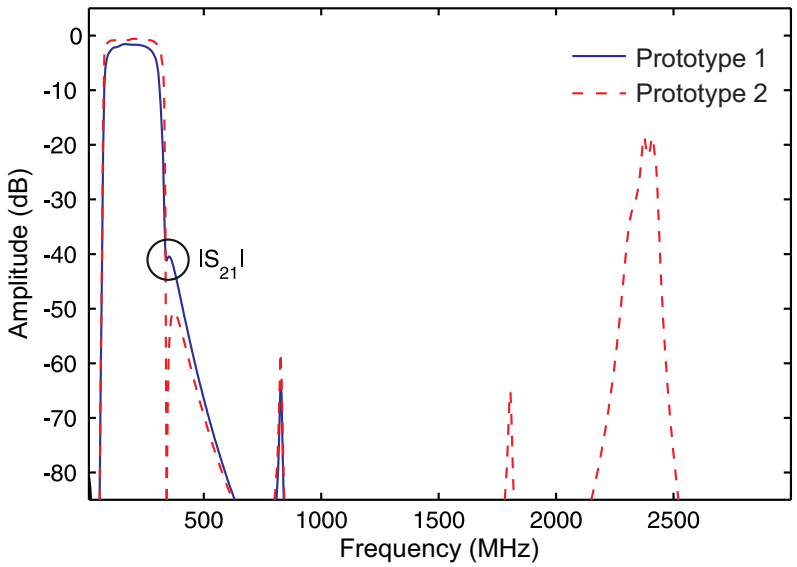

(b) Broadband response.

Figure 3.28: Simulated power transmission ($|S_{21}|$) and reflection ($|S_{11}|$) curves of the designed UWB BPF—Prototypes 1 and 2— [81].

can become excessive. Besides, through feed-forward signal-energy interactions between the propagation paths of the transversal sections, filtering profiles with high selectivity—including out-of-band TZs—are attained. Note that in case that in-band insertion loss is a major concern, mixed distributed/lumped-element building blocks can be employed at the expense of larger size.

Firstly, a new methodology to convert distributed-element analog signal-interference filters into pure lumped-element ones has been presented. Its principle is to split the transmission-line segments shaping the signal-interference TFSs into sub-segments that are later substituted by transversal LC T-type networks. This method can be generalized to a large variety of signal-interference TFSs (since most of them do not contain coupled-line stages) and any type of filtering profile. The design formulas for the transversal signal-interference filtering section based on two in-parallel transmission-line segments have been provided. The trade-off between frequency accuracy and number of LC sections and its associated increased insertion loss has been examined. For practical validation, a LPF and a BPF prototype have been designed at the layout level.

Secondly, the miniaturization of signal-interference planar filters through capacitive-loading techniques has been demonstrated. Similarly to the first technique, the transmission-line segments that shape the signal-interference TFS are divided into quarter-wavelength-at-f_d transmission-line sub-segments. They are then replaced with a shorter transmission line with higher characteristic impedance loaded by two short-circuited lumped capacitors. Once again, the method is applicable to any filtering profile and most of signal-interference TFSs. Here, the detailed analysis of the in-parallel transmission-line-based TFS has been expounded. Note that this technique can be more appropriate for higher frequencies than the previous approach since there are no lumped inductors limiting the operating frequency range, aside from less insertion losses. Besides, a capacitively-loaded multi-cell approximation with the purpose of improving the model accuracy has been reported. Such a capacitive-loading technique combined with the line-meandering one allows to reach up to a 4 $\times$ size reduction. In order to experimentally validate this concept, a wide-band single-band BPF and a dual-band BPF prototype have been fully built and tested. In addition, simulated results at the layout level of a three-state reconfigurable-bandwidth BPF prototype have been presented.

Finally, new lumped-element signal-interference filters that are inspired on the TFS formed by the power quadrature coupler in reflection-type configuration have been proposed. Unlike the two previous solutions, the aim of this method is to replace directly the whole distributed-element TFS with a lumped-element one. Two multi-stage synthesis examples—single- and dual-band passband type—using such TFS structure have been presented. For validation, two different implementations at the layout level of the single-band BPF—lumped- and mixed lumped/distributed-element realizations—have been designed confirming its viability.

Chapter 4

Design of hybrid SAW/microstrip signal-interference microwave filters

Over the last few years, the new generation of mobile communication systems demand RF transceivers capable of working in compliance with multiple standards and containing diverse functionalities [83]. In this context, the BPFs integrated in the RF front-ends must show increased filtering selectivity and low in-band insertion loss in addition to small physical size. Acoustic wave (AW) resonators, such as those exploiting SAW or bulk acoustic wave (BAW) phenomena, are the most widely used technology for those filters. This is mainly due to their high Q—in the order of 1000—and their very compact physical dimensions—typical commercial chip size of 3 mm $\times$ 3 mm $\times$ 1 mm—occupying a tiny fraction of the volume of their cavity– and ceramic-type counterparts, in which Q is inversely proportional to size [84]-[85]. Note that the SAW technology is a mature and low-cost technology—fabricated on wafers—which provides high performance up to about 1.5 GHz. On the other hand, BAW resonators offer higher Q with lower insertion loss in the frequency range from 1.5 to 6 GHz, making them a complementary solution to SAW filtering [86].

There are three main architectures traditionally employed to design SAW-resonator-based filters: ladder, lattice, and self-cascaded topologies [84], [87]-[89]. They all provide remarkable performance in terms of passband insertion loss, filtering selectivity, and reduced size. Nevertheless, their fractional bandwidth (FBW) is directly related to the electromechanical coupling coefficient $\left(k_t^2\right)$ of the constituent SAW resonators, as illustrated in Figure 1 in [87]. Typical values for this FBW are limited to the range $0.4k_t^2$–$0.8k_t^2$, depending on the selected topology. Thus, since commercially available SAW resonators commonly exhibit k_t^2 values from 0.05% to 0.1%, the applicability of such classic SAW-based circuit architectures is constrained to practical RF filter implementations with FBWs less than 0.1%. New advances in piezoelectric materials, which allow to reach k_t^2 values up to $\sim$ 25% such as in [90] and in [91], and the cascade connection of multiple AW filters with adjacent

passbands, as expounded in [92], have enabled to enlarge the bandwidth of AW-resonator-based BPFs. However, this has been done at the expense of Q degradation for both techniques, the increase of temperature dependency in the RF performance in the first methodology, and the passband-flatness deterioration in the second one, which is really sensitive to fabrication tolerances and variations of the material properties. Other recently-reported alternatives effectively combine conventional microwave elements and AW resonators. Following this trend, two SAW-resonator-based Π-type sections are cascaded and connected to the input/output ports of a high-order filtering network through microstrip coupled-line sections in [93]. In yet another approach, multi-stage filters whose filtering cells are shaped by a SAW resonator in parallel with one or two transmission lines are reported in [94]. These design techniques give rise to FBWs of 10-17% and 44-47%, respectively. Note that both prototypes present much higher passband insertion loss than traditional approaches, since microwave elements with relatively low Q are included—Q_u of microstrip lines is typically in the order of 200-250 [71]—, and occupy a larger area because these transmission lines are quarter-wavelength multiples at the design frequency, f_d. Also, it is worth noting that most of the filters reported to date require AW resonators of different frequencies and impedances—related to the k_t^2—, which therefore need for accurate fabrication and manufacturing processes because heterogenous AW-resonator arrangements present problems regarding the control of their natural frequencies.

This chapter is thus intended to propose new hybrid-SAW/microstrip BPFs operating under signal-interference principles that exhibit broader bandwidths than pure-SAW filters and low in-band insertion loss. Taking advantage of the interesting electrical features of SAW devices—both resonators and filters—, three novel methods for the design of narrow-band BPFs merging microstrip transmission lines and commercially-available surface-mounted SAW devices are proposed hereafter. In the first methodology, one- and two-port SAW resonators that operate as resonating nodes are inserted into a conventional signal-interference TFS transferring part of the high-Q properties of these resonators to the entire filter. In the second approach, one-port SAW resonators, behaving as non-resonating nodes, are strategically embedded into both branches of a bi-path signal-interference TFS. It takes benefit from the abrupt spectral transition existing between the resonance and the anti-resonance frequency of the resonators to create a very-sharp cut-off slope whilst the overall passband is shaped by the constructive signal-interference effect taking place between both signal-propagation paths. Lastly, an original method to broaden the bandwidth of commercial SAW RF BPFs is presented. It consists of inserting the very-narrow-band SAW BPF in one of the branches of the bi-path signal-interference TFS so that a wider overall bandpass filtering action can be attained through constructive feed-forward signal-energy interactions. Worthy of special mention is the fact that the FBW of the three devised BPF approaches is no longer limited by the k_t^2 of the constituent SAW resonators. Furthermore, unlike conventional all-AW BPFs, these new filter configurations utilize one single type of SAW element in their entire structure, alleviating the influence of the fabrication and assembly processes over the electrical performance. Moreover, if a BPF intended to theoretically exhibit the same narrow-band characteristics were designed utilizing classic

signal-interference TFSs [10], the lengths of its transmission lines would be much larger leading to huge overall circuit size. Besides, the insertion loss corresponding to the planar substrate would make its physical realization unviable, in addition to the presence of multiple closely-spaced replicas of the passband, inherent to such frequency-periodic structures. These approaches therefore extend the applicability of signal-interference filters to very-narrow-band designs.

The organization of this chapter is detailed hereafter. Firstly, the technique based on the inclusion of in-band one-port or two-port SAW resonators in one of the constituent electrical paths of the signal-interference TFS is presented in Section 4.1. Its operative principle is illustrated through four synthesis examples: two ideally-synthesized TFSs with embedded one-port SAW resonators and two TFSs including two-port SAW resonators. For higher-order filters, multi-stage realizations are introduced. Besides, lumped-element approaches in which the transmission-line segments are replaced with LC T-type transversal networks are expounded for circuit-area saving purposes. For practical validation, a three-stage narrow-band BPF prototype is developed at the layout level. Secondly, the approach that incorporates one-port SAW resonators acting as non-resonating nodes in both electrical paths of the signal-interference TFS is introduced in Section 4.2. The exploitation of the abrupt frequency transition existing between the resonance and the anti-resonance frequencies of the SAW resonators to generate a very-sharp passband edge is demonstrated by means of several new synthesis examples. Its extension to multi-stage arrangements is also described. A two-stage BPF prototype based on the proposed TFSs is manufactured and measured in order to validate the concept. As a final synthesis procedure, the inclusion of SAW RF filters in the bi-path signal-interference TFS with the purpose of bandwidth enlargement is described in Section 4.3. For theoretical demonstration, a set of examples following this novel technique are synthesized. To corroborate its practical viability, a two- and a three-stage BPF prototype are experimentally developed and tested. Note that the philosophy adopted in all these designs, which merge SAW resonators and microwave elements, is different from previous studies based on coupled-resonator structures, as in [93] and [95]. At the end of this chapter, the most relevant conclusions of the reported hybridized SAW/microstrip signal-interference BPFs are expounded in Section 4.4.

4.1 Filters based on TFSs with embedded in-band one- and two-port SAW resonators as resonating nodes

As stated above, a new procedure aimed at extending the applicability of signal-interference BPFs to narrow-band designs is presented in this section. Its principle is to embed a high-Q resonator—either a one-port or a two-port SAW resonator—into one of the electrical paths shaping a conventional multi-path signal-interference TFS, so that the high-Q characteristics of the resonator are partially transferred to the overall filter. Adjustable bandwidth and out-of-band TZs can be produced to attain very-narrow-band filtering actions in more compact dimensions than in classic signal-interference TFSs. For high-selectivity requisites, multi-stage series-cascaded arrangements are also expounded. Moreover, lumped-element realizations that are

more suitable for the lower part of the microwave spectrum are proposed.

4.1.1 Concept

In order to describe the operational principle of this first devised approach, two synthesis examples of filtering profiles along with design rules to adjust their bandwidth are detailed hereafter.

Synthesis example I: TFS with one-port SAW resonator

The bi-path signal-interference TFS with an embedded one-port SAW resonator is depicted in Figure 4.1. Here, Z and θ denote the characteristic impedance and electrical length of these transmission-line segments making up the TFS, whereas Z_0 corresponds to the reference impedance. The Butterworth-Van Dyke (BVD) equivalent circuit model of the one-port AW resonators [96] is adopted for synthesis purposes. This simplified BVD lumped-element model, represented in Figure 4.1(a), consists of two parallel branches—namely, the motional and the static capacitance arms—and accurately predicts the frequency behavior of one-port AW resonators around the design frequency [97]. The spectral profile of the one-port SAW element contains a series (f_s) and a parallel (f_p) resonance frequency, which can be calculated as follows:

$$f_s = \frac{1}{2\pi\sqrt{L_m C_m}} \qquad f_p = \frac{1}{2\pi\sqrt{L_m\left(\frac{C_m C_0}{C_m + C_0}\right)}} \tag{4.1}$$

Because the impedance is minimized at f_s, this frequency is named resonance frequency, while f_p is the anti-resonance frequency since the motional impedance is maximum at this value. If such BVD model is incorporated into one of the branches, the resulting TFS is shaped by a pure transmission-line path exhibiting moderate-Q performance and a mixed-technology SAW/microstrip path with higher effective Q. According to the signal-interference philosophy, the overall filtering action stems from the signal-energy interaction between both paths: constructive interferences within the passband region and destructive interferences throughout the rejected bands. Moreover, several TFSs can be cascaded in series for higher-order filter realizations, as shown in Figure 4.1(a). For design purposes, the following considerations must be taken into account:

- The high-Q properties of the SAW resonator are reasonably transferred to the overall bandpass filtering action.
- The bandwidth of the SAW resonator can be notably increased by means of constructive interferences.
- TZs—TZ_1 and TZ_2—can be created at both passband sides through destructive interactions between both electrical paths. This occurs at those frequencies at which the transmission admittance parameter (Y_{21}) of one transversal

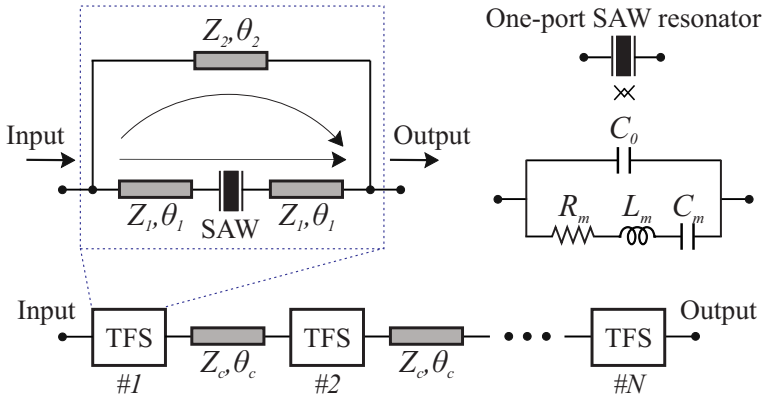

(a) Schematic (building TFS, BVD model of the one-port SAW resonator, and N-stage-series-cascaded BPF).

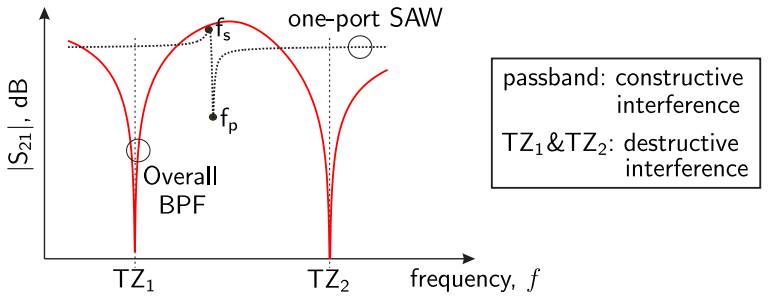

(b) Operating principle.

Figure 4.1: Detail and operating principle of the first type of hybrid-technology SAW/microstrip TFS.

path is canceled by that of the other. The TZ locations can be easily controlled by properly adjusting the transmission-line parameters.

For theoretical demonstration, Figure 4.2 plots examples of ideal synthesized power transmission responses of a TFS with an embedded 433.2-MHz one-port SAW resonator, where the design frequency f_d is chosen equal to f_s. It specifically shows how the bandwidth of the TFS can be effectively controlled by reallocating the TZs through different pairs of electrical lengths—values of $\theta_1(f_d)$ and $\theta_2(f_d)$—, while keeping static the values of their line impedances. In this example, the BVD model of a one-port SAW resonator from RFM has been utilized with the following extracted component values: $R_m = 26.46\ \Omega$, $L_m = 67.145\ \mu$H, $C_m = 2.00385$ fF, and $C_0 = 2.3$ pF.

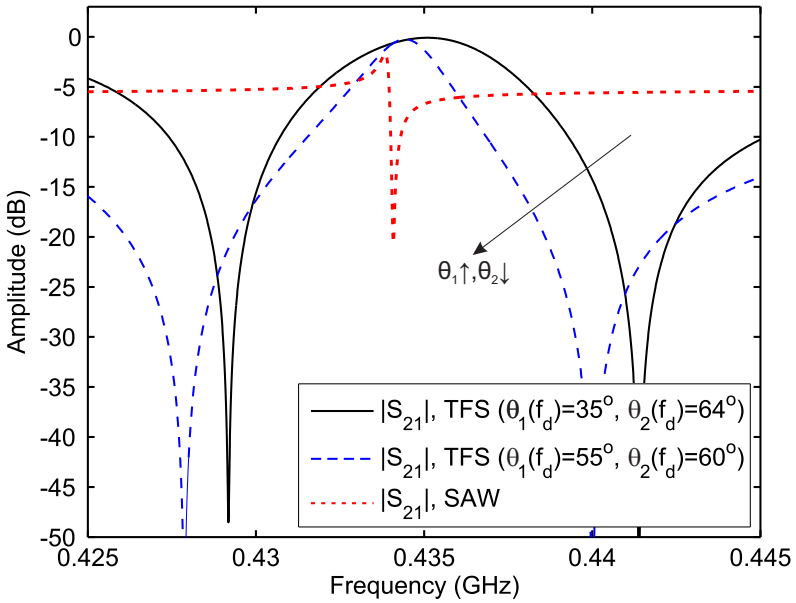

Figure 4.2: Examples of ideal synthesized power transmission ($|S_{21}|$) response of the TFS of Figure 4.1(a) and its embedded one-port SAW resonator: bandwidth control of the TFS as a function of $\theta_1(f_d)$ and $\theta_2(f_d)$ ($Z_0 = 50\ \Omega$, $Z_1 = 0.8Z_0$, and $Z_2 = 2Z_0$).

Synthesis example II: TFS with two-port SAW resonator

As second synthesis example, a TFS incorporating a two-port SAW resonator in one of its branches is shown in Figure 4.3. Note that two-port SAW resonators exhibit a frequency profile with only one resonance frequency so that its lumped-element equivalent model differs from that of the one-port resonators. The operating principle of this second BPF approach is similar to that of the first synthesized example, although an additional transmission-line path can be added in order to broaden the overall bandwidth.

To illustrate such a concept, two examples of filtering profiles associated to this TFS are considered. Both of them utilize a two-port SAW resonator model inspired by a commercial one from *RFMR*® (branch RP1308) at $f_s = 433.2$ MHz with

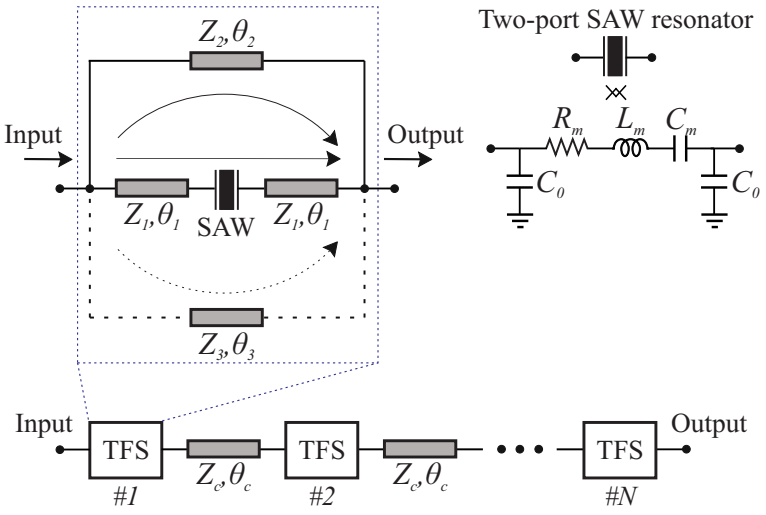

Figure 4.3: Schematic of the second type of hybrid-technology SAW/microstrip TFS (building TFS, BVD model of the two-port SAW resonator, and N-stage-series-cascaded BPF).

the following parameters: $R_m = 99.5\ \Omega$, $L_m = 476.4175\ \mu$H, $C_m = 0.28332$ fF, and $C_0 = 1.9$ pF. These two examples are based on the bi-path TFS that exhibits a 3-dB relative bandwidth of ≈0.14% and frequency-asymmetrical selectivity. Their power transmission and reflection coefficients are depicted in Figure 4.4. As observed, the TZs can be shifted between the lower and the upper stopband by properly modifying the values of the characteristic impedances and electrical lengths of the corresponding transmission lines. The achievement of sharp-rejection slopes at either one of the other side of the TFS passband can be of particular interest in the design of duplexers, where higher attenuation levels are required in the stopbands where the other channels are located for inter-channel isolation purposes.

4.1.2 Multi-TFS-cascaded designs

As it was pointed out previously in Figures 4.1 and 4.3, higher-selectivity filtering actions can be attained by cascading in series several similar and dissimilar TFSs. This allows higher out-of-band power rejection levels and improved passband amplitude flatness to be obtained. These advantages are corroborated with the development of multi-stage arrangements using the two proposed TFSs, as detailed below.

Synthesis example I: Multi-stage arrangements with one-port-SAW-resonator-based TFSs

According to the bi-path signal-interference TFS with embedded one-port SAW resonator in Figure 4.1(a), Figures 4.5 and 4.6 depict the results of some examples of ideal synthesized multi-section BPFs. Note that these designs employ a BVD model corresponding to a 433.9-MHz one-port SAW resonator from *EPCOS*® with the following parameters: $R_m = 18\ \Omega$, $L_m = 79.82\ \mu$H, $C_m = 1.685$ fF, and $C_0 = 2.3$

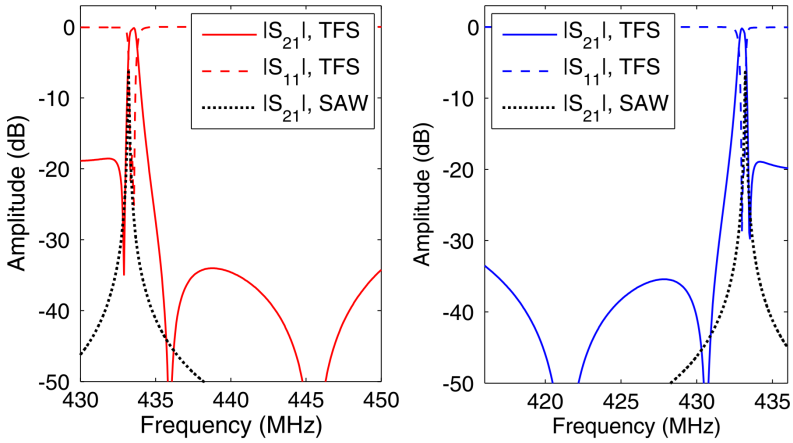

Figure 4.4: Power transmission ($|S_{21}|$) and reflection ($|S_{11}|$) curves for two examples of the ideal synthesized TFS of Figure 4.3—transversal path 3 is ignored—and its embedded two-port SAW resonator. (a) Sharper rejection at the lower stopband ($Z_1 = 4Z_0$, $Z_2 = 4Z_0$, $\theta_1(f_d) = 42.6°$, and $\theta_2(f_d) = 182.4°$). (b) Sharper rejection at the upper stopband ($Z_1 = 4Z_0$, $Z_2 = 0.825Z_0$, $\theta_1(f_d) = 50.8°$, and $\theta_2(f_d) = 178°$).

pF.

- Figure 4.5 plots the power transmission and reflection parameters of an ideal synthesized three-stage narrow-band BPF design consisting of the series-cascade connection of three identical TFSs with embedded one-port SAW resonators, as the one in Figure 4.1. For comparison purposes, the power transmission curves of the building TFS and the one-port SAW resonator are also drawn. As observed, the sharpness of the passband edges increases notably when cascading three identical TFSs, exhibiting in-band equiripple-type behavior and a minimum in-band power matching level of 20 dB while maintaining the TZ allocation.

- Figure 4.6 presents the control of the bandwidth of this three-stage BPF design by simply adjusting the electrical length θ_2. As can be seen, an 8°-variation of this parameter modifies the 3-dB relative bandwidth from 0.77% to 0.35% while preserving the TZ generation at both passband sides.

Synthesis example II: Multi-stage arrangements with two-port-SAW-resonator-based TFSs

By adopting the three-path signal-interference TFS with an embedded two-port SAW resonator presented in Figure 4.3, a two-stage filter exhibiting a 3-dB relative bandwidth of 0.92% is synthesized. It employs the aforementioned 433.2-MHz two-port SAW resonator model with the following parameters: $R_m = 99.5\ \Omega$, $L_m = 476.4175\ \mu$H, $C_m = 0.28332$ fF, and $C_0 = 1.9$ pF.

The power transmission and reflection responses of the ideally-synthesized two-stage filter are plotted in Figure 4.7, along with the power transmission coefficients

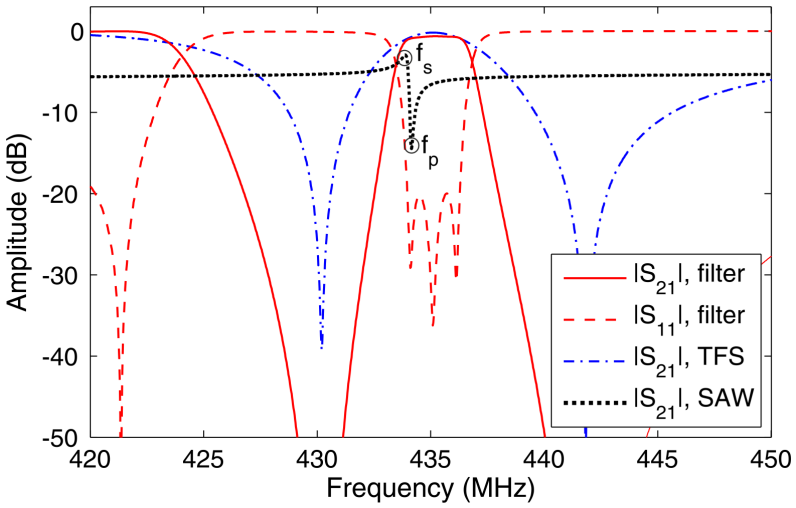

Figure 4.5: Power transmission ($|S_{21}|$) and reflection ($|S_{11}|$) responses of an ideal synthesized three-stage BPF shaped by the series-cascade connection of three identical TFSs as in Figure 4.1. The power transmission parameters of the one-port SAW resonator and the single TFS are also depicted. Design parameter values: $Z_1 = 2Z_0$, $Z_2 = 0.8Z_0$, $Z_c = 0.7Z_0$, $\theta_1(f_d) = 32°$, $\theta_2(f_d) = 34°$, and $\theta_c(f_d) = 19°$.

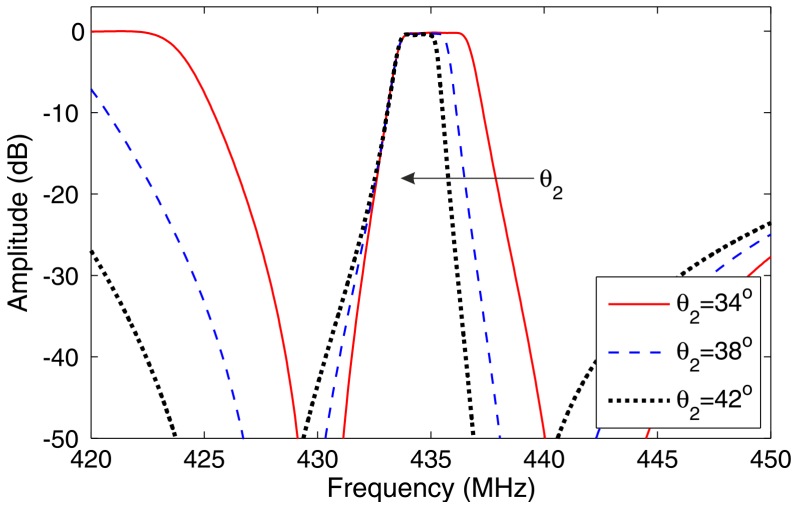

Figure 4.6: Bandwidth control of the power transmission parameter ($|S_{21}|$) of the three-stage BPF by only acting on $\theta_2(f_d)$.

of the single TFS and the two-port SAW resonator. Note that this filter presents a three-pole quasi-elliptic-type profile with perfect equiripple passband. Moreover, the bandwidth of its building TFS is 6.5 times larger than that of the examples in Figure 4.4—bi-path TFS case—.

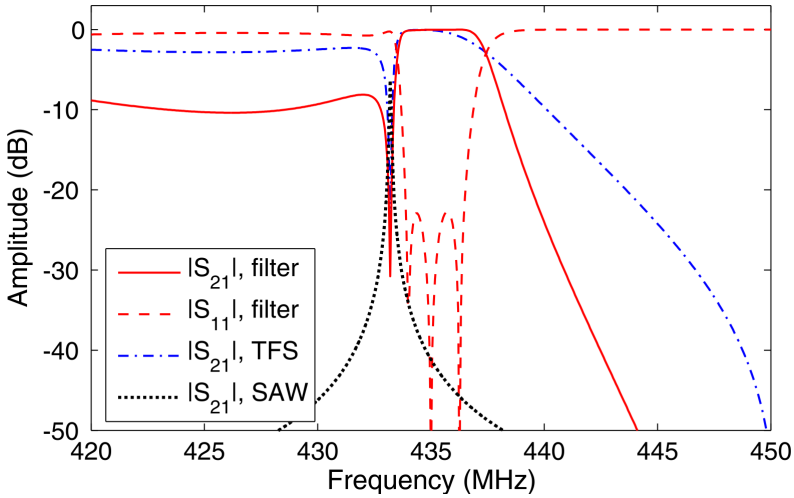

Figure 4.7: Power transmission ($|S_{21}|$) and reflection ($|S_{11}|$) responses of an ideal synthesized two-stage BPF shaped by the series-cascade connection of two identical TFSs as in Figure 4.3—transversal path 3 is considered—. The power transmission parameters of the two-port SAW resonator and the single TFS are also depicted. Design parameter values: $Z_1 = 3.94Z_0$, $Z_2 = 4Z_0$, $Z_3 = Z_0$, $Z_c = 1.2Z_0$, $\theta_1(f_d) = 39°$, $\theta_2(f_d) = 185.7°$, $\theta_3(f_d) = 89°$, and $\theta_c(f_d) = 115°$.

4.1.3 Lumped-element designs

The examples reported in this section are high-order BPF designs based on the cascade connection of several TFSs in case of high-order filtering specifications. However, as well-known, the transmission-line segments of these multi-stage implementations can become bulky elements at low regions of the microwave band. The solution to this problem is to use an equivalent lumped-element realization for these lines with approximately similar electrical performance but reduced circuit size, as discussed in Chapter 3.

By following this approach, Figure 4.8 compares the power transmission and reflection responses of the three-stage transmission-line-based BPF of Figure 4.5 with those of its associated lumped-element implementation based on *LC* T-type cells according to the technique in Section 3.1. As can be seen, the agreement obtained between the distributed and the lumped-element versions of this filter is fairly close throughout the represented spectral range, hence confirming the viability of signal-interference structures combining discrete elements and SAW resonators—even when considering the basic single-cell lumped-element model of the transmission lines.

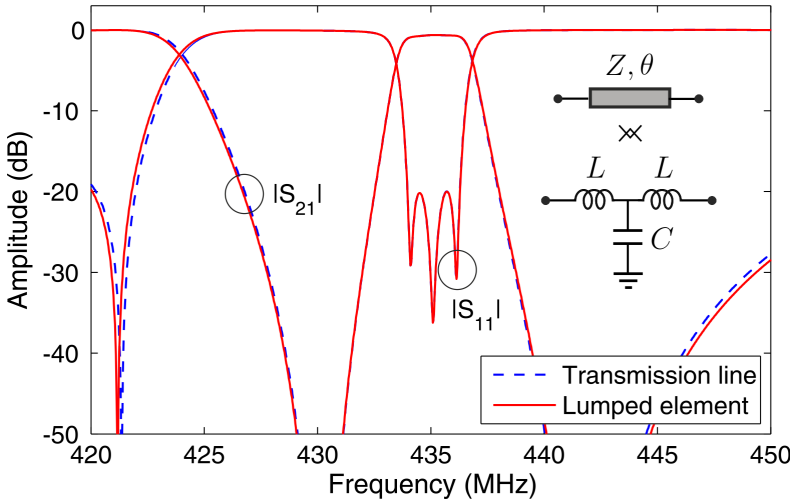

Figure 4.8: Power transmission ($|S_{21}|$) and reflection ($|S_{11}|$) responses of the three-stage BPF design of Figure 4.1(a) and its lumped-element approximation. Design parameter values—$Z_0 = 50\ \Omega$ is assumed—for path 1: $L_1 = 10.52$ nH and $C_1 = 1.94$ pF; path 2: $L_2 = 4.49$ nH and $C_2 = 5.13$ pF; cascading network: $L_c = 2.15$ nH and $C_c = 3.41$ pF.

4.1.4 Experimental results

For practical verification, a multi-stage narrow-band BPF prototype made up of three series-cascaded identical TFSs—as the one in Figure 4.1(a)—has been developed. It uses microstrip technology and the on-chip one-port SAW resonator model RO3101E-1 from *RFM*® with $f_s = 433.9$ MHz [98], [99]. The microstrip substrate employed in such a design is RO4003C of *Rogers*^{TM} with the following parameters: relative dielectric permittivity $\varepsilon_r = 3.55$, dielectric thickness $h = 1.52$ mm, dielectric loss tangent $\tan\delta_D = 0.0027$, and metal thickness $t = 35\ \mu$m [46].

Regarding the design, simulation and optimization process of this filter, the commercial software package *AWR Microwave Office*^{TM} of *AWR Corporation* was utilized [47]. In order to obtain the simulated filtering response as close as possible to the expected real results, the measured S-parameters of the commercial one-port SAW resonator RO3101E-1 which were obtained through a previous Through-Reflect-Line(TRL)-based characterization are used in such circuit simulations [100]. This is done to take into account the potential undesired effects produced by the spurious modes of this type of resonators, which are not contemplated by the single-mode BVD equivalent model.

Prototype: Narrow-band bandpass filter

The narrow-band 50-Ω-referred BPF prototype was ideally synthesized to show a 3-dB absolute bandwidth of 2.35 MHz around 434.66 MHz—resulting in a 3-dB relative bandwidth of 0.54%—. The resulting values for the design parameters of its three identical TFSs are $Z_1 = 100\ \Omega$, $Z_2 = 40\ \Omega$, $\theta_1(f_s) = 33°$, and $\theta_2(f_s) = 34°$. Two cascading transmission-line segments with $Z_c = 30\ \Omega$ and $\theta_c(f_s) = 17°$ are used. The layout of the prototype and a photograph of the assembled circuit for

the TRL calibration setup to characterize the commercial chip of one-port SAW resonator are shown in Figure 4.9.

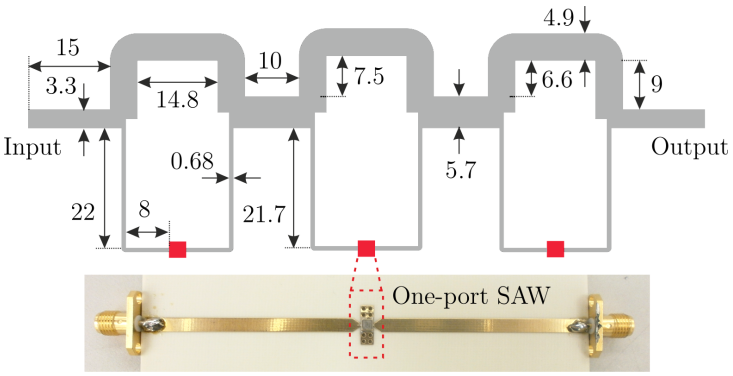

Figure 4.9: Layout—non-redundant dimensions, in mm, are indicated—of the three-stage SAW/microstrip BPF prototype based on the TFS of Figure 4.1(a) and photograph of the manufactured circuit for TRL-based characterization of the one-port SAW resonator [98].

Figure 4.10(a) represents the power transmission and reflection coefficients of the developed BPF prototype for three different scenarios: firstly, considering ideal transmission lines and the BVD equivalent model of the SAW resonator; secondly, replacing the ideal transmission lines with microstrip ones along with the SAW-resonator BVD model; and thirdly, employing microstrip lines and the measured S-parameters of the commercial one-port SAW resonator. As shown, the engineered approach to design signal-interference narrow-band BPFs is reasonably validated despite some undesired effects. They are due to the spurious modes of the real one-port SAW resonator that are manifest in the overall filtering response. These unwanted effects taking place inside the SAW resonator, such as reflections from the edges of the metallic fingers of its interdigital transducer, are perceptible in the overall filtering response as spurious transmission peaks in the stopband and, more disturbingly, as ultra-narrow-band notches in the passband. For illustration purposes, the correspondence between the SAW spurious modes and the unwanted effects in the filtering profile is shown in Figure 4.10(b) in both amplitude and phase terms of the power transmission parameter of the resonator covering the passband frequency range.

Nonetheless, the obtained results reflect a 3-dB relative bandwidth of 0.46%, power in-band insertion loss below 0.64 dB, and in-band power matching levels higher than 12.3 dB when the measured S-parameters of the SAW resonator are considered. This translates into a minimum Q_u of 5900—assuming conductor and dielectric losses—for an equivalent third-order BPF showing the same behavior, which is not possible to realize in practice through fully-microstrip implementations—Q_u is limited to about 100-200 in microstrip technology [71]—. Moreover, as explained before, this bandwidth is also unachievable in classic all-SAW filter structures, since their passband width is limited by the electromechanical coupling coefficient k_t^2 of the SAW resonators—$k_t^2 = 1 - (f_s/f_p)^2 = 0.1\%$ in this example—.

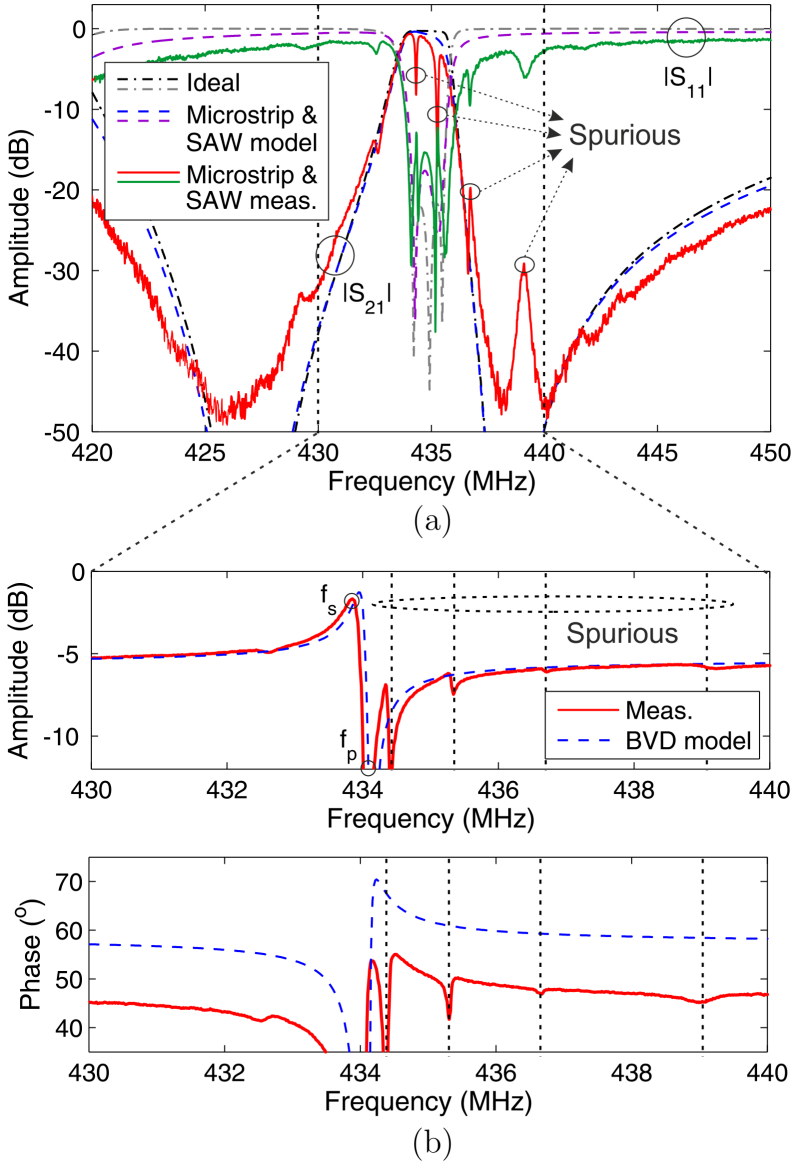

Figure 4.10: Example of narrow-band BPF and one-port SAW-resonator responses. (a) Power transmission ($|S_{21}|$) and reflection ($|S_{11}|$) parameters of the three-stage BPF design—ideal transmission lines with one-port SAW-resonator BVD model, microstrip lines with commercial one-port SAW-resonator BVD model, and microstrip lines with commercial one-port SAW-resonator measurements—. (b) Amplitude/phase transmission (S_{21}) curves of the assembled one-port SAW resonator and comparison with its BVD model [98].

4.2 Filters based on TFSs with embedded one-port SAW resonator as non-resonating node

In this second section, alternative planar signal-interference TFSs with embedded one-port SAW resonators that operate as non-resonating nodes are presented for narrow-band BPF design. Their operational foundations consist of exploiting the abrupt spectral transition existing between the resonance (f_s) and the anti-resonance (f_p) frequencies of the one-port SAW resonator to create a very sharp cut-off slope. Once again, the overall filtering bandwidth can be adjusted by adequately modifying the design parameters of the constituent transmission-line segments. Its application to multi-stage high-order BPF design and a comparison with its traditional fully-planar signal-interference TFS counterpart are also expounded.

4.2.1 Concept

The circuit architecture of the second type of mixed-technology SAW/microstrip TFSs is shown in Figure 4.11(a). It consists of two in-parallel transmission-line paths with embedded one-port SAW resonators into both of them, whose equivalent BVD model is also detailed in Figure 4.11(a). Here, Z corresponds to the characteristic impedance and θ denotes the electrical length of the constituent transmission lines, respectively. Its operative principle is represented in Figure 4.11(b), in which three aspects must be highlighted:

- The utilized one-port SAW resonators work as non-resonating nodes. This means that the ultra-abrupt spectral transition appearing between the resonance (f_s) and the antiresonance (f_p) frequencies is used to create a very sharp passband edge instead of being exploited to shape the filter passband. This is done to reduce the effect of the upper spurious modes of the one-port SAW resonator—which are the most critical ones—on the overall TFS transmission band in a practical realization (as it was observed in the TFS of Section 4.1, in which they damage the in-band frequency response). Nonetheless, the latter is achieved at the expense of slightly-increased in-band power insertion loss, since the high-Q features of the one-port SAW resonators are only partially transferred to the overall TFS.

- The whole passband action is shaped by the constructive feed-forward signal-energy interaction taking place between both signal-propagation paths of the TFS within this spectral range. Therefore, its bandwidth can be flexibly varied by means of the transmission-line parameters of the TFS.

- Two additional TZs—TZ_1 and TZ_3, as illustrated in Figure 4.11(b)—are obtained from perfect signal-energy suppressions occurring within the TFS, leading to increased power attenuation levels in the stopbands. They are spectrally located at those frequency values at which the transmission admittance parameters (Y_{21}) of both electrical paths are mutually canceled. Thus, the spectral locations of TZ_1 and TZ_3 can also be adjusted through the transmission-line variables of the TFS.

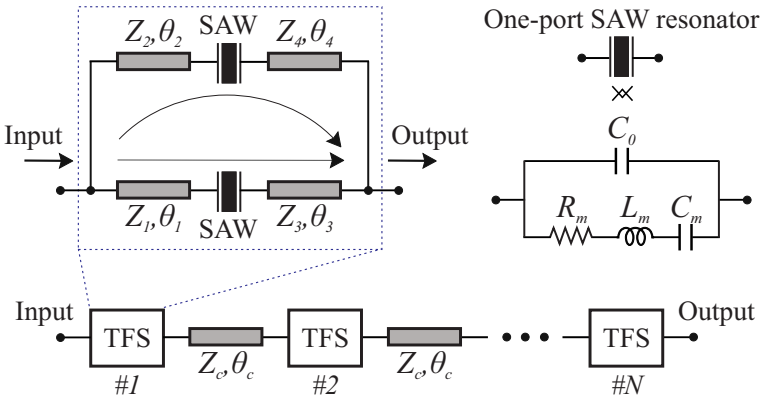

(a) Schematic (building TFS, BVD model of the one-port SAW resonator, and N-stage-series-cascaded BPF).

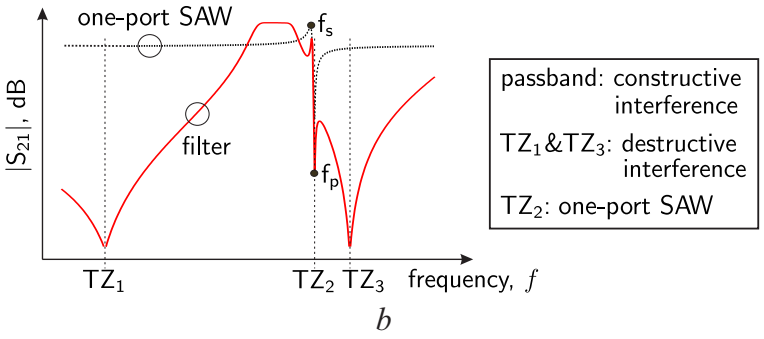

(b) Operating principle.

Figure 4.11: Detail and operating principle of the second type of hybrid-technology SAW/microstrip TFS.

For illustrative purpose, Figure 4.12 shows some examples of narrow-band filtering profiles synthesized with the TFS of Figure 4.11(a) along with that of the SAW resonator. In particular, Figure 4.12(a) demonstrates the flexibility of this TFS regarding the reallocation of the TZ_1, which can be controlled by only one design parameter—$\theta_1(f_d)$ in this example—. All cases employ the BVD equivalent model of a one-port SAW resonator from *RFM*® with $f_s = f_d = 433.9$ MHz, $R_m = 26.46$ Ω, $L_s = 67.145$ μH, $C_s = 2.00385$ fF, and $C_p = 2.3$ pF. It should be mentioned that the bandwidth can be additionally controlled by inserting external impedance transformers at the input/output terminals of the TFS.

4.2.2 Multi-TFS-cascaded designs

With the purpose of obtaining greater levels of filtering selectivity, increased in-band amplitude flatness, and higher out-of-band power rejection levels in the attenuated bands with regard to those of a single TFS, similar and dissimilar TFSs can be cascaded in series through transmission-line segments. This is illustrated in Figure 4.11(a). Following this design strategy, Figures 4.13 and 4.14 plot some examples of ideal synthesized multi-section BPFs. Note that the same parameter values for the BVD equivalent model of the one-port SAW resonator as in the example of Figure 4.12 are considered. These examples are as follows:

- Figure 4.13 represents the power transmission and reflection parameters of two- and three-stage BPF designs formed by identical replicas of a TFS with an embedded one-port SAW resonators into both branches. For comparison purposes, the parameters of the single TFS and the one-port SAW resonator are also depicted. As can be seen, each TFS contributes with one pole to the overall quasi-elliptic BPF transfer functions, which exhibit in-band equiripple-type behavior and a minimum in-band power matching level of 20 dB in both examples. It must be further noted that the overall BPF response preserves the same TZs as its building TFS, whose multiplicity is increased by the number of inter-cascaded TFSs.

- Figure 4.14 shows the filtering profile of a BPF example composed of two dissimilar TFSs—TFS 1 and TFS 2—. By doing so, N^{th}-order quasi-elliptic-type bandpass filtering responses exhibiting up to $2N+1$ TZs can be achieved. A larger variety of attenuation masks can be satisfied by this high-order BPF configuration, while preserving the in-band amplitude flatness.

4.2.3 Comparison with the classic signal-interference TFS

As mentioned in the introduction of this chapter, the combination of SAW resonators and microstrip elements enables to extend the applicability of signal-interference structures to very-narrow-band BPF design. This is because traditional fully-planar counterparts, as in [12], would require extremely lengthy transmission-line segments with the subsequent prohibitive insertion losses. It is therefore instructive to compare the frequency response obtained with both approaches. Thus, a BPF

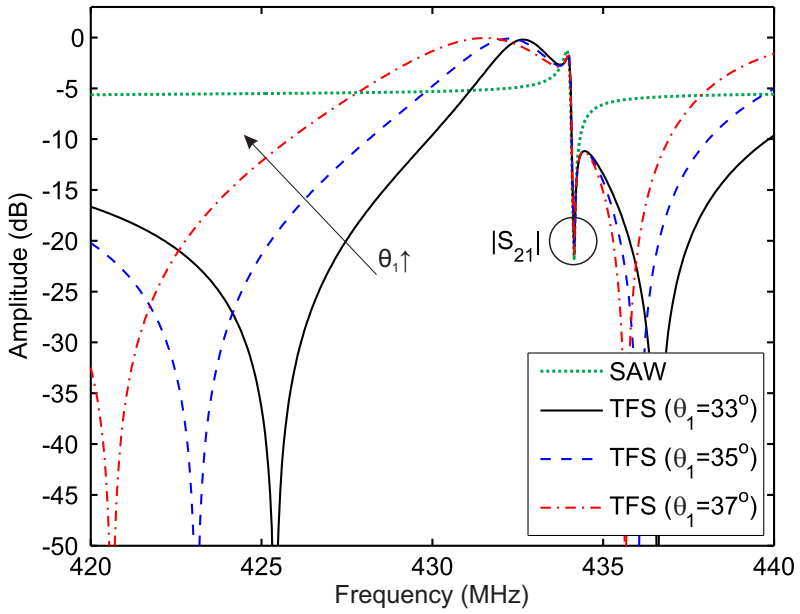

(a) $|S_{21}|$.

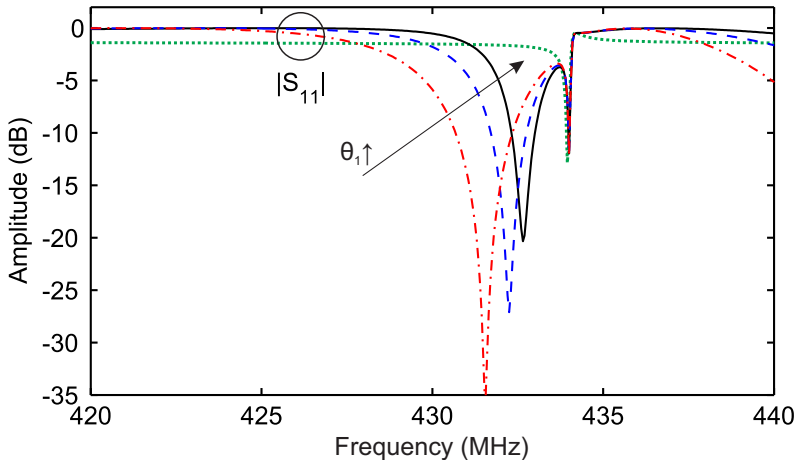

(b) $|S_{11}|$.

Figure 4.12: Examples of ideal synthesized power transmission ($|S_{21}|$) and reflection ($|S_{11}|$) responses of the TFS of Figure 4.11(a) and its SAW device: bandwidth control of the TFS as a function of $\theta_1(f_d)$ ($Z_1 = 2Z_0$, $Z_2 = 1.2Z_0$, $Z_3 = 1.4Z_0$, $Z_4 = 1.2Z_0$, $\theta_2(f_d) = 70°$, $\theta_3(f_d) = 50°$, and $\theta_4(f_d) = 30°$).

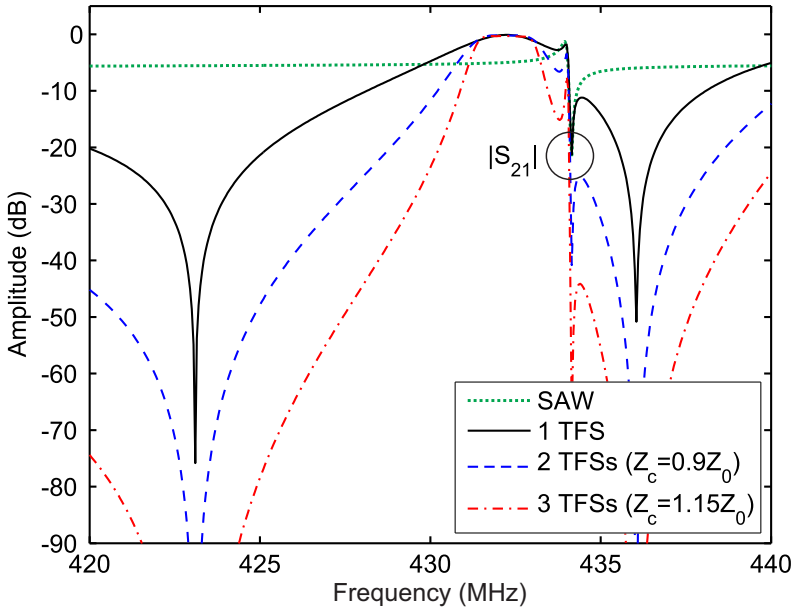

(a) $|S_{21}|$.

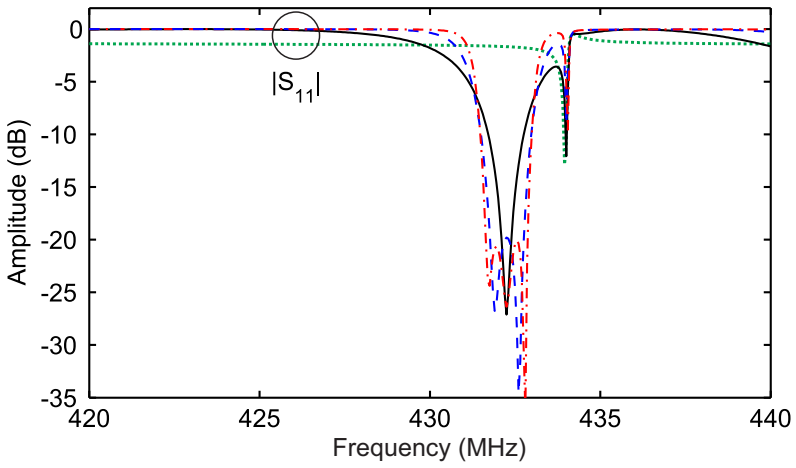

(b) $|S_{11}|$.

Figure 4.13: Examples of ideal synthesized power transmission ($|S_{21}|$) and reflection ($|S_{11}|$) responses of multi-TFS-series-cascaded BPFs—TFS of Figure 4.11(a)—and its embedded SAW device and building TFS: identical TFSs ($Z_1 = 2Z_0$, $Z_2 = 1.22Z_0$, $Z_3 = 1.4Z_0$, $Z_4 = 1.2Z_0$, $\theta_1(f_d) = 35°$, $\theta_2(f_d) = 70°$, $\theta_3(f_d) = 50°$, $\theta_4(f_d) = 30°$, and $\theta_c(f_d) = 85°$).

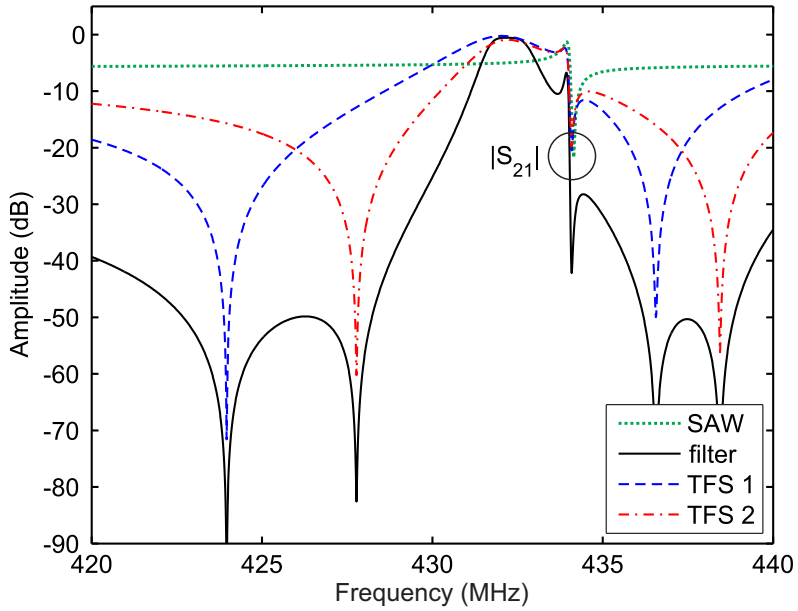

(a) $|S_{21}|$.

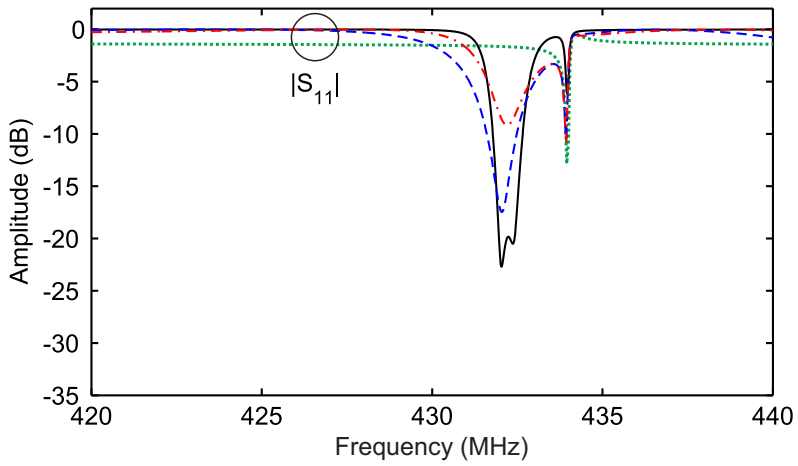

(b) $|S_{11}|$.

Figure 4.14: Ideal synthesized power transmission ($|S_{21}|$) and reflection ($|S_{11}|$) responses of two-TFS-series-cascaded BPFs—TFS of Figure 4.11(a)—and its embedded SAW device and building TFS: dissimilar TFSs (TFS 1: $Z_1 = 2.1Z_0$, $Z_2 = 1.14Z_0$, $Z_3 = 1.4Z_0$, $Z_4 = 1.1Z_0$, $\theta_1(f_d) = 35°$, $\theta_2(f_d) = 70°$, $\theta_3(f_d) = 50°$, and $\theta_4(f_d) = 30°$; TFS 2: $Z_1 = 2.06Z_0$, $Z_2 = 1.2Z_0$, $Z_3 = 1.4Z_0$, $Z_4 = 1.2Z_0$, $\theta_1(f_d) = 34°$, $\theta_2(f_d) = 70°$, $\theta_3(f_d) = 45°$, and $\theta_4(f_d) = 35°$; inter-TFS cascading line: $Z_c = 1.6Z_0$, and $\theta_c(f_d) = 65°$).

shaped by the series cascade of three replicas of the bi-path signal-interference TFS expounded in [12] is synthesized to exhibit the same center frequency—$f_0 = 431.85$ MHz—, 3-dB absolute bandwidth—equal to 2.1 MHz, resulting in a 3-dB relative bandwidth of 0.5%—, and impedance level—$Z_0 = 50\ \Omega$—as its equivalent approach of Figure 4.13. The values of the design parameters of the BPF example based on the classic TFS are as follows:

- TFS—as the one of Figure 1 and according to equations (1) and (2) in [12]—: $Z_1 = 0.583Z_0$, $Z_2 = 1.4Z_0$, $\theta_1(f_0) = 9090°$, and $\theta_2(f_0) = 9270°$.
- Inter-TFS cascading line: $Z_c = Z_0$ and $\theta_c(f_0) = 180°$.

Figure 4.15 depicts the ideal power transmission responses of both third-order BPFs, which are respectively based on the mixed-tecnology TFS of Figure 4.11(a) and its conventional TFS counterpart of [12]. Regarding the ideal implementations, in addition to the obvious size-reduction advantage, it can be observed that the new approach features broader stopband bandwidths and higher out-of-band power-rejection levels by avoiding the spectral periodic replicas of the passband. This benefit comes from the incorporation of the SAW elements, which "breaks" the spectrally-periodic behavior of the structure. Besides, Figure 4.15 depicts the simulated power transmission profiles of the microstrip implementations of both designs, when a substrate RO4003C from *Rogers*^{TM}—relative dielectric permittivity $\varepsilon_r = 3.55$,, dielectric thickness $h = 1.52$ mm, dielectric loss tangent $\tan\delta_D = 0.0027$, and metal thickness $t = 35\ \mu$m [46]—is utilized. Whilst the filtering behavior is reasonably kept in the mixed-technology approach, it is completely distorted in the classic-TFS-based BPF owing to the prohibitive losses inherent to its excessively-long transmission-line sections. This means that such very-narrow-band BPF designs are unfeasible in practice for traditional signal-interference architectures, which are more suitable for moderate-to-UWB specifications, due to substrate loss limitations of the planar technology—more advanced technologies, such as superconductors, are not considered [101], [102]—.

4.2.4 Experimental results

For practical validation, a two-stage 50-Ω narrow-band BPF prototype with mixed SAW/microstrip technology has been designed, fabricated, and tested. Concerning the design, simulation, optimization, and testing processes of the circuit, the following aspects must be highlighted:

- The microstrip substrate RO4003C of *Rogers*^{TM} was selected whose parameters are: relative dielectric permittivity $\varepsilon_r = 3.55$, dielectric thickness $h = 1.52$ mm, dielectric loss tangent $\tan\delta_D = 0.0027$, and metal thickness $t = 35\ \mu$m, [46].
- The commercial on-chip one-port SAW resonator model RO3101E-1 from *RFM*® with $f_s = 433.9$ MHz was employed [99]. The S-parameters of this SAW resonator were considered in the simulations thanks to a previous TRL-based characterization performed for it.

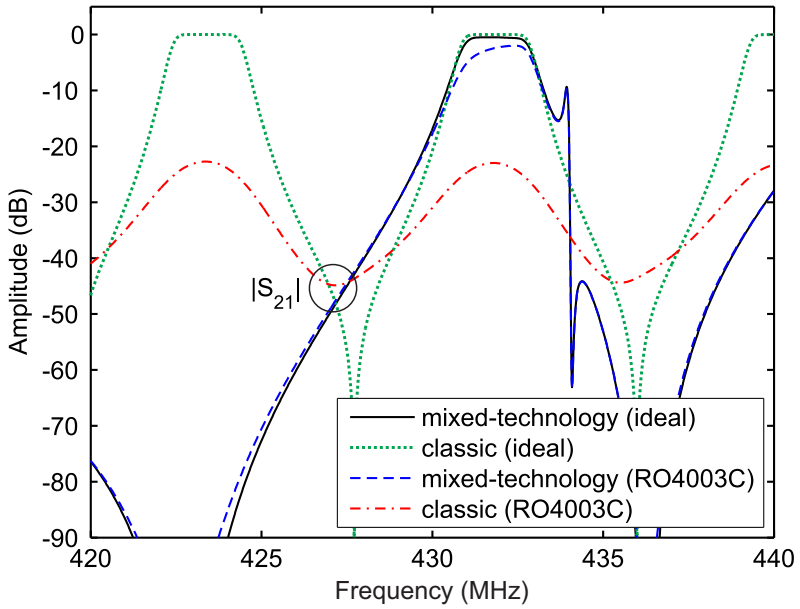

Figure 4.15: Comparison between the power transmission responses ($|S_{21}|$) of the three-stage BPF example of Figure 4.13 and its fully-planar classic counterpart of [12] for ideal transmission lines and microstrip lines of the planar substrate Rogers RO4003C.

- The commercial software package *Advanced Design Systems*^{TM} of *Keysight Technologies* was employed to carry out the circuit simulations [74].
- The commercial software package *High Frequency Structure Simulator v10.0 (HFSS)* of *Ansoft*^{TM} was used to perform 3D full-wave EM simulation by the FEM [48].
- An E8361A network analyzer of *Agilent*^{TM} was used for the measurements [75].

Prototype: Narrow-band bandpass filter

The 50-Ω-referred second-order mixed microstrip/SAW-resonator-type narrow-band BPF prototype is synthesized to show a center frequency equal to 432.6 MHz, a 3-dB relative bandwidth of 0.5%, and in-band input/output power matching levels higher than 20 dB as ideal specifications. The chosen values for the design parameters of the two identical TFSs are $Z_1 = 100\ \Omega$, $Z_2 = 64.7\ \Omega$, $Z_3 = 68\ \Omega$, $Z_4 = 60.9\ \Omega$, $\theta_1(f_d) = 33.5°$, $\theta_2(f_d) = 69.7°$, $\theta_3(f_d) = 50°$, and $\theta_4(f_d) = 24°$. The two cascading lines have $Z_c = 50\ \Omega$ and $\theta_c(f_d) = 60°$ as selected values, all of these at $f_s = 433.9$ MHz. The layout and a photograph of the manufactured filter prototype are shown in Figure 4.16.

The ideal, simulated, and measured power transmission and reflection coefficients of the developed prototype are compared in Figure 4.17. As observed, the principle is clearly demonstrated although some unpredicted effects appear in the measured results. They consist of some narrow-band transmission peaks in the stopband region and some deterioration of the in-band amplitude flatness. This

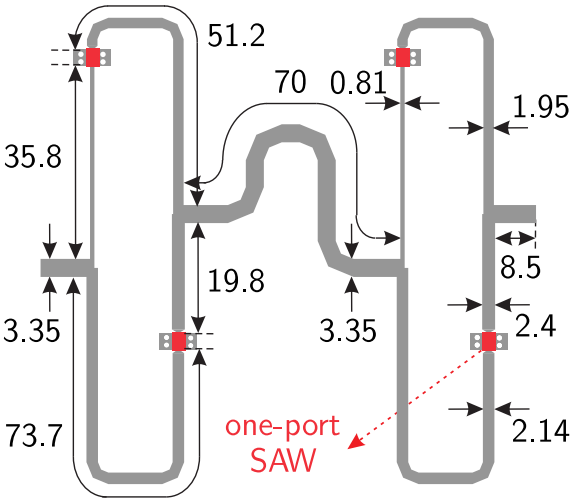

(a) Layout (non-redundant dimensions, in mm, are indicated).

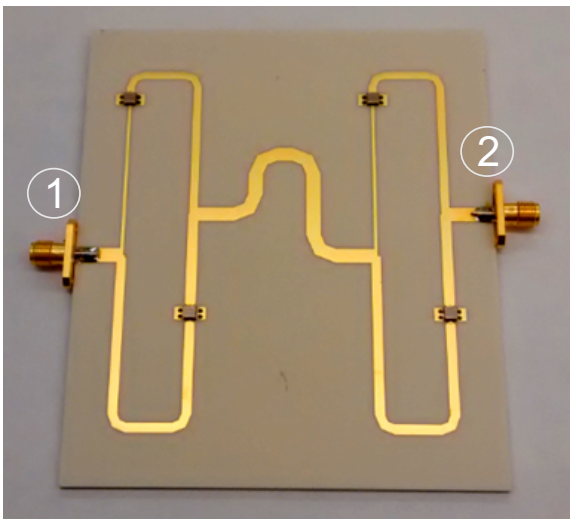

(b) Photograph (microstrip substrate: RO4003C of *Rogers*).

Figure 4.16: Layout and photograph of the manufactured two-stage SAW/microstrip BPF prototype based on the TFS of Figure 4.11(a) [103].

undesired phenomena is caused by the spurious modes of the on-chip commercial SAW resonators that creates abrupt amplitude/phase changes at these frequencies, as illustrated in Figure 4.17(b). Nevertheless, a minimum in-band insertion loss of 1.88 dB, in-band input power matching higher than 1.88 dB, and a 3-dB relative bandwidth of 0.49% are attained. This leads to an effective Q_u of 1350 for an equivalent two-pole BPF with the same behavior, that is much better than that of a fully microstrip design—Q_u below 200—. As mentioned before, the resulting bandwidth —about $5k_t^2$ in this example—could not be attained by pure SAW filter schemes—limited to approximately $k_t^2 = 1-(f_s/f_p)^2 = 0.1\%$ for the chosen commercial on-chip SAW resonator—.

4.3 Filters based on TFSs with embedded in-band SAW bandpass filter

Lastly, a technique to increase the bandwidth of on-chip SAW RF BPFs is reported in this section. Through the insertion of a SAW BPF in one of the branches of the bi-path signal-interference TFS, a broader filtering action than that offered by the SAW BPF itself is attained. Such bandwidth enlargement comes from constructive signal-energy interactions taking place between the TFS electrical paths in the overall passband range. TZs are also created through signal-energy suppressions, leading to highly-selective bandpass filtering response in multi-TFS-cascaded structures. They also exhibit advantages in terms of lower in-band insertion loss, broader attenuated bands, and smaller physical size when compared to their fully distributed-element counterparts.

4.3.1 Concept

The operational principle of the third class of hybrid-SAW/microstrip TFS consists of inserting a narrow-band bandpass circuit in only one of the electrical paths of a two-path feed-forward signal-interference TFS as depicted in Figure 4.18. Here, Z and θ correspond to the characteristic impedance and electrical length, respectively, of the transmission-line segments of the TFS. The SAW BPF acts as a multi-resonant node in this case, so it contributes to shape the overall transmission band and can be located in the middle or in the edge of the resulting passband. This increased flexibility is explained by the influence of the spurious modes of the SAW BPF that is less prominent than for the SAW resonators in the approaches of Sections 4.1 and 4.2, in which very deep in-band notches were created.

Concerning the functional principle of this novel TFS, the following aspects must be remarked:

- The overall BPF passband is obtained by means of the constructive effect taking place between the two signal components coming from its two transversal paths at the output node, resulting in a broadening-passband phenomenon around the frequency range of the building SAW BPF. This is translated into a significant reduction of the lengths of the transmission-line segments forming

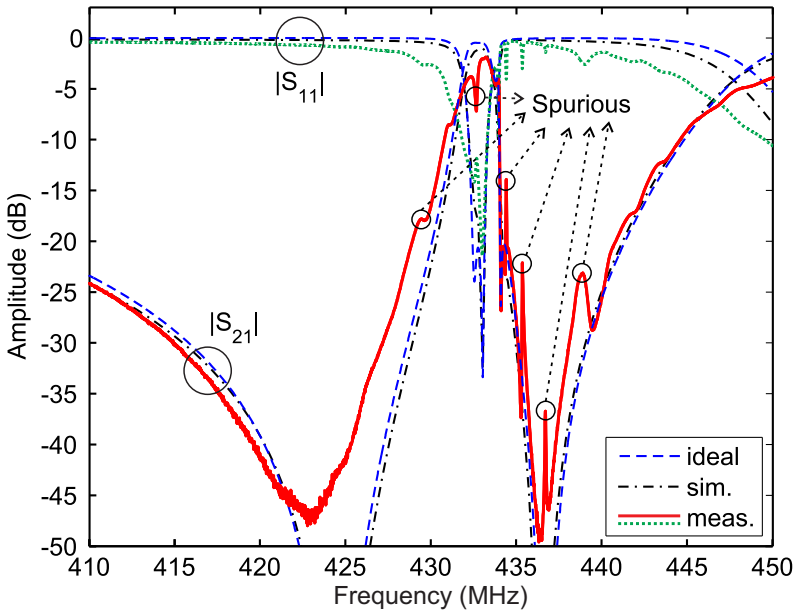

(a) S-parameters of the manufactured prototype.

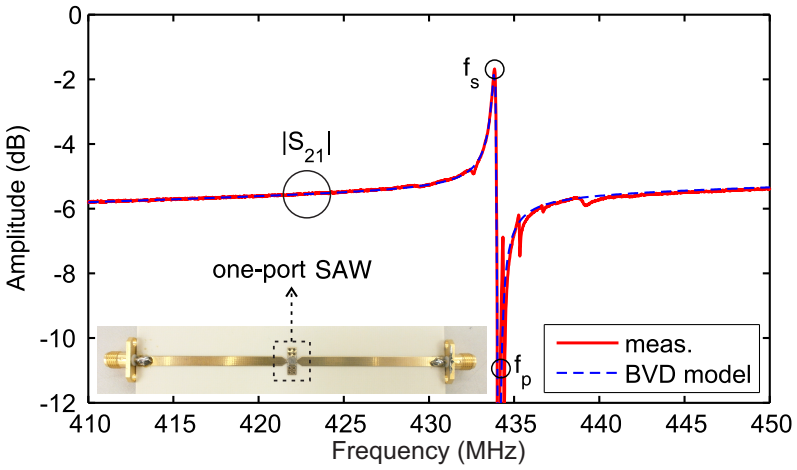

(b) BVD-model and measured power transmission responses of its constitutive one-port on-chip SAW resonator (the photograph of the assembled circuit for its TRL-characterisation is included).

Figure 4.17: Ideal, simulated and measured power transmission ($|S_{21}|$) and reflection ($|S_{11}|$) responses of the manufactured narrow-band BPF prototype based on the TFS of Figure 4.11(a) along with the ideal and measured power transmission curve of its embedded SAW element [103].

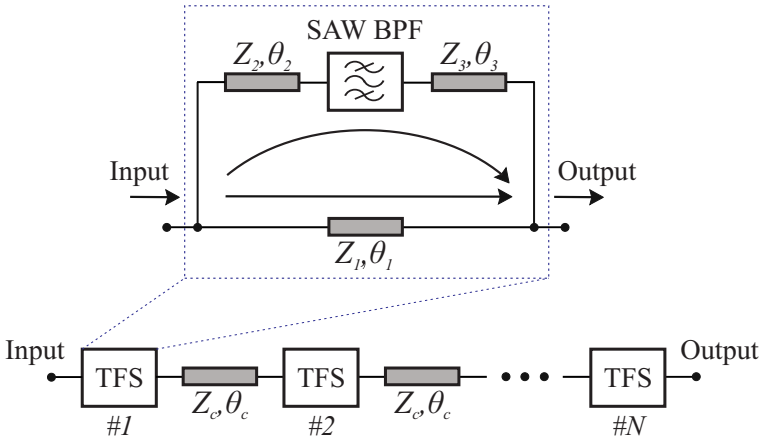

(a) Schematic (building TFS and N-stage-series-cascaded BPF).

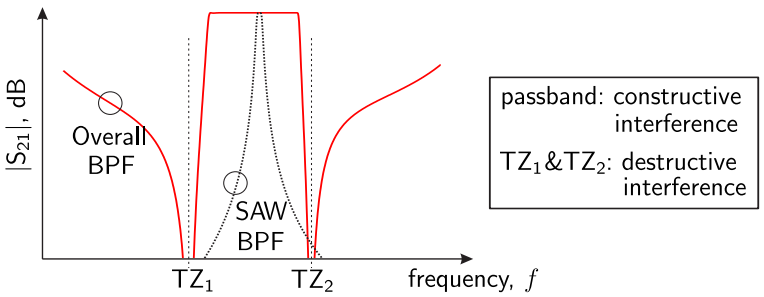

(b) Operating principle.

Figure 4.18: Detail and operating principle of the third type of hybrid-technology SAW/microstrip TFS.

the SAW/microstrip TFS when compared to its traditional fully-distributed-element TFS counterpart to achieve the same bandwidth, as it will be shown in 4.3.3.

- Two TZs—TZ_1 and TZ_2 in Figure 4.18(b)—are generated from a perfect signal-energy cancelation occurring between the two feed-forward electrical paths of the TFS at these frequencies. By doing so, sharp-rejection capability can be attained in its transfer function. Note that, as in the previous TFSs, these TZs are generated at those spectral positions where the overall transmission admittance parameter Y_{21} of the TFS becomes zero or tends to infinity.

- Regarding the location of the TZs, they can be easily controlled by adequately adjusting the design parameters of the constitutive transmission-line segments, so that different passband specifications can be met.

- Passbands with symmetrical or asymmetrical out-of-band rejection levels can be created by appropriately controlling the transmission-line design parameters.

For theoretical demonstration, two different examples of synthesized TFSs based on the circuit scheme of Figure 4.18(a) are represented in Figure 4.19. In both cases, a Z_0-level third-order Butterworth-type response with center frequency $f_d = 916$ MHz and 3-dB bandwidth of 11.5 MHz—resulting in a 3-dB relative bandwidth of 1.26%—was employed as narrow-band BPF, playing the same role as the SAW BPF—note that this Butterworth-type filter exhibits the same center frequency and bandwidth as the on-chip commercial SAW BPF utilized in the practical realizations of Section 4.3.4—. As a result, a quasi-elliptic-type third-order filtering profile with a bandwidth that is significantly broader than that of the embedded Butterworth-type BPF is attained. Note also that, although it is demonstrated how the passband-width of this type of TFSs can be flexibly controlled through the impedance-line variables, a wide variety of bandpass filtering profiles can be synthesized if all design variables are adjusted. Among them, it is worth highlighting transfer functions with strong spectral asymmetry as in Figure 4.20, which are highly demanded for the channel BPFs of duplexers. In this case, the narrow-band BPF is located closer to the particular TFS passband edge at which a more-abrupt cut-off slope is obtained. This feature will be exploited in the physical implementations of Section 4.3.4, where the SAW BPF is located at one edge of the overall transmission band of the entire multi-TFS-cascaded BPF prototype.

4.3.2 Multi-TFS-cascaded designs

As demonstrated in Section 4.2.2 for the second class of mixed-technology SAW/microstrip TFS, multi-stage arrangements can be considered for improved-selectivity BPF development as in Figure 4.18(a). Those TFSs are cascaded in series through simple transmission-line segments. This statement is corroborated in Figure 4.21. It depicts the ideal power transmission and reflection curves of specific examples of two- and three-stage BPFs, along with the same parameters for its building TFS

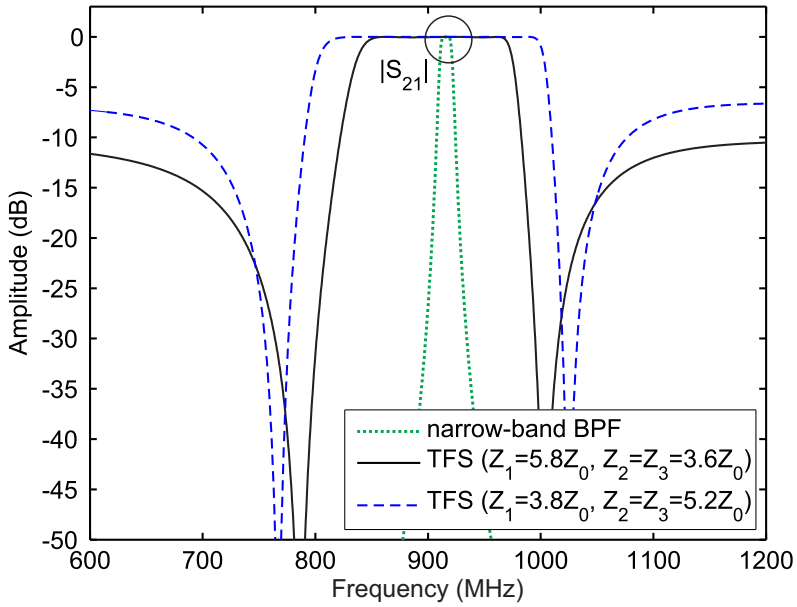

(a) $|S_{21}|$.

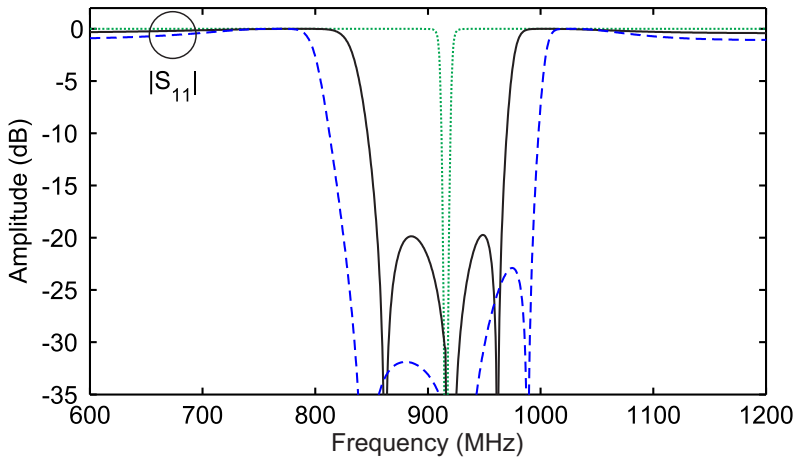

(b) $|S_{11}|$.

Figure 4.19: Examples of ideal synthesized power transmission ($|S_{21}|$) and reflection ($|S_{11}|$) responses of the TFS of Figure 4.18(a) and its embedded narrow-band BPF: bandwidth control of the TFS as a function of impedance-line parameters ($\theta_1(f_d) = 181°$ and $\theta_2(f_d) = \theta_3(f_d) = 95°$).

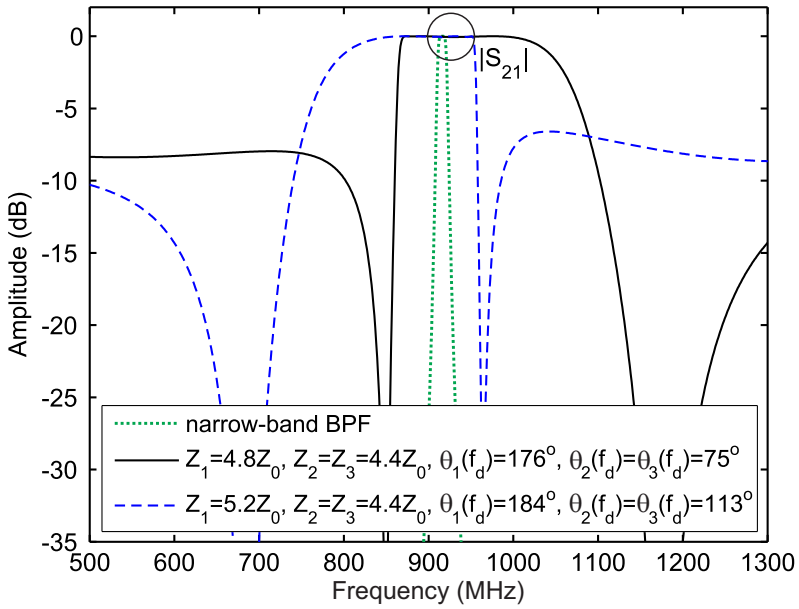

Figure 4.20: Examples of ideal synthesized power transmission ($|S_{21}|$) responses of the TFS of Figure 4.18(a) and its embedded narrow-band BPF: TFS with strong spectral asymmetry.

and embedded narrow-band BPF. In particular, for both multi-stage BPFs, the TFS with larger passband-width of Figure 4.19 was selected. It is worth stressing the remarkable increase of the out-of-band attenuation levels and sharpness of cut-off slopes when compared to those of the isolated TFS, while keeping a minimum in-band input power matching level of 20 dB. In addition, dissimilar TFSs could also be used for the synthesis of quasi-elliptic-type bandpass filtering responses featuring up to $2N$ different TZs.

4.3.3 Comparison with the classic signal-interference TFS

To corroborate the advantages of this new SAW/microstrip filtering topology, the TFS example synthesized in Section 4.3.1—in particular the narrower-band case of Figure 4.19(a)—is compared with its equivalent traditional fully-planar TFS in [12] in this section. With this purpose, the classic TFS was synthesized to exhibit the same passband specifications as the former. Particularly, its center frequency is set as $f_0 = 904$ MHz and its bandwidth equal to 141 MHz—15.6% in relative terms—. The values for the design parameters of the traditional TFS counterpart are then as follows—according to Figure 1 and equations (1) and (2) in [12]—: $Z_1 = 2.24Z_0$, $Z_2 = 0.69Z_0$, $\theta_1(f_0) = 450°$, and $\theta_2(f_0) = 630°$.

The ideal power transmission and reflection curves of both TFSs are plotted in Figure 4.22. As in the hybrid TFS of Figure 4.15, the new TFS approach outperforms the classic one in terms of in-band amplitude flatness, abruptness of filter flanks, stopband bandwidths, and out-of-band power attenuation levels. This is again achieved for shorter transmission-line segments in the SAW/microstrip TFS. It results in the size reduction of a real implementation, which becomes even more noticeable in smaller-FBW BPF designs.

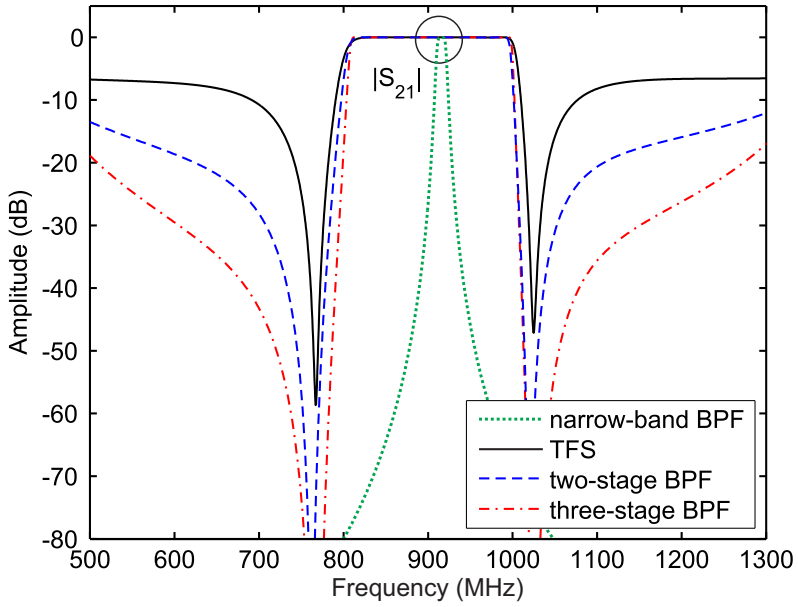

(a) $|S_{21}|$.

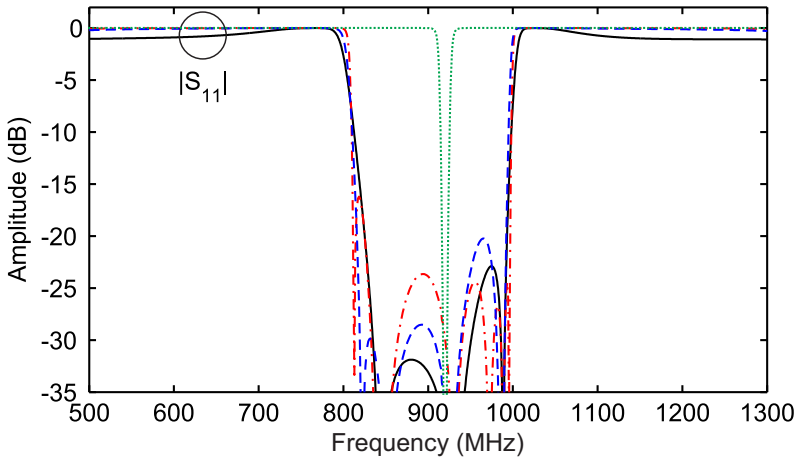

(b) $|S_{11}|$.

Figure 4.21: Examples of ideal synthesized power transmission ($|S_{21}|$) and reflection ($|S_{11}|$) responses of multi-TFS-series-cascaded BPFs—TFS of Figure 4.18(a)—and its narrow-band BPF: identical TFSs ($Z_1 = 3.8Z_0$, $Z_2 = Z_3 = 5.2Z_0$, $\theta_1(f_d) = 181°$, $\theta_2(f_d) = \theta_3(f_d) = 95°$, and $\theta_c(f_d) = 0°$).

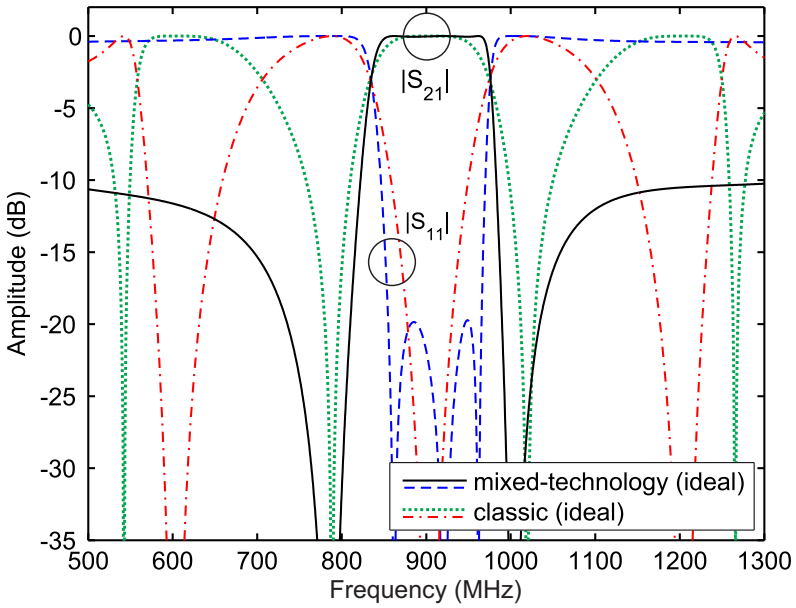

Figure 4.22: Comparison between the ideal power transmission ($|S_{21}|$) and reflection ($|S_{11}|$) responses of a synthesized example of the TFS in Figure 4.18(a)—narrower-band case of Figure 4.19—and its classic fully-planar counterpart in [12] for ideal transmission lines and microstrip lines implemented in the substrate Rogers RO4003C.

4.3.4 Experimental results

The proposed technique for the bandwidth enlargement of on-chip SAW RF filters is experimentally confirmed here through the development and testing of two 50-Ω-referred mixed-technology microstrip/SAW signal-interference BPF prototypes—two-stage and three-stage designs—. With regard to the design, simulation, manufacturing, and measurement processes of the developed prototypes, the following points must be emphasized:

- The microstrip substrate RO4003C of *Rogers*^{TM} was chosen with the following parameters: relative dielectric permittivity $\varepsilon_r = 3.55$, dielectric thickness $h = 1.52$ mm, dielectric loss tangent $\tan\delta_D = 0.0027$, and metal thickness $t = 35$ μm [46].

- The commercially available on-chip SAW BPF model B3718 from *EPCOS*® exhibiting a center frequency of 916 MHz and a 3-dB absolute bandwidth equal to 11.5 MHz—which leads to a 3-dB relative bandwidth of 1.26%—is embedded into the TFSs of both prototypes [105].

- The commercial software package *High Frequency Structure Simulator v10.0 (HFSS)* of *Ansoft*^{TM} was used to carry out the 3D full-wave EM simulations by the FEM of the prototype [48].

- An E8361A network analyzer of *Agilent*^{TM} was utilized for the measurements [75].

Prototype 1: Two-stage narrow-band bandpass filter

The first proposed prototype is a 50-Ω second-order signal-interference BPF constituted by two identical series-cascaded TFSs [106]. It is designed to ideally exhibit a center frequency of 878 MHz and a 3-dB absolute bandwidth of 80.1 MHz—9.1% in relative terms—. To meet these specifications, the obtained values for the electrical variables—after a post-design optimization—are as follows ($Z_0 = 50\ \Omega$ and $f_d = 916$ MHz): $Z_1 = 175\ \Omega$, $Z_2 = Z_3 = 102\ \Omega$, $Z_c = 25\ \Omega$, $\theta_1(f_d) = 173°$, $\theta_2(f_d) = \theta_3(f_d) = 65.5°$, and $\theta_c(f_d) = 22°$. The layout and a photograph of the built SAW/microstrip BPF prototype 1 are shown in Figure 4.23.

The power transmission and reflection coefficients of the enhanced-bandwidth filter—assuming ideal transmission lines—along with the measurements provided by the manufacturer for the on-chip SAW BPF inserted into both TFSs are plotted in Figure 4.24. As can be seen, the passband of the SAW BPF was situated at the upper side of the overall filtering response for two main reasons: firstly, in order to preserve the sharp-rejection characteristics of the SAW BPF in the upper passband region; and secondly, to prevent the conceived BPF from the upper spurious modes—above $f_d = 916$ MHz—which are more critical than the lower ones. Notwithstanding, the influence of the SAW BPF is clearly visible on the whole transfer function in terms of an amplitude ripple and the presence of some undesired ultra-narrow notches caused by its lower spurious modes. Note also the appearance of two TZs produced by pure signal-energy cancelations within the TFS.

Figure 4.25 presents the simulated and measured power transmission, reflection, and in-band group-delay profiles of the manufactured prototpye. As shown, there is a close agreement between predicted and experimental results, except from some increase in the insertion-loss levels. This can be attributed to several reasons, such as higher-than-expected radiation loss caused by the very thin transmission lines of the circuit or a greater insertion loss level in the soldered SAW BPF chips than the one that was measured by the manufacturer to extract its S-parameters. The resulting RF performance parameters measured in the built prototype are as follows: center frequency of 890 MHz, 3-dB absolute bandwidth equal to 56.9 MHz—giving rise to a 3-dB relative bandwidth of 6.39%—which is 5× higher than the one of the on-chip SAW BPF itself—or, subsequently, 3× higher than the k_t^2—considering that the FBW of the SAW BPF is ≈0.6%, minimum passband insertion loss of 2.2 dB, and in-band input/output power matching levels higher than 9.7 dB.

Prototype 2: Three-stage narrow-band bandpass filter

The second manufactured prototype expounded in this section corresponds to a 50-Ω third-order signal-interference BPF shaped by the series-cascaded connection of three equal TFSs [103]. It is aimed at showing an ideal center frequency of 870 MHz and a 3-dB absolute bandwidth of 95 MHz—resulting in a 3-dB relative bandwidth of 10.9%—. Once the single TFS was synthesized as a low-order approximation of the overall transfer function, the entire three-stage BPF was optimized to maximize as much as possible the in-band power matching levels. The final values for the design parameters are set as follows ($Z_0 = 50\ \Omega$ and $f_d = 916$ MHz): $Z_1 = 160$

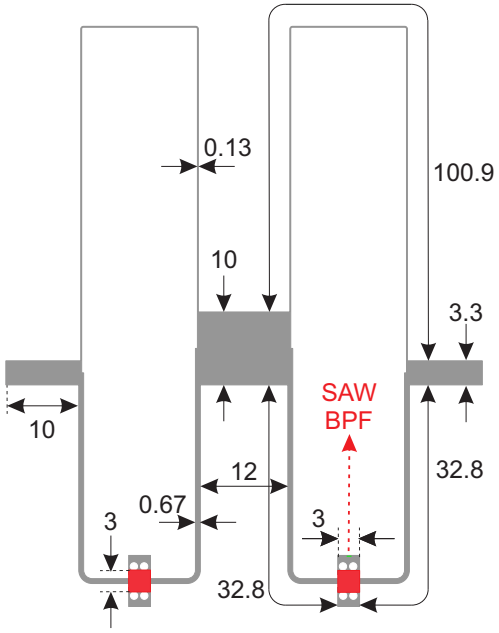

(a) Layout (non-redundant dimensions, in mm, are indicated).

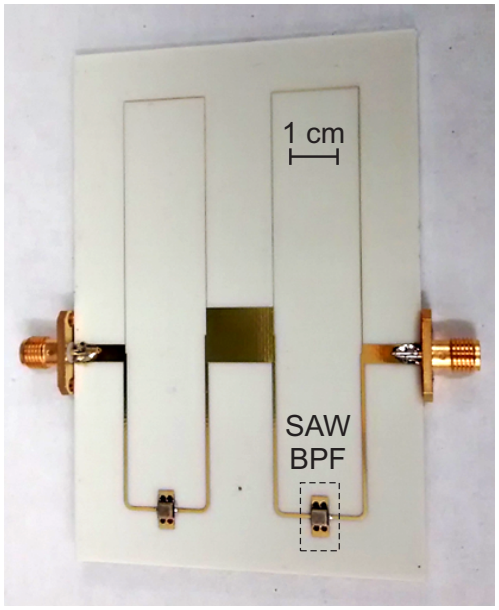

(b) Photograph (microstrip substrate: RO4003C of *Rogers*).

Figure 4.23: Layout and photograph of the manufactured two-stage SAW/microstrip BPF prototype 1 based on the TFS of Figure 4.18(a) [106].

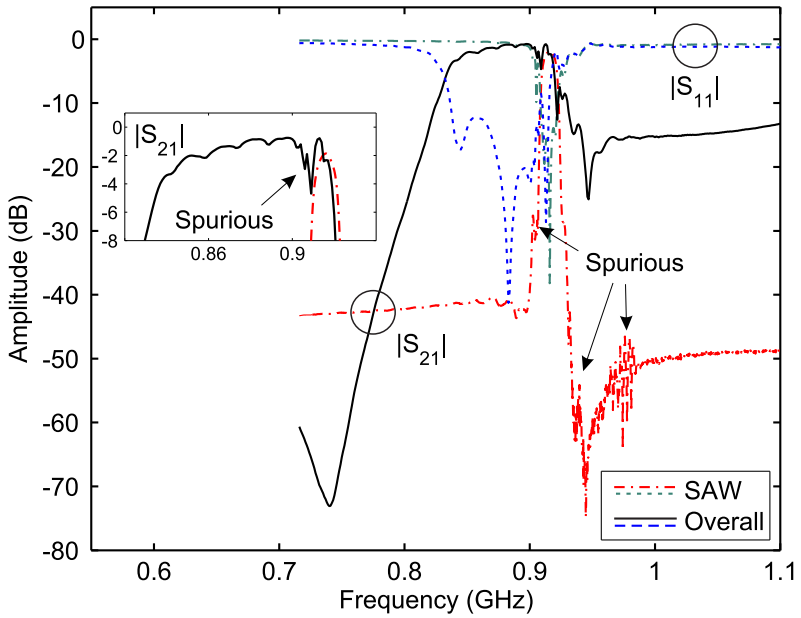

Figure 4.24: Simulated power transmission ($|S_{21}|$) and reflection ($|S_{21}|$) responses of the manufactured two-stage SAW/ transmission-line BPF circuit prototype 1 based on the TFS of Figure 4.18(a) assuming ideal transmission-line sections. The measured power transmission and reflection parameters of its constitutive on-chip SAW BPF chip are also shown [106].

Ω, $Z_2 = Z_3 = 100\ \Omega$, $Z_c = 35\ \Omega$, $\theta_1(f_d) = 174°$, $\theta_2(f_d) = \theta_3(f_d) = 72°$, and $\theta_c(f_d) = 20°$. The layout and a photograph of the built SAW/microstrip BPF prototype 2 are shown in Figure 4.26.

The power transmission and reflection curves of the designed BPF, along with the measured ones available from the manufacturer for the commercial on-chip SAW BPF embedded into its constitutive TFS, are plotted in Figure 4.27. As can be seen, the SAW BPF was located at the upper side of the overall passband to further increase the cut-off slope sharpness in the upper region of the whole transmission band. Furthermore, the noticeable enlargement of the bandwidth with regard to the one inherent to the original SAW BPF must be appreciated. Nevertheless, the effect of the SAW BPF in the entire BPF transmission band is still perceptible in the form of an unusual amplitude ripple and an undesired very-narrow in-band notch produced by the first lower spurious mode. In addition, as in the previous prototype, stopband TZs are also generated owing to destructive signal-interaction phenomena occurring within the TFS.

The simulated and measured power transmission and reflection profiles of this prototype are depicted in Figure 4.28. As shown, the agreement attained between the simulated and experimental results is reasonably close for demonstration purposes, although some increase of the in-band power insertion loss level is also visible here. Its origins are the same as those explained for the previous prototype. The main measured performances of the built BPF are as follows: 874.4-MHz center frequency, 3-dB absolute bandwidth of 88.3 MHz—translated into a 3-dB relative bandwidth of 10.1%—which is 7.7 times higher than that of the constituent on-chip SAW BPF—

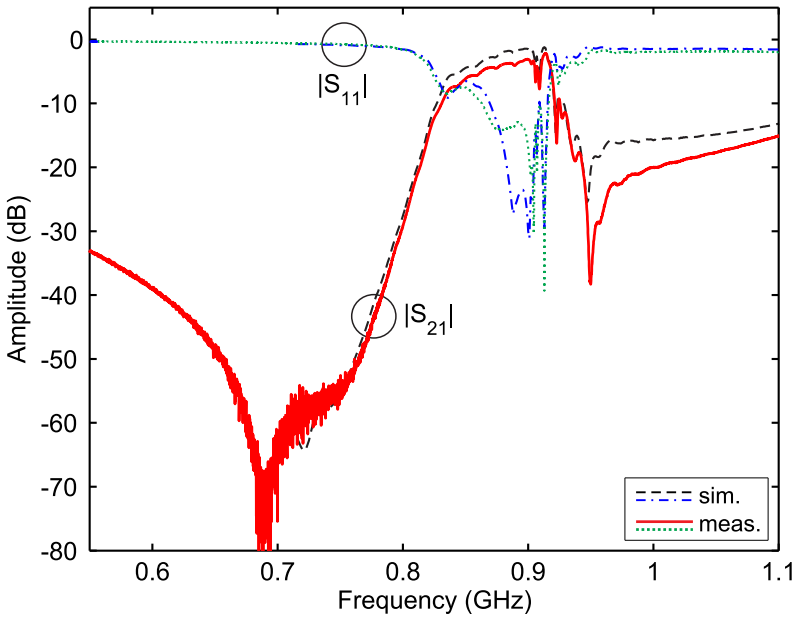

(a) $|S_{21}|$ and $|S_{11}|$.

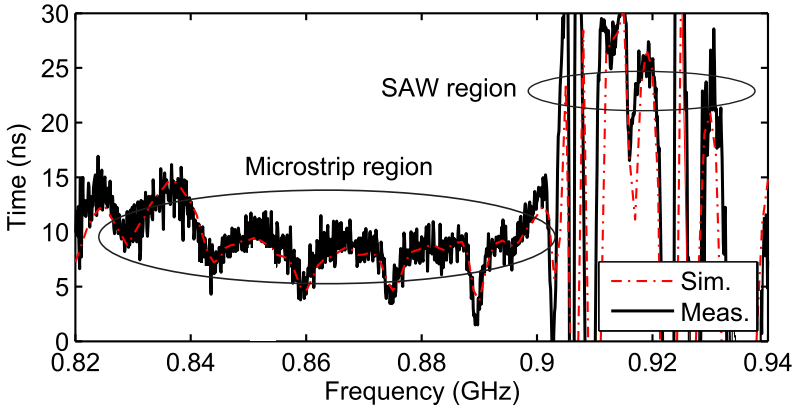

(b) τ_g (dominant microstrip and SAW regions in the filter passband are indicated).

Figure 4.25: EM simulated and measured power transmission ($|S_{21}|$), reflection ($|S_{11}|$), and in-band group-delay (τ_g) responses of the manufactured two-stage SAW/ transmission-line BPF circuit prototype based on the TFS of Figure 4.18(a) [106].

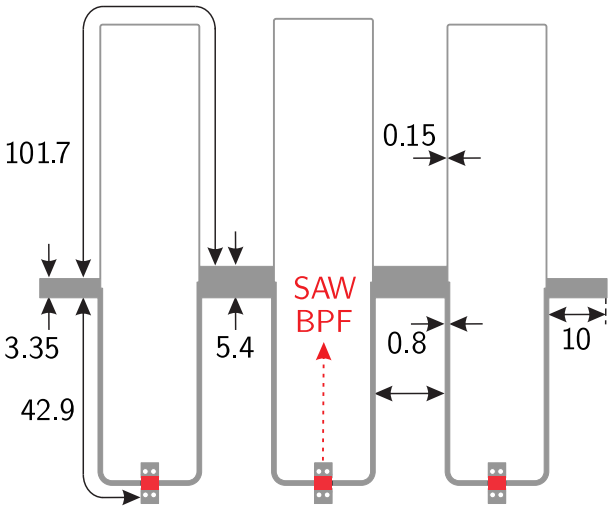

(a) Layout (non-redundant dimensions, in mm, are indicated).

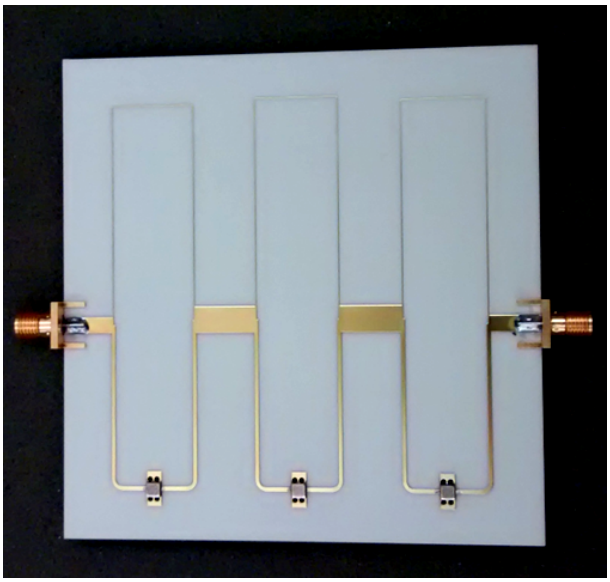

(b) Photograph (microstrip substrate: RO4003C of *Rogers*).

Figure 4.26: Layout and photograph of the manufactured three-stage SAW/microstrip BPF prototype 2 based on the TFS of Figure 4.18(a) [103].

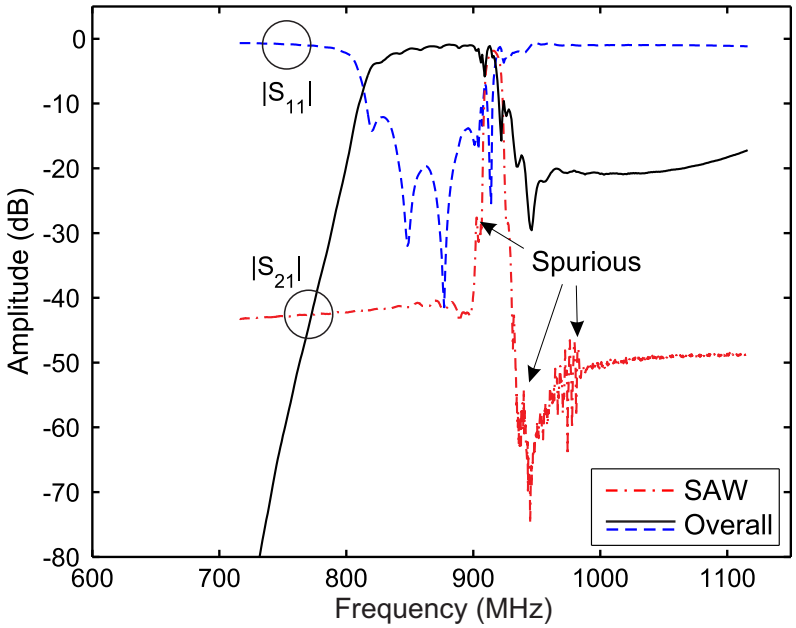

Figure 4.27: Simulated power transmission ($|S_{21}|$) and reflection ($|S_{11}|$) responses of the manufactured three-stage SAW/transmission-line BPF circuit prototype 2 based on the TFS of Figure 4.18(a) assuming ideal transmission-line sections and measured power transmission parameter of its constitutive on-chip SAW BPF chip [103].

3-dB FBW 4.8 times larger than the AW resonator k_t^2 considering that the FBW of the SAW BPF is $0.6k_t^2$—, minimum in-band power insertion loss levels of 2.4 dB, and in-band input power matching levels above 10.1 dB—except for the in-band notch frequency where it is 7.7 dB—.

4.4 Conclusion

This chapter has reported a new family of analog narrow-band BPF designs which merge microstrip and SAW technology—either SAW resonators or SAW RF BPFs—. Its aim is to extend the suitability of feed-forward signal-interference filters, which have been mostly exploited in moderate-to-UWB designs, to narrow-band designs. Moreover, these new configurations can achieve larger bandwidth than traditional pure-SAW-resonator-based filter architectures.

The first technique is based on inserting one-port or two-port SAW resonators, acting as resonating-nodes into one of the branches of a multi-path TFS so that the high-Q properties of those resonators are substantially transferred to the transfer function of the TFS. In the second approach, a one-port SAW resonator is embedded into both signal-propagation paths of a bi-path TFS as non-resonating node. The purpose here is to take advantage of the ultra-abrupt spectral transition existing between the resonance and the antiresonance frequency of the SAW resonator to shape a very sharp upper cut-off slope in the overall transfer function. In the third configuration, by inserting SAW BPFs into one branch of the two-path TFS, a

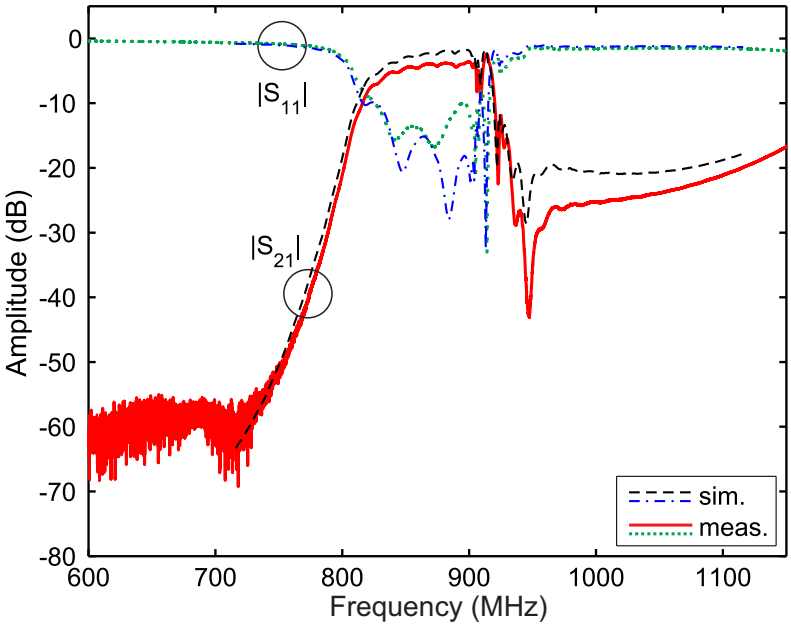

Figure 4.28: Simulated (EM) and measured power transmission ($|S_{21}|$) and reflection ($|S_{21}|$) responses of the manufactured three-stage SAW/transmission-line BPF circuit prototype 2 based on the TFS of Figure 4.18(a) [103].

passband wider than that of the single SAW BPF itself can be obtained. These three design procedures prove the potential of mixing SAW devices and transmission lines under signal-interference principles for enhanced-performance BPF design. In all of them, the resulting bandwidth and TZs allocation can be easily controlled through the variables of the constituent transmission-line segments. Note also that several replicas of the TFS—similar or dissimilar ones—can be cascaded in series to realize higher-order filtering structures by increasing the out-of-band power rejection levels in the stopbands.

For practical validation, a three-stage narrow-band BPF prototype with embedded 433.9-MHz one-port SAW resonator has been developed at the layout level under the principle of the first technique. Its 3-dB relative bandwidth is 0.46% at 434.66 MHz, which is ≈5 × greater than k_t^2 of its embedded SAW element. With regard to the the second approach, a two-stage narrow-band BPF prototype incorporating 433.9-MHz one-port SAW resonators has been developed and tested. It exhibits a 3-dB relative bandwidth of 0.49% at 432.6 MHz, which is ≈5 × higher than the k_t^2. Finally, followign the third technique, two- and three-stage narrow-band BPF prototypes with embedded 916-MHz SAW BPFs have been built and measured. They have a 3-dB relative bandwidth of 6.39% at 890 MHz and 10.1% at 874.4 MHz, respectively, which are 5 and 7.7 × higher than that of its building SAW BPF. Despite the negative effects associated to the spurious modes of the SAW devices that appear as a key limiting factor, the usefulness of these techniques has been fairly demonstrated. Note that such narrow bandwidths are unachievable through fully-microstrip signal-interference BPF realizations owing to the necessity of larger transmission lines and, subsequently, higher in-band insertion losses, in addition to

the unwanted presence of multiple spurious bands. Additional practical benefits of these BPFs are their inherent 50-Ω matching—avoiding the necessity of external impedance-scaling networks—and the use of SAW elements of the same characteristics, which make them more robust to manufacturing and assembly tolerances.

Chapter 5

Design of multi-function signal-interference microwave filtering devices

Traditionally, the design of RF/microwave chains has been conceived as the cascade connection of different "*mono-function*" components [107]. This means that microwave devices have been separately engineered to provide a single RF processing action, under specific performance requirements and for a certain reference impedance—typically equal to 50 Ω—, to be then interconnected through matching and transition networks. Thus, the combined transfer characteristic comes from the aggregation of each individual response. This classic philosophy presents nevertheless some drawbacks to be commented, as follows:

- When combining mono-function building blocks, they interact between them altering the overall performance. Note that the final solution often requires several post-design iterations in which the incorporation of inter-block RF interfaces—e.g., matching networks—is considered.
- Higher losses are introduced owing to the aggregation of multiple interconnection elements.
- The interconnection networks can have a negative influence in the operational bandwidth of the whole system in case they are not spectrally-broad enough.
- The physical area occupied by the full RF chain can be excessive for modern systems with stringent size requirements.

In the light of the above, a new philosophy based on the development of multi-function RF/microwave devices has lately acquired popularity. This means the incorporation of several high-frequency processing actions in a single module. Note also that this co-design approach could give rise to improved electrical performance and compactness. This can be of great interest especially for the RF front-ends of current wireless communication multi-standard systems with flexible multi-band operation [108], [109]. There are numerous examples of these multi-function circuits

so far, such as the bandpass filtering low-noise amplifier reported in [110] and the filtering patch antenna described in [111].

This chapter therefore concentrates on the development of multi-function high-frequency circuits operating under signal-interference principles. To this aim, signal-interference TFSs are inserted into the branches of mono-function circuits to provide them with single/multi-band filtering capability. In particular, three types of dual-function devices are proposed: Wilkinson-type power dividers, impedance transformers, and balanced BPFs, all of them exhibiting sharp-rejection filtering actions for moderate-to-UWB specifications and single/multi-band designs.

The organization of this chapter is as follows: firstly, the operating principle and the theoretical foundations of the new single/multi-band Wilkison-type filtering power divider is described in Section 5.1. For practical validation, four different prototypes are built and tested. They are a microstrip tri-band, a microstrip quad-band, and a lumped-element dual-band filtering power divider, and as well as a channelized active BPF that utilizes a single-band circuit of this type for its signal-division/combination blocks. Secondly, similar to the previous case, the theoretical foundations together with the design equations for the engineered single/multi-band filtering impedance transformer are provided in Section 5.2. In this case, to validate the concept, a single-band example is synthesized to demonstrate the influence of the TFS in the impedance-matching process. As practical proof of concept, a dual-band and a UWB single-band prototype are fabricated and measured. Thirdly, balanced BPFs based on embedded signal-interference TFSs exhibiting high common-mode rejection are presented in Section 5.3, along with corresponding single– and dual-band synthesis examples. A single-band balanced BPF is manufactured and characterized for demonstration purposes. Finally, the main conclusions of this work are summarized in Section 5.4.

5.1 Single- and multi-band Wilkinson-type filtering power dividers

Wilkinson-type single-band power dividers, either in its traditional version [112] or in more sophisticated approaches with frequency reconfigurability [113], are key components in a wide range of RF/microwave systems. This is due to the high-isolation levels attainable between their output terminals, which makes them perfect candidates for signal-division/combination blocks in a rich variety of subsystems such as Doherty power amplifiers [114], feeding networks for array antennas [115], and channelized filters [117]. This widespread use is the reason for exploring Wilkinson-type power dividers capable of simultaneously featuring single- and multi-band filtering operation, since many other higher-level RF subsystems could take advantage of it.

Regarding Wilkinson-type power dividers operating in multiple frequency bands, there have been many approaches reported to date. They are commonly based on planar technologies but following distinct design strategies. A brief review of them is reported here. As first example, [115] and [116] presented dual-band power splitters that make use of CRLH transmission-line segments. Another different strategy was

expounded in [118], in which tri-band power dividers were developed using three-section transmission-line transformers. The philosophy adopted in [119] inserts open- and short-ended stubs in the branches of the power divider so as to obtain dual-band operation, whereas this behavior was attained in [120]-[122] by means of coupled-line arrangements. This study allows identifying some limitations associated with the reported multi-band Wilkinson-type power dividers. They are as follows:

- Most of these solutions can hardly be extrapolated to devices with an arbitrary number of operative frequencies.
- Some of the electrical characteristics of these approaches, such as the location of the multiple bands and their associated bandwidths, are not easily adjustable.
- They all exhibit narrow-band behavior.
- They lack filtering capability between their operating frequencies in order to reject undesired signals.
- Prior-art design alternatives incorporating coupled-line sections can not be extrapolated to pure-lumped-element realizations, which are more suitable for the lower part of the microwave spectrum or other technologies such as MMIC, as explained in Chapter 3.

As already mentioned, this section introduces a new class of Wilkinson-type power-distribution circuits with single/multi-band filtering capability due to the insertion of transversal signal-interference cells into their branches. More specifically, the two-path in-parallel-transmission-line signal-interference cell is chosen [12], although this family of multi-frequency power dividers can be generalized to any type of signal-interference TFS; e.g., those exhibiting spectrally-asymmetrical behavior based on stepped-impedance lines or stub-loaded approaches [30], [123]. This work is completed with the theoretical design framework not only for distributed-element realizations but also for its equivalent lumped-element counterpart. The demonstration of multi-stage and frequency-asymmetrical designs, as well as its application to more sophisticated RF devices such as a channelized active BPFs, is also shown.

5.1.1 Theoretical foundations

The circuit detail of the devised single/multi-band Wilkinson-type filtering power divider, particularized in this case for a TFS consisting of two in-parallel transmission-line segments, is shown in Figure 5.1. Its underlying principle is to replace the transmission-line arms of the classic Wilkinson power divider with TFSs referred to the same impedance levels. Thus, single/multi-band operation along with the filtering behavior intrinsic to the signal-interaction transversal cell can be achieved simultaneously.

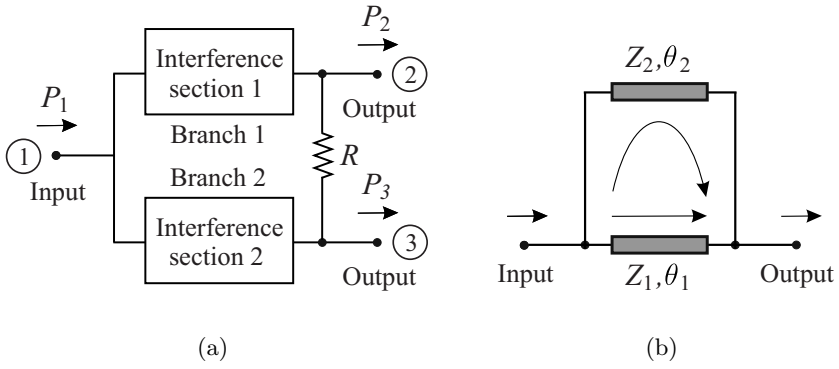

Figure 5.1: Detail of the single/multi-band Wilkinson-type filtering power divider and its building signal-interference TFS. (a) Filtering power divider. (b) Signal-interference TFS.

Design equations

By taking port 1 as the input terminal of the devised filtering power divider and nodes 2 and 3 as its output ports as shown in Figure 5.1(a), design formulas for its electrical variables can be deduced. They enable the synthesis of an N-band power-distribution/filtering profile with power-division ratio between ports 3 and 2 of k^2:1 (i.e., $P_2 = P_1/(1+k^2)$ and $P_3 = k^2 P_1/(1+k^2)$). These design equations for the electrical lengths θ_1 and θ_2 at the design frequency f_d, line impedances Z_1 and Z_2, isolation resistor R, and generated operational frequencies $f_1, f_2, \ldots, f_N$, respectively, are as follows (Z_0 is the impedance level):

$$\theta_1(f_d) = N \times 90^\circ \qquad \theta_2(f_d) = (N+2) \times 90^\circ \tag{5.1}$$

$$\text{Branch 1 (port 2):} \qquad \frac{1}{Z_1} - \frac{1}{Z_2} = \frac{1}{Z_0\sqrt{k(1+k^2)}} \tag{5.2}$$

$$\text{Branch 2 (port 3):} \qquad \frac{1}{Z_1} - \frac{1}{Z_2} = \frac{1}{Z_0}\sqrt{\frac{k^3}{1+k^2}} \tag{5.3}$$

$$R = Z_0\left(\frac{k^2+1}{k}\right) \tag{5.4}$$

$$\{f_1, f_2, \ldots, f_N\} = \left\{\frac{2pf_d}{N+1}, \qquad p = 1, 2, \ldots, N\right\} \tag{5.5}$$

It should be mentioned that, similarly to the conventional Wilkinson power divider, external quarter-wavelength transformers at the output terminals 2 and 3 with line impedances of $Z_0\sqrt{k}$ and $Z_0/\sqrt{k}$, respectively, must be added for unbalanced single-band designs to attain perfect power matching at all ports at the design frequency f_d. In the case of multi-band devices showing unequal power division between the output ports, multi-section wide-band transformers—whose power-matching range must cover all the operating frequencies—instead of the latter can

be employed to obtain the required impedance conversion at all the operative frequencies [4]. Note that multi-band transformers can also be employed for the same goal with size-compactness advantage—for instance, a signal-interference cell as the one depicted in Figure 5.1(b) to increase filtering selectivity, whose characteristic impedances Z_{m1} and Z_{m2} must meet the condition $1/Z_{m1} - 1/Z_{m2}$ to be equal to $1/(Z_0\sqrt{k})$ and $\sqrt{k}/Z_0$, respectively (i.e., one degree of freedom concerning the control of the bandwidth is available in each transformer)—.

For illustrative purposes, Figures 5.2, 5.3, and 5.4 present the S-parameters in amplitude of three examples of single- (case $N = 1$), triple- (cases $N = 3$), and sextuple-band (case $N = 6$) Wilkinson-type filtering power splitters with unequal and equal power-division ratios, respectively. In the multi-band cases, the phase responses associated to the power transmission coefficients are also plotted. Note in the two latter figures that the required $\pm 90°$ phase value is achieved at all the operative frequencies so that perfect output power isolation and power matching at all ports are simultaneously obtained.

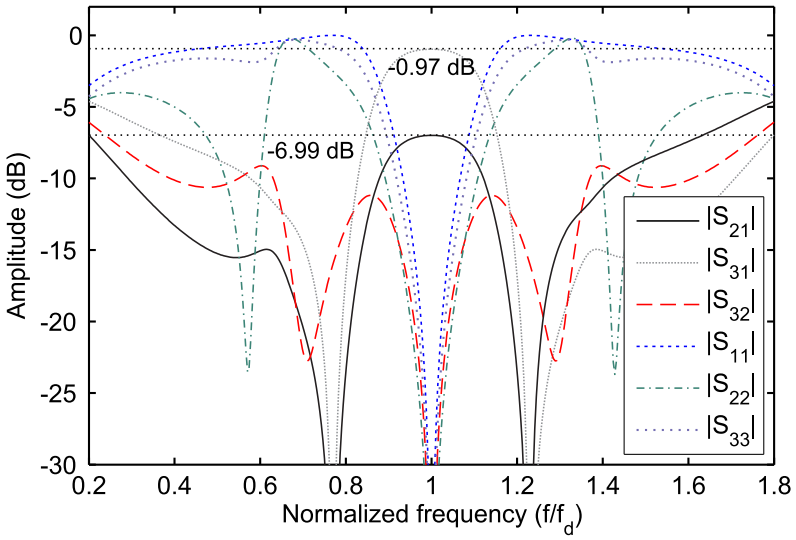

Figure 5.2: S-parameters of an ideal synthesized single-band Wilkinson-type filtering power divider with asymmetrical power-division ratio between ports 3 and 2 of 4:1—$k = 2$—. Design values for Branch 1 (port 2): $Z_1 = Z_0\sqrt{5/2}$, $Z_2 = Z_0\sqrt{10}$, $\theta_1(f_d) = 90°$, and $\theta_2(f_d) = 270°$. Design values for Branch 2 (port 3): $Z_1 = (Z_0/2)\sqrt{5/8}$, $Z_2 = Z_0\sqrt{5/8}$, $\theta_1(f_d) = 90°$, and $\theta_2(f_d) = 270°$. $R = 5Z_0/2$ and 90°-at-f_d electrical-length transformers at terminals 2 and 3 with impedances of $Z_0\sqrt{2}$ and $Z_0/\sqrt{2}$, respectively, are included.

Besides, similarly to any type of signal-interference filters—such as those reported in [12], [23], and [30]—, the electrical characteristics of the synthesized dual-function response can be controlled by properly adjusting the design parameters of the constituent transmission lines. As an example, in Figure 5.5 the operative bandwidths for the passbands of a triple-band frequency response with symmetrical power division, $N = 3$, and $k = 1$, is controlled by modifying the Z_2 value as long as equations (5.1)-(5.5) are fulfilled. As can be seen, the higher the values for the line-impedance variables are, then the broader the bandwidths of all passbands become. A more detailed demonstration of the flexibility offered by this type of circuits for the syn-

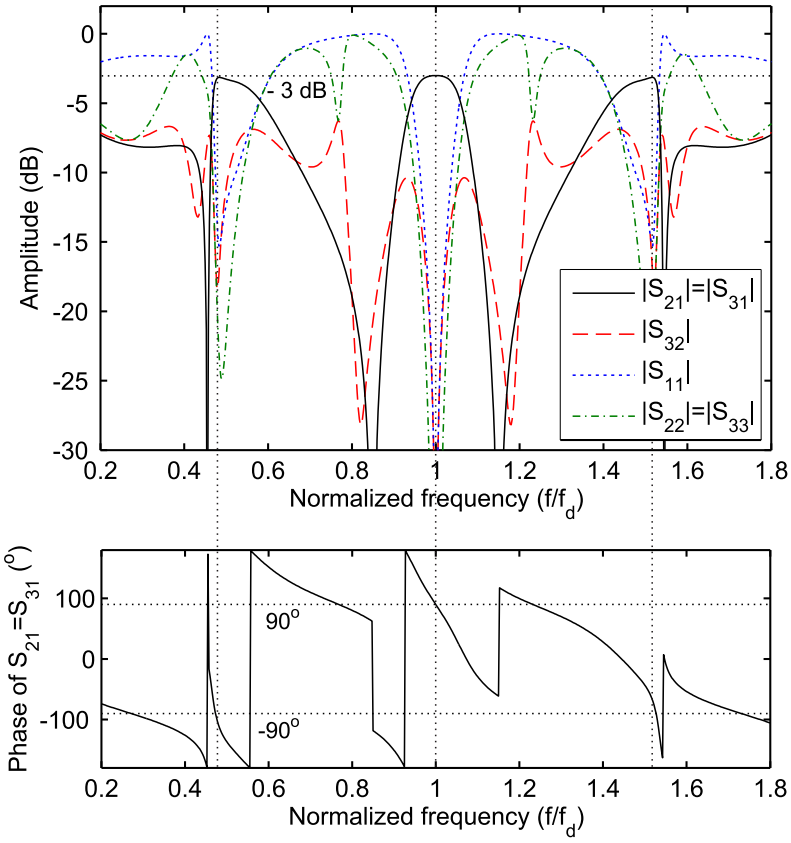

Figure 5.3: S-parameters—amplitude and phase responses for $S_{21} = S_{31}$—of an ideal synthesized triple-band Wilkinson-type filtering power divider with symmetrical power-division ratio between ports 2 and 3—$k = 1$—. Design values for both branches: $Z_1 = Z_0/\sqrt{2}$, $Z_2 = Z_0\sqrt{2}$, $\theta_1(f_d) = 270°$, $\theta_2(f_d) = 540°$, and $R = 2Z_0$.

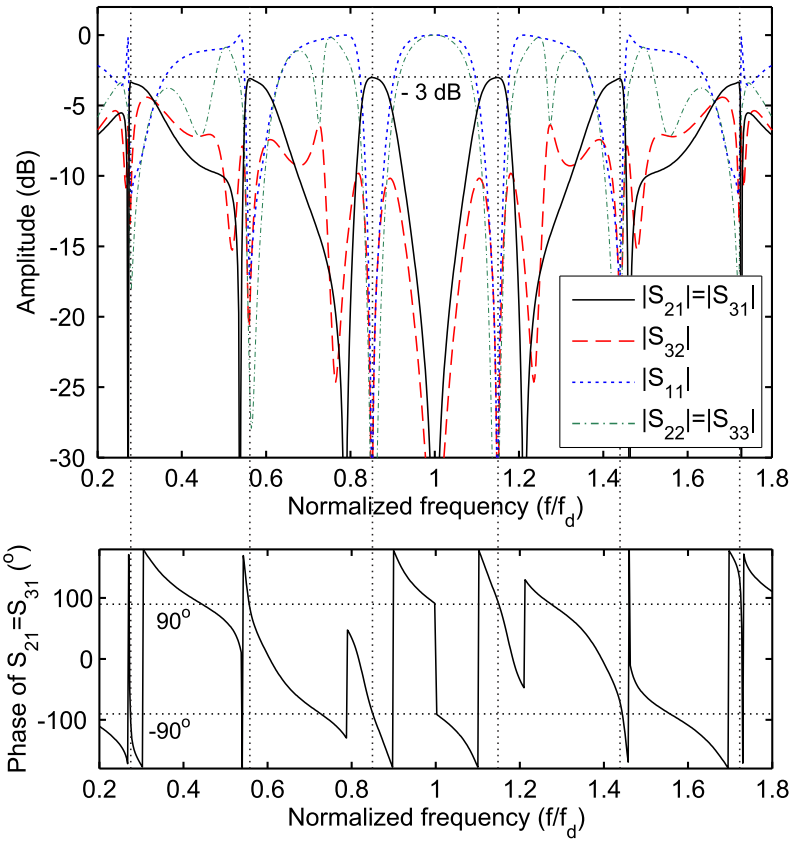

Figure 5.4: S-parameters—amplitude and phase responses for $S_{21} = S_{31}$—of an ideal synthesized sextuple-band Wilkinson-type filtering power divider with symmetrical power-division ratio between ports 2 and 3—$k = 1$—. Design values for both branches: $Z_1 = Z_0/\sqrt{2}$, $Z_2 = Z_0\sqrt{2}$, $\theta_1(f_d) = 540°$, $\theta_2(f_d) = 720°$, and $R = 2Z_0$.

thesis of more general responses is presented in Section 5.1.1 with the realization of multi-stage and frequency-asymmetrical power-distribution/filtering functions.

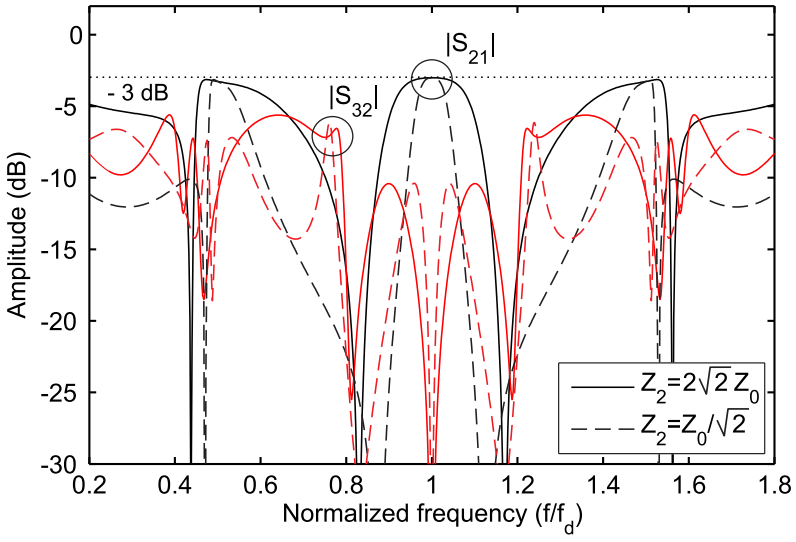

Figure 5.5: Bandwidth control of the ideal synthesized triple-band Wilkinson-type filtering power splitter—power transmission and isolation responses—with symmetrical power division—$k = 1$—and according to the design equations (5.1)-(5.5).

Lumped-element approximation

As highlighted in the introduction of this section, one of the major advantages of this kind of single/multi-band Wilkinson-type filtering power-distribution circuits when compared to previous transmission-line-based approaches, such as those in [120] and [121], is the absence of coupled-line stages. This feature allows pure-lumped-element realizations to be accomplished with the purpose of reducing circuit size, which can become prohibitive for distributed-element implementations in the lower part of the microwave band—below 1 GHz—, according to the philosophy expounded in Chapter 3. This is particularly critical for multi-band prototypes with a high number of operative frequencies, owing to incurred higher circuit size, as inferred from equation (5.1).

With this aim, the lumped-element realization proposed in Section 3.1 is applied to these structures. As was expounded in Chapter 3, this technique is based on partitioning a transmission-line segment, whose characteristic impedance and electrical length are Z and θ, respectively, into M equal-length sub-segments which can be modeled as LC T-type sub-cells. This is illustrated in Figure 5.6. Thus, by imposing a perfect correspondence at f_d between the impedance parameters $Z_{ij}(i, j = 1, 2)$ of the transmission-line sub-segment and its associated LC sub-cell as symmetrical two-port networks, the following design equations are derived:

$$L = \frac{Z(1 - \cos(\theta(f_d)/M))}{2\pi f_d \sin(\theta(f_d)/M)} \qquad C = \frac{\sin(\theta(f_d)/M)}{2\pi f_d Z} \tag{5.6}$$

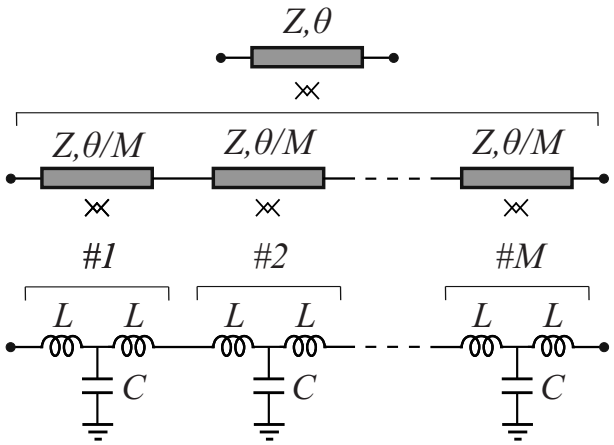

Figure 5.6: *LC* T-type equivalent model of a transmission line.

It is worth remembering that the exact equivalence between the transmission line and its *LC* counterpart is obtained at the design frequency f_d, so if a more accurate convergence outside this fixed frequency f_d is needed—for instance, in order to cover the broad spectral range of a multi-band circuit—, a higher M value is required.

As a supporting example, Figure 5.7 compares the power transmission and the output isolation parameters drawn in Figure 5.3 corresponding to the triple-band design and those of their equivalent lumped-element approximation for $\theta(f_d) = 90°$, and $M = 2$ and 6. The resulting normalized lumped-element values ($L_n \equiv Lf_d/Z_0$ and $C_n \equiv Cf_dZ_0$) after using (5.6) are as follows:

- Transmission-line electrical path of $Z_1 = Z_0/\sqrt{2}$ and $\theta_1(f_d) = 270°$: $L_{n1} = 0.0466$ and $C_{n1} = 0.16$ ($M = 2$) and $L_{n1} = 0.0148$ and $C_{n1} = 0.06$ ($M = 6$).
- Transmission-line electrical path of $Z_2 = Z_0\sqrt{2}$ and $\theta_2(fd) = 450°$: $L_{n2} = 0.0932$ and $C_{n2} = 0.08$ ($M = 2$) and $L_{n2} = 0.0296$ and $C_{n2} = 0.029$ ($M = 6$).

Figure 5.7 corroborates the aforementioned trade-off between frequency response convergence and number of *LC* sub-cells, M, in the equivalent model. As observed, the highest agreement between the distributed circuit and its lumped-element equivalent is obtained for $M = 6$ in the represented spectral range.

Multi-stage and frequency-asymmetrical designs

As well known, signal-interference filters improve their filtering selectivity by means of multi-TFS-cascade arrangements. This can be extrapolated to the proposed Wilkinson-type filtering power dividers by inserting higher-order signal-interference filters into the divider arms that are formed by several cascaded transversal filtering cells instead of a single one. Figure 5.8 illustrates this principle in which the TFSs are assumed to be different with the purpose of simplifying the optimization process of the whole component. Moreover, resistors must be added between both branches at these connecting points between the TFSs and the cascading lines of characteristic impedance Z_m and electrical length θ_m that shape each branch.

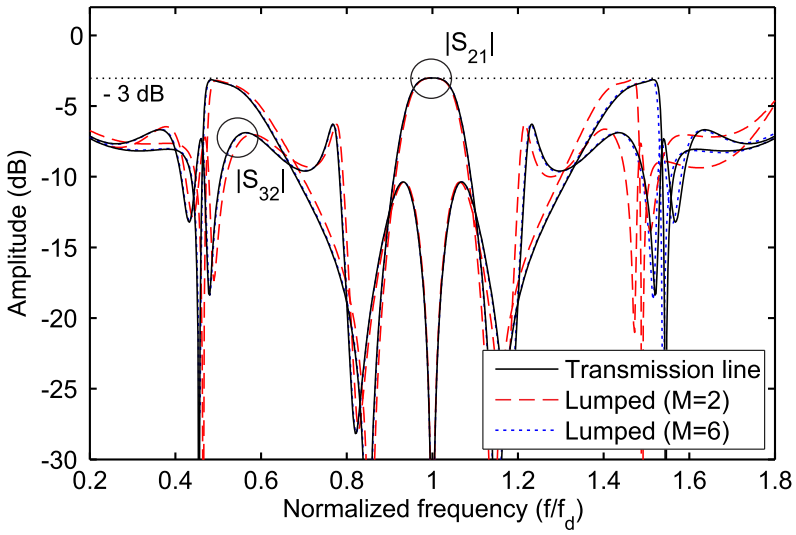

Figure 5.7: Power transmission ($|S_{21}|$) and isolation ($|S_{32}|$) responses of the ideal synthesized triple-band Wilkinson-type filtering power divider and its lumped-element approximation ($\theta(f_d) = 90°$, $M = 2$ and 6).

Through the latter, high power matching and output-isolation levels can be attained simultaneously at all its ports.

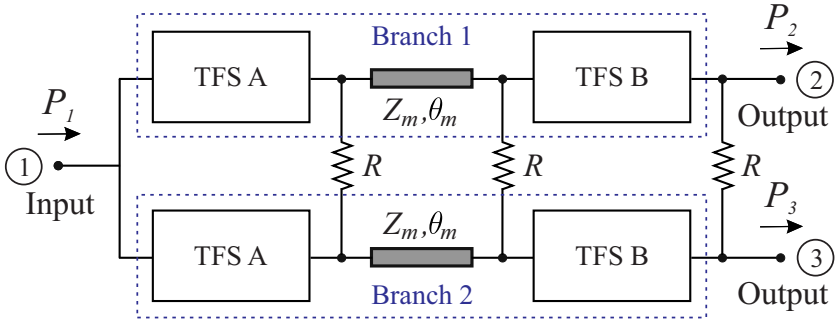

Figure 5.8: Schematic of two-stage 3-dB Wilkinson-type filtering power divider.

The S-parameters in amplitude for an ideal single-band example with a 3-dB relative bandwidth of 22% synthesized according to the circuit of Figure 5.8 are depicted in Figure 5.9. Although the equations and guidelines expounded in Section 5.1.1 were first considered in the design process, a final optimization of the whole device was necessary. Thus, a minimum input power matching and an output isolation level of 20 dB was set as optimization goal, whilst power matching levels for the output ports 2 and 3 above 15 dB were enforced. The resulting increase in filtering selectivity with regard to the single-stage device is remarkable. A 3-dB signal division throughout its full passband is also attained in accordance with the expected dual-function behavior.

As already mentioned, other class of signal-interference transversal cells can also be applied for the same purpose. For example, those reported in [18] and [30] so as to respectively feature power distribution with UWB single-band filtering—relative

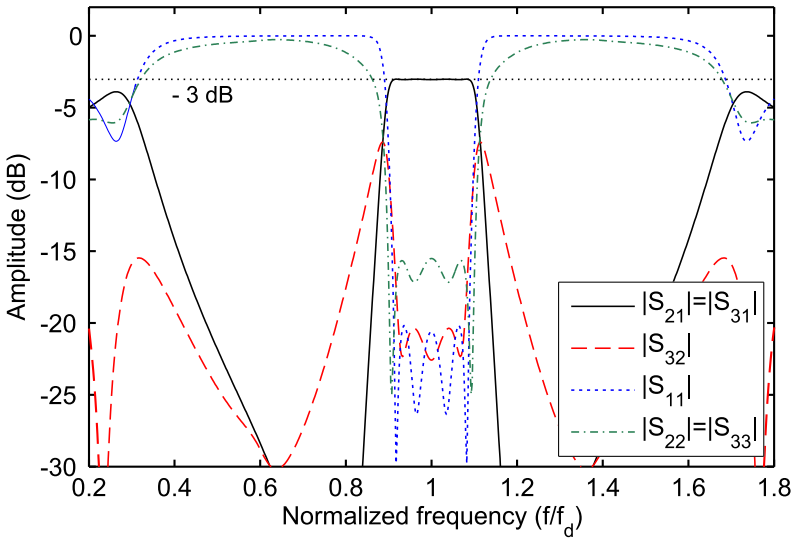

Figure 5.9: S-parameters in magnitude of the ideal synthesized two-stage bandpass 3-dB Wilkinson-type filtering power divider. Design values for TFS A: $Z_{1A} = 1.122Z_0$, $Z_{2A} = 2.026Z_0$, $\theta_{1A}(f_d) = 90°$, and $\theta_{2A}(f_d) = 270°$. Design values for TFS B: $Z_{1B} = 0.486Z_0$, $Z_{2B} = 0.846Z_0$, $\theta_{1B}(f_d) = 90°$, and $\theta_{2B}(f_d) = 270°$. Cascading line: $Z_m = 2.236Z_0$ and $\theta_m(f_d) = 90°$. Resistor: $R = 2Z_0$.

bandwidth greater than 100%—and dual-band filtering with strong spectral asymmetry between the dual passbands. In the former, the presence of coupled-line stages could hinder its extrapolation to pure-lumped-element-based implementations. In the latter, the arbitrary selection of the dual-band center frequencies and bandwidths could be constrained by the mandatory requisite of reasonable output-isolation and power-matching levels for all ports. For verification, Figure 5.11 plots the S-parameters in amplitude for an ideal synthesized 3-dB two-band Wilkinson-type filtering power divider with spectral asymmetry between passbands. This is attained through the insertion of the stepped-impedance-line TFS of Figure 5.10 into the arms of Figure 5.1(a)—the resulting design equations can be deduced by mixing equations (5.1)-(5.5) with those of the proposed circuit in Figure 1 of [30]—. As shown in Figure 5.11, the obtained results confirm the viability of the devised dual-function approach to meet a general set of specifications.

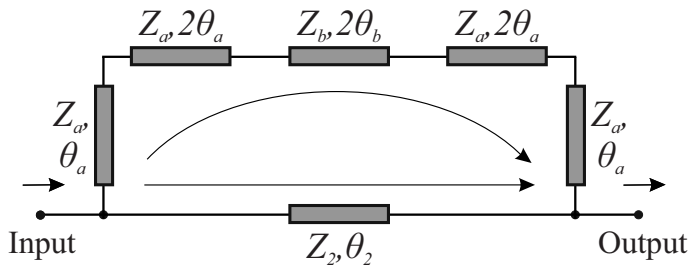

Figure 5.10: Schematic of stepped-impedance-line signal-interference TFS.

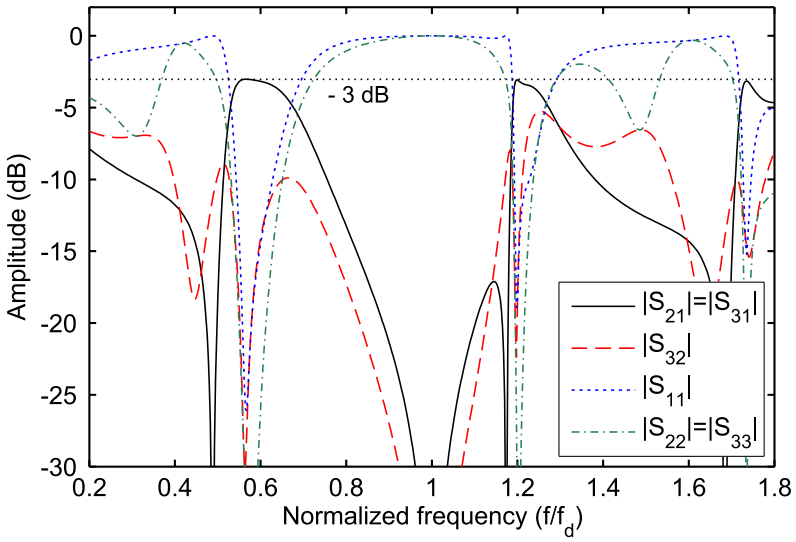

Figure 5.11: S-parameters in magnitude of the ideal synthesized spectrally-asymmetrical dual-band 3-dB Wilkinson-type filtering power divider. Design parameter values for the stepped-impedance-line TFS: $Z_a = (3\sqrt{2}/5)Z_0$, $Z_b = 11Z_0/(5\sqrt{2})$, $Z_2 = Z_0\sqrt{2}$, $\theta_a(f_d) = 69.12°$, $\theta_b(f_d) = 35°$, and $\theta_2(f_d) = 180°$. Resistor: $R = 2Z_0$.

5.1.2 Experimental results

With the purpose of proving the practical viability of this novel type of signal-interference single/multi-band Wilkinson-type filtering power divider architecture, three different 50-Ω-referred prototypes have been designed, constructed, and measured. They consists of a triple- and a quad-band microstrip circuit, and a dual-band circuit in lumped-element-based technology. Moreover, its usefulness as building blocks of more sophisticated RF/microwave components is corroborated through the fabrication and characterization of a two-branch channelized active BPF with enhanced selectivity.

For their implementation, it must be highlighted that:

- The microstrip substrate RO4003C *Rogers*^{TM} with the following parameters was used: relative dielectric permittivity $\varepsilon_r = 3.55$,, dielectric thickness $h = 1.52$ mm, dielectric loss tangent $\tan\delta_D = 0.0027$, and metal thickness $t = 35$ μm, [46]. Ground connections were implemented by means of 1-mm-diameter metallic via holes.

Regarding the design, simulation, and testing processes of these circuits, the following logistic media were utilized:

- Commercial software package *Advanced Design Systems*^{TM} of *Keysight Technologies*: circuit simulation and 2.5-D EM simulation by the Frequency-Domain MoM of all prototypes [74].

- E8361A network analyzer of *Agilent*^{TM}: measurements [75].

Prototype 1: Tri-band microstrip filter/divider

As first practical prototype, a triple-band Wilkinson-type power divider within the frequency range 1.3-4.7 GHz with symmetrical power division—i.e., $k = 1$—has been designed, fabricated, and characterized [124]. The values for the design parameters of the multi-band TFS embedded into both branches of the power divider are as follows ($Z_0 = 50\ \Omega$, $f_d = 3$ GHz): $Z_1 = 35.35\ \Omega$, $Z_2 = 70.71\ \Omega$, $\theta_1(f_d) = 270^\circ$, and $\theta_2(f_d) = 450^\circ$. An additional transmission-line segment of characteristic impedance of 70.71 Ω and electrical length of 90° at the design frequency f_d was attached at the input/output ports of the multi-band filtering cells to make easier their connection between elements in the whole power divider. These connecting lines must not be confused with the external quarter-wavelength transformers needed at the output ports of the power splitter for asymmetrical power-division realizations, as it was outlined in Section 5.1.1. Moreover, the mandatory offset condition of ±90° between the phase transmission responses of the two branches of the power divider at their multi-band operational frequencies is satisfied. These lines also cause a slight variation of the output-power-isolation and power-matching levels for those operative frequencies which are more separated from f_d. Thus, the output-power-isolation and power-matching requisites at all ports can be met at the same time. For this ideal design, the triple-band operative frequencies are exactly 1.6, 3, and 4.4 GHz, which give rise to transmission bands with 3-dB absolute bandwidths of 430, 406, and 430 MHz, respectively. The layout and a photograph of the built prototype are shown in Figure 5.12. A 100-Ω isolation resistor model ERA-3AEB101V from *Panasonic* was utilized between the output ports.

The ideal theoretical, simulated, and measured S-parameters in magnitude of the triple-band Wilkinson-type power-distribution circuit are depicted in Figure 5.13. As observed, apart from some narrowing effect and in-band insertion-loss increase of the third passband—due to factors such as the added sub-miniature version A (SMA) connectors or more-than-expected radiation loss—, the agreement obtained between predicted and experimental results is close enough to validate this configuration of multi-band Wilkinson-type filtering power divider.

Prototype 2: Quad-band microstrip filter/divider

The second design example is a microstrip filtering/power-division circuit with four-band response within the spectral range 1-5 GHz—i.e., $f_d = 3$ GHz—and symmetrical power distribution between its outputs ports—i.e., $k = 1$— [125]. After applying the formulas (5.1)-(5.5) for $Z_0 = 50\ \Omega$, $f_d = 3$ GHz, $N = 4$, and $k = 1$ ($Z_2 = 2Z_1$ is assumed for the degree of freedom to meet a certain bandwidth specification, as it was detailed in Section 5.1.1), the following values are obtained for the design parameters of the signal-interference TFS to be embedded into its arms: $Z_1 = 35.35\ \Omega$, $Z_2 = 70.71\ \Omega$, $\theta_1(f_d) = 360^\circ$, $\theta_2(f_d) = 540^\circ$, and $R = 100\ \Omega$. To make the connection process of the quad-band filtering sections at their input nodes and with the 100-Ω resistor at their output terminals easier, two additional transmission-line segments with characteristic impedance $Z_c = 70.71\ \Omega$ and electrical length of $\theta_c(f_d) = 90^\circ$ were inserted at these points—these lines are different from

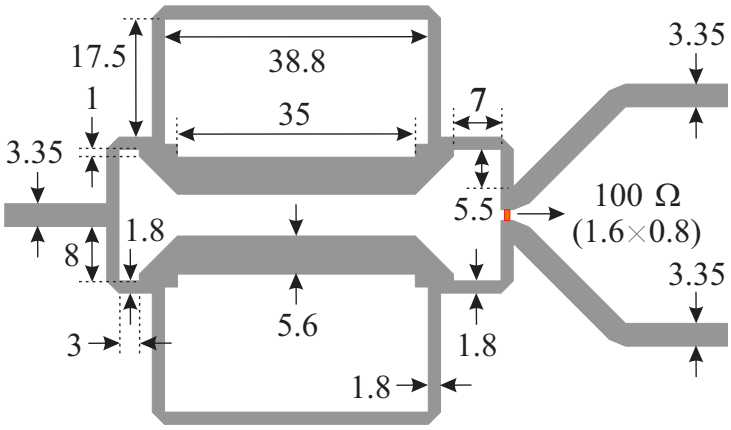

(a) Layout (non-redundant dimensions, in mm, are indicated).

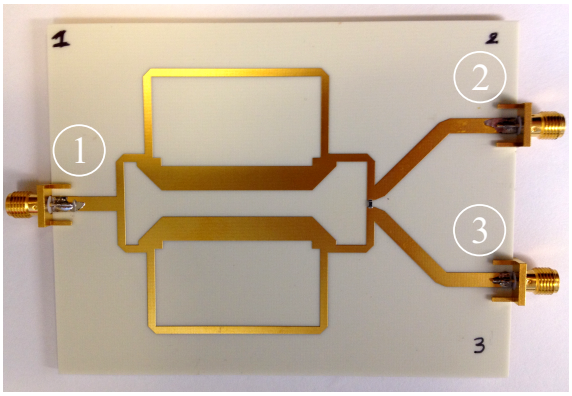

(b) Photograph (microstrip substrate: RO4003C of *Rogers*).

Figure 5.12: Layout and photograph of the manufactured triple-band Wilkinson-type filtering power divider (prototype 1) [124].

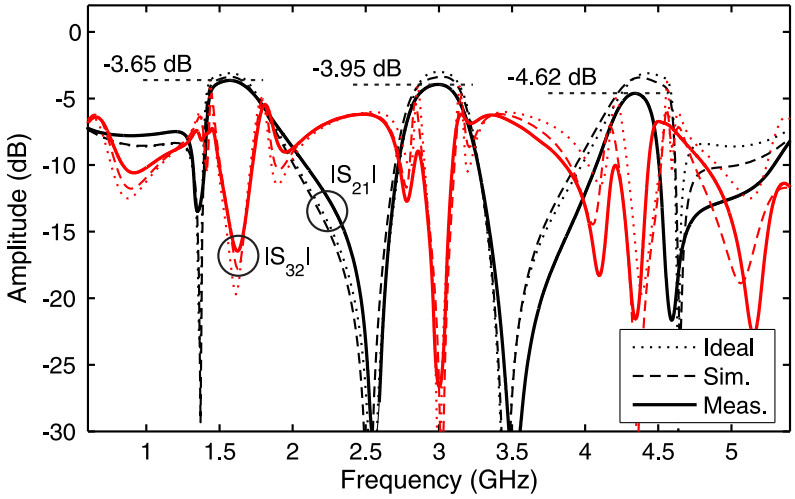

(a) $|S_{21}|$ and $|S_{32}|$.

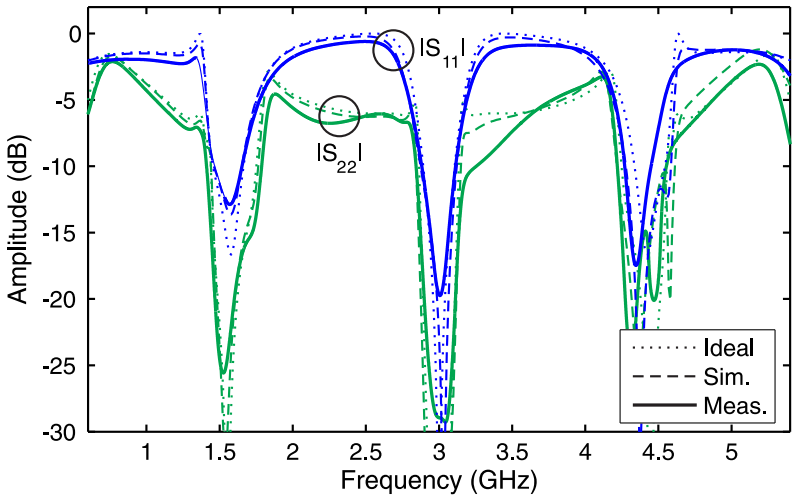

(b) $|S_{11}|$ and $|S_{22}|$.

Figure 5.13: Ideal theoretical, EM-simulated, and measured S-parameters in magnitude of the manufactured microstrip triple-band Wilkinson-type filtering power divider prototype [124].

the external transformers required at the output ports in case of asymmetrical power distribution, as explained before—. Note that these lines preserve the required offset condition of ±90° between the phase transmission responses of both branches at their multiple operative frequencies. Once again, these lines produce an unwanted small spectral deviation of the operative frequencies—that could be counteracted through the technique in [30]—and a slight variation of the output-power-isolation and power-matching levels. Nevertheless, reasonable levels for the power isolation and matching parameters at all ports can be achieved at the same time. For this ideal design, the center frequencies of the lower-to-upper passbands are 1.32, 2.44, 3.56, and 4.68 GHz and their 3-dB absolute bandwidths are 360, 332, 332, and 360 MHz, respectively. The layout and a photograph of the manufactured microstrip quad-band Wilkinson-type filter/power-divider prototype are shown in Figure 5.14. A 100-Ω resistor model ERA-3AEB101V from Panasonic was employed to isolate the output ports.

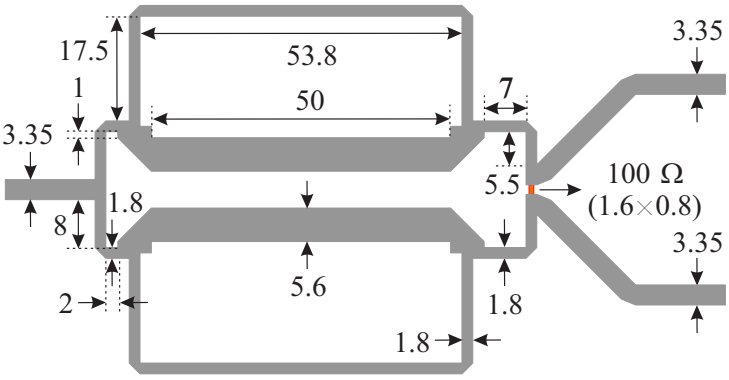

(a) Layout (non-redundant dimensions, in mm, are indicated).

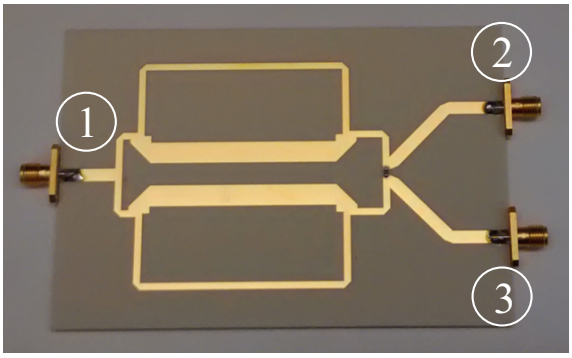

(b) Photograph (microstrip substrate: RO4003C of *Rogers*).

Figure 5.14: Layout and photograph of the manufactured quad-band Wilkinson-type filtering power divider (prototype 2) [125].

The ideal theoretical, simulated, and measured S-parameters in magnitude of the quad-band Wilkinson-type filtering power-distribution circuit are depicted in Figure

5.15. As in prototype 1, some discrepancies are observed between the simulated and measured results in terms of power insertion-loss increase and a transfer-function spectral narrowing that is more noticeable in the upper passbands. This is due to higher-than-expected radiation-loss levels and the effect of the SMA connectors used for circuit characterization. Nevertheless, the agreement obtained between predicted and experimental results is again close enough to verify the concept.

Prototype 3: Dual-band lumped-element filter/divider

As third proof-of-concept prototype, the development of a lumped-element filtering/power-splitting circuit showing a symmetrical power-division action—i.e., $k = 1$—between its two output nodes has been carried out. Its transfer function between the input access and each output port was synthesized to exhibit a dual-passband filtering profile within the spectral interval of 0.2-0.6 GHz—i.e., $f_d = 0.4$ GHz—. Firstly, the fully distributed-element realization was obtained after applying the equations (5.1)-(5.5) for $Z_0 = 50\ \Omega$, $f_d = 0.4$ GHz, $N = 2$, and $k = 1$—$Z_2 = 1.9Z_1$ is assumed for the degree of freedom in this case—. Then, the lumped-element approach is adopted by considering the replacement of each quarter-wavelength-at-f_d transmission-line segment with two LC T-type sections, so as to avoid an excessive number of components. Thus, the ideal values for their inductors and capacitors were calculated by using (5.6) for $\theta(f_d) = 90^\circ$ and $M = 2$. As in the two previous examples, two transmission-line segments with characteristic impedance $Z_c = 70.71\ \Omega$ and electrical length $\theta_c(f_d) = 90^\circ$ were added at the input/output terminals of the signal-interference sections to alleviate the inter-connection complexity. The obtained theoretical values for the L and C elements forming the ideal dual-band filtering/power-dividing device are as follows:

- Embedded signal-interference TFS: four T-type LC cells of $L_1 = 5.51$ nH and $C_1 = 8.41$ pF (transmission-line electrical path of $Z_1 = 33.46\ \Omega$ and $\theta_1(f_d) = 180^\circ$) and eight T-type LC cells of $L_2 = 10.46$ nH and $C_2 = 4.43$ pF (transmission-line electrical path of $Z_2 = 63.5\ \Omega$ and $\theta_1(f_d) = 360^\circ$).
- Inter-connecting lines ($Z_c = 70.71\ \Omega$ and $\theta_c(f_d) = 90^\circ$): two T-type LC cells of $L_c = 11.65$ nH and $C_c = 3.98$ pF.

For this ideal lumped-element design, the center frequencies of the lower and upper passbands are 0.282 and 0.513 GHz, whereas their 3-dB absolute bandwidths are 65 and 58 MHz, respectively.

Because a large amount of discrete elements are involved in this circuit, its design process was more tedious. Once the ideal design is synthesized, a new post-design iteration is necessary to take into account the available nominal values for commercial lumped components and their measured S-parameters files given by the manufacturers, as well as the effect of the microstrip footprints—short-line sections to solder the discrete elements—and the metallic via holes for grounding. It is worth mentioning that, when possible, pairs of adjacent inductors were grouped into one to further reduce the number of required discrete elements. The layout and a photograph of the manufactured lumped-element dual-band Wilkinson-type

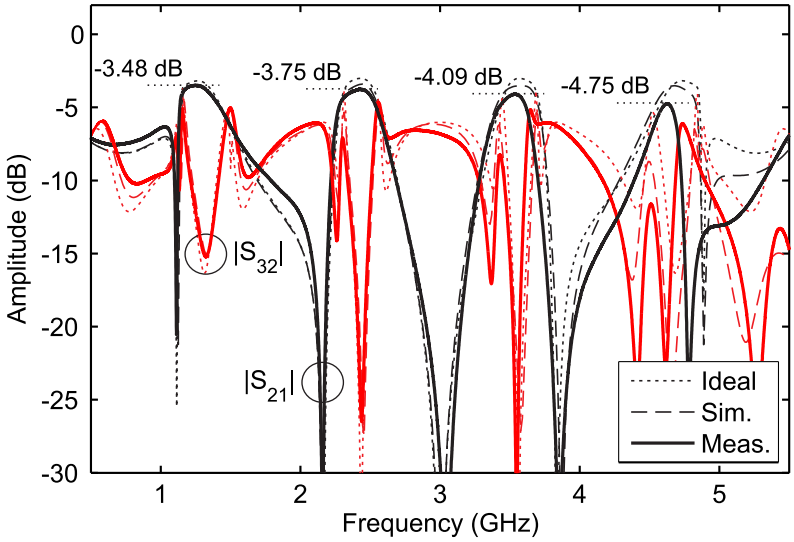

(a) $|S_{21}|$ and $|S_{32}|$.

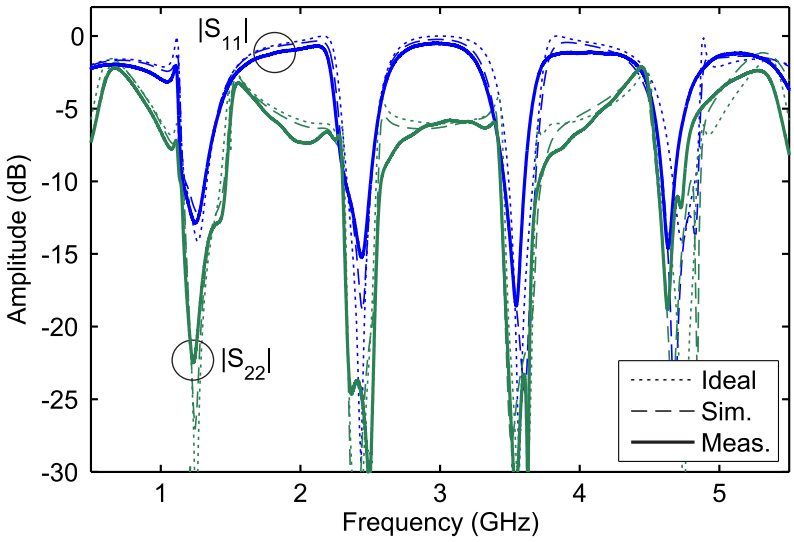

(b) $|S_{11}|$ and $|S_{22}|$.

Figure 5.15: Ideal theoretical, EM-simulated, and measured S-parameters in magnitude of the manufactured microstrip quad-band Wilkinson-type filtering power divider prototype [125].

filter/power-divider prototype are shown in Figure 5.16. The values of the associated commercial components selected for its lumped elements are listed in Table 5.1.

Table 5.1: Components for the manufactured lumped-element dual-band filter/divider prototype

Element	Value	Manufacturer	Part Number	Q_{min} at f_d [a]
L_1	5.6 nH	Coilcraft	0805HQ-5N6XJLB	53.2
L_1'	12 nH	Coilcraft	0805HQ-12NXJLB	55.8
L_2	12 nH	Coilcraft	0805HQ-12NXJLB	55.8
L_2'	22 nH	Coilcraft	0805HT-22NTJLB	49.6
L_c	16 nH	Coilcraft	0805HQ-16NXJLB	70.5
L_c'	20 nH	Coilcraft	0805HQ-20NXJLB	69.1
C_1	6.8 pF	Johanson Tech.	R15C6R8	1000
C_2	3.6 pF	Johanson Tech.	R15C3R6	1000
C_c	2.7 pF	Johanson Tech.	R15C2R7	1000
R	100 Ω	Panasonic	ERA6AEB101V	—

[a] Q_{min} at f_d ($f_d = 0.4$ GHz): minimum quality factor (exact values extracted for the inductors from the S-parameter files given by the manufacturer and estimated values in the case of the capacitors from the curves available in the datasheet).

Figure 5.17 depicts the ideal theoretical, simulated, and measured S-parameters of the lumped-element dual-band filter/power-divider circuit. Its measured amplitude and phase imbalance responses between the output terminals 2 and 3 are expected to be more critical in this case due to the large number of soldered discrete components and associated assembly tolerances. Again, the agreement obtained between the simulation and the measurements is sufficiently close to verify the suitability of the devised dual-functionality circuit for discrete-element-based realizations. Some minor discrepancies appear consisting in a small frequency shift of the overall transfer function to the lower spectral region and a bandwidth reduction for the upper band. The latter is a common effect in multi-band signal-interference circuits, that can be attributed to the frequency-dependency of the losses, which have a stronger influence on the signal-combination action taking place at the higher frequency side [12].

Prototype 4: Channelized active bandpass filter

The aim of this final design example is to prove the potential of the devised filtering/power-splitting configuration to improve the operational features and reduce the occupied size of more sophisticated RF/microwave filtering devices. Specifically, it shows the application of the dual-function circuit described in this section as filtering signal-splitter/combiner in a two-branch channelized active BPF. Note that such circuit could also be viewed as a two-channel balanced microwave amplifier with added filtering capability.

As reviewed in Chapter 1, microwave channelized active BPFs were first proposed by C. Rauscher in [32] as an evolution of RF transversal active BPFs—such

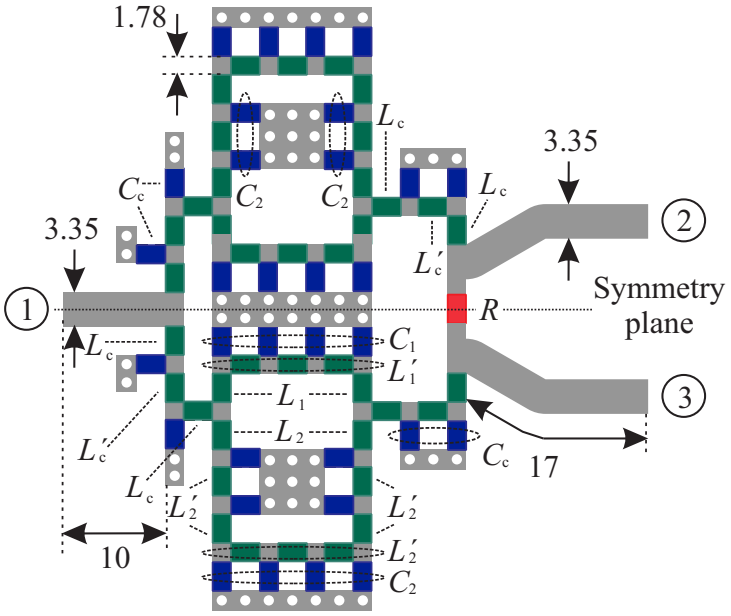

(a) Layout (non-redundant dimensions, in mm, are indicated).

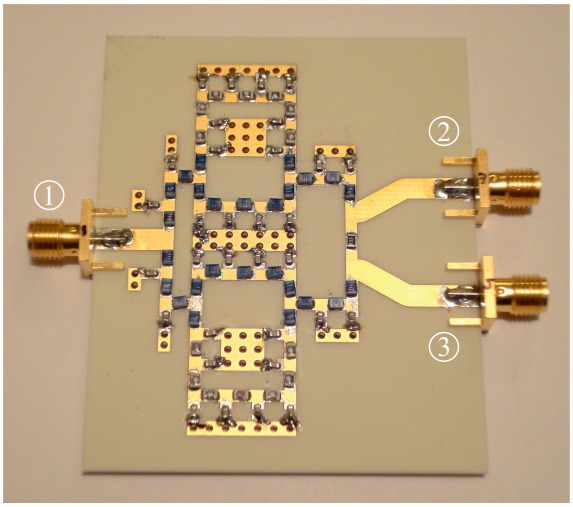

(b) Photograph (microstrip substrate: RO4003C of *Rogers*).

Figure 5.16: Layout and photograph of the manufactured lumped-element dual-band Wilkinson-type filtering power divider (prototype 3) [125].

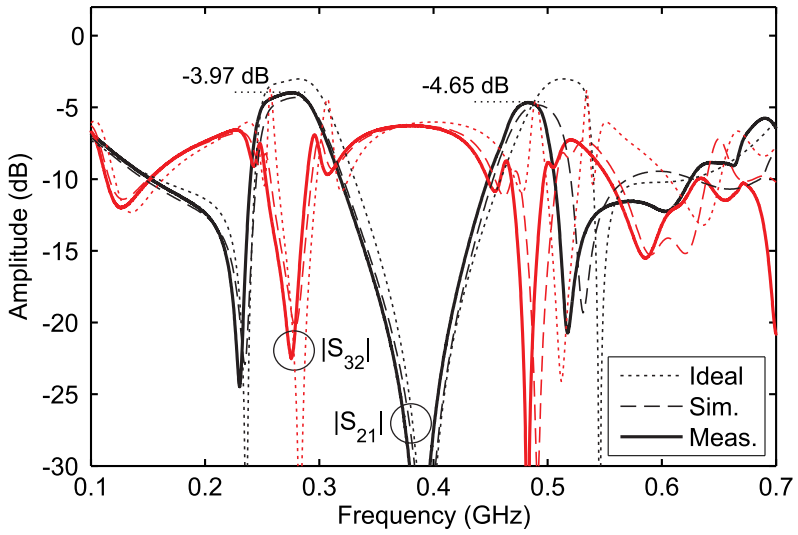

(a) $|S_{21}|$ and $|S_{32}|$.

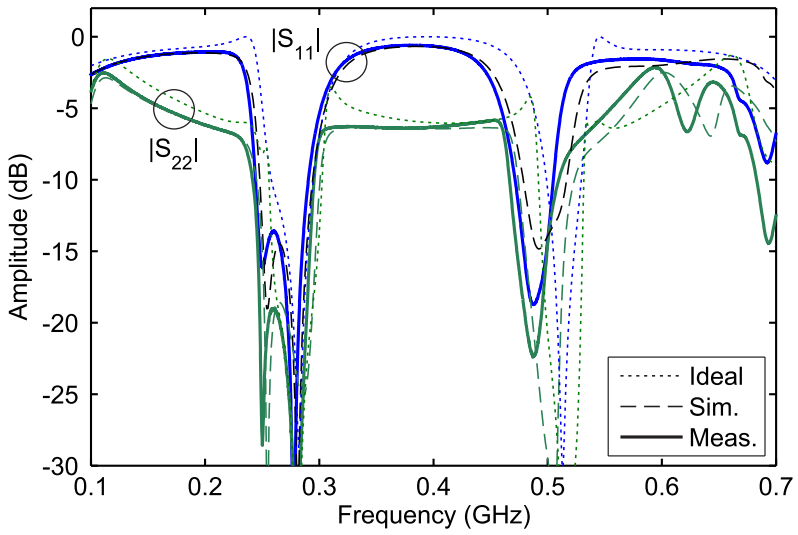

(b) $|S_{11}|$ and $|S_{22}|$.

Figure 5.17: Ideal theoretical, EM-simulated, and measured S-parameters in magnitude of the manufactured lumped-element dual-band Wilkinson-type filtering power divider prototype [125].

as those reported in [31] and [58]—with the purpose of attaining high-selectivity requirements without drastically raising the number of passive resonators—as well known, they can become bulky and lossy in fully-integrated platforms such as monolithic microwave integrated circuits (MMICs)—. This is done through a multi-path transversal network with diverse low-order filtering channels, each of them with different phase transmission responses, in which the selectivity enhancement stems from the inter-channel interference taking place at the output node of the whole structure. This interference must be constructive in the passband range and destructive in the out-of-band region to increase the stopband rejection levels and sharpness of the cut-off slopes through the generation of TZs.

An analytical methodology for the synthesis of channelized active BPFs in their two-branch version was reported in [117]. It consists of the combination of two channels with the same amplitude transmission response, as illustrated in the block diagram of Figure 5.18(a). The difference between their phase transmission responses is created by an extra transmission-line segment that acts as frequency-dependent delay block in one of its channels. The characteristic impedance of this line must be equal to the reference impedance level Z_0 and its electrical length $\theta(f_0) = 2n\pi\,(n \in \mathbb{N})$, where f_0 is the passband center frequency. Note that as a higher n value is selected, sharper cut-off slopes and more TZs are produced but at the expense of increased circuit size and lower power rejection enhancement in some spectral parts of the attenuated band. The idea behind this work is to substitute the classic 3-dB Wilkinson circuits that feature the power division/combination processes by the filtering counterparts described in this section, as depicted in Figure 17(a). Thus, the referred long delay line is no longer needed. Through this technique, a selectivity enhancement when compared to the classic approach—due to the interference action taking place inside the filtering divider/combiner—and reduced circuit size are simultaneously attained. This operating principle is illustrated in Figure 5.18(b).

For theoretical validation, Figure 5.19 shows the power transmission curve of an ideal synthesized Z_0-impedance-referred two-branch channelized BPF exhibiting a 3-dB relative bandwidth of 12.5% when considering 3-dB single-band Wilkinson-type filter/power-distribution circuits (i.e., $N = 1$, $k = 1$, and $f_d = f_0$) for $Z_2 = 2Z_1$, and including the inter-connection lines of characteristic impedance $Z_c = Z_0\sqrt{2}$ and electrical length $\theta_c(f_d) = 90°$. The specifications of the low-order (second-order) passive BPF of the parallel-coupled-line type [126] to be embedded into its channels was obtained by applying the design methodology of [117], resulting in a relative bandwidth of 5% referred to a ripple level of 0.026 dB. With the purpose of providing a comparison, the ideal power transmission response of the low-order filter and the new and conventional two-branch channelized BPFs for $n = 2$ and 3, respectively, are also depicted. Benefits to be highlighted for the new channelized approach are higher attenuation levels in most of the stopband range and the avoidance of the long delay line—length of 4π and 6π at f_0 for $n = 2$ and 3, respectively—of the transversal direction.

The ideal synthesized two-branch channelized BPF exploiting the new approach has been designed, manufactured, and tested for a center frequency $f_0 = 3$ GHz. A photograph of the developed prototype and the layout of the single-band Wilkinson-

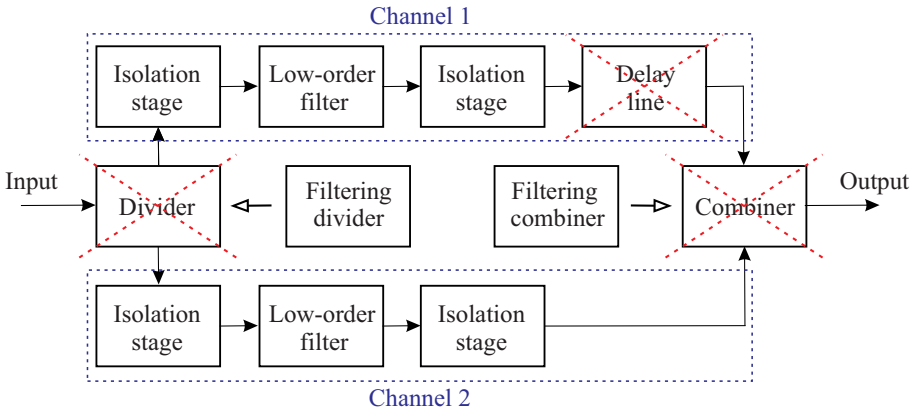

(a) Block diagram of the proposed approach.

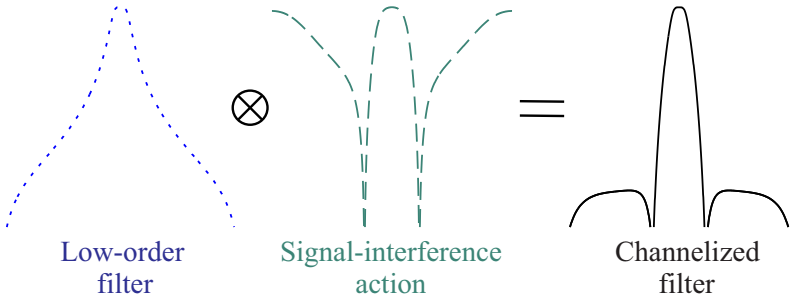

(b) Principle.

Figure 5.18: Two-branch channelized active BPF.

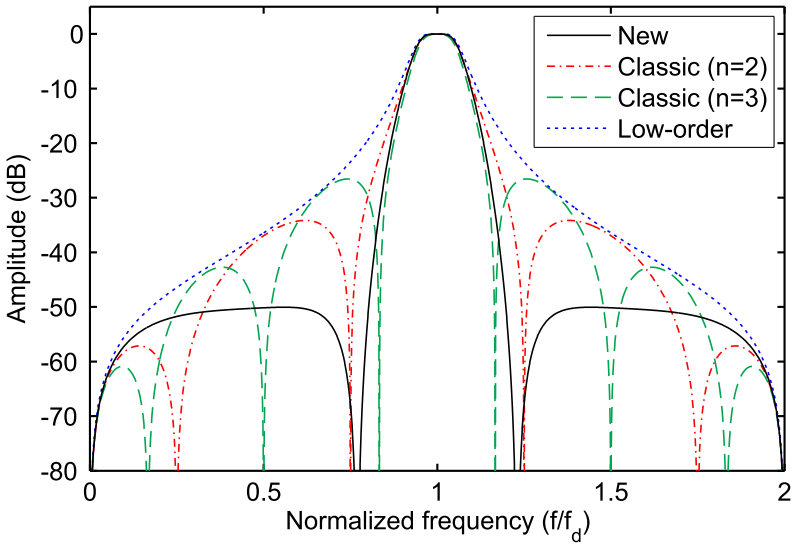

Figure 5.19: Ideal power transmission ($|S_{21}|$) response of the ideal synthesized channelized BPF based on the new and classic—$n = 2$ and 3—approaches along with the ideal transfer function of its low-order passive BPF.

type filter/power-divider device implementing its signal-splitting/combining stages are shown in Figure 5.20. For the isolation stages, a low-noise amplifier with low reverse power transmission—model RF3376 from *RFMD* [127]—and Π-type resistive attenuators of 4 dB at their input/output terminals were utilized.

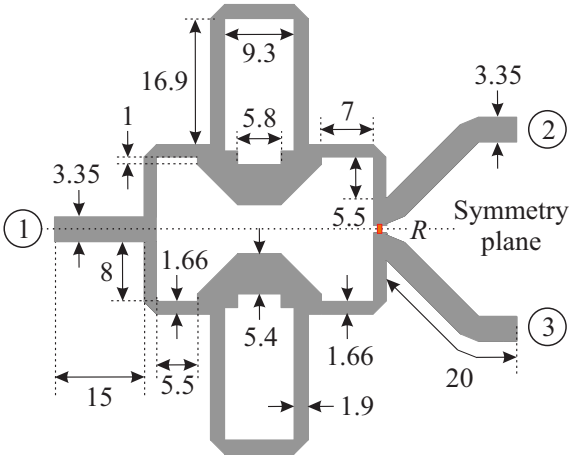

(a) Layout (non-redundant dimensions, in mm, are indicated).

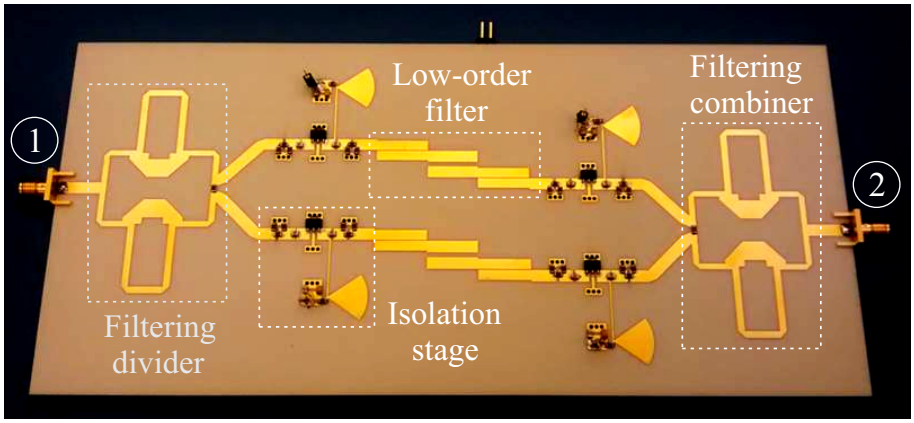

(b) Photograph (microstrip substrate: RO4003C of *Rogers*).

Figure 5.20: Layout of the single-band filter/power-dividing stage and photograph of the manufactured two-branch channelized active BPF (prototype 4) [125].

The measured power transmission, reflection, and reverse-isolation curves of the built two-branch channelized active BPF prototype and the power transmission curve of its constituent low-order filter are represented in Figure 5.21. As observed, a very similar behavior to that of the ideal design of Figure 5.19 is obtained, fully validating the concept.

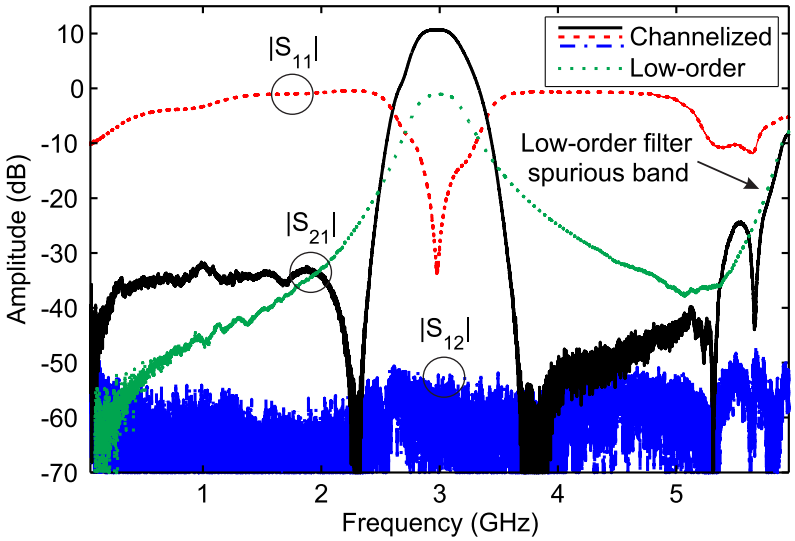

Figure 5.21: Measured power transmission ($|S_{21}|$), reflection ($|S_{11}|$), and reverse-isolation ($|S_{12}|$) curves of the manufactured channelized BPF prototype along with the measured power transmission response of its low-order coupled-line-type filter [125].

5.1.3 Comparison with state-of-the-art multi-band Wilkinson-type power dividers

Table 5.2 compares the new proposed multi-band Wilkinson-type power dividers with the most significant state-of-the-art approaches that have been recently reported [116], [118]-[122]. As can be seen, the implementation with the highest number of operative frequencies—four in total—has been realized using this new approach. As already stated, main benefits of it are its filtering capability and generation of multiple out-of-band TZs in order to isolate the operative frequencies unlike coupled-line-based designs. In addition, FBWs higher than 20% can be attained, which is more difficult to realize in coupled-line implementations. However, the design in [119] based on stub-loading techniques has a comparable FBW of 22.2%, whereas the one in [116] exhibits a much larger one of 94.2%. Nevertheless, when compared to the approach in [119], the new solution presents higher selectivity. On the other hand, the design in [116] relies on CRLH transmission-lines that leads to an increased design complexity. Indeed, the final implementation of the CRLH device is obtained by means of an optimization process in an EM simulator unlike the multi-band divider based on signal-interference techniques where design equations are provided. It is the latter along with its generalization to an arbitrary number of operative frequencies that make this approach a good candidate for a plurality of applications.

Table 5.2: Comparison of multi-band Wilkinson-type power dividers based on signal-interference techniques with state-of-the-art approaches.

Reference	Implementation	Number of operative frequencies	Operative frequencies (Ghz)	Filtering capability	Out-of-Band Transmission Zeros	FBW (%)	Additional In-band Insertion Loss (dB)	Valid for N passbands
A	Microstrip	3	1.6 3 4.4	Yes	Yes	26.9 13.5 9.8	0.65 0.95 1.62	Yes
B	Microstrip	4	1.24 2.34 3.54 4.63	Yes	Yes	30.7 14.6 8.9 5.1	0.48 0.75 1.09 1.75	Yes
C	Lumped Elements	2	0.276 0.483	Yes	Yes	22.1 8.9	0.97 1.65	Yes
[116]	Microstrip CRLH	2	1.89 6.675	Yes	Yes	94.2 12.9	0.5 0.5	No
[118]	Microstrip	3	0.9 1.17 2.43	No	No	– – –	≈ 2 ≈ 4 ≈ 5	No
[119]	Microstrip	2	1.8 5.8	Yes	Yes	22.2 10.0	0.27 0.87	No
[120]	Microstrip	2	0.9 2.45	No	No	– –	0.08 0.08	No
[121]	Microstrip	2	1.1 2.2	No	No	– –	0.15 0.19	No
[122]	Hybrid	2	0.5 2	No	No	– –	0.1 0.3	No

5.2 Single- and multi-band filtering impedance transformers

Impedance-matching networks are widely-used devices in RF/microwave systems. Their aim is to match a given impedance level to another prescribed one at a single frequency or over a frequency band, whose bandwidth depends on the final application. For example, the maximum power-transfer achievement between two blocks, the return loss optimization between an antenna and a low-noise amplifier, and the achievement of low-noise characteristics in active circuits [4].

A classic exponent of impedance-matching network is the quarter-wavelength transformer. Such a simple component allows to match any pair of real source and load impedances at a single frequency. Note also that it can be combined with other series or shunt reactive elements in case a complex load impedance needs to be matched. Moreover, it can be extended to multi-section designs for applications demanding more bandwidth than that attainable with a single quarter-wavelength stage.

In this section, dual-function microwave devices simultaneously providing filtering and impedance transformation between two different real impedances are presented. This means more flexibility when compared to classic resonator-based filters in which a transfer function is synthesized, under Butterworth or Chebyshev polynomials, but between two imposed equal real-valued source and load impedances—normally equal to 50 Ω—. Thus, the intrinsic power-matching action within the passband range can only be set for these specific impedance values, once the filter impedance level is fixed. With the aim of extending its applicability, [128] presents the generalization of this synthesis method to an arbitrary complex load impedance.

This section therefore concentrates on the development of impedance transformers with single/multi-band filtering capability between two real impedances for single- and multi-section versions by exploiting signal-interference principles. Specifically, quarter-wavelength transformers are replaced with signal-interference TFSs that are shaped by two in-parallel transmission-line segments. Owing to the feed-forward signal-energy iteration taking place between the two TFS electrical paths, high-selectivity filtering actions can be attained while preserving the impedance-transformation functionality.

5.2.1 Theoretical foundations

The concept behind the engineered generalized TFS that replaces a single transformer between arbitrary source (R_{in}) and load (R_L) real impedances is shown in Figure 5.22. As already said, this TFS is based on two transmission-line segments connected in parallel, whose design parameters are chosen according to [10] and [12] for single- and multi-band designs, respectively.

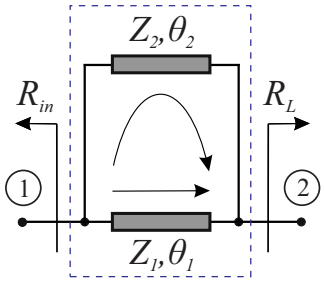

Figure 5.22: Signal-interference TFS for generalized input/output impedances.

Design equations

The design equations for the characteristic impedances Z_1 and Z_2 and the electrical lengths θ_1 and θ_2 of the impedance-transforming TFS have been derived in order to provide perfect matching between the external impedances R_{in} and R_L with spectral symmetry with regard to the design frequency, f_d. They are as follows:

- For the single-band case of [10]:

$$\theta_1(f_d) = N \times 90^\circ \qquad \theta_2(f_d) = (4N + M) \times 90^\circ \tag{5.7}$$

$$\frac{1}{Z_1} + \frac{1}{Z_2} = \frac{1}{Z_{ref}} \qquad Z_{ref} = \sqrt{R_{in} R_L} \tag{5.8}$$

- For the multi-band case of [12]:

$$\theta_1(f_d) = N \times 90^\circ \qquad \theta_2(f_d) = (N + 2) \times 90^\circ \tag{5.9}$$

$$\frac{1}{Z_1} - \frac{1}{Z_2} = \frac{1}{Z_{ref}} \qquad Z_{ref} = \sqrt{R_{in} R_L} \tag{5.10}$$

$$\{f_1, f_2, ..., f_N\} = \left\{ \frac{2P f_d}{N+1}, \quad P = 1, 2, ..., N \right\} \tag{5.11}$$

Here, $M, N \in \mathbb{N}$ and $f_1, f_2, ..., f_N$ are the center frequencies of the passbands. Note that multi-band responses can also be obtained for high values of the M and N indexes of equation (5.7) in the single-band case, whereas single-band transfer functions can be synthesized for $N = 1$ in the multi-band case with equation (5.9).

In order to illustrate the principle of such a dual-function device, Figure 5.23 plots the power transmission and the input-power-matching curves of two ideal synthesized examples of a triple-band TFS for $R_{in} = Z_0$ and $R_L = 2Z_0$ when the characteristic impedance Z_2 of equation (5.10) is equal to $Z_{ref}/2$ and $3Z_{ref}/2$, respectively. As can be seen, perfect power matching at those center frequencies given by equation (5.11) and simultaneous triple-band filtering actions with inter-band TZs are achieved. Moreover, it is demonstrated that broader passband widths are obtained as higher

values for the line impedance variables are considered. This is a common feature to its classic (i.e., 50-Ω referred) signal-interference filter counterpart.

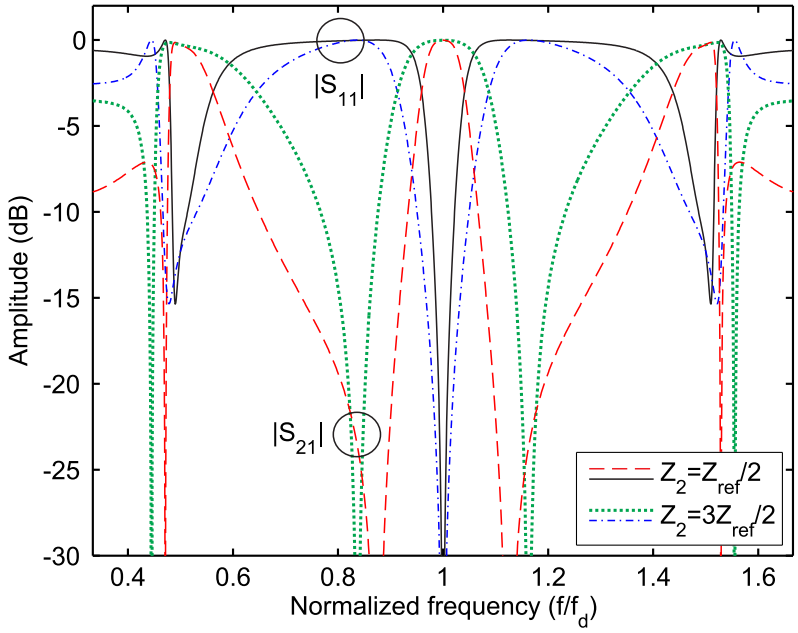

Figure 5.23: Power transmission ($|S_{21}|$) and reflection ($|S_{11}|$) responses of the ideal synthesized triple-band signal-interference TFSs for $R_{in} = Z_0$ and $R_L = 2Z_0$.

Multi-stage designs

When higher-order designs are required, a multi-section arrangement can be taken into account satisfying higher in-band power matching and out-of-band rejection levels. This design strategy is detailed in Figure 5.24, where the different TFSs must be properly scaled in impedance for the purpose of allowing the transition between R_{in} and R_L. Specifically, if the multiple TFSs were directly connected without cascading lines, the following design equations would be satisfied:

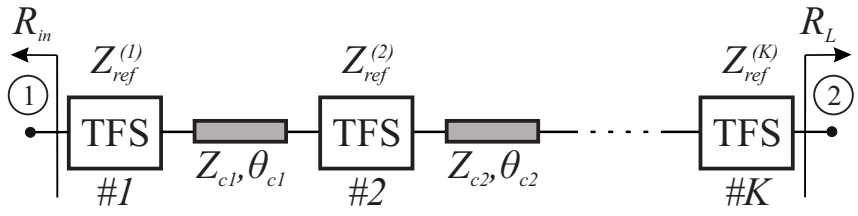

Figure 5.24: Multi-stage filtering impedance transformer with signal-interference TFSs

- For an odd K:

$$\frac{Z_{ref}^1}{Z_{ref}^2} \cdot \frac{Z_{ref}^3}{Z_{ref}^4} \cdot \ldots \cdot Z_{ref}^K = \sqrt{R_{in} R_L} \tag{5.12}$$

- For an even K:

$$\frac{Z_{ref}^{1}}{Z_{ref}^{2}} \cdot \frac{Z_{ref}^{3}}{Z_{ref}^{4}} \cdot ... \cdot \frac{Z_{ref}^{K-1}}{Z_{ref}^{K}} = \sqrt{\frac{R_{in}}{R_L}} \tag{5.13}$$

If the cascading lines were incorporated as illustrated in Figure 5.24, their electrical lengths should be an integer multiple of 90° at the design frequency f_d to preserve the spectral symmetry of the overall transfer function with regard to f_d. Note that in the case that these lines are odd multiples of 90°, their line impedances should be included in equations (5.12) and (5.13). Notwithstanding, an optimization process of the characteristic impedances of the whole network is necessary in order to improve the filtering selectivity and the power matching levels in all the operating bands, as proven in the following subsections.

5.2.2 Experimental results

To prove the practical viability of the devised technique, two different 50-Ω-referred prototypes have been synthesized, built, and characterized. They are a dual-band signal-interference filtering/impedance-transformation circuit and an UWB single-band prototype in microstrip technology, which both feature impedance-transformation ratios of 2:1. Concerning its manufacturing, it must be remarked that:

- The microstrip substrate RO4003C *Rogers*^{TM} with the following parameters was used: relative dielectric permittivity $\varepsilon_r = 3.55$,, dielectric thickness $h =$ 1.52 mm, dielectric loss tangent $\tan\delta_D = 0.0027$, and metal thickness $t = 35$ μm [46]. Ground connections were implemented by means of 1-mm-diameter metallic via holes.

- Commercial resistors PAT series from *Vishay Thin Film* are utilized as load resistance [129].

With relation to the design, simulation, and testing process, the following logistic media was employed:

- Commercial software package *Advanced Design Systems*^{TM} of *Keysight Technologies*: circuit simulation of both prototypes [74].

- Commercial software package *High Frequency Structure Simulator v10.0 (HFSS)* of *Ansoft*^{TM}: 3-D full-wave EM simulation by the FEM of both prototypes [48].

- E8361A network analyzer of *Agilent*^{TM}: measurements [75].

Prototype 1: dual-band filtering impedance transformer

The first prototype is a dual-band filtering impedance transformer with an input impedance $R_{in} = Z_0$=50 Ω and a load impedance $Z_L = 2Z_0 = 100$ Ω [130]. It was

ideally synthesized to show two passbands whose center frequencies are 2.05 and 3.95 GHz—i.e., $f_d = 3$ GHz—and their absolute bandwidths are 250 MHz with regard to a 20-dB input power-matching level —resulting in 12.2% and 6.3%, respectively, in relative terms.

In order to obtain an impedance transformation along with a highly-selective filtering action, the whole circuit was designed through the series-cascade connection of two dissimilar TFSs by means of a connecting line, as described in Section 5.2.1. Although the equations previously derived were considered in the design process, a final optimization of the full circuit structure was done to increase the in-band power-matching levels. Thus, the final design parameters of the ideal circuit—with $N = 2$ in equation (5.9)—are as follows:

- TFS 1: $Z_1 = 28.9\ \Omega$, $Z_2 = 63.4\ \Omega$, $\theta_1(f_d) = 180°$, and $\theta_2(f_d) = 360°$.
- TFS 2: $Z_1 = 45.3\ \Omega$, $Z_2 = 106.7\ \Omega$, $\theta_1(f_d) = 180°$, and $\theta_2(f_d) = 360°$.
- Cascading line: $Z_c = 65.7\ \Omega$, and $\theta_c(f_d) = 180°$.

The input power-matching and the power transmission curves between the two impedances R_{in} and R_L of the ideal synthesized dual-band filtering impedance transformer are drawn in Figure 5.25. As can be seen, the frequency specification mask is fulfilled and a third-order quasi-equirriple-type behavior is obtained in the bands of interest. It must be emphasized the presence of inter-band TZs at both sides of each passband and the attainment of sharp-rejection characteristic, which is an inherent feature of signal-interference filtering structures.

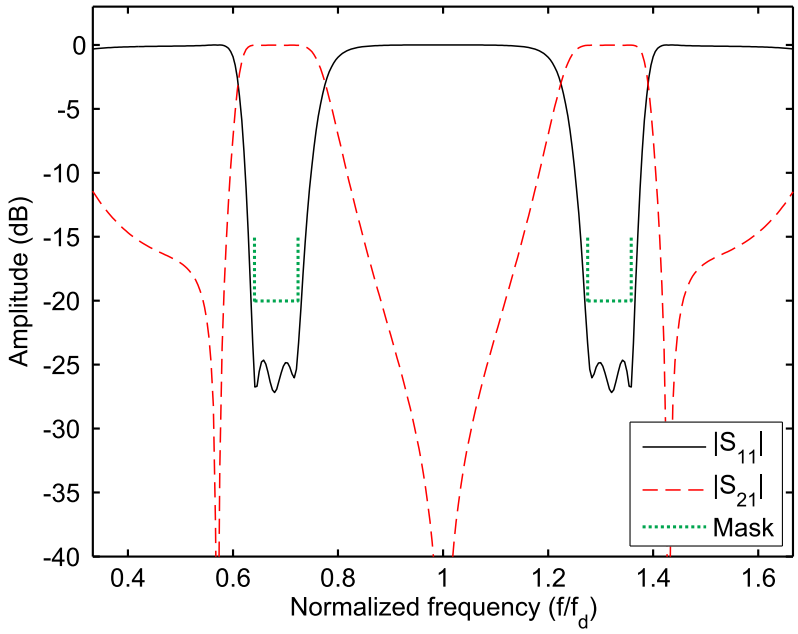

Figure 5.25: Power transmission ($|S_{21}|$) and reflection ($|S_{11}|$) responses—for $R_{in} = 50\ \Omega$ and $R_L = 25\ \Omega$—and prefixed input-power-matching mask of the ideal synthesized dual-band filtering impedance transformer [130].

The layout and a photograph of the built microstrip prototype of the dual-band filtering impedance transformer are presented in Figure 5.26. The simulated—both circuit-model and EM predictions—and the measured input-power-matching coefficients, in addition to its circuit-model simulated transfer function, are compared in Figure 5.27. As demonstrated, a fairly-close agreement between theoretical and experimental results is obtained, hence validating the practical suitability of the proposed technique.

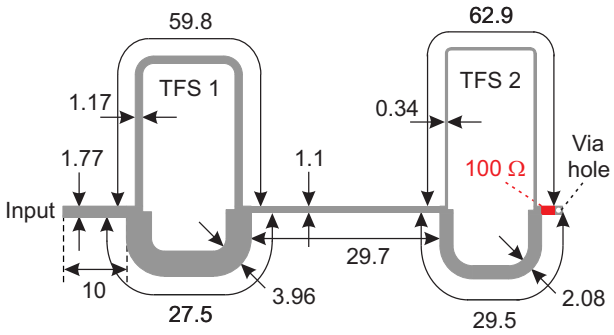

(a) Layout (non-redundant dimensions, in mm, are indicated).

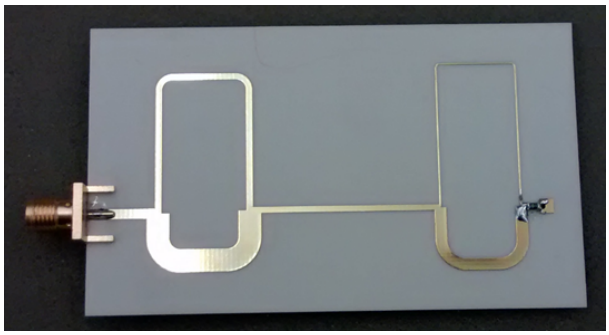

(b) Photograph (microstrip substrate: RO4003C of *Rogers*).

Figure 5.26: Layout and photograph of the manufactured microstrip dual-band filtering impedance transformer (prototype 1) [130].

Prototype 2: Ultra-wideband single-band filtering impedance transformer

As a second prototype, an UWB single-band filtering impedance transformer for an input impedance $R_{in} = Z_0 = 50\ \Omega$ and a load impedance $Z_L = Z_0/2 = 25\ \Omega$ is developed. In this case, the center frequency and the 20-dB-input-power-matching-level-referred absolute bandwidth for the ideal synthesized circuit were chosen to be 3 GHz—i.e., $f_d = 3$ GHz—and 1.1 GHz—resulting in a 36.7% bandwidth in relative terms—, respectively.

For this prototype, three dissimilar TFSs were cascaded, by means of two extra connecting lines. After applying the design guidelines of Section 5.2.1 and optimizing

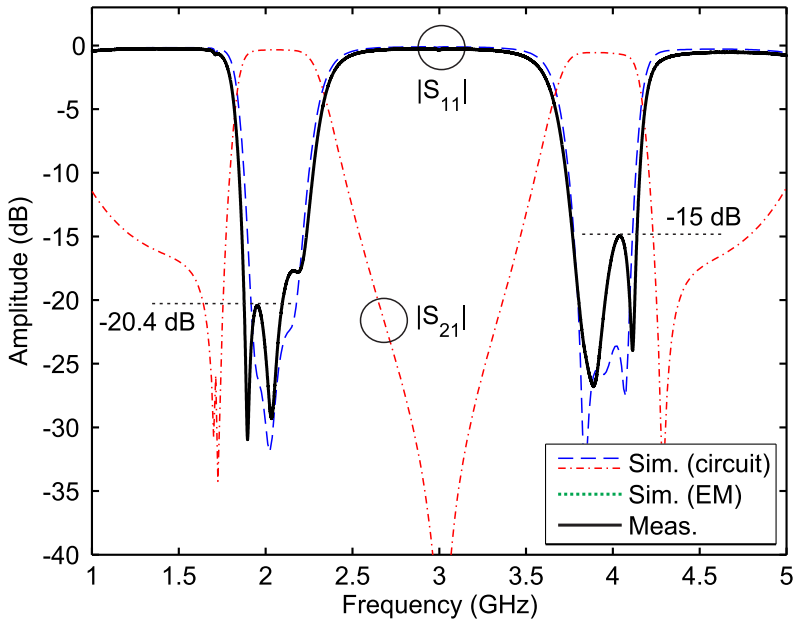

Figure 5.27: Simulated—circuit-model and EM— and measured power reflection responses ($|S_{11}|$) and simulated—circuit-model—power transmission response ($|S_{21}|$) of the manufactured microstrip dual-band filtering impedance transformer (prototype 1)—$R_{in} = 50\ \Omega$ and $R_L = 25\ \Omega$—, [130].

all the parameters of the circuit, the following values were obtained for its electrical variables—replacing $N = M = 1$ in equation (5.7)—:

- TFS 1: $Z_1 = 103\ \Omega$, $Z_2 = 97\ \Omega$, $\theta_1(f_d) = 90°$, and $\theta_2(f_d) = 450°$.
- TFS 2: $Z_1 = 89.7\ \Omega$, $Z_2 = 48.8\ \Omega$, $\theta_1(f_d) = 90°$, and $\theta_2(f_d) = 450°$.
- TFS 3: $Z_1 = 55.7\ \Omega$, $Z_2 = 46.6\ \Omega$, $\theta_1(f_d) = 90°$, and $\theta_2(f_d) = 450°$.
- Cascading line 1: $Z_{c1} = 39.5\ \Omega$ and $\theta_{c1}(f_d) = 270°$.
- Cascading line 2: $Z_{c2} = 27.1\ \Omega$ and $\theta_{c2}(f_d) = 270°$.

The input-power-reflection and power-transmission curves of the ideal synthesized UWB single-band filtering impedance transformer are plotted in Figure 5.28. As can be seen, the fixed power-matching requirements are satisfied. Once again, a sharp-rejection transfer function with multiple out-of-band TZs is attained, exhibiting a sixth-order quasi-equiripple-type passband in this case.

The layout and a photograph of the developed microstrip prototype of UWB single-band filtering impedance transformer are shown in Figure 5.29. The simulated —circuit-model and EM predictions—and the measured input-power-matching profiles, along with its circuit-model-based simulated power transmission response, are represented in Figure 5.30. In this case, as expected from the EM simulated results, the power-matching levels of the measured circuit suffer some deterioration in the passband. This can be caused by the the high number of poles within the passband

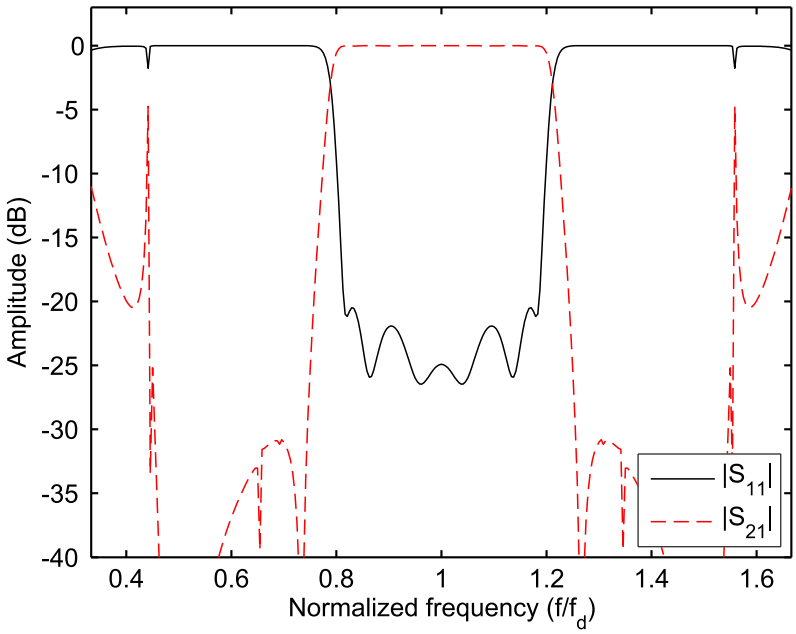

Figure 5.28: Power transmission ($|S_{21}|$) and reflection ($|S_{11}|$) response—for $R_{in} = 50\ \Omega$ and $R_L = 25\ \Omega$—and prefixed input-power-matching mask of the ideal synthesized UWB single-band filtering impedance transformer [130].

range, that makes its response more sensitive to undesired effects not contemplated by the circuit-model simulator and to manufacturing tolerances.

5.3 Single- and dual-band balanced bandpass filters

Although originally developed for low-frequency analog and digital devices, balanced circuits have gained a relevant significance in a wide range of RF/microwave applications in recent years. This comes as a result of the rapid development of mobile and wireless communication systems with more stringent requirements to be met. The key advantage of balanced circuits when compared to their single-ended counterparts is their higher immunity to electromagnetic interference (EMI) sources. These include external noise, crosstalk, coupled noise from adjacent circuitry, and environmental noise, among others [131]. Over the last years, a considerable effort has been specially put into the area of planar filter design based on balanced structures, coping with wideband-to-UWB requirements for single/dual-band operation [132]. In this context, high-selectivity and sharp-rejection capabilities when operating in the differential mode of operation, and high power rejection levels in the common mode of operation over the frequency band of interest are highly desired.

Numerous approaches regarding the design of single-band balanced BPFs have been proposed so far. For instance, one design methodology is the series-cascade connection of stub-loaded branch-line couplers to realize UWB filtering as presented in [133] and [134]. This type of configurations was slightly modified by embedding open-coupled-line stages into the arms of the couplers in [135] with the purpose of

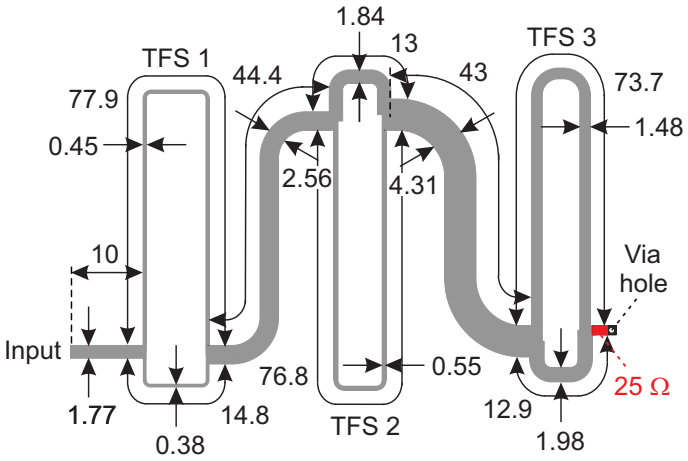

(a) Layout (non-redundant dimensions, in mm, are indicated).

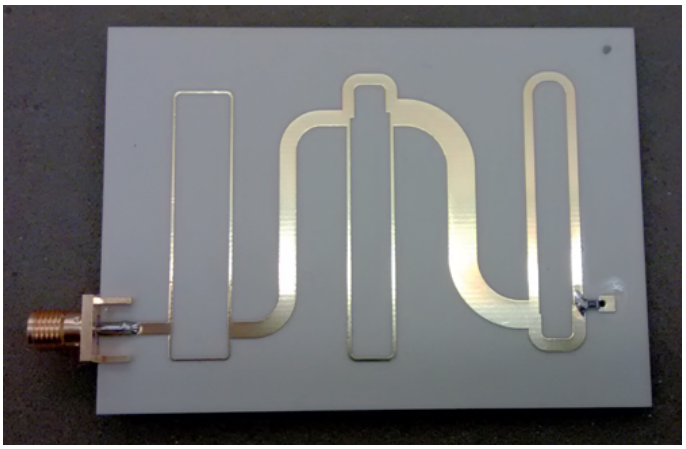

(b) Photograph (microstrip substrate: RO4003C of *Rogers*).

Figure 5.29: Layout and photograph of the manufactured microstrip UWB single-band filtering impedance transformer (prototype 2) [130].

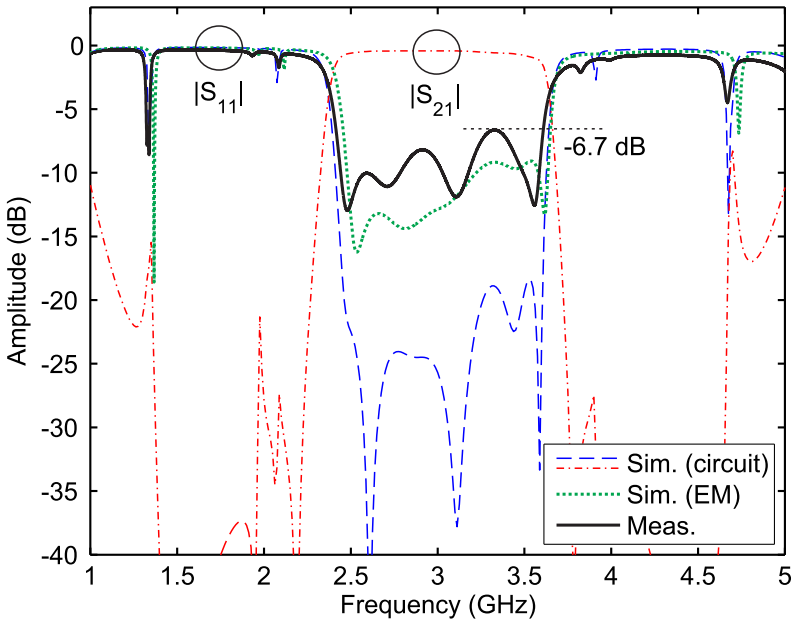

Figure 5.30: Simulated—circuit-model and EM— and measured reflection responses ($|S_{11}|$) and simulated—circuit-model—power transmission response ($|S_{21}|$) of the manufactured microstrip UWB single-band filtering impedance transformer (prototype 2)—$R_{in} = 50\ \Omega$ and $R_L = 25\ \Omega$— [130].

broadening the narrow stopbands that exist between the periodic replicas of their passbands. Yet another approach reported in [136] was the use of T-shaped structures that results in wider common-mode suppression and higher circuit compactness. But, nonetheless, the prevailing trend towards the design of single-band BPFs consists of multi-mode-resonator schemes. In this direction, balanced BPFs that show good performance in terms of TZ generation under differential-mode operation and high common-mode rejection have been addressed by using ring-resonator building blocks in [137]-[139]. In addition, balanced BPFs shaped by SIRs have been presented in [140]-[141] with high attenuation levels in the common mode of operation in the desired frequency band, but without close-to-band TZs in their differential-mode transfer functions. Also, single-band balanced BPFs based on transversal circuit networks have been recently suggested. Thus, UWB balanced BPFs were implemented in microstrip technology by means of 180° phase shifters and 360°-at-f_d transmission-line segments in [142]. In this line of work, double-sided parallel-stripline (DSPSL) balanced BPFs were fabricated with their subsequent size reduction as described in [143] and [144]. Nonetheless, the last three approaches exhibit moderate common-mode rejection—i.e., attenuation levels for the common-mode in the range 10-20 dB—within the spectral range of the differential-mode passband.

To a minor extent, some of the aforementioned techniques applied to single-band configurations have been also exploited in dual-band designs. For instance, topologies based on coupled-line sections were realized in [145] and [146] obtaining wideband common-mode suppression. On the other hand, the incorporation of SIRs into balanced structures has proven to have benefits in terms of high common-mode

rejection in both single- and double-layer substrates as shown in [147] and [148]. However, it must be remarked that these designs can hardly be extrapolated to BPFs with more than two passbands and, in some cases, are sensitive to fabrication tolerances owing to its physical conformation with coupled-line stages and lumped elements.

This section is therefore aimed at the design of single/dual-band balanced BPFs by embedding signal-interference TFSs into the two identical parts of a balanced circuit. This is translated into the simultaneous attainment of high-selectivity and sharp-rejection capabilities in the differential-mode transfer function and high in-band attenuation levels for their common mode of operation. Note that the engineered approach outperforms most of the related prior-art configurations in terms of in-band common-mode rejection levels. Besides, low in-band insertion-loss levels under differential-mode operation and higher robustness to fabrication deviations owing to the absence of coupled-line stages are observed. In particular, the well-known bi-path signal-interference TFS of [10] and [12] is utilized for demonstration purposes.

5.3.1 Theoretical foundations

In a balanced circuit, complementary signals—those that share the same amplitude with a 180° phase difference—are transmitted by a pair of terminals. Thus, a balanced filter can be seen as a differential two-port or single-ended four-port network as illustrated in Figure 5.31, where nodes 1 and 2 are paired as the differential input port and nodes 3 and 4 constitute the differential output port.

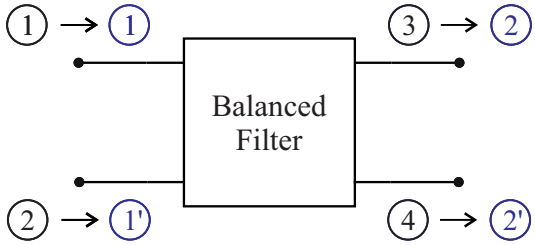

Figure 5.31: Balanced filter: differential two-port or single-ended four-port network.

Therefore, the full characterization of balanced filters cannot be made by single-ended S-parameters. It needs for the so-called mixed-mode S-parameters [149]. The transformation between single-ended and mixed-mode S-parameters is given according to the following equations:

$$S_{dd} = \frac{1}{2}\begin{bmatrix} S_{dd}^{11} = (S_{11} - S_{12} - S_{21} + S_{22}) & S_{dd}^{12} = (S_{13} - S_{14} - S_{23} + S_{24}) \\ S_{dd}^{21} = (S_{31} + S_{32} - S_{41} + S_{42}) & S_{dd}^{22} = (S_{33} - S_{34} - S_{43} + S_{44}) \end{bmatrix} \tag{5.14}$$

$$S_{dc} = \frac{1}{2}\begin{bmatrix} S_{dc}^{11} = (S_{11} + S_{12} - S_{21} - S_{22}) & S_{dc}^{12} = (S_{13} + S_{14} - S_{23} - S_{24}) \\ S_{dc}^{21} = (S_{31} + S_{32} - S_{41} - S_{42}) & S_{dc}^{22} = (S_{33} + S_{34} - S_{43} - S_{44}) \end{bmatrix} \tag{5.15}$$

$$S_{cd} = \frac{1}{2}\begin{bmatrix} S_{cd}^{11} = (S_{11} - S_{12} + S_{21} - S_{22}) & S_{cd}^{12} = (S_{13} - S_{14} + S_{23} - S_{24}) \\ S_{cd}^{21} = (S_{31} - S_{32} + S_{41} - S_{42}) & S_{cd}^{22} = (S_{33} - S_{34} + S_{43} - S_{44}) \end{bmatrix} \quad (5.16)$$

$$S_{cc} = \frac{1}{2}\begin{bmatrix} S_{cc}^{11} = (S_{11} + S_{12} + S_{21} + S_{22}) & S_{cc}^{12} = (S_{13} + S_{14} + S_{23} + S_{24}) \\ S_{cc}^{21} = (S_{31} + S_{32} + S_{41} + S_{42}) & S_{cc}^{22} = (S_{33} + S_{34} + S_{43} + S_{44}) \end{bmatrix} \quad (5.17)$$

where S_{dd}^{21} and S_{dd}^{11} are the power transmission and reflection responses under differential-mode operation, and S_{cc}^{21} and S_{cc}^{11} are those for its common mode of operation. The other sub-matrices S_{dc} and S_{cd} represent the conversion from differential-mode to common-mode operation and vice versa.

Signal-interference balanced filter

The engineered balanced circuit consists of two identical halves that are formed by a signal-interference TFS and two shunt 90°-at-f_d transmission-line segments with characteristic impedances equal to Z_{s1} and Z_{s2}, as illustrated in Figure 5.32. Note that for further increasing in-band power matching levels, two additional 90°-at-f_d transmission-line segments with characteristic impedances Z_{m1} and Z_{m2} are connected to the input/output ports of the whole balanced filter. Moreover, any class of signal-interference TFS can be utilized as building block in this design methodology.

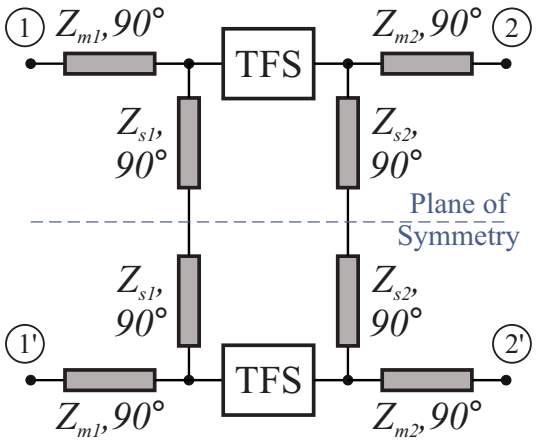

Figure 5.32: Engineered balanced BPF with embedded signal-interference TFS (the values of the electrical lengths are calculated at the design frequency f_d).

The functional principles of the balanced BPF illustrated in Figure 5.32 can be summarized as follows:

- The in-band characteristics of the whole balanced BPF under differential-mode operation are practically those inherited to the embedded signal-interference TFS. The filtering action is then defined by the in-band constructive and out-of-band destructive signal-energy interactions taking place between the different electrical paths of the signal-interference TFS.

- In the differential mode of operation, a virtual ground is created in the plane of symmetry. This allows to cancel the signal power transmission at the even harmonics of f_d. This is a substantial improvement in terms of filtering capability when compared to the transfer function of the building signal-interference TFS.

- When operating in common mode, a TZ is created at f_d owing to the virtually-open-circuited stubs. It should be remarked that such stubs can be physically-short-circuited to enhance the common-mode power rejection levels.

Figure 5.33 presents an illustrative example of the proposed balanced BPF concept. In particular, it shows the power transmission and reflection responses in the differential and common modes of operation for a synthesis example of an ideal single-band balanced BPF along with those of its signal-interference TFS. This building TFS is formed by two different in-parallel transmission-line segments—as the signal-interference TFS of Figure 1 in [10]—where the values of its design parameters have been chosen as follows (Z_0 is the reference impedance): $Z_1 = Z_2 = 2Z_0$ and $m = n = 1$. Loading stubs with characteristic impedances $Z_{s1} = Z_{s2} = 2Z_0/3$ are selected. Moreover, with the aim of further increasing the in-band power attenuation levels under common-mode operation, a physical ground is placed at the connection point of the stubs with a characteristic impedance Z_{s1}. As observed in Figure 5.33, a signal-interference filtering action that exhibits higher selectivity than that of its embedded signal-interference TFS is obtained for differential mode.

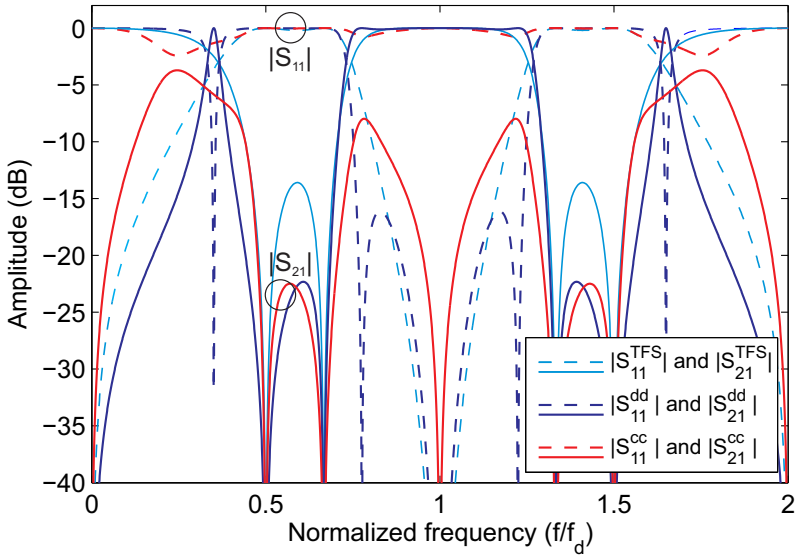

Figure 5.33: Ideal power transmission ($|S_{21}|$) and reflection ($|S_{11}|$) responses of the differential and common modes of a synthesized example of the balanced BPF circuit in Figure 5.32 and $|S_{21}|$ and $|S_{11}|$ coefficients of its embedded signal-interference TFS.

Multi-TFS-cascaded designs

As already mentioned in this Ph.D. Thesis, the series-cascade connection of multiple TFSs leads to increased sharpness of the cut-off slopes, amplitude flatness, and out-of-band power rejection levels of the overall filter transfer function. This technique can also be applied to balanced filter configurations. As an example, a two-stage design is presented in Figure 5.34, where a T-shaped inter-TFS cascading network shaped by three 90°-at-f_d transmission-line segments—whose characteristic impedances are Z_{casc} and Z_{s3}—is utilized. It must be remarked that these TFSs are designed to be different—i.e., showing a spectral offset of their passbands—. Its purpose is to generate more out-of-band TZs at distinct frequency locations within the interval $[0, 2f_d]$ and, hence, further extend the stopband bandwidths and rejection levels in the differential mode of operation.

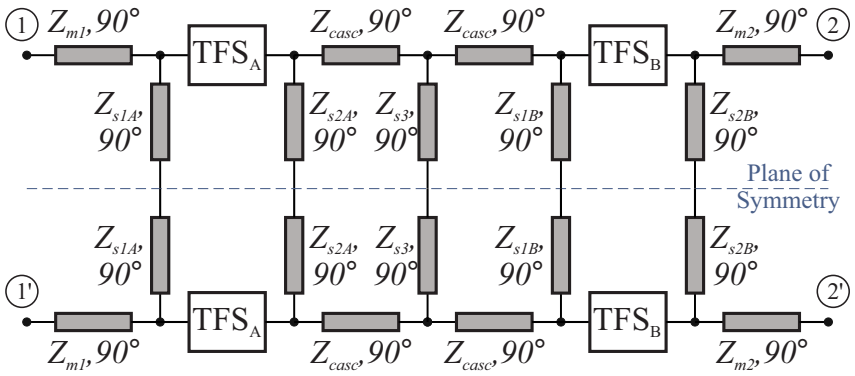

Figure 5.34: Two-TFS series-cascaded balanced BPF with embedded signal-interference TFS.

To better illustrate the aforementioned selectivity-enhancement technique in signal-interference differential-mode BPFs, two synthesis examples are shown hereafter for a given reference impedance Z_0.

The first synthesis example consists of a single-band balanced BPF. It was synthesized to exhibit 25-dB-input-power-matching-level-referred relative bandwidth of 14.5% around f_d in the differential mode of operation and a 64.3-dB attenuation-level-referred relative bandwidth of 48.5% in the common mode of operation. The optimized values for its design parameters are chosen as follows:

- TFS A: bi-path signal-interference TFS of Figure 2 in [12] with $Z_{1A} = 0.5Z_0$, $Z_{2A} = Z_0$, $\theta_{1A}(f_d) = 90°$, and $\theta_{2A}(f_d) = 270°$.
- TFS B: bi-path signal-interference TFS of Figure 1 in [10] with $Z_{1B} = 2.106Z_0$, $Z_{2B} = 1.9Z_0$, $\theta_{1B}(f_d) = 90°$, and $\theta_{2B}(f_d) = 450°$.
- Loading stubs: $Z_{s1A} = Z_{s2A} = Z_{s1B} = 0.5Z_0$ and $Z_{s2B} = 1.4Z_0$. Stubs 1A and 2B are physically short-circuited.
- Cascading network: $Z_{casc} = 2.1Z_0$ and $Z_{s3} = 0.5Z_0$.
- Matching input/output lines: $Z_{m1} = Z_{m2} = 0.88Z_0$.

Figure 5.35 shows the ideal power transmission and reflection responses in the differential and common modes of operation for the synthesized single-band balanced BPF along with the power transmission coefficients of its constituent signal-interference TFSs. As shown, the use of dissimilar TFSs gives rise to six close-to-passband TZs. Note also that, as previously mentioned, there is no signal transmission in the even harmonic frequencies of f_d. Besides, a minimum 28.5-dB out-of-band power rejection level for the stopbands is achieved for its differential mode of operation.

The second synthesis example corresponds to a dual-band balanced BPF. It was designed to show two passbands whose center frequencies are $0.7f_d$ and $1.3f_d$ and their 15-dB-input-power-matching-level-referred relative bandwidths are equal to 12.5% and 6.7%, respectively, in its differential-mode transfer function. A minimum common-mode power-attenuation level of 33 dB is obtained over the spectral range from $0.61f_d$ to $1.39f_d$. The optimized values for its design parameters are as follows:

- TFS A: bi-path signal-interference TFS of Figure 2 in [12] with $Z_{1A} = 0.5Z_0$, $Z_{2A} = 0.7Z_0$, $\theta_{1A}(f_d) = 180°$, and $\theta_{2A}(f_d) = 360°$.
- TFS B: bi-path signal-interference TFS of Figure 2 in [12] with $Z_{1B} = 0.758Z_0$, $Z_{2B} = 1.816Z_0$, $\theta_{1B}(f_d) = 180°$, and $\theta_{2B}(f_d) = 360°$.
- Loading stubs: $Z_{s1A} = 1.46Z_0$, $Z_{s2A} = 0.72Z_0$, $Z_{s1B} = 0.662Z_0$, and $Z_{s2B} = 0.522Z_0$.
- Cascading network: $Z_{casc} = Z_0$ and $Z_{s3} = 0.56Z_0$. Stub 3 is physically short-circuited.
- Matching input/output lines: $Z_{m1} = 1.208Z_0$ and $Z_{m2} = 0.65Z_0$.

The ideal power transmission and reflection responses of the synthesized dual-band balanced BPF for the differential and the common modes of operation, along with the power transmission coefficients of its constituent signal-interference TFSs, are depicted in Figure 5.36. As can be seen, two TZs are created at the lower and upper sides of the lower and upper passbands, respectively, whereas inter-band TZs are also generated at f_d. As previously expounded, additional TZs located at DC and $2f_d$ are created. Also, out-of-band power rejection levels above 15 dB for the lower and upper stopbands are obtained.

5.3.2 Experimental results

To prove the practical viability of the proposed balanced BPF design methodology based on embedded signal-interference TFSs, a 50-Ω-referred single-band BPF prototype has been synthesized, manufactured, and characterized. In relation to the design, fabrication, and testing processes of this circuit, it must be remarked that:

- The microstrip substrate RO4003C *Rogers*^{TM} with the following parameters was utilized: relative dielectric permittivity $\varepsilon_r = 3.55$, dielectric thickness $h =$ 1.52 mm, dielectric loss tangent $\tan\delta_D = 0.0027$, and metal thickness $t = 35$

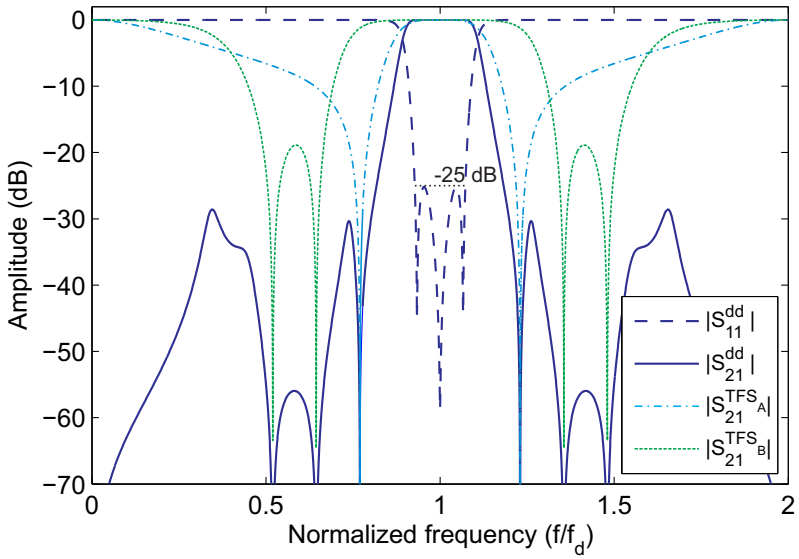

(a) Overall balanced BPF in differential mode ($|S_{21}^{dd}|$ and $|S_{11}^{dd}|$) and building single TFSs ($|S_{21}^{TFS_A}|$ and $|S_{21}^{TFS_B}|$).

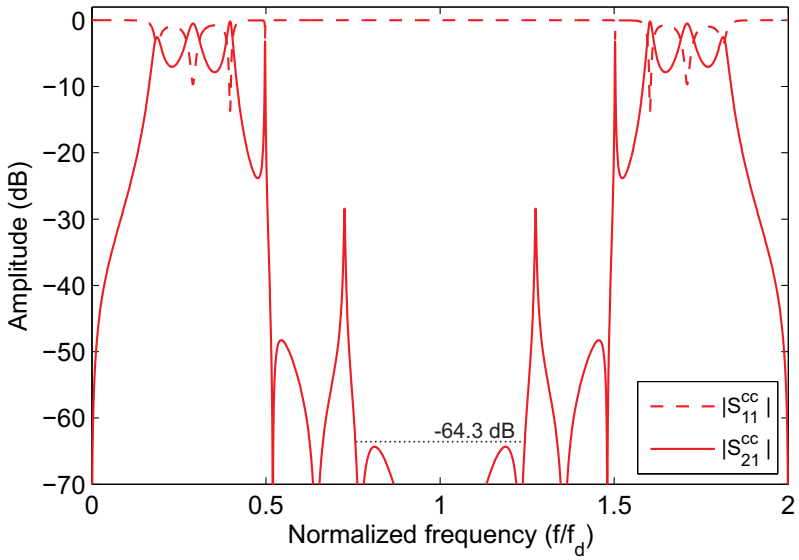

(b) Overall balanced BPF in common mode ($|S_{21}^{cc}|$ and $|S_{11}^{cc}|$).

Figure 5.35: Ideal power transmission ($|S_{21}|$) and reflection ($|S_{11}|$) responses of an example two-TFS single-band balanced BPF in differential and common modes and $|S_{21}|$ coefficients of its building signal-interference TFSs.

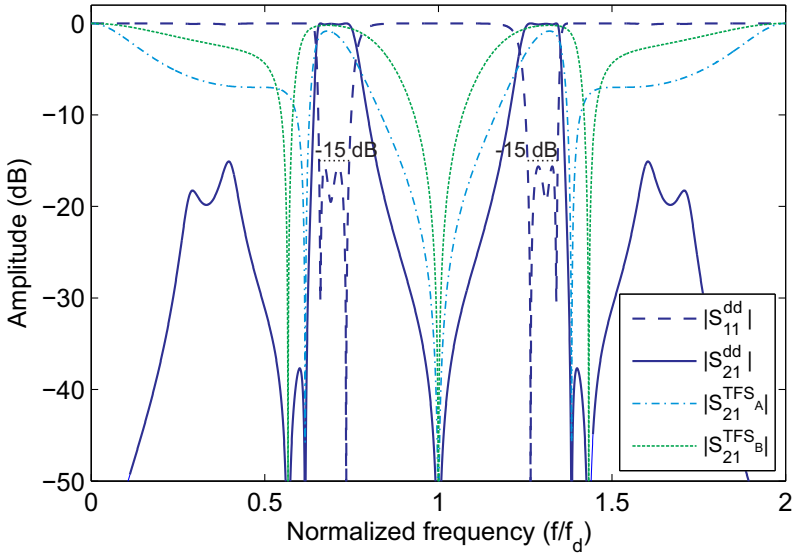

(a) Overall balanced BPF in differential mode ($|S_{21}^{dd}|$ and $|S_{11}^{dd}|$) and and building single TFSs ($|S_{21}^{TFS_A}|$ and $|S_{21}^{TFS_B}|$).

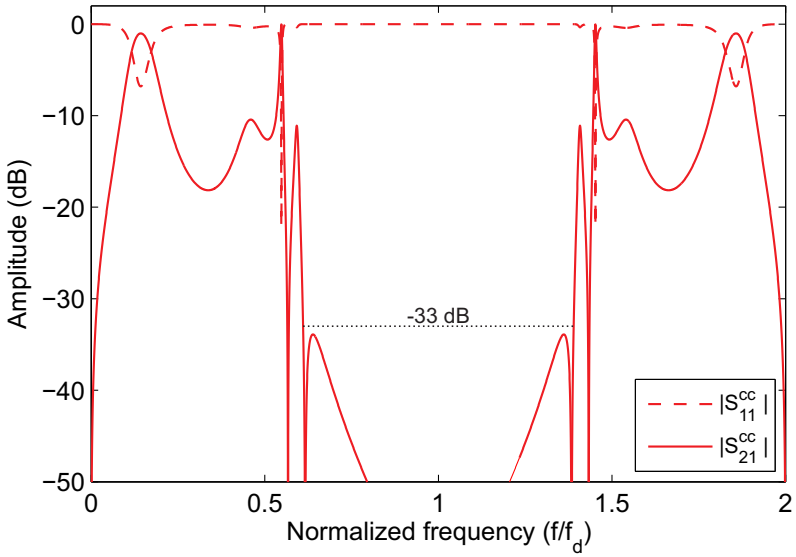

(b) Overall balanced BPF in common mode ($|S_{21}^{cc}|$ and $|S_{11}^{cc}|$).

Figure 5.36: Ideal power transmission ($|S_{21}|$) and reflection ($|S_{11}|$) responses of example of synthesized two-TFS balanced dual-band BPF in differential and common modes and $|S_{21}|$ coefficients of its building signal-interference TFSs.

μm [46]. Ground connections were implemented by means of 0.8-mm-diameter metallic via holes.

- The commercial software package *Advanced Design Systems*^{TM} of *Keysight Technologies* was employed for the circuit and 2.5-D EM simulation by the Frequency-Domain MoM of the prototype [74].
- An E8361A network analyzer of *Agilent*^{TM} was utilized to carry out the measurements [75].

Prototype: Single-band balanced bandpass filter

The built prototype is the physical implementation of the previously-synthesized example of the two-stage single-band balanced BPF in Figure 5.35 for $Z_0 = 50\ \Omega$ and $f_d = 2$ GHz [150]. Its differential-mode transfer function was designed to ideally exhibit a 3-dB absolute bandwidth of 420 MHz—i.e., 23.6% in relative terms—and a 25-dB-input-power-matching-level-referred absolute bandwidth of 290 MHz, whereas a 64.3-dB-attenuation-level-referred absolute bandwidth of 970 MHz around 2 GHz is enforced for its common mode of operation. The layout and a photograph of the manufactured microstrip single-band balanced BPF prototype are shown in Figure 5.37.

The simulated—circuit model and EM predictions—and measured power transmission and reflection parameters of the manufactured prototype for the differential and the common modes of operation are depicted in Figure 5.38. As can be seen, a reasonable agreement is reached between EM simulated and experimental results, except for a slight frequency shift—measured center frequency of 1.93 GHz—and some deterioration of the in-band power matching levels that are higher than 9.4 dB in the differential mode of operation. These discrepancies can be attributed to some undesired effects that are not contemplated by the circuit simulator, such as substrate dispersion, unexpected radiation, and fabrication tolerances. A 3-dB absolute bandwidth of 338 MHz—i.e., 17.5% in relative terms—and out-of-band power rejection levels greater than 21.6 and 20.8 dB for the lower and the upper stopbands, respectively, are achieved. Moreover, multiple TZs are produced in the differential-mode transfer function. In addition, power attenuation levels higher than 49 dB are obtained in the frequency range from 1.32 to 2.20 GHz in the common mode of operation. It is worth mentioning that such high common-mode power-attenuation levels in the frequency band where the differential-mode passband is located are greater than those reached by most of the related prototypes that are available in the technical literature—in particular, they are comparable to the levels measured in the prototypes based on SIRs in [140] and [141], but showing the additional benefit of close-to-passband TZ generation in the differential mode of operation—.

To complete the full characterization of the manufactured prototype, the simulated and measured group-delay responses over the frequency range from 1.5 to 2.5 GHz in the differential mode of operation are compared in Figure 5.39. As observed, a fairly-close agreement is obtained between both curves. Besides, Figure 5.40 plots the common-to-differential-mode ($|S_{21}^{cd}|$) and the differential-to-common-mode ($|S_{21}^{dc}|$) conversion parameters in transmission, which are respectively lower

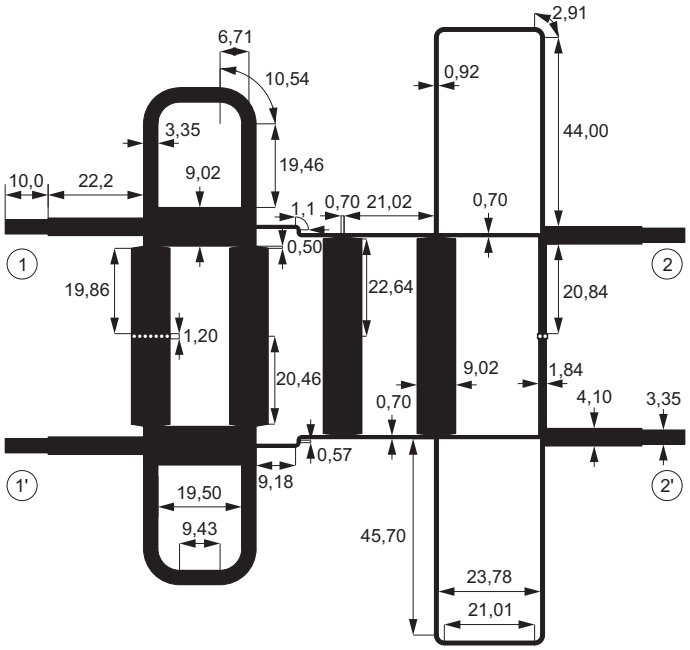

(a) Layout (non-redundant dimensions, in mm, are indicated).

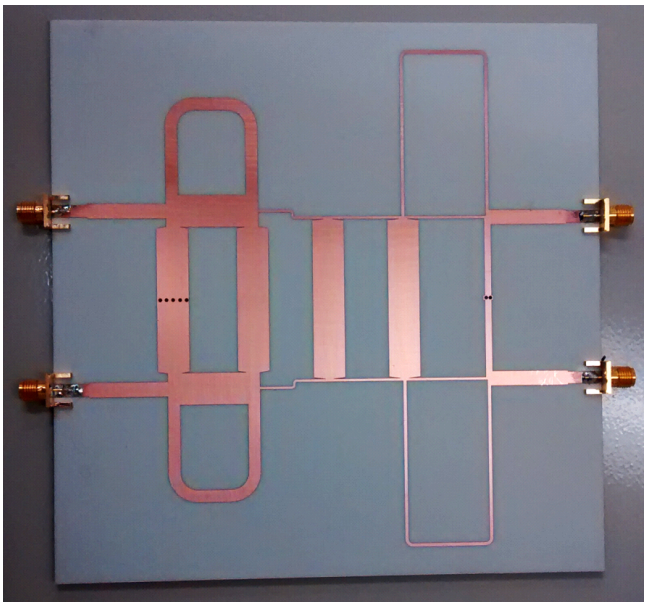

(b) Photograph (microstrip substrate: RO4003C of *Rogers*).

Figure 5.37: Layout and photograph of the manufactured microstrip balanced single-band BPF prototype [150].

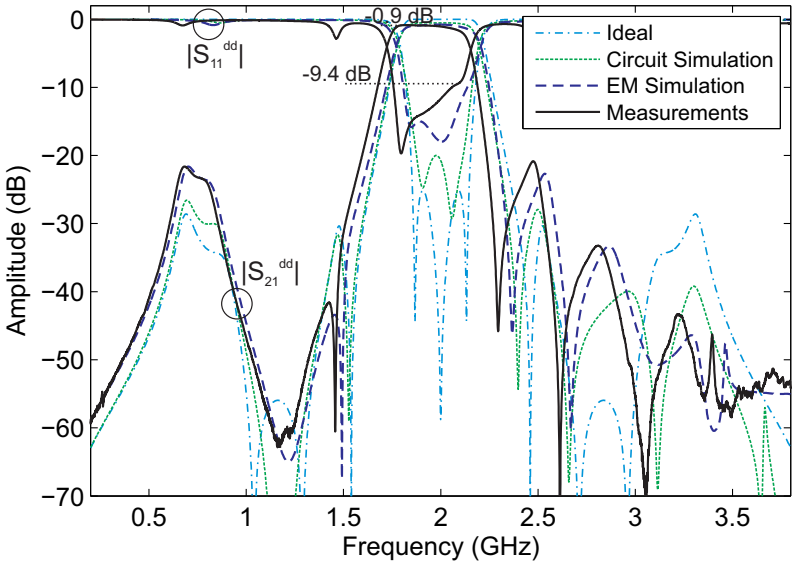

(a) Differential-mode parameters ($|S_{21}^{dd}|$ and $|S_{11}^{dd}|$).

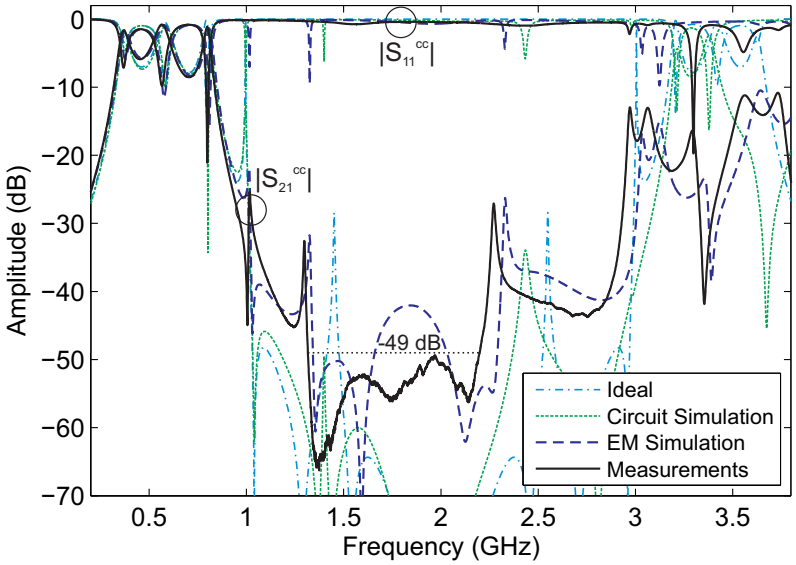

(b) Common-mode parameters ($|S_{21}^{cc}|$ and $|S_{11}^{cc}|$).

Figure 5.38: Ideal, simulated (circuit and EM model), and measured power transmission ($|S_{21}|$) and reflection ($|S_{11}|$) responses of the manufactured microstrip balanced single-band BPF prototype [150].

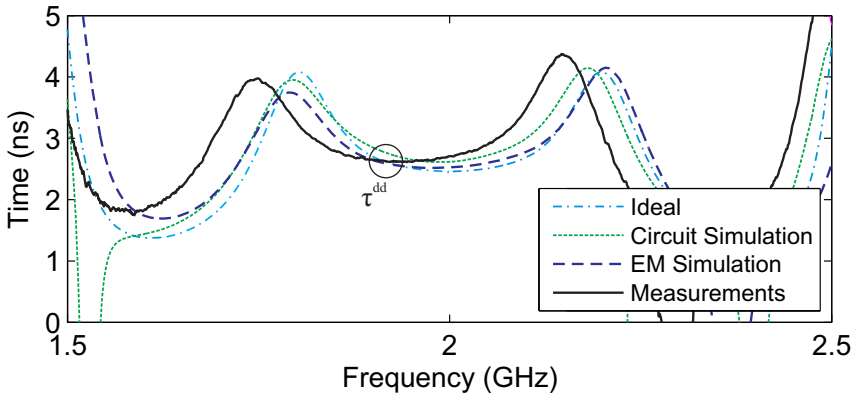

Figure 5.39: Ideal, simulated (circuit and EM model) and measured group-delay (τ_g^{dd}) responses of the manufactured microstrip balanced single-band BPF prototype in differential mode [150].

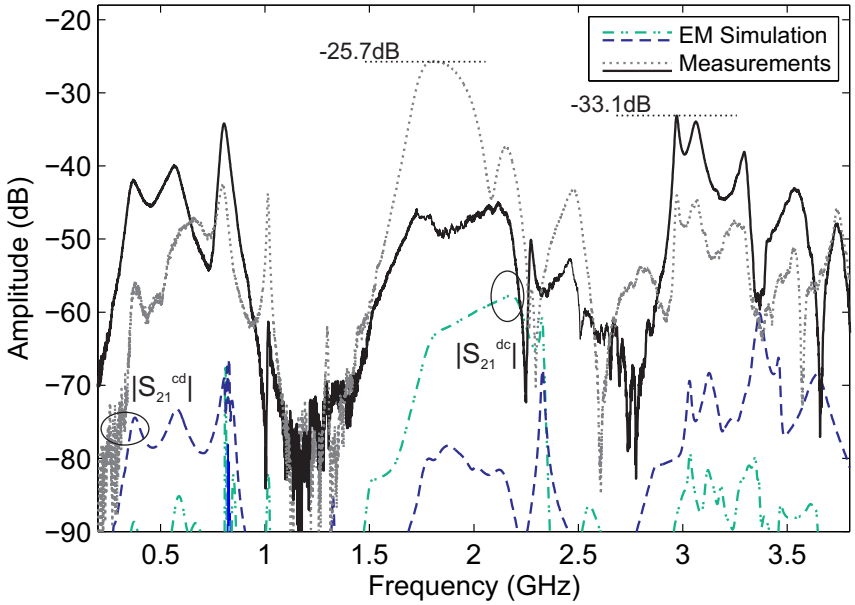

Figure 5.40: Simulated and measured common-to-differential-mode ($|S_{21}^{cd}|$) and differential-to-common-mode ($|S_{21}^{dc}|$) power transmission responses of the manufactured microstrip balanced single-band BPF prototype [150].

than 25.7 and 33.1 dB for the band of interest.

5.4 Conclusion

This chapter has presented novel classes of RF/microwave dual-function planar circuits based on signal-interference techniques. Through the strategic incorporation of signal-interference TFSs into conventional mono-function circuits, high-selectivity filtering actions with multiple TZs can be attained while featuring the processing action inherent to the original device itself. Unlike previously reported multi-function

devices with filtering capability, this philosophy is generalized for any number of operative frequencies from moderate-to-UWB specifications. Although a signal-interference TFS shaped by two in-parallel transmission-line segments is adopted in the realizations of this study, other classes of signal-interference TFSs can be utilized, such as stepped-impedance-line-based ones for frequency-asymmetrical multi-band designs. Moreover, since coupled-line stages are avoided, pure-lumped-element realizations can be used in order to reduce its physical size. In particular, this technique is applied to three types of microwave devices: Wilkinson-type filtering power dividers, filtering impedance transformers, and balanced filters.

Concerning Wilkinson-type power dividers with single/multi-band filtering capability, the design equations and guidelines for its theoretical synthesis have been provided. Besides, they have been generalized to multi-stage arrangements and even frequency-asymmetrical designs. For practical validation, triple- and quad-band microstrip prototypes and a dual-band lumped-element-based prototype for the spectral ranges 1-5 GHz and 0.2-0.6 GHz, respectively, have been synthesized, built, and tested. The potential of the suggested filtering power dividers has been exploited in more-sophisticated RF/microwave filtering components through the realization of a modified two-branch channelized active BPF. By using this filtering/power-divider structure for its single-band signal-division/combination stages, a more efficient implementation presenting greater selectivity and smaller size than its conventional counterpart is attained.

In relation to filtering/impedance-transforming circuits, the analytical formulas and guidelines for the synthesis of single- and multi-band realizations have been expounded. The extension of such technique to multi-stage designs is also provided. Furthermore, a dual-band prototype in the frequency range from 1.5 to 4.5 GHz and an UWB single-band prototype in the spectral range from 2 to 4 GHz have been successfully designed, built, and characterized in order to demonstrate its practical viability.

Finally, balanced BPFs based on embedded signal-interference TFSs have been also demonstrated. The design guidelines for its theoretical synthesis have been expounded along with two design examples for single- and dual-band cases, both formed by two dissimilar TFSs. Aside from the high-selectivity and sharp-rejection capabilities attained in the differential mode of operation, high in-band power-attenuation levels in the common mode of operation have been proved. Note that the use of dissimilar TFSs allows to broaden the bandwidth of the rejected bands in the differential-mode transfer function through the generation of a higher number of TZs at distinct spectral locations. Besides, this type of balanced signal-interference filters presents a significant advantage when compared to traditional single-ended signal-interference ones for further selectivity enhancement. This is because the signal propagation is canceled at the even harmonic frequencies of f_d. As a proof of concept, a two-stage balanced single-band BPF centered at about 2 GHz was built in microstrip technology and tested. Note that it exhibits higher common-mode power-rejection levels than most of the related prior-art circuits.

Chapter 6

Conclusions

This chapter summarizes the major contributions and results derived from this Ph.D. Dissertation in Section 6.1. It also includes a description of the future research lines in Section 6.2. The chapter concludes with a list of the publications obtained from the main contributions of this Ph.D. Thesis in Section 6.3.

6.1 Concluding remarks

This Doctoral Thesis have accomplished the synthesis and realization of advanced microwave filtering devices based on signal-interference principles. The main contributions and conclusions derived from the research activities carried out within the framework of this Thesis are recapitulated in this section.

In the first part, two design aspects not usually contemplated in signal-interference filters have been addressed through the combination of common classic filtering techniques with such structures. They are the improvement of filter selectivity without nearly deteriorating the in-band group-delay variation and the attainment of spectrally-asymmetrical transfer functions. For the former, an engineered multi-TZ-generation transversal cell is added to the input/output terminals of a basic filter, giving rise to two signal-propagation paths. By doing so, several TZs are created in the stopband regions, whereas the in-band characteristics—amplitude and group-delay variation—are almost preserved. Note that this approach has been tested for diverse filtering profiles. With regard to obtaining frequency responses with spectral asymmetry, stub-loading procedures have been adopted. It has been demonstrated that the incorporation of short-circuited stubs in strategic points of the signal-interference TFSs results in spectrally-asymmetrical transfer functions exhibiting broader bandwidth and greater rejection levels for their attenuated bands. These enhancements make signal-interference filter architectures more suitable for their use in digital communication systems for the first case and for multi-standard communication systems for the second one.

The second part of this work has concentrated on the proposal of fully-lumped- and hybrid distributed/lumped-element realizations of signal-interference filters in order to reduce their physical size. With this aim, three different design approaches

have been devised: 1) the replacement of electrically-short transmission-line segments with LC T-type transversal networks, 2) the miniaturization of 90°-electrically-long-at-f_d transmission-line segments by means of capacitive-loading techniques, and 3) the development of lumped-element quadrature-coupler-based signal-interference TFSs. All three approaches attain a remarkable size reduction when compared to their fully-distributed-element counterparts, which is a feature highly-demanded in RF systems operating in the lower part of the microwave band.

The third part has presented a new family of mixed-technology SAW/microstrip signal-interference BPFs. As a result, the suitability of signal-interference filters—conceived for moderate-to-ultra-narrow-band designs in the first instance—is extended to narrow-band bandpass filtering specifications. Its principle is to embed SAW resonators or SAW RF filters into the branches of conventional signal-interference TFSs, so that the high-Q features of the SAW device are substantially or partially transferred to the overall BPF. It should be noticed that such narrow-band bandwidths are unachievable by means of fully-distributed-element signal-interference implementations due to large occupied area and the significant insertion losses associated with the planar substrate.

Lastly, signal-interference dual-function microwave devices have been successfully developed in the fourth part. By exploiting the incorporation of bi-path signal-interference TFSs, Wilkinson-type power dividers, impedance transformers, and balanced filters with added single/multi-band filtering capabilities have been conceived. Thus, highly-selective filtering actions with multiple TZs and the processing action inherent to the original device can be simultaneously attained. Note that, unlike most of prior-art multi-function microwave devices exhibiting filtering actions, this methodology has been generalized for an arbitrary number of passbands.

Moreover, it must be highlighted the high experimental content of this Ph.D. Dissertation with the design, manufacturing, and characterization of seventeen physical prototypes in PCB technology for a variety of frequency ranges. In addition, other six prototypes have been simulated at the layout level. They all show a good compromise between predicted and measured results, fully validating the approaches described in this work as well as the theoretical foundations behind them.

6.2 Future research lines

This Ph.D. Dissertation have addressed some existing limitations of conventional signal-interference RF/microwave filters. Nevertheless, new research lines can be envisaged from the results obtained in this work. Here is a brief summary of these lines:

- Up to now, the majority of microwave filters based on signal-interference principles have been manufactured in conventional planar technologies. However, with the advent of the new generation of mobile communications (5G) and other millimeter-wave systems, the demand for millimeter-wave filters is being relaunched. The physical implementation of signal-interference filter structures in other types of technologies more suitable for high frequencies, such as

substrate integrated waveguide (SIW), needs therefore to be explored.

- With regard to the multi-TZ-generation transversal cell of Chapter 2 aimed at enhancing the selectivity of a given basic filter without damaging its in-band group-delay variation, its realization could be addressed through lumped-element approaches. Note that, in some of the manufactured prototypes, the area occupied by the coupled-line stage is even larger than that of the original filter. Thus, such investigation could lead to more-compact designs.

- The lumped-element equivalent circuits devised in Chapter 3 aimed at reducing the size of bi-path signal-interference TFSs at low microwave frequencies could be extended to other classes of signal-interference TFSs. For example, those based on hybrid couplers arranged in reflection mode and for bandstop-type response.

- The incorporation of lumped elements into signal-interference TFSs could be exploited for tuning purposes by replacing the fixed capacitors with electronically-controllable ones.

- In relation with the narrow-band signal-interference BPFs of Chapter 4 based on the combined use of SAW/microstrip technology, another family of high-Q resonators could be employed. Thus, the undesired effect of the SAW-resonator spurious modes over the overall frequency response—leading to the appearance of deep in-band notches—could be avoided.

- Chapter 5 has corroborated the practical usefulness of signal-interference transversal filtering networks for the achievement of dual-function microwave devices. Moreover, the potential of this type of structures has been already proven on more-complex devices such as a channelized active BPF. This opens the door to its application to many other microwave devices with the purpose of providing them with single/multi-band filtering capabilities. For example, balanced-to-unbalanced circuits or Butler matrices with added filtering functionality.

6.3 List of publications

The scientific contributions developed in this Ph.D. Thesis have been published in several international journals and conferences. Some of these publications have been already cited in previous chapters. In total, this Doctoral Thesis has resulted in 2 international journals, 11 international conferences—another work has been recently submitted—and 1 workshop that are subsequently listed, in chronological order, in Sections 6.3.1, 6.3.2, and 6.3.3. Moreover, 1 additional international journal and 2 additional international conferences somehow related to the content of this Ph.D. Thesis are enumerated in Section 6.3.4

6.3.1 International journals

[**J1**] R. Gómez-García, **R. Loeches-Sánchez**, D. Psychogiou, and D. Peroulis, "Single/multi-band Wilkinson-type power dividers with embedded transversal filtering sections and application to channelized filters," *IEEE Trans. Circuits Syst. I, Reg. Papers*, vol. 62, no. 6, pp. 1518–1527, Jun. 2015.

[**J2**] R. Gómez-García, D. Psychogiou, **R. Loeches-Sánchez**, and D. Peroulis, "Hybrid surface-acoustic-wave/microstrip signal-interference bandpass filters," accepted in *IET Microw. Antennas Propag.,* 2016.

6.3.2 International conferences

[**C1**] **R. Loeches-Sánchez**, R. Gómez-García, B. Jarry, J. Lintignat, and B. Barelaud, "Lumped-element-based single/dual-passband analog filters using signal-interference principles," in *2012 IEEE Int. Conf. on Electronics, Circuits and Systems,* Seville, Spain, Dec. 9–12, 2012, pp. 252–255.

[**C2**] **R. Loeches-Sánchez**, and R. Gómez-García, "A type of lumped-element-based analog filters based on transversal circuit networks," in *2013 IEEE Int. Circuits Syst. Symp.,* Beijing, China, May 19–23, 2013, pp. 1272–1275.

[**C3**] M. Sánchez-Renedo, R. Gómez-García, and **R. Loeches-Sánchez**, "Microstrip filters with selectivity improvement using the new concept of signal-interference source/load coupling," in *2013 IEEE MTT-S Int. Microw. Symp.,* Seattle, WA, USA, Jun. 2–7, 2013, pp. 1–4.

[**C4**] **R. Loeches-Sánchez,** M.-Á. Sánchez-Soriano, and R. Gómez-García, "Frequency-asymmetrical signal-interference microwave planar filters based on stub-loaded transversal filtering sections," in *2014 IEEE Radio Wireless Symp.*, Newport Beach, CA, USA, Jan. 19–23, 2014, pp. 160–162.

[**C5**] **R. Loeches-Sánchez**, D. Psychogiou, D. Peroulis, and R. Gómez-García, "A class of planar multi-band Wilkinson-type power divider with intrinsic filtering functionality," in *2015 IEEE Radio Wireless Symp.*, San Diego, CA, USA, Jan. 25–28, 2015, pp. 138–140.

[**C6**] **R. Loeches-Sánchez**, D. Psychogiou, D. Peroulis, and R. Gómez-García, "Sharp-rejection highpass and dual-band bandpass planar filters with multi-transmission-zero-generation transversal cell," in *2015 IEEE Radio Wireless Symp.,* San Diego, CA, USA, Jan. 25–28, 2015, pp. 147–149.

[**C7**] D. Psychogiou, D. Peroulis, **R. Loeches-Sánchez**, and R. Gómez-García, "Analog signal-interference narrow-band bandpass filters with hybrid transmission-line/SAW-resonator transversal filtering sections," in *2015 IEEE Int. Circuits Syst. Symp.,* Lisbon, Portugal, May 24–27, 2015, pp. 281–284.

[**C8**] R. Gómez-García, D. Psychogiou, **R. Loeches-Sánchez**, and D. Peroulis, "Bandwidth enlargement in acoustic-wave RF bandpass filters with planar

transversal circuits," in *45th Eur. Microw. Conf.,* Paris, France, Sep. 7–10, 2015, pp. 426–429.

[C9] **R. Loeches-Sánchez**, D. Psychogiou, R. Gómez-García, and D. Peroulis, "Miniaturized signal-interference planar filters," in *45th Eur. Microw. Conf.,* Paris, France, Sep. 7–10, 2015, pp. 542–545.

[C10] **R. Loeches-Sánchez**, D. Psychogiou, R. Gómez-García, and D. Peroulis, "Transformers with incorporated filtering capabilities exploiting signal-interference principles," in *2015 IEEE Int. Conf. Commun. Antennas and Electron. Syst.,* Tel Aviv, Israel, Nov. 2–4, 2015, pp. 1–5.

[C11] **R. Loeches-Sánchez**, D. Psychogiou, R. Gómez-García, and D. Peroulis, "Application of capacitive-loading size-reduction techniques to multi-band and reconfigurable-bandwidth signal-interference planar bandpass filters," accepted in *2016 IEEE Radio Wireless Symp.*, Austin, TX, USA, Jan. 24–27, 2016.

[C12] **R. Loeches-Sánchez**, D. Psychogiou, R. Gómez-García, and D. Peroulis, "A class of differential-mode single/dual-band bandpass planar filters based on signal-interference techniques," submitted to *IEEE Wireless and Microw. Tech. Conf.,* Clearwater, FL, USA, April. 11–13, 2016.

6.3.3 Workshops

[W1] R. Gómez-García, M. -A. Sánchez-Soriano, M. Sánchez-Renedo, **R. Loeches-Sánchez**, G. Torregrosa-Penalva, and E. Bronchalo, "Multi-function filtering devices based on signal-interference techniques," in the workshop *Recent Advances on RF/Microwave Multi-Function Filtering Devices*, in *2013 IEEE MTT-S Int. Microw. Symp.*, Seattle, WA, USA, Jun. 2–7, 2013.

6.3.4 Other publications

[J3] D. Psychogiou, R. Gómez-García, **R. Loeches-Sánchez**, and D. Peroulis, "Hybrid acoustic-wave-lumped-element-resonators (AWLRs) for high-Q bandpass filters with quasi-elliptic frequency response," *IEEE Trans. Microw. Theory Tech.*, vol. 63, no. 7, pp. 2233–2244, Jul. 2015.

[C12] R. Gómez-García, M. Sánchez-Renedo, and **R. Loeches-Sánchez**, "Signal-interference microstrip duplexers," in *2013 IEEE Radio Wireless Symp.,* Austin, TX, USA, Jan. 20–23, 2013, pp. 175–178.

[C13] R. Gómez-García, **R. Loeches-Sánchez**, J.-M. Muñoz-Ferreras, J. P. Borrego, J. P, Magalhaes, N. B. Carvalho, J. M. N. Vieira, and F. Pérez-Martínez, "Dual-band lowpass/bandpass periodic-type microstrip filter with Long-Term-Evolution (LTE) service mitigation," in *2014 IEEE 5th Latin American Symp. on Circ. and Syst.*, Santiago, Chile, Feb. 25–28, 2014, pp. 1–4.

Bibliography

[1] A. E. Grant, and J. H. Meadows, *Communication Technology Update and Fundamentals*, 14th ed. Focal Press, Oxford, UK, 2014.

[2] D. Raychaudhuri, and M. Gerla, *Emerging Wireless Technologies and the Future Mobile Internet*. Cambridge University Press, New York, NY, USA, 2011.

[3] W. Webb, *Being Mobile: Future Wireless Technologies and Applications*. Cambridge University Press, Cambridge, UK, 2010.

[4] D. M. Pozar, *Microwave Engineering*, 2nd ed. Wiley, New York, NY, USA, 1998.

[5] R. J. Cameron, C. M. Kudsia, and R. R. Mansour, *Microwave Filters for Communication Systems*. John Wiley & Sons, Inc., Hoboken, NJ, USA, 2007.

[6] Ministerio de Industria, Energía y Turismo del Gobierno de España, "REAL DECRETO 863/2008," de 23 de mayo, por el que se aprueba el Reglamento de desarrollo de la Ley 32/2003, de 3 de noviembre, General de Telecomunicaciones, en lo relativo al uso del dominio público radioeléctrico.

[7] I. Hunter, *Theory and Design of Microwave Filters, IET Electromagnetic Wave Series*, no. 48. The Institution of Engineering and Technology, London, United Kingdom, 2006.

[8] J. S. Hong, and M. J. Lancaster, *Microstrip Filters for RF/Microwave Applications*, John Wiley & Sons, Inc., New York, NY, USA, 2001.

[9] C. Rauscher, "A new class of microwave active filters," in *IEEE Int. Microwave Symp. Dig.,* San Diego, CA, USA, May 23–27, 1994, pp. 605–608.

[10] R. Gómez-García and J. I. Alonso, "Design of sharp-rejection and low-loss wideband planar filters using signal-interference techniques," *IEEE Microw. Wireless Compon. Lett.,* vol. 15, no. 8, pp. 530–532, Aug. 2005.

[11] R. Gómez-García, M. Sánchez-Renedo, B. Jarry, J. Lintignat, and B. Barelaud, "A class of microwave transversal signal-interference dual-passband planar filters," *IEEE Microw. Wireless Compon. Lett.,* vol. 19, no. 3, pp. 158–160, March 2009.

[12] R. Gómez-García, J. M. Muñoz-Ferreras, and M. Sánchez-Renedo, "Microwave transversal six-band bandpass planar filter for multi-standard wireless applications," in *2011 IEEE Radio Wireless Symp.,* Phoenix, AZ, USA, Jan. 16–19, 2011, pp. 166–169.

[13] C. M. Cheng, and C. F. Yang, "Develop quad-band (1.57/2.45/3.5/5.2 GHz) bandpass filters on the ceramic substrate," *IEEE Microw. Wireless Compon. Lett.*, vol. 20, no. 5, pp. 268–270, May 2010.

[14] L. Y. Ren, "Quad-band bandpass filter based on dual-plane microstrip/DGS slot structure," *IET Electron. Lett.,* vol. 46, no. 10, pp. 691–692, May 2010.

[15] R. Gómez-García, J. I. Alonso, and D. Amor-Martín, "Using the branch-line directional coupler in the design of microwave bandpass filters," *IEEE Trans. Microw. Theory Techn.*, vol. 53, no. 10, pp. 3221–3229, Oct. 2005.

[16] R. Gómez-García, "High-rejection wideband signal-interference microstrip filters using rat-race couplers," *IEEE Electron. Lett.,* vol. 42, no. 20, pp. 1162–1163, Sep. 2006.

[17] R. Gómez-García, "Wide-band microwave bandpass filters with hybrid rings," in *2007 IEEE MTT-S Int. Microw. Symp.,* Honolulu, HI, USA, Jun. 3–8, 2007, pp. 739–742.

[18] M.-A. Sánchez-Soriano, E. Bronchalo, and G. Torregrosa-Penalva, "Compact UWB bandpass filter based on signal-interference techniques," *IEEE Microw. Wireless Compon. Lett.,* vol. 19, no. 11, pp. 692–694, Nov. 2009.

[19] W. J. Feng and W. Q. Che, "Ultra-wideband bandpass filter using broadband planar Marchand balun," *IEEE Electron. Lett.,* vol. 47, no. 3, pp. 198–199, Feb. 2011.

[20] R. Gómez-García, and M. Sánchez-Renedo, "Microwave single/multi-band planar filters with Bagley-polygon-type four-port power dividers," in *IEEE MTT-S Int. Microw. Symp.,* Montreal, QC, Canada, Jun. 17–22, 2012, pp. 1-3.

[21] R. Gómez-García, M. A. Sánchez-Soriano, M. Sánchez-Renedo, G. Torregrosa-Penalva, and E. Bronchalo, "Low-pass and bandpass filters with ultra-broad stopband bandwidth based on directional couplers," *IEEE Trans. Microw. Theory Techn.,* vol. 61, no. 12, pp. 4365–4375, Dec. 2013.

[22] M. K. Mandal, P. Mondal, and S. Sanyal, "Low insertion loss, wideband bandpass filters with sharp rejection characteristics," *IET Microw. Antennas Propag.*, vol. 4,no. 1, pp. 99–105, Jan. 2010.

[23] M. A. Sánchez-Soriano, G. Torregrosa-Penalva, and E. Bronchalo, "Compact wideband bandstop filter with four transmission zeroes," *IEEE Microw. Wireless Compon. Lett.,* vol. 20, no. 6, pp. 313–315, Jun. 2010.

[24] H. R. Zhu, W. Shen, and J. F. Mao, "A novel bandstop filter with wide stopband using signal interference technology," in *2012 IEEE Int. Workshop Microw. and Millim. Wave Circuit and Sytem Tech.,* Chengdu, China, Apr. 19–20, 2012, pp. 1–4.

[25] Q. X. Chu, and L. L. Qiu, "Sharp-rejection bandstop filter based on signal-interference technique integrating with conventional open stubs," in *2014 IEEE MTT-S Int. Microw. Symp.,* Tampa, FL, Jun. 1–6, 2014, pp. 1–3.

[26] R. Gómez-García, M. Sánchez-Renedo, B. Jarry, J. Lintignat, and B. Barelaud, "Microwave multipath dual-passband filters for wide-band applications," in *2009 IEEE Eur. Microw. Conf.,* Roma, Italy, Sep. 29 – Oct. 1, 2009, pp. 109–112.

[27] R. Gómez-García, and M. Sánchez-Renedo, "Microwave dual-band bandpass planar filters based on generalized branch-line hybrids," *IEEE Trans. Microw. Theory Techn.,* vol. 58, no. 12, pp. 3760–3769, Dec. 2010.

[28] R. Gómez-García, and M. Sánchez-Renedo, "Application of generalized Bagley-polygon four-port power dividers to designing microwave dual-band bandpass planar filters," in *IEEE MTT-S Int. Microw. Symp.,* Anaheim, CA, May 23–28, 2010, pp. 580-583.

[29] M. A. Sánchez-Soriano, and R. Gómez-García, "Sharp-rejection wide-band dual-band bandpass planar filters with broadly-separated passbands," *IEEE Microw. Wireless Compon. Lett.,* vol. 25, no. 2, pp. 97–99, Feb. 2015.

[30] R. Gómez-García, J.M. Muñoz-Ferreras, and M. Sánchez-Renedo, "Signal-interference stepped-impedance-line microstrip filters and application to duplexers," *IEEE Microw. Wireless Compon. Lett.,* vol. 21, no. 8, pp. 421–423, Aug. 2012.

[31] C. Rauscher, "Microwave active filters based on transversal and recursive principles," *IEEE MTT-S Int. Microw. Symp.,*, vol. 33, no. 12, pp. 1350–1360, Dec. 1985.

[32] C. Rauscher, "Microwave channelized active filters A new modular approach to achieving compactness and high selectivity," in *IEEE MTT-S Int. Microw. Symp.,* vol. 44, no. 1, pp. 122-132, Jan. 1996.

[33] C. Rauscher, "Two-branch microwave channelized active bandpass filters," *IEEE MTT-S Int. Microw. Symp.,* vol. 48, no. 3, pp. 437–444, Mar. 2000.

[34] O. García-Pérez, A. García-Lampérez, V. González-Posadas, M. Salazar-Palma, and D. Segovia-Vargas, "Dual-band recursive active filters with composite right/left-handed transmission lines," *IEEE Trans. Microw. Theory Techn.,* vol. 57, no. 5, pp. 1180–1187, May 2009.

[35] S. Darfeuille, J. Lintignat, R. Gómez-García, Z. Sassi, B. Barelaud, L. Billonnet, B. Jarry, H. Marie, and P. Gamand, "Silicon-integrated differential bandpass filters based on recursive and channelized principles and methodology to compute their exact noise figure," *IEEE Trans. Microw. Theory Techn.,* vol. 54, no. 12, pp. 4381–4396, Dec. 2006.

[36] D. Segovia-Vargas, O. García-Pérez, V. González-Posadas, and F. Aznar-Ballesta, "Dual-band tunable recursive active filter," *IEEE Microw. Wireless Compon. Lett.,* vol. 21, no. 2, pp. 92–94, Feb. 2011.

[37] A. C. Guyette, "Design of fixed- and varactor-tuned bandstop filters with spurious suppression," in *40th IEEE Eur. Microw. Conf.,* Paris, France, Sep. 2010, pp. 288–291.

[38] M. A. Sánchez-Soriano and J. -S. Hong, "Reconfigurable lowpass filter based on signal interference techniques," in *2011 IEEE MTT-S Int. Microw. Symp.,* Baltimore, MD, USA, Jun. 5–10, 2011, pp. 1–4.

[39] M. A. Sánchez-Soriano, R. Gómez-García, M. Sánchez-Renedo, G. Torregrosa-Penalva, and E. Bronchalo, "Reconfigurable-bandwidth bandpass filter based on signal-interference techniques," in *2013 IEEE Eur. Microw. Conf.,* Nuremberg, Germany, Oct. 6–10, 2013, pp. 1035–1038.

[40] J. G. Proakis, *Digital Communications*, 5th ed. McGraw Hill, New York, NY, USA, 2008.

[41] H. -T. Hsu, H. -W. Yao, K. A. Zaki, and A. E. Atia, "Synthesis of coupled-resonators group-delay equalizers," *IEEE Trans. Microw. Theory Techn.,* vol. 50, no. 8, pp. 1960–1968, Aug. 2002.

[42] S. Amari and U. Rosenberg, "New building blocks for modular design of elliptic and self-equalized filters," *IEEE Trans. Microw. Theory Techn.*, vol. 52, no. 2, pp. 721–736, Feb. 2004.

[43] H. Shaman and J.-S. Hong, "Wideband bandstop filter with crosscoupling," *IEEE Trans. Microw. Theory Techn.,* vol. 55, no. 8, pp. 1780–1785, Aug. 2007.

[44] H. Shaman and J.-S. Hong, "Input and output cross-coupled wideband bandpass filter," *IEEE Trans. Microw. Theory Techn.,* vol. 55, no. 12, pp. 2562–2568, Dec. 2007.

[45] Datasheet of laminate substrate Taconic CER-10.
`http://www.taconic-add.com/pdf/cer10.pdf`

[46] Datasheet of laminate substrate Rogers RO4003C.
`https://www.rogerscorp.com/documents/726/acm/RO4000-Laminates---Data-sheet.pdf`

[47] Website of AWR Microwave Office software.
`http://www.awrcorp.com/es/products/microwave-office`

[48] Website of ANSYS HFSS software.
`http://www.ansys.com/es_es//Productos/Flagship+Technology/ANSYS+HFSS`

[49] Website of Sonnet software.
`http://www.sonnetsoftware.com/`

[50] Operating manual of HP 8720C Network Analyzer
`http://literature.cdn.keysight.com/litweb/pdf/08720-90135.pdf?id=621021`

[51] M. Sánchez-Renedo, R. Gómez-García, and R. Loeches-Sánchez, "Microstrip filters with selectivity improvement using the new concept of signal-interference source/load coupling," in *2013 IEEE MTT-S Int. Microw. Symp.,* Seattle, WA, USA, Jun. 2–7, 2013, pp. 1–4.

[52] S. Amari, U. Rosenberg, and J. Bornemann, "Singlets, cascaded singlets, and nonresonating node model for advanced modular design of elliptic filters," *IEEE Microw. Wireless Compon. Lett.,* vol. 14, no. 5, pp. 237–239, May 2004.

[53] R. Loeches-Sánchez, D. Psychogiou, D. Peroulis, and R. Gómez-García, "Sharp-rejection highpass and dual-band bandpass planar filters with multi-transmission-zero-generation transversal cell," in *2015 IEEE Radio Wireless Symp.,* San Diego, CA, USA, Jan. 25–28, 2015, pp. 147–149.

[54] R. Loeches-Sánchez, M. A. Sánchez-Soriano, and R. Gómez-García, "Frequency-asymmetrical signal-interference microwave planar filters based on stub-loaded transversal filtering sections," in *2014 IEEE Radio Wireless Symp.,* Newport Beach, CA, USA, January 19-22, 2014, pp. 160–162.

[55] I. J. Bahl, *Lumped Elements for RF and Microwave Circuits*, Artech House Microwave Library, Norwood, MA, USA, 2003.

[56] "IEEE Standard Letter Designations for Radar-Frequency Bands," *IEEE Std 521-2002*, pp. 1–3, Jan. 2003.

[57] M. A. Morgan and T. A. Boyd, "Theoretical and experimental study of a new class of reflectionless filter," *IEEE Trans. Microw. Theory Techn.,* vol. 59, no. 5, pp. 1214–1221, May 2011.

[58] K. W. Tam, P. Vitor, and R. P. Martins, "MMIC active filter with tuned transversal element," *IEEE Trans. Circuit Syst. II,* Analog Digit. Signal Process., vol. 45, pp. 632–634, May 1998.

[59] R. Loeches-Sánchez, and R. Gómez-García, "A type of lumped-element-based analog filters based on transversal circuit networks," in *2013 IEEE Int. Circuits Syst. Symp.,* Beijing, China, May 19–23, 2013, pp. 1272–1275.

[60] Datasheet of laminate substrate Taconic TLC-30.
`http://www.taconic-add.com/pdf/tlc.pdf`

[61] T. Hirota, A. Minakawa, and M. Muraguchi, "Reduced-size branch-line and rat-race hybrids for uniplanar MMIC's," *IEEE Trans. Microw. Theory Techn.,* vol. 38, no. 3, pp. 270–275, Mar. 1990.

[62] M. C. Scardelletti, G. E. Ponchak, and T. M. Weller, "Miniaturized Wilkinson power dividers utilizing capacitive loading," *IEEE Microw. Wireless Compon. Lett.,* vol. 12, no. 1, pp. 6–8, Jan. 2002.

[63] J.-T. Kuo, J.-S. Wu, and Y.-C. Chiou, "Miniaturized rat race coupler with suppression of spurious passband," *IEEE Microw. Wireless Compon. Lett.,* vol. 17, no. 1, pp. 46–48, Jan. 2007.

[64] S. Lee and Y. Lee, "Generalized miniaturization method for coupled-line band-pass filters by reactive loading," *IEEE Trans. Microw. Theory Techn.,* vol. 58, no. 9, pp. 2383–2391, Sep. 2010.

[65] E. Pistono, P. Ferrari, L. Duvillaret, J.-M. Duchamp, and A. Vilcot, "A compact tune-all bandpass filter based on coupled slow-wave resonators," in *35th Eur. Microw. Conf.,* Paris, France, Oct. 3–7, 2005, pp. 1–4.

[66] H. Issa, J. Duchamp, P. Ferrari, and S. Abou-Chahine, "Miniature DBR with series capacitive loading," in *2010 Mediterranean Microw. Symp.,* Guzelyurt, Turkey, Aug. 25–27, 2010, pp. 144–147.

[67] W.-H. Liao, C.-S. Chen, and Y.-S. Lin, "Single-chip integration of electronically switchable bandpass filter for 3.5GHz WiMAX application," in *2010 IEEE MTT-S Int. Microw. Symp.,* Anaheim, CA, USA, May 23–28, 2010, pp. 1368–1371.

[68] D. Psychogiou and D. Peroulis, "Tunable VHF miniaturized helical filters," *IEEE Trans. Microw. Theory Techn.,* vol. 62, no. 2, pp. 282–289, Feb. 2014.

[69] H. Ghali and T. A. Moselhy, "Miniaturized fractal rat-race, branch-line, and coupled-line hybrids," *IEEE Trans. Microw. Theory Techn.,* vol. 52, no. 11, pp. 2513–2520, Nov. 2004.

[70] D. Psychogiou and J. Hesselbarth, "Comparing miniaturization techniques for microstrip 180° hybrid ring junctions," in *2010 Mediterranean Microw. Symp.,* Guzelyurt, Turkey, Aug. 25–27, 2010, pp. 29–32.

[71] L. -G. Maloratsky, "Reviewing the basics of microstrip lines," *Microwaves and RF,* pp. 79–88, Mar. 2000.

[72] R. Loeches-Sánchez, D. Psychogiou, R. Gómez-García, and D. Peroulis, "Miniaturized Signal-Interference Planar Filters," in *45th Eur. Microw. Conf.,* Paris, France, Sep. 6–11, 2015.

[73] Datasheet of multi-layer high-Q capacitors Johanson S-series
`http://www.johansontechnology.com/downloads/JTI-CAT-MLCC-HighQ.pdf`

[74] Website of Advanced Design System software.
`http://www.keysight.com/en/pc-1297113/advanced-design-system-ads?cc=ES&lc=eng`

[75] Operating manual of Keysight E8361A Network Analyzer
`http://literature.cdn.keysight.com/litweb/pdf/E8361-90007.pdf?id=451064`

[76] J.-M. Muñoz-Ferreras and R. Gómez-García, "A digital interpretation of frequency-periodic signal-interference microwave passive filters," *IEEE Trans. Microw. Theory Techn.,* vol. 61, no. 11, pp. 2663–2640, Nov. 2014.

[77] R. Loeches-Sánchez, D. Psychogiou, R. Gómez-García, and D. Peroulis, "Miniaturized Capacitively-Loaded Multi-Band and Reconfigurable-Bandwidth Signal-Interference Planar Bandpass Filters," in *2016 IEEE Radio Wireless Symp.*, Austin, TX, USA, Jan. 24–27, 2016.

[78] M.-A. Sánchez-Soriano, R. Gómez-García, M. Sánchez-Renedo, G. Torregrosa-Penalva, and E. Bronchalo, "Reconfigurable-bandwidth bandpass filters based on signal-interference techniques," in *43rd Eur. Microw. Conf.,* Nuremberg, Germany, Oct. 6–10, 2013, pp. 1035–1038.

[79] C. J. Hwang, L. B. Lock, I. G. Thayne, and K. Elgaid, "W-band microstrip bandpass filter using branch-line coupler with open stubs," *Microw. Opt. Tech. Lett.,* vol. 52, no. 6, pp. 1436–1439, Jun. 2010.

[80] R. W. Vogel, "Analysis and design of lumped- and lumped-distributed-element directional couplers for MIC and MMIC applications," *IEEE Trans. Microw. Theory Techn.,* vol. 40, no. 2, pp. 253–262, Feb. 1992.

[81] R. Loeches-Sánchez, R. Gómez-García, B. Jarry, J. Lintignat, and B. Barelaud, "Lumped-element-based single/dual-passband analog filters using signal-interference principles," in *2012 IEEE Int. Conf. on Electronics, Circuits and Systems,* Seville, Spain, Dec. 9-12, 2012, pp. 252-255.

[82] J. Lee and K. Sarabandi, "A synthesis method for dual-passband microwave filters," *IEEE Trans. Microw. Theory Techn.*, vol. 55, no. 6, pp. 1163–1170, Jun. 2007.

[83] J.-E. Mueller, T. Bruder, P. Herrero, N. Norholm, P. Olesen, J. Rizk, and L. Schumacher, "Requirements for reconfigurable 4G front-ends," in *IEEE MTT-S Int. Microw. Symp. Dig.,* Seattle, WA, USA, Jun. 2–7, 2013, pp. 1–4.

[84] F. Z. Bi and B. P. Barber, "Bulk acoustic wave RF technology," *IEEE Microw. Mag.,* vol. 9, no. 5, pp. 65–80, Oct. 2008.

[85] C. Campbell, *Surface Acoustic Wave Devices for Mobile and Wireless Communications.* 1st Ed., Orlando, FL, USA: Academic Press, 1998.

[86] P. Warder, and N. Layus, "Selecting filters for challenging mobile applications worldwide," *Int. Microw. Journal,* vol. 56, no. 11, pp. 96–106, Nov. 2013.

[87] S. Gong and G. Piazza, "Design and analysis of Lithium-Niobate-based high electromechanical coupling RF-MEMS resonators for wideband filtering," *IEEE Trans. Microw. Theory Techn.,* vol. 61, no. 1, pp. 403–414, Jan. 2013.

[88] S. Gong and G. Piazza, "An 880 MHz ladder filter formed by arrays of laterally vibrating thin film Lithium Niobate resonators," in *IEEE 27th Int. MEMS Conf.,* San Francisco, CA, USA, Jan. 26–30, 2014, pp. 1241–1244.

[89] T. Omori, Y. Tanaka, K. Hashimoto and M. Yamaguchi, "Synthesis of frequency response for wideband SAW ladder type filters," in *IEEE Ultrason. Symp.,* New York, NY, USA, Oct. 28–311, 2007, pp. 2574–2577.

[90] G. Endoh, O. Kawachi, and M. Ueda, "A study of leaky SAW on piezoelectric substrate with high coupling factor," in *IEEE Ultrason. Symp.,* Caesars Tahoe, NV, USA, Oct. 17–20, 1999, pp. 309–312.

[91] S. Gong and G. Piazza, "Multi-frequency wideband RF filters using high electromechanical coupling laterally vibrating lithium niobate MEMS resonators," in *IEEE 26th Int. MEMS Conf.,* Taipei, Taiwan, Jan. 20–24, 2013, pp. 785–788.

[92] J. Meltaus, V. P. Plessky, A. Gortchakov, S. Harma, and M. M. Salomaa, "SAW filter based on parallel-connected CRFs with offset frequencies," in *IEEE Ultrason. Symp.,* Honolulu, HI, USA, Oct. 5–8, 2003, pp. 2073–2076.

[93] X. Lu, K. Mouthaan, and Y. T. Soon, "Wideband bandpass filters with SAW-filter-like selectivity using chip SAW resonators," *IEEE Trans. Microw. Theory Techn.,* vol. 62, no. 1, pp. 28–36, Jan. 2014.

[94] X. Lu, K. Mouthaan, and Y. T. Soon, "Wideband bandpass filters with high passband selectivity using SAW-like resonators," in *Asia-Pacific Microw. Conf.,* Seoul, Korea, Nov. 5–8, 2013, pp. 485–487.

[95] T. Lee, A. C. Guyette, E. J. Naglich, and D. Peroulis, "Coupling matrix-based SAW filter design," in *2014 IEEE MTT-S Int. Microw. Symp.,* Tampa, FL, USA, Jun. 1-6, 2014.

[96] J. D. Larson, R. C. Bradley, S. Wartenberg, and R. C. Ruby, "Modified Butterworth-Van Dyke circuit for FBAR resonators and automated measurement system," in *IEEE Ultrason. Symp.,* San Juan, PR, USA, Oct. 22–25, 2000, pp. 863–868.

[97] H. Campanella, *Acoustic wave and electromechanical resonators; concept to key applications.* 1st Ed., Norwood, MA, USA: Artech House, 2010.

[98] D. Psychogiou, D. Peroulis, R. Loeches-Sánchez, and R. Gómez-García, "Analog signal-interference narrow-Band bandpass filters with hybrid transmission-line/SAW-resonator transversal filtering sections," in *2015 IEEE Int. Circuits Syst. Symp.,* Lisbon, Portugal, May 24–27, 2015, pp. 281–284.

[99] Datasheet of 1-port SAW resonator Murata RO3101E-1
`www.rfm.com/products/data/ro3101e-1.pdf`

[100] J. Fleury, and O. Bernard, "Designing and characterizing TRL fixture calibration standards for device modeling," *Applied Microwave and Wireless,* vol. 13, no. 10, pp. 26–42, Oct. 2001.

[101] G. Tsuzuki, S. Ye, and S. Berkowitz, "Ultra selective HTS bandpass filter for 3G wireless application," *IEEE Trans. Applied Supercond.,* vol. 13, no. 2, pp. 261–264, Feb. 2003.

[102] J. -F. Seaux, S. Courreges, S. Bila, V. Madrangeas, M. Maignan, and C. Zanchi, "An eight pole self-equalised quasi-elliptic superconductor planar filter for satellite applications," in *35th Eur. Microw. Conf.,* Paris, France, Oct. 4–6, 2005.

[103] R. Gómez-García, D. Psychogiou, R. Loeches-Sánchez, and D. Peroulis, "Hybrid surface-acoustic-wave/microstrip signal-interference bandpass filters," *IET Microw. Antennas Propag.,* 2015.

[104] Datasheet of 1-port SAW resonator EPCOS R900
`http://media.digikey.com/pdf/Data%20Sheets/Epcos%20PDFs/B39431R900U410.pdf`

[105] Datasheet of SAW RF filter TDK B3718
`http://en.tdk.eu/inf/40/ds/ae/B3718.pdf`

[106] R. Gómez-García, D. Psychogiou, R. Loeches-Sánchez, and D. Peroulis, "Bandwidth enlargement in acoustic-wave RF bandpass filters with planar transversal circuits," in *45th Eur. Microw. Conf.,* Paris, France, Sep. 6–11, 2015.

[107] N. Yang, C. Caloz, and K. Wu, "Greater than the sum of its parts," *IEEE Microw. Mag.,* vol. 11, no. 4, pp. 69–82, Jun. 2010.

[108] R. Gómez-García, F. M. Ghannouchi, N. B. Carvalho, and H. C. Luong, "Advanced circuits and systems for CR/SDR applications," *IEEE J. Select. Emerging Topics Circuits Syst.,* vol. 3, no. 4, pp. 485–488, Dec. 2013.

[109] W. J. Chappell, E. J. Naglich, C. Maxey, and A. C. Guyette, "Putting the radio in Software-defined radio: Hardware developments for adaptable RF systems," *Proc. IEEE,* vol. 102, no. 3, pp. 307–320, Mar. 2014.

[110] Y.-S. Lin, J.-F. Wu, W.-F. Hsia, P.-C. Wang, and Y.-H. Chung, "Design of electronically switchable single-to-balanced bandpass low-noise amplifier," *IET Microw. Antennas Propag.,* vol. 7, no. 7, pp. 510–517, May 2013.

[111] Y. Yusuf, H. Cheng, and X. Gong, "Co-designed substrateintegrated waveguide filters with patch antennas," *IET Microw. Antennas Propag.,* vol. 7, no. 7, pp. 493–501, May 2013

[112] E. J. Wilkinson, "An N-way hybrid power divider," *IRE Microw. Theory Tech.,* vol. 8, no. 1, pp. 116–117, Jan. 1960.

[113] D. Psychogiou, Z. Yang, and D. Peroulis, "RF-MEMS enabled power divider with arbitrary power division ratio," in *42nd Eur. Microw. Conf.*, Amsterdam, The Netherlands, Oct. 28 Nov. 2, 2012, pp. 53–56.

[114] W. Chen, S. Zhang, Y. Liu, Y. Liu, and F. M. Ghannouchi, "A concurrent dual-band uneven Doherty power amplifier with frequency-dependent input power division," *IEEE Trans. Circuits Syst. I, Reg. Papers,* vol. 61, no. 2, pp. 552–561, Feb. 2014

[115] M. Bemani and S. Nikmehr, "Dual-band N-way series power divider using CRLH-TL metamaterials with application in feeding dual-band linear broadside array antenna with reduced beam squinting," *IEEE Trans. Circuits Syst. I, Reg. Papers,* vol. 60, no. 12, pp. 3239–3246, Dec. 2013.

[116] G.-C. Wu, G. Wang, J.-J. Sun, X.-J. Gao, and Y.-W. Wang, "Compact dual-band power divider based on dual composite right/left-handed transmission line," *IET Electron. Lett.,* pp. 759–761, vol. 50, no. 10, May 8th, 2014.

[117] R. Gómez-García, J.I. Alonso, and C. Briso-Rodríguez, "On the design of high-linear and low-noise two-branch channelized active bandpass filters, " *IEEE Trans. Circuits Syst. II, Analog Digit. Signal Process.,* vol. 50, no. 10, pp. 695–704, Oct. 2003.

[118] M. Chongcheawchamnan, S. Patisang, M. Krairiksh, and I. D. Robertson, "Tri-band Wilkinson power divider using a three-section transmission-line transformer," *IEEE Microw. Wireless Compon. Lett.,* vol. 16, no. 8, pp. 452–454, Aug. 2006.

[119] H. Zhang and H. Xin, "Designs of dual-band Wilkinson power dividers with flexible frequency ratios," in *2008 IEEE MTT-S Int. Microw. Symp.,* Atlanta, GA, USA, Jun. 15–20, 2008, pp. 1223–1226.

[120] M. J. Park, "Two-section cascaded coupled line Wilkinson power divider for dual-band applications," *IEEE Microw. Wireless Compon. Lett.,* vol. 19, no. 4, pp. 188–190, Apr. 2009.

[121] Y. Wu, Y. Liu, and Q. Xue, "An analytical approach for a novel coupled-line dual-band Wilkinson power divider," *IEEE Trans. Microw. Theory Techn.,* vol. 59, no. 2, pp. 286–294, Feb. 2011.

[122] N. Gao, G. Wu, and Q. Tang, "Design of a novel compact dual-band Wilkinson power divider with wide frequency ratio," *IEEE Microw. Wireless Compon. Lett.,* vol. 24, no. 2, pp. 81–83, Feb. 2014.

[123] R. Loeches-Sánchez, M.-Á. Sánchez-Soriano, and R. Gómez-García, "Frequency-asymmetrical signal-interference microwave planar filters based on stub-loaded transversal filtering sections," in *2014 IEEE Radio Wireless Symp.*, Newport Beach, CA, USA, Jan. 19–22, 2014, pp. 160–162.

[124] R. Loeches-Sánchez, D. Psychogiou, D. Peroulis, and R. Gómez-García, "A class of planar multi-band Wilkinson-type power divider with intrinsic filtering functionality," in *2014 IEEE Radio Wireless Symp.*, San Diego, CA, USA, Jan. 25–28, 2015, pp. 138–140.

[125] R. Gómez-García, R. Loeches-Sánchez, D. Psychogiou, and D. Peroulis, "Single/multi-Band Wilkinson-type power dividers with embedded transversal filtering sections and application to channelized filters," *IEEE Trans. Circuits Syst. I, Reg. Papers,* vol. 62, no. 6, pp. 1518–1527, Jun. 2015.

[126] G. Matthaei, E. M. T. Jones, and L. Young, *Microwave Filters, Impedance-Matching Networks, and Coupling Structures.* Norwood, MA: Artech House, 1980.

[127] Datasheet of RF amplifier RFMD RF3376
`http://www.rfmd.com/store/downloads/dl/file/id/28441/rf3376_data_sheet.pdf`

[128] K. L. Wu and W. Meng, "A direct synthesis approach for microwave filters with a complex load and its application to direct diplexer design," *IEEE Trans. Microw. Theory Techn.,* vol. 55, no. 5, pp. 1100–1017, May 2007.

[129] Datasheet of on-chip resistor Vishay PAT series
`http://www.vishay.com/docs/60024/pat.pdf`

[130] R. Loeches-Sánchez, D. Psychogiou, R. Gómez-García, and D. Peroulis, "Transformers with incorporated filtering capabilities exploiting signal-interference principles," in *2015 IEEE Int. Conf. Commun. Antennas and Electron. Syst.,* Tel Aviv, Israel, Nov. 2–4, 2015.

[131] M. Kaur, S. Kakar, and D. Mandal, "Electromagnetic interference," in *3rd Int. Conf. Electronics Computer Technology,* Kanyakumari, India, Apr. 2011, vol. 4, pp. 1–5.

[132] W. Feng, W. Che, and Q. Xue, "The proper balance: overview of microstrip wideband balance circuits with wideband common mode supression," *IEEE Microw. Mag.,* vol. 16, no. 5, pp. 55–68, Jun. 2015.

[133] T.B. Lim, and L. Zhu, "A differential-mode wideband bandpass filter on microstrip line for UWB application," *IEEE Microw. Wireless Compon. Lett.,* vol. 19, no. 10, pp. 632–634, Oct. 2009.

[134] T. B. Lim, and L. Zhu, "Differential-mode ultra-wideband bandpass filter on microstrip line," *IET Electron. Lett.,* vol. 45, no. 22, pp. 1124–1125, Oct. 2009.

[135] X. H. Wu and Q.-X. Chu, "Differential wideband bandpass filter with high-selectivity and common-mode suppression," *IEEE Microw. Wireless Compon. Lett.,* vol. 23, no. 12, pp. 644–646, Dec. 2013.

[136] W. J. Feng, and W. Q. Che, "Novel wideband differential bandpass filters based on T-shaped structure," *IEEE Trans. Microwave Theory Techn.,* vol. 60, no. 6, pp. 1560–1568, Jun. 2012.

[137] W. J. Feng, W. Che, and Q. Xue, "Balanced filters with wideband common mode suppression using dual-mode ring resonators," *IEEE Trans. Circuits Syst. I, Reg. Papers,* vol. 62, no. 6, pp. 1499–1507, Jun. 2012.

[138] L. L. Qiu, and Q. X. Chu, "Balanced bandpass filter using stub-loaded ring resonator and loaded coupled feed-line," *IEEE Microw. Wireless Compon. Lett.,* vol. 25, no. 10, pp. 654–656, Oct. 2015.

[139] W. J. Feng, W. Che, Y. Ma, and Q. Xue, "Compact wideband differential bandpass filters using half-wavelength ring resonator," *IEEE Microw. Wireless Compon. Lett.,* vol. 23, no. 2, pp. 654–656, Feb. 2013.

[140] P. Vélez, J. Naqui, A. Fernández-Prieto, M. Durán-Sindreu, J. Bonache, J. Martel, F. Medina, and F. Martín, "Differential bandpass filters with common-mode suppression based on stepped impedance resonators (SIRs)," in *IEEE MTT-S Int. Microw. Symp.,* Seattle, WA, USA, Jun. 2–7, 2013, pp. 1–4.

[141] M. Sans, J. Selga, P. Vélez, A. Rodríguez, J. Bonache, V. E. Boria, and F. Martín, "Automated design of common-mode suppressed balanced wideband bandpass filters by means of aggressive space mapping," *IEEE Trans. Microwave Theory Techn.,* vol. 63, no. 12, pp. 3896–3908, Dec. 2015.

[142] X. H. Wang, H. L. Zhang, and B. Z. Wang, "A novel ultra-wideband differential filter based on microstrip line structures," *IEEE Microw. Wireless Compon. Lett.,* vol. 23, no. 3, pp. 128–130, Mar. 2013.

[143] X. H. Wang, Q. Xue, and W. W. Choi, "A novel ultra-wideband differential filter based on double-sided parallel-strip line," *IEEE Microw. Wireless Compon. Lett.,* vol. 20, no. 8, pp. 471–473, Aug. 2010.

[144] W. J. Feng, W. Q. Che, T. F. Eibert, and Q. Xue, "Compact wideband differential bandpass filter based on the double-sided parallel-strip line and transversal signal-interaction concepts," *IET Microw. Antennas Propag.,* vol. 6, no. 2, pp. 186–195, Apr. 2012.

[145] Y. H. Cho, and S. W. Yun, "Design of balanced dual-band bandpass filters using asymmetrical coupled lines," *IEEE Trans. Microwave Theory Techn.,* vol. 61, no. 8, pp. 2814–2820, Aug. 2013.

[146] L. Yang, W. W. Choi, K. W. Tam, and L. Zhu, "Balanced dual-band bandpass filter with multiple transmission zeros using doubly short-ended resonator coupled line," *IEEE Trans. Microwave Theory Techn.,* vol. 63, no. 7, pp. 2225–2232, Jul. 2015.

[147] J. Shi, and Q. Xue, "Dual-band and wide-stopband single-band balanced bandpass filters with high selectivity and common-mode suppression," *IEEE Trans. Microwave Theory Techn.,* vol. 58, no. 8, pp. 2204–2212, Aug. 2010.

[148] K. Wang, L. Zhu, S. W. Wong, D. Chen and, Z. C. Guo, "Balanced dual-band BPF with intrinsic common-mode suppression on double-layer substrate," *IET Electron. Lett.,* vol. 51, no. 9, pp. 705–707, Sep. 2015.

[149] A. Arbelaez-Nieto, E. Cruz-Perez, J. L. Olvera-Cervantes, A. Corona-Chavez, and H. Lobato-Morales, "The perfect balance - A design procedure for balanced bandpass filters," *IEEE Microw. Mag.,* vol. 16, no. 10, pp. 54–65, Nov. 2015.

[150] R. Loeches-Sánchez, D. Psychogiou, R. Gómez-García, and D. Peroulis, "A class of differential-mode single/dual-band bandpass planar filters based on signal-interference techniques," submitted to *IEEE Wireless and Microw. Tech. Conf.,* Clearwater, FL, USA, April. 11–13, 2016.